DIN 67SD4379
16 OCTOBER 1967

FINAL REPORT

VOYAGER SPACECRAFT

PHASE B, TASK D

VOLUME II (BOOK 3 OF 5)

SYSTEM DESCRIPTION

PREPARED FOR

GEORGE C. MARSHALL SPACE FLIGHT CENTER

UNDER MSFC CONTRACT NO. NAS8-22603

GENERAL ELECTRIC
MISSILE AND SPACE DIVISION
Valley Forge Space Technology Center
P.O. Box 8555 • Philadelphia 1, Penna.

VOLUME SUMMARY

The Voyager Phase B, Task D Final Report is contained in four volumes. The volume numbers and titles are as follows:

Volume I	Summary
Volume II	System Description
Book 1	Guidelines and Study Approach, System Functional Description
Book 2	Telecommunication
Book 3	Guidance and Control Computer and Sequencer Power Subsystem Electrical System
Book 4	Engineering Mechanics Propulsion Planet Scan Platform
Book 5	Design Standards Operational Support Equipment Mission Dependent Equipment
Volume III	Implementation Plan
Volume IV	Engineering Tasks
Book 1	Effect of Capsule RTG's on Spacecraft
Book 2	Applicability of Apollo Checkout Equipment
Book 3	Central Computer
Book 4	Mars Atmosphere Definition
Book 5	Photo-Imaging

VOYAGER TASK D
VOLUME II
SYSTEM DESCRIPTION

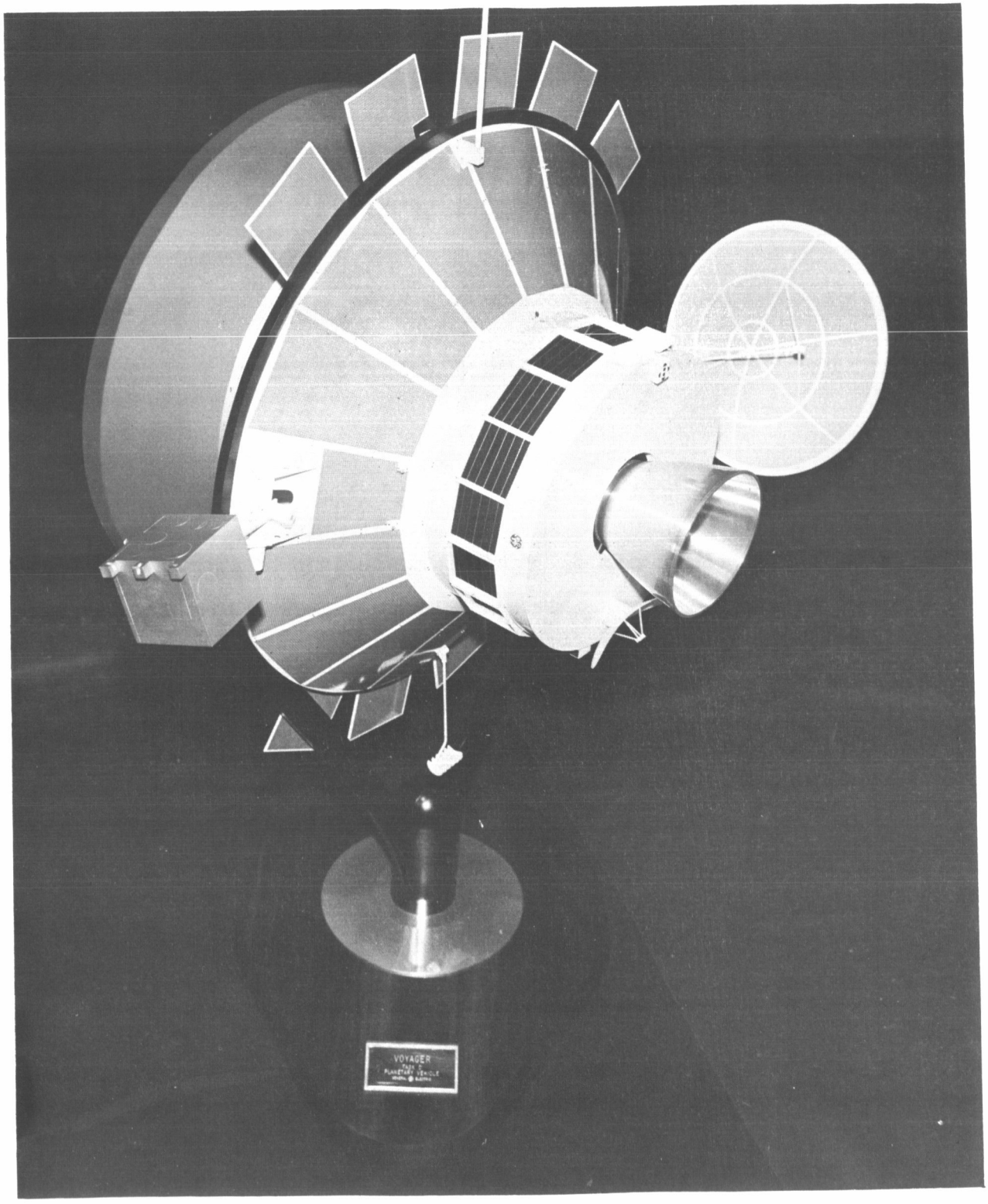

Voyager Planetary Vehicle (Task D)

VOYAGER TASK D
Volume II
PREFACE

This volume describes the design of the Voyager Spacecraft System, the Operational Support Equipment requirements, and the Mission Dependent Equipment requirements resulting from the system update study.

The mission concept for Voyager has not changed substantially since the previous Phase B, Task B study in late 1965. The Saturn V Launch Vehicle is used to inject two identical planetary vehicles on a Mars trajectory. Each planetary vehicle consists of a flight spacecraft and a flight capsule and, after separation from the Saturn V, the two vehicles provide complete mission redundancy. The flight spacecraft serves as a bus to deliver the flight capsule into Mars orbit from which it subsequently descends and soft lands to carry out surface experiments. The flight spacecraft then carries out an orbiting science mission for periods ranging from six months for early missions to two years for subsequent missions.

The flight spacecraft developed in this system update is shown in the illustration on the page opposite. This design is described in detail in this volume which is organized in the following major sections:

Section	Subject	Identification No.
I	Guidelines and Study Approach	VOY-D-100
II	System Functional Description and Analysis	VOY-D-200
III	Subsystem Functional Description and Analysis	VOY-D-300
IV	Design Standards	VOY-D-400
V	Operational Support Equipment	VOY-D-500
VI	Mission Dependent Equipment	VOY-D-600

Section I describes the study approach and discusses major constraints and guidelines that were imposed, with emphasis on requirements or guidelines which have changed since the last Voyager System design study.

Section II is a system level description of the resulting spacecraft design and its interfaces with other systems. Major system analyses and trade studies, such as trajectory and orbit selection, are covered.

Section III describes the baseline design of each subsystem, with discussion of alternates that were considered in arriving at the selected design.

Section IV covers some limited areas of design standards to be applied to the Voyager spacecraft.

Section V is an analysis of Operational Support Equipment (OSE) requirements and an evaluation of a number of OSE concepts with selection of a preferred approach.

Section VI analyzes the space flight operation together with the current and planned capabilities of the deep space network to define probable requirements for mission dependent hardware and software to support the mission.

VOY-D-320
GUIDANCE AND CONTROL

VOY-D-320
GUIDANCE AND CONTROL

1. DESCRIPTION

Voyager Guidance and Control is comprised of three equipment subsystems: attitude control, cold gas jet, and autopilot. The functional relation between these three is depicted in Figure 1. The electronic assembly of this subsystem is shown in Figure 2. The sensor and reaction control location on the spacecraft is shown on Figure 3.

These subsystems maintain the spatial attitude of the Voyager Spacecraft during the four major mission phases: cruise, maneuver, guidance correction, and orbital.

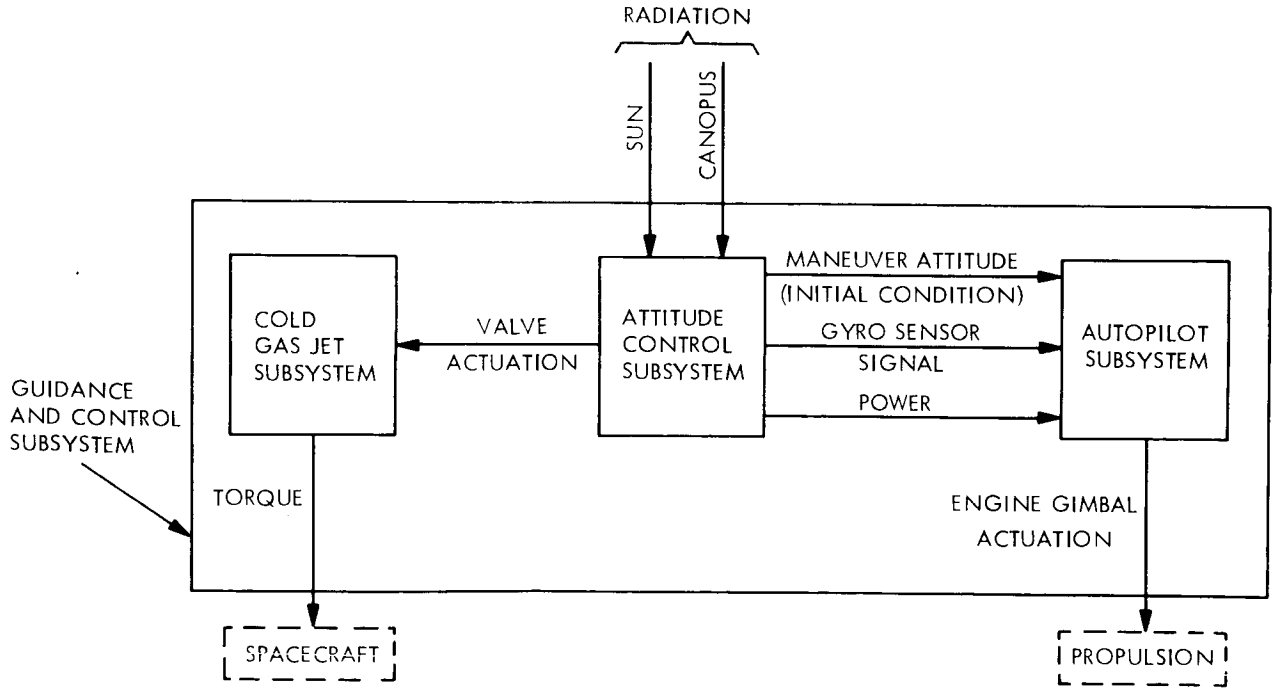

Figure 1. Guidance and Control Subsystem Block Diagram

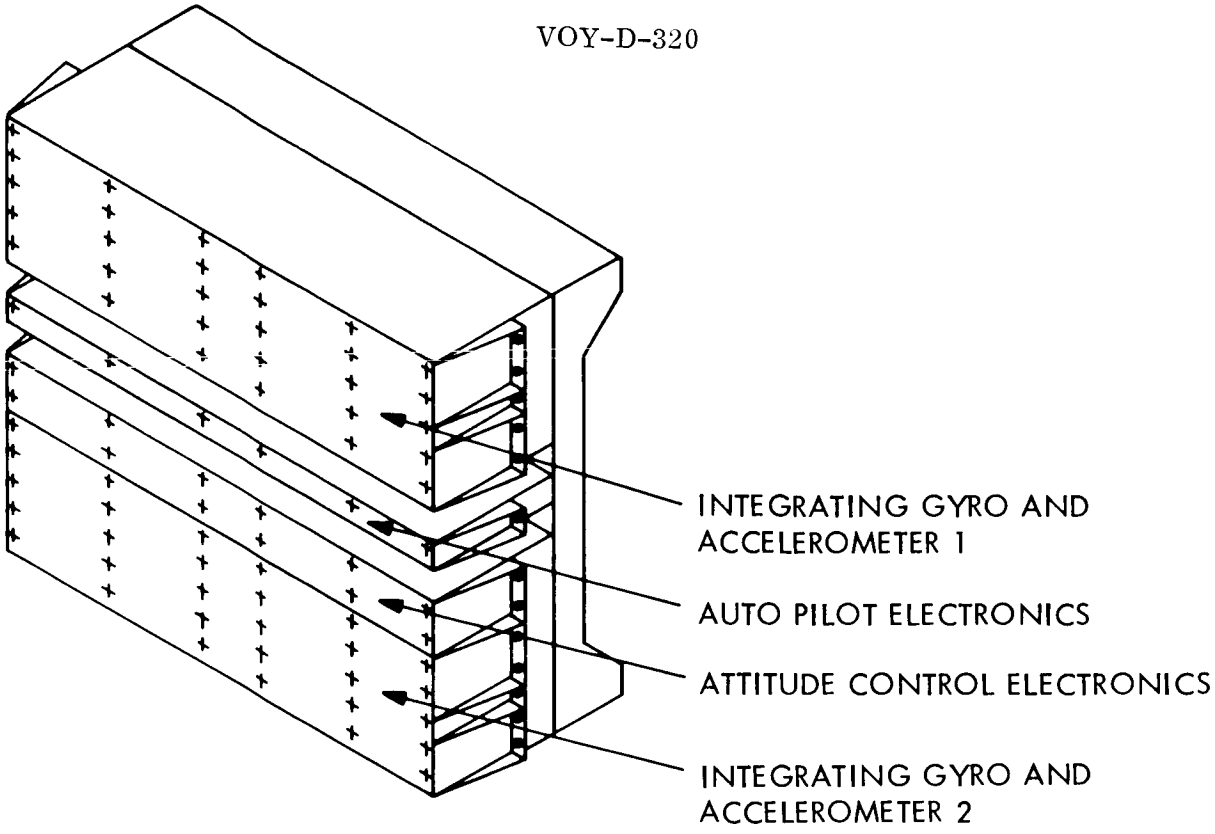

Figure 2. Guidance and Control Electronic Assembly

1.1. ATTITUDE CONTROL

The attitude control subsystem acquires and stabilizes the spacecraft to the external attitude references from any initial attitude and rates up to 3 degrees per second. It then maintains the spacecraft attitude relative to these references to less than 3/4 degree during the heliocentric cruise and Mars orbital phases. It also maneuvers the spacecraft, by sequential rotations, to any arbitrary spatial attitude necessary to perform velocity change or capsule separation maneuvers.

The attitude control subsystem consists of: optical sensors (sun sensors in pitch and yaw, and star sensor in roll) to determine attitude deviations from the references; gyroscopes which provide rate signals during acquisition of references and position signals during maneuvers; and electronic circuitry which processes the sensor signals to operate the appropriate solenoid valves of the cold gas jet subsystem.

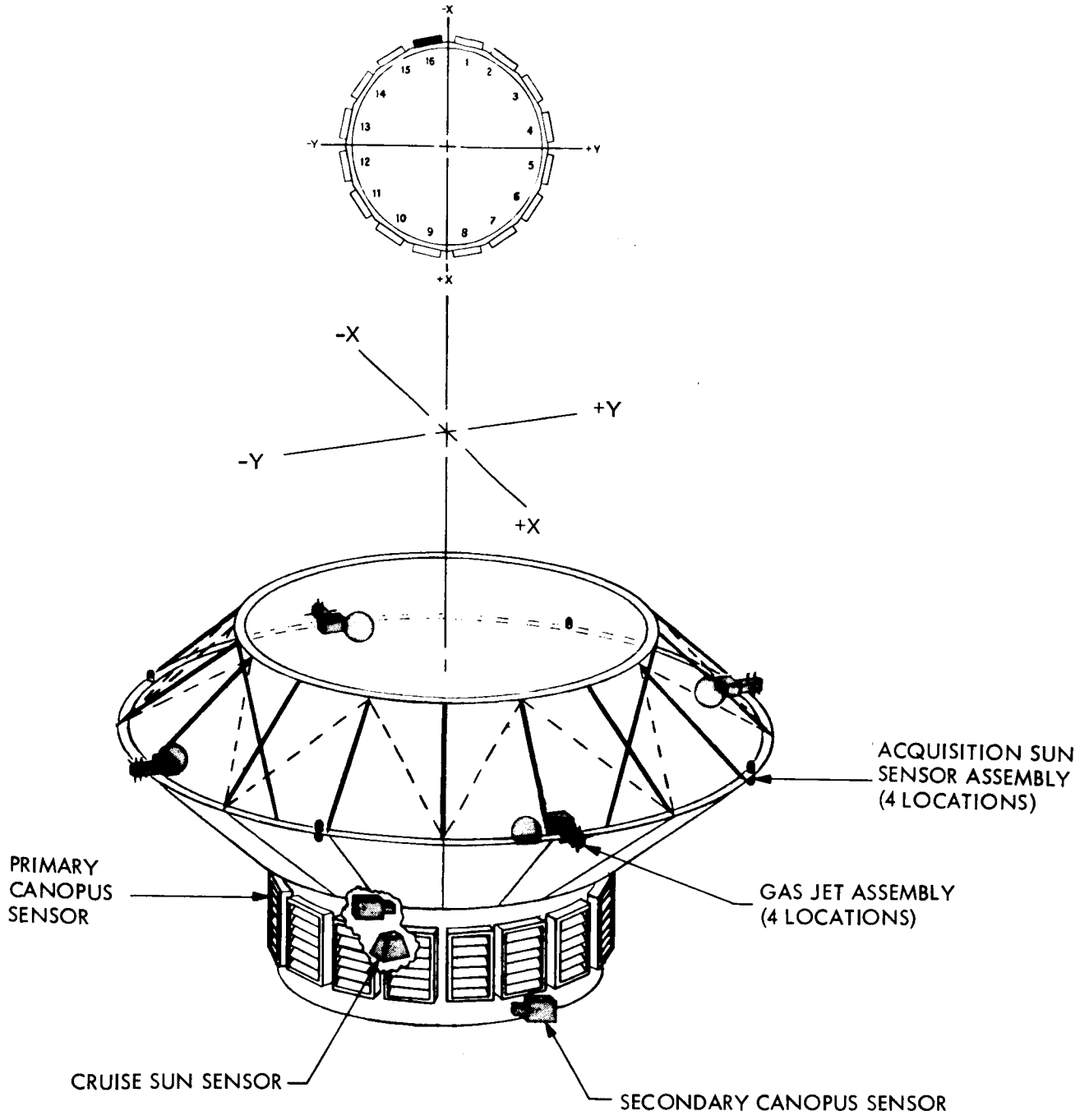

Figure 3. Guidance and Control Equipment Location

The subsystem has three basic functions or modes of operation: acquisition mode, cruise mode, and maneuver (or inertial) mode.

1.1.1. Acquisition Mode

In the acquisition mode, the roll star sensor is initially locked out, wide field of view sun sensors are used in pitch and yaw, and rate signals are provided by the gyroscopes. The system acquires the sun reference in two axes in less than 20 minutes from the start of acquisition. After this, the narrow field of view cruise sun sensors are switched in, the Canopus sensor enabled, and the vehicle is made to roll about the sun line in search of Canopus. When the star comes in the field of view of the sensor, acquisition is completed. The Canopus search and acquisition can take up to 70 minutes.

1.1.2. Cruise Mode

In the cruise mode, the cruise (narrow field of view) sun sensors are controlling pitch and yaw axes and the Canopus sensor controls the roll axis. The gyros are off and damping is obtained by derived rate.

1.1.3. Maneuver Mode

In the maneuver mode, the optical sensors are replaced by the gyros operating in position mode. Gyros are torqued in sequence to produce a vehicle rate about the desired axis. The time the gyros are torqued is controlled to yield the desired rotation. This same basic mode is employed during an inertial hold except that the gyro torquers are not energized.

1.2. REACTION CONTROL SUBSYSTEM

The reaction control subsystem applies torques to the spacecraft as required by the attitude control system to perform its function of acquiring and holding its references and to maneuver the spacecraft to desired attitudes.

The reaction control subsystem consists of tanks which contain the propellant (nitrogen), regulators, filters, fill valves, solenoid valves, and nozzles. The electrical signal which actuates the solenoid valves is provided by the attitude control system.

1.3. AUTOPILOT

The autopilot maintains the inertial attitude of the vehicle during propulsion thrusting. This subsystem consists of gyroscopes, signal processing electronics, rocket engine gimbal actuators, an accelerometer and switching logic. The mutual operation of these components perform the autopilot function. The gyroscopes are also used by the attitude control system and are described as part of that subsystem. The gimbal actuator requirements are developed in VOY-D-323 while the design studies are described in VOY-D-363.

The gyroscopes generate signals proportional to spacecraft angular position. These signals are processed by lead networks and amplifiers in the autopilot electronics.

1.4. PLANETARY SCAN PLATFORM CONTROL

The positioning control system of the PSP is described in VOY-D-380.

2. MISSION SEQUENCE

The operation of the G&C subsystem can be summarized in the context of the mission sequence. Shortly after separation from the launch vehicle, the attitude control subsystem is energized. It goes into its acquisition mode and stabilizes the Spacecraft to the Sun and Canopus. It is then in the cruise mode until the first midcourse maneuver which occurs several days after separation from the launch vehicle. At this point the attitude control subsystem is put into the maneuver mode and the Spacecraft is rotated to the desired attitude for execution of the midcourse maneuver. During rocket engine thrusting the maneuver attitude is maintained by the autopilot. After termination of thrusting, the attitude control subsystem goes into its acquisition mode and reacquires the Sun and Canopus.

The system is then in the cruise mode and continues in this mode until the second midcourse maneuver which may occur several weeks or months after the first. The sequence of the first maneuver is then repeated. At termination of that maneuver, the Sun and Canopus are reacquired. Cruise proceeds until the maneuver mode is again assumed and the Spacecraft is rotated to the appropriate attitude for the orbit insertion maneuver. During orbit insertion as the rocket engines are thrusting, the autopilot maintains the attitude of the vehicle. After orbit insertion has been accomplished, the attitude control system again reacquires the Sun and Canopus and the system is in the steady state cruise or orbit mode.

Finally, during the orbital phase of the mission, the references may be occulted by Mars. Inasmuch as this event is anticipated and accurately predictable in time, the attitude control system will be commanded to go into an occultation mode which will permit the attitude control system to go to an inertial hold mode while the references are occulted.

3. SYSTEM UPDATE

The guidance and control work that was performed as part of the over-all system update builds on and extends the previous work performed during the Task A, B and C studies. Many of the designs and decisions made previously are still valid and did not require re-evaluation. Among these are the choice of the Sun and Canopus as references, the use of an on-off attitude control system, and the use of gyros for the principal source of rate information during reference acquisitions. The studies that were performed fall into two general categories: those resulting from configuration, mission and system changes, and those resulting from technology changes.

An effort was made to provide an integrated system by considering the effects of the conclusions of each study both upon the system and the other related studies. Because all the work was done concurrently, there was insufficient time to complete this task. Certain of the trade study results are therefore not reflected in the system descriptions. However, no important technical interferences are known to exist.

VOY-D-320
GUIDANCE AND CONTROL

VOY-D-321
ATTITUDE CONTROL SUBSYSTEM

VOY-D-321
ATTITUDE CONTROL SUBSYSTEM

1. SCOPE

The attitude control subsystem controls the spacecraft angular orientation at all times except during rocket motor firing periods. It consists of sun sensors, a star sensor, rate integrating gyros, and processing electronics. A cold gas jet reaction control system receives electrical signals from the attitude control subsystem and, as a result of these signals, applies torques to the spacecraft. The reaction control system is described separately in section VOY-D-322. The system searches, acquires and stablizes the spacecraft to the sun and Canopus. This orientation is maintained except when establishing some desired orientation to perform a trajectory correction.

The present study was performed to update the system designs of Tasks A and B. Many decisions made previously are still valid and do not require re-evaluation. Among these are the choice of the sun and Canopus reference systems, the use of an on–off attitude control subsystem, and the use of gyros for the rate measurements during initial stabilization. The studies that were performed fell into two general categories: those resulting from configuration, mission, and system changes; and those resulting from technological changes.

2. TRADE STUDIES AND ANALYSES

2.1 PROPELLANT MOTION COUPLING WITH ATTITUDE CONTROL

2.1.1 Introduction

The selection of a liquid propulsion system to perform orbit insertion results in potential complications to the design of the spacecraft control system. The problem may be further increased when mission flexibility is increased by providing a single tank design for all launch opportunities. Typically, the propellant mass can be significantly greater than the rigid body mass. Depending on the particular mission or phase within a mission, it is possible for this large mass to have a considerable amount of freedom.

During the course of a Voyager mission, two different types of forces act on the propellant. These result in different dynamic equations of motion of the liquid propellant. During powered flight such as in midcourse maneuvers and orbit insertion, the rocket engine thrust causes spacecraft acceleration. It is this acceleration which defines the propellant motion, or slosh, during engine firing. The characteristics of this slosh and its effect on the control system is discussed in the autopilot subsystem section; VOY-D-323.

During cruise, the major external force acting on the spacecraft is from solar pressure, which results in very low translational accelerations. In this phase, the predominant force acting on the fluid is that of surface tension rather than acceleration. The Bond number, which is the ratio of acceleration to surface tension forces, is in this case low. The equations of motion of the propellant are dominated by the surface tension forces. The investigation of the fluid dynamics, the development of mathematically analogous systems, and the study of the interaction of the propellant dynamics with the control system are covered in this section.

A comprehensive analysis of the fluid motion at low bond numbers is not known to exist. This ask was undertaken during the systems update, however its completion is beyond the scope of the current program.

The objectives of the propellant motion studies initiated during the system update are: (a) to improve the quantitative understanding of the propellant dynamics at low gravity; (b) from this understanding to develop a model and (c) study the effect of this model on the operation of the control system. The emphasis during the system update has been on the first two of these. This work is summarized in the ensuing paragraphs and reported in detail in the appendices.

In view of the difficulties of obtaining solutions to specific fluid motion problems for clean, unobstructed tanks, it was decided that the current effort would not be concerned with the added analytical difficulties associated with baffles, screens, and containment devices in general. It is recognized that such devices may be very effective in reducing

or preventing propellant motions, and in this manner removing control system problems altogether. In the actual system, it is fully expected that these devices will be used and indeed they are described in the propulsion system part of this report. In view of the limited experience with containment devices, some question about their effectiveness exists. Hence, the more analytically tractable clean tank chosen for study represents a potentially real situtation.

2.1.2 Propellant Behavior at Low and Zero Gravity

Liquid propellant behavior at low and zero "g" has been investigated intensively during the system update, and some significant results have been obtained. The analysis which is described in appendix A, is based on an inviscid, incompressible flow theory.

The natural frequencies and modes of small oscillations of liquid in a rigid spherical tank with a spherical ullage have been determined, and a solution for the forced linear oscillations has also been obtained from which the effective mass can be calculated. The location of the ullage in the tank is arbitrary. In the literature, the solution was only available for the very special case in which the spherical ullage is located at the center of the spherical tank, but a wall-bound ullage is known to be a more stable configuration. The latter case, which is thus of the highest practical importance, particularly for the Voyager program, is naturally another special case of the general situation that has been investigated; the solution has thus become known.

The spherical shape of the ullage corresponds to the condition of zero "g". Furthermore, when the spherical ullage is wallbound, the contact angle is zero. In the more general case of low (but not zero) "g" and arbitrary contact angle, the sloshing problem has also been formulated. The first step is to determine the static configuration of the liquid-vapor interface. For a description of the interface, the spherical coordinates are used, in contrast to the common practice of using cylindrical coordinates, to avoid the possible difficulty of having to deal with a multiple-valued surface in the case of a spherical tank with a nearly spherical

ullage which represents the Voyager case. The general formulation of the low-g sloshing problem, however, is not restricted to the spherical tank.

A small study was performed to evaluate viscous effects. As anticipated, these were found to be negligible.

2.1.3 Modeling Studies

2.1.3.1 Introduction

Fluid modeling studies have been performed in parallel with the analytic studies of the dynamics of fluid motion. The initial efforts employed a single simple pendulum representing the sloshing mass as is done in high-g sloshing. Limitations of this model led to the development of a multimass model. The models have been developed intuitively, drawing on high-g fluid dynamics and on the dynamics of planar physical models representative of zero gravity. The validity of these models can only be established through comparison of model dynamics to the fluid dynamics for specific situations. Thus, the analytical studies are of critical importance.

2.1.3.2 Single Mass Pendulum Model

The single mass pendulum model is similar to the high-g model. Pendulum length remains constant while the pendulum mass is about 85 percent of the high-g pendulum mass representing sloshing in a deep cylindrical tank. The applicability is classically limited to small amplitude oscillations.

In an effort to accommodate the motion of the ullage throughout the tank, consideration has been given to a variable arm length pendulum model, but no convenient solution of this was found.

2.1.3.3 Multimass Model

The simple pendulum model did not account for the motion of the ullage that was observed in physical models. In particular, the physical models show the ullage leaving the walls and moving about the tank as rotation was developed in the fluid. As rotation progressed, the

ullage could rest on the axis of rotation. Translation of the tank can result in the ullage traveling across the tank. Both phenomena are inconsistent with the simple pendulum model, which has a constant armlength.

To surmount these difficulties, a multimass model was developed and is described in Appendix B. The model parameters are derived from physical properties of the system, i.e., the model duplicates the mass deployment of the fluid, with the result that the model is valid for translation and for rotation. The planar form of the model is shown in Figure 1. The point C is massless and serves as the pivot point for the masses m*. Point C moves in response to the motion of the masses m*. The radial lengths X_b (defining the ullage position) and X_c (defining the location of the pivot point) remain colinear. The arm length ℓ and the masses m* are fixed parameters, dependent on the fill ratio and the requirement that the model match physical properites of the system.

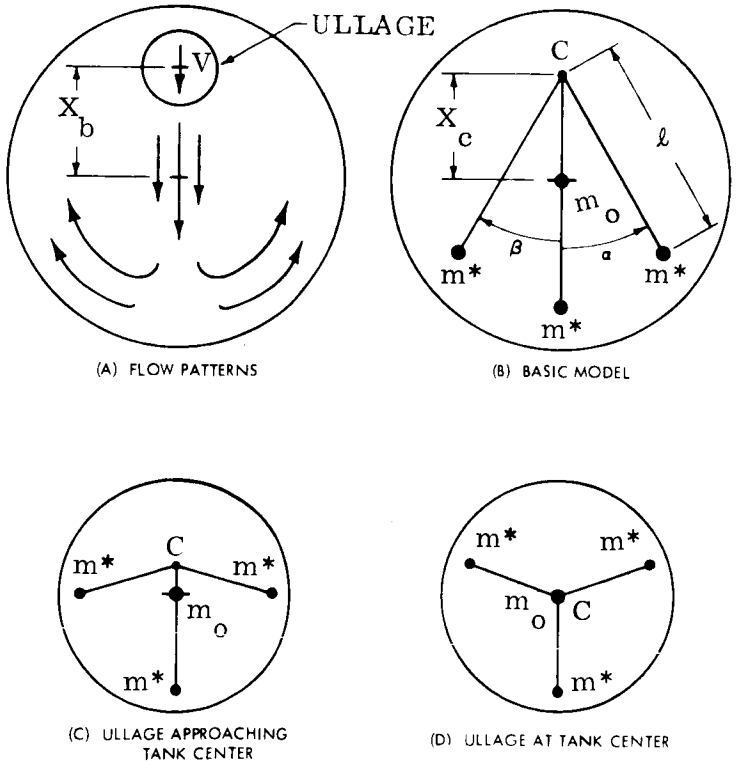

Figure 1. The Multimass Model

The motion of the model as the ullage translates toward the center consists of the pivot point C moving toward the center as the angles α and β increase. The off axis masses move along the streamlines shown in Figure 1. It is important to note that the cause/effect of this explanation are the reverse of the physical situation. This motion is produced when the tank receives a downward acceleration (producing a buoyant force on the ullage). The masses m* respond to the acceleration with their motion constrained by the fixed arm length ℓ.

Rotational motion produces centrifugal forces which move the masses m* toward the wall as the angles α and β increase. The pivot point C moves toward the center of the tank as the m* goes toward the wall corresponding to the motion of the ullage to the center of the tank.

2.1.4 Control System Operation

The viscous effects of the propellants on the operation of the control system were investigated for the following situation: the tanks are completely full (or very nearly so) and the control system is in a stable limit cycle.

The dynamics of the system can be approximated by:

$$T = (I_R + m_p \ell_p^2)\dot{\omega} + T_p \qquad T_p = C_p(\omega - \omega_p) = K I_p \dot{\omega}_p$$

where:

I_R = the moment of inertia of the rigid body part of the vehicle.

I_p = the moment of inertia of the propellant about its center of mass.

m_p = the propellant mass.

l_p = the distance of the propellant center of mass from the total spacecraft center of mass.

K = Inertia coefficient which is proportional to viscosity.

C_p = Viscous torque coupling coefficient.

Analytical studies of fluid motions have confirmed the expectation that viscous coupling is very small. Control system design can then be based on a rigid body system having an inertia

$$I' = I_R + m_p l_p^2$$

As further verification, the control system was simulated with the complete expression for torque using the viscous coupling as determined from the fluid studies. This simulation demonstrated that the limit cycle period of the complete formulation differs negligibly from the results using the simplified inertia I'.

2.2 SYSTEM MECHANIZATION

The various Attitude Control Subsystem configuration studies which were performed are reported in this section.

2.2.1 Alternate Acquisition Methods

Task Description: Determine whether alternate methods of acquisition should be provided in the event of failures in both integrating gyro packages. In the present Voyager attitude control subsystem, gyros are necessary to perform the following functions:

a. Initial acquisition and reacquisition.

b. Maneuvers.

c. Inertial control during occultation of celestial references in Mars orbit.

If failures occur in both gyro packages prior to Mars orbit insertion, the mission cannot be completed. This is true even if a method of acquisition without gyros is provided, because the spacecraft is no longer capable of maneuvering. Thus, midcourse guidance corrections and orbit insertion are not possible. In the presence of these gyro failures early in the mission, an alternate method of acquisition contributes little to mission success.

Once the vehicle is in orbit about Mars, the situation is different. The gyros' only remaining function, other than a possible orbital correction maneuver, is to provide an attitude reference when either of the celestial references is occulted. If after a gyro failure the vehicle can be controlled during or immediately after an occulation, the mission can be continued successfully. Otherwise the mission fails. If a method of acquisition can be provided to allow the spacecraft to recover control after an occulation, it would provide the difference between continued operation and immediate failure. It is assumed here that in the event of gyro failure, the spacecraft would be allowed to drift during an occultation, and that the reference would be beyond the sensor field-of-view at the end of the occultation.

Three methods of providing acquisition were considered. These are all relatively simple techniques, which require little or no additional equipment. More elaborate methods were not considered. The three control loops employ:

a. Celestial sensors followed by a lead network.

b. Celestial sensors plus torque integral feedback.

c. Celestial sensors plus a separate three-rate gyro package.

No attempt has been made to determine acquisition performance with a computer simulation. However, a qualitative estimate is that the first two systems could acquire about the yaw and pitch axes, although not as rapidly as the nominal system. This is possible because of the wide linear range of the acquisition sun sensors (±40 degrees). However, roll control cannot be accomplished because of the relatively narrow field-of-view of the Canopus sensor about the roll axis (±4 degrees). The third method provides acquisition in all three axes but at the cost of an additional gyro package.

The decision was made not to include any additional acquisition capability. For the spacecraft in orbit, this guards against all gyro failures, except failure of a gyro

in both gyro packages. It is felt there is no reason to single out this area to protect against multiple failures.

2.2.2 Sensor Field-of-View Requirements

Task Description: The present configuration requires eight sun sensors to provide 4 π steradian coverage with the flight capsule in place. It is possible to reduce the required coverage, and thereby the number of sun sensors, by modifying the acquisition procedure. A study was made to determine the most advantageous system.

The spacecraft is required to acquire the sun from any arbitrary initial attitude. There are two straightforward sun sensor configurations that can be used to accomplish this:

a. Provide 4 π steradian coverage. This is done on the present system.

b. Provide a sensor configuration with a limited field of view. Generate 4 π steradian coverage by rotating the sensor, probably by rotating the spacecraft. This method is used on Surveyor.

The second method is explained with the aid of Figure 2, which is based upon the Surveyor system. The acquisition sun sensor field-of-view is a 196 degree disk centered on the pitch axis, and 10 degrees wide. The following steps are performed to acquire the sun:

a. Eliminate initial vehicle angular rates about all three axes.

b. Roll. A 360 degree roll provides 4π steradian coverage.

c. Roll maneuver is stopped when the sun is acquired.

d. Yaw. Stop when narrow view sun sensor (field-of-view along the roll axis) acquires the sun.

The advantage of this system is that it requires fewer sun sensors. This is of minor value because sun sensors are light and highly reliable devices.

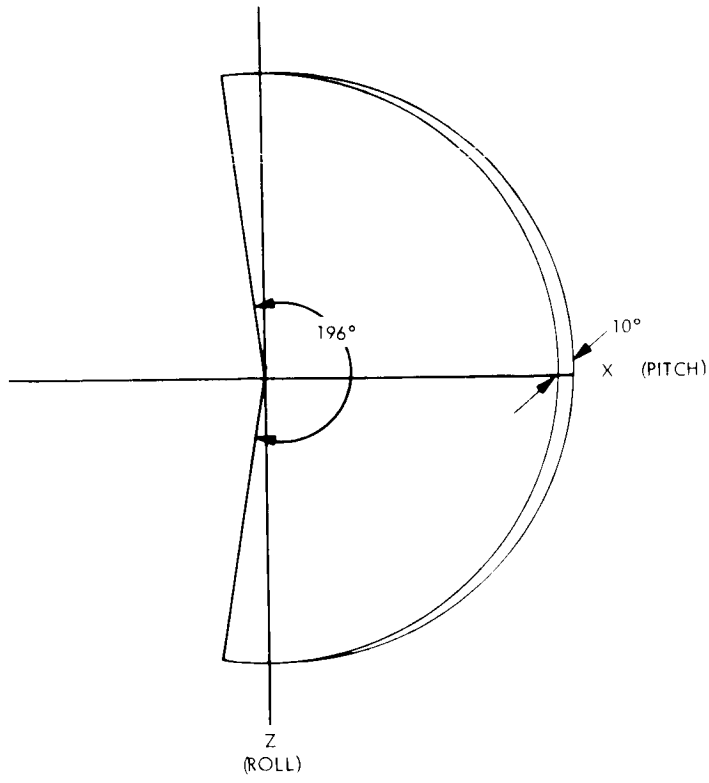

Figure 2. Sun Sensor Field-of-View and Orientation

There are several important disadvantages:

a. The system requires a longer time to acquire the sun. In the present system, pitch and yaw rates are limited to 0.25 degree/sec during sun acquisition. The maximum time required to slew to the sun is

$$t = \frac{180 \text{ deg}}{0.25 \text{ deg/sec}}$$

$$= 720 \text{ sec}$$

For the limited field-of-view sensor, the worst case sun location requires the vehicle to roll 360 - 10 degrees, and then yaw 180 degrees. This requires,

$$t = \frac{350 + 180}{0.25}$$

$$= 2120 \text{ sec}$$

The limited field-of-view system requires an additional 1400 seconds or 23.3 minutes, ignoring settling times.

The spacecraft battery size is a function of the time off the sun during the orbit insertion maneuver. An additional delay of 23.3 minutes in acquiring the sun would add 20 to 25 lb to battery weight. This is sufficient reason to reject the limited field-of-view sun sensor.

b. The system requires additional logic to provide automatic acquisition.

c. Whenever the sun is lost, the vehicle must roll to reacquire. Canopus is lost, and Canopus acquisition is necessary after sun acquisition is completed. If the sun is lost in the present system, it may be reacquired without loss of Canopus, depending upon spacecraft orientation.

The limited field-of-view sun sensor system is not recommended.

2.2.3 Improvement of Maneuver Accuracy

Task Description: In the present system, maneuvers are performed in a given axis by torquing its gyro at a known rate for a known time. A significant portion of the error in the commanded position results because the vehicle position in its limit cycle deadband is not known at the start of the maneuver. Although present guidance requirements do not demand improved accuracy of maneuver, it was of interest to investigate whether reasonably simple methods of improving accuracy were available.

A substantial portion of the error in a commanded position is caused by the control system deadband. This is illustrated in Table 1 which presents the results of an error analysis of a

Table 1. Maneuver Error Analysis Standard Deviation of Final Pitch Error, $\sigma_{\epsilon\ X}$, Following a 45 Degree Yaw, 45 Degree Pitch Maneuver.

Error Source	Magnitude (degrees)	Variance (degrees^2)
Control system deadband (Celestial mode)	0.458	0.06992
Sensor repeatability	0.141	0.00222
Control electronics drift	0.046	0.00024
Sensor mounting alignment	0.050	0.00028
Threshold detector variations	0.023	0.00006
Control system deadband (Gyro sensing mode)	0.458	0.04102
C&S timer resolution	0.089	0.00090
Turn rate uncertainty	0.178	0.00348
Gyro drift	0.154	0.00260
Autopilot	0.300	0.01000
		0.13072
$\sigma_{\epsilon\ X} = \sqrt{0.13072}$		
$= 0.362$ deg		

typical maneuver consisting of a 45 degree yaw rotation followed by a 45 degree pitch rotation.* The standard deviation of the final pitch error ($\sigma_{\epsilon x}$) is found to be 0.362 degree. The results for the standard deviation of the yaw error ($\sigma_{\epsilon y}$) are identical, except that the turn rate uncertainty and timer resolution errors must be multiplied by cos θ pitch. The final result is:

$$\sigma_{\epsilon x} = 0.362 \text{ degree}$$

$$\sigma_{\epsilon y} = 0.358 \text{ degree}$$

Two notes of explanation concerning the error analysis are necessary. First, why does the control system deadband appear twice? The deadband contribution to maneuver error occurs in two ways. When the spacecraft is switched to gyro control at the start of the maneuver, the spacecraft body axes are misaligned with respect to the celestial reference system by up to one-half the deadband. This is the error source called "control system deadband" (celestial mode). The maneuver is performed with respect to an inertial reference coordinate system. This reference system is established by the gyros and is coincident with the spacecraft body axes at the instant of switching to gyro control. Therefore, this inertial reference coordinate system is misaligned with the celestial reference system in each axis by an amount up to one-half the deadband. The maneuver is now performed by rotating the vehicle in the inertial reference coordinate system. The error resulting from rotation about misaligned axes is listed as control system deadband (gyro sensing mode). At the conclusion of the maneuver, the spacecraft will oscillate within its deadband until the thruster is fired. At this point, the autopilot provides continuous control with respect to the inertial reference coordinate system, eliminating the deadband error.

*This analysis is described in detail in document VC220FD111 which is included in Spacecraft Functional Description, Volume A (Book 1 of 2) of the Phase IA Task B preliminary design.

The control system deadband error variances differ because the gyro sensing mode term must be multiplied by a trigonometric term which provides the effect of the initial yaw rotation.

The pitch and yaw errors are neither completely independent nor completely correlated. This fact is significant since the results of the conversion of two one-dimensional pointing errors depend upon the degree of correlation. For the purpose of this analysis, the errors will be assumed to be completely correlated. This provides the maximum value of pointing error. The total error is the vector sum of the individual errors.

$$\sigma_{\epsilon T} = \sqrt{\sigma_{\epsilon x}^{2} + \sigma_{\epsilon y}^{2}}$$

$$= 0.509 \text{ deg.}$$

The $3\sigma_{\epsilon T}$ value = 1.527 degree. For two-dimensional errors, probabilities equivalent to 1σ and 3σ values are 39 percent and 99 percent respectively.

If the control system deadband could be reduced to one-fifth its present value, the standard deviation of the pointing error would be reduced to $\sigma_{\epsilon T} = 0.215$ degree $3\sigma_{\epsilon T} = 0.645$ degree.

There are three basic methods of reducing the control system deadband error. These are:

a. Measure the misalignment between the inertial and celestial coordinate systems, and modify the maneuver accordingly.

b. Align the celestial and inertial coordinate systems prior to the first rotation.

c. Reduce the deadband.

Methods for accomplishing these functions are discussed in the following section.

The simplest method to measure the misalignment between the inertial and celestial coordinate systems is to record the celestial sensor outputs at the time the spacecraft is switched to inertial control, and transmit them to Earth. This gives the misalignment of each axis with respect to the celestial coordinate system. The required maneuver is modified to include the effects of the misalignment, and transmitted to the spacecraft.

The advantage of this system is that it requires no changes in the present system. There are two significant disadvantages: (1) There is a delay in performing the maneuver equal to the round trip communications times plus the time required to determine the modified maneuver. Throughout this time the spacecraft is on gyro control. Therefore, gyro drift errors will be increased. For 1973, the maximum communications time at Mars arrival is 11.3 minutes. With a gyro drift rate of 0.25 deg/hr., this delay could introduce a misalignment error of .094 deg. (2) The final commanded maneuver cannot be determined until the sensor data is received from the spacecraft. Allowing 10 minutes for this function results in an additional misalignment error of 0.042 deg.

Brief consideration was given to performing these steps automatically on-board the spacecraft. The benefits gained do not warrant the additional system complexity, and so this approach was ruled out.

Two methods for aligning the celestial and inertial coordinate systems prior to the first rotation were considered. One is to delay switching to gyro control after the command is given until the spacecraft is in the center of its deadband. This presents several problems:

a. In nominal limit cycle operation, it takes 79 minutes to traverse the deadband. Thus, there could be a 79 minute delay in each axis concurrently in switching to gyro control.

b. If the spacecraft is in a soft limit cycle, it may never cross the center of the deadband.

c. This method requires additional circuitry and logic.

Another method of aligning the inertial and celestial reference systems is to place the spacecraft on gyro control with the gyros being updated by the celestial sensors. This is illustrated in Figure 3. The switch must be held in the align position long enough so that the inertial and celestial reference systems coincide. The length of time to accomplish this is a function of the outer loop gain. Additional study is necessary to determine this value.

This is an attractive mode of operation. It requires no additional equipment other than the switching required to provide the control loop. It does not cause additional error. The disadvantage is that is may require significant time; however, during this delay the spacecraft is not accumulating any additional error.

The deadband can be reduced by either increasing the control loop gain or decreasing the input voltage required to trip the threshold detector. This directly reduces the deadband error. An estimated value of the magnitude of the reduced deadband is ±0.1 deg, approximately one-fifth of the original value. The present system already provides for gain changes in the pitch and yaw channels to compensate for decreasing solar cell output as the spacecraft - sun distance increases. It would be relatively simple to add an additional gain change to the pitch and yaw channels, and to provide a gain change in the roll channel.

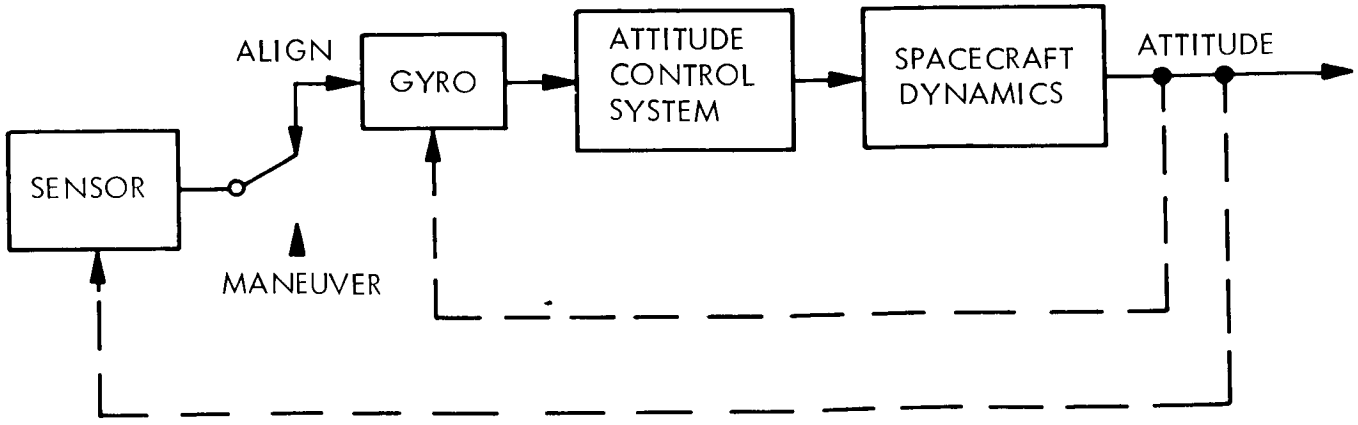

Figure 3. Control Loop to Align Inertial and Celestial Coordinate Reference Systems

To perform a maneuver in this mode, the spacecraft would be commanded to operate with the reduced deadband. After a period of time allowed for the spacecraft to settle on the reduced deadband, the maneuver is performed. At the conclusion of the maneuver, the vehicle reverts to nominal deadband.

This is also an attractive mode of operation, requiring little additional circuitry and easy to implement. It does require more gas to operate with a reduced deadband, but the amount is insignificant. When the deadband is reduced to one-fifth its nominal value, gas consumption rate increases by a factor of five. However, limit cycle gas consumption is a small part of the total, and the increased gas consumption rate lasts only until the maneuver has been completed.

Maneuver accuracy in the present system is satisfactory. For this reason, none of the improved methods discussed here has been selected. If an accuracy improvement were necessary, the most attractive method is to reduce the deadband. In addition, the technique of measuring the misalignment via telemetry and modifying the maneuver is always available.

2.2.4 Reacquisition After Maneuvers

Task Description: Following a maneuver, the present system employs its normal automatic acquisition mode to reacquire the sun and Canopus. This method will be compared with the procedure of reversing the maneuver rotations to return to the nominal attitude.

With a practical autopilot design, residual spacecraft yaw and pitch rates following a maneuver are 0.3 to 0.5 deg/sec. (System requirement is 1.0 deg/sec). These rates are caused by limit cycle operation of the gimbal actuators and liquid fuel slosh.

The spacecraft rotation that will result from these rates, for a single axis, is given by the expression:

$$\theta = \frac{\omega^2}{2\alpha}$$

For $\omega = 0.5$ deg/sec and a nominal control acceleration α of 0.0129 deg/sec^2, the rotation is equal to 9.7 degrees. This results in the loss of the intertial reference coordinate system maintained by the gyros whose input axis gimbal freedom is 6 degrees. It becomes impossible to retrace the maneuver to return to nominal attitude.

Even if it were possible to perform this maneuver, there are no important advantages to doing so. On the other hand, the present system has the significant advantage of reorienting the spacecraft to the sun as rapidly as possible.

2.2.5 Occultation of Celestial References

Task Description: The present system employs gyro memory when references are occulted. Gyros are turned on at the first occultation and remain on thereafter. Switching is controlled by the logic control unit for sun occultations, and by the C&S for Canopus occultations. This entire system will be studied to identify potential problem areas and to reconsider methods of operation.

2.2.5.1 Operation of Present System

The following command sequences together with the automatic reacquisition sequence provide control during occultation periods in the present system. The gyros are commanded on before the onset of a sun or Canopus occultation period and are kept on for the entire period. An occultation period is that period of the Mars orbit phase that contains an occultation of one of the references in each orbit.

For a sun occultation the enable sun occultation mode command is given prior to the onset of the occultation period. The logic control unit then automatically switches the pitch and yaw loops to intertial position control at the start of an occultation. This is determined by noting that all sun sensor outputs are below a predetermined level. When the logic control unit determines that the sun is present, it switches the pitch and yaw loops back to the cruise mode configuration. If the coarse sun gate signal is not present at this time, a complete reacquisition sequence is directed. This would not occur normally. If the Canopus acquisition gate is

lost during the sun occultation, the roll loop will automatically be switched to inertial position control rather than the Canopus search mode. At the conclusion of the last sun occultation in an occultation period, the switch to cruise mode command is given which cancels the previous enable sun occultation mode command.

The system operates somewhat differently for Canopus occultations, than for solar occultations. For the orbit selected during Task B, the range of spacecraft anamolies referenced to the terminator encompassing all Canopus occultations represented only one hour of the orbital period. During each orbit containing a Canopus occultation, the roll axis is switched to inertial control for the one hour period that includes the occultation. The signals that switch the roll axis between inertial control and cruise mode come from the C&S. These signals are based upon the true anomaly of the spacecraft which is provided to the C&S by the outboard gimbal angle of the Planet Scan Platform (PSP).

The commands sent by the C&S are: (a) Switch to roll inertial control, and (b) Switch to cruise mode. Upon receipt of the first command, the roll loop is switched to inertial control while the pitch and yaw loops remain in the cruise mode configuration. If the coarse sun gate signal is lost during a Canopus occultation, the logic control unit will switch all axes to the rate mode and reacquire the sun, whereupon it will switch the pitch and yaw loops to the cruise mode and the roll loop to inertial control. Canopus search will not take place until the second command, switch to cruise mode, is given.

The Canopus sensor may lose track of Canopus if either excessive light from the bright limb of Mars enters the sensor shield, or if one of Mars' natural satellites passes through the sensors' field of view. Since the orbits of the spacecraft and the natural satellites are known, interferences can be predicted and the system will be commanded to either a roll drift mode by disabling the roll pneumatic drivers, or a roll inertial hold mode during the periods when interferences are anticipated.

2.2.5.2. Problem Areas

One important problem area has been identified in the present system operation, during Canopus occultations.

The mode switching signals are derived by the C&S from the PSP outboard gimbal angle. This is undesirable for three reasons:

a. It requires an interface between two otherwise unrelated subsystems.

b. Vehicle control during the Canopus occultation period is dependent upon satisfactory operation of the entire PSP control system. This reduces the reliability of the attitude control system.

c. The PSP outboard gimbal angle can be used to predict Canopus occultations only when the PSP is tracking the local vertical.

Two experiments have been identified, and others may be found, in which the PSP is directed off the local vertical. These are the UV spectrometer and high resolution TV experiments. Even if these instruments were located on a second PSP, it detracts from the versatility of the PSP in future missions to require that it track the local vertical.

No problems have been found with the system operation during solar occultations.

2.2.5.3. Operation During Canopus Occultation

Three different methods of operation during Canopus occultation periods have been considered. These are described below.

a. Stored Time Commands in the C&S. Canopus occultations can be predicted and corresponding switching commands stored in the C&S. It is not necessary to predict the occultations accurately; it is sufficient to predict a period which will bracket the occultation. This is a simple solution but has several important disadvantages.

It is not possible to predict occultation times accurately prior to analysis of orbital tracking data. Therefore, the Canopus occultation mode cannot be made to operate automatically. Even with tracking data, predictions can be made for a several week period, but not for several months. In orbit prediction the most uncertain quantity is the true anomaly of the spacecraft in orbit.

The present organization of the C&S requires that one word of memory be used for each mode switching command. Two commands are required per orbit. If the orbit period is eight hours, 180 words are required to provide the mode switching for Canopus occultations in one month. The present C&S memory has a capacity of 512 words of which approximately 20 percent remain unused. This would provide switching for 17 days.

The time of coverage could be doubled if the C&S were only required to provide the command to switch to roll inertial control. A simple fixed interval timer could be used to provide the command to return to cruise mode.

b. IR Sensor. An IR sensor with a wide field of view can be mounted with its viewing axis parallel to the Canopus sensor axis. The function of the IR sensor is to detect the presence of Mars when it approaches the Canopus sensor field of view. This is illustrated in Figure 4.

The IR sensor can be a simple device since its only function is to distinquish between Mars and space with low accuracy. When Mars is within the IR sensor's field-of-view, the roll channel is switched to inertial control. When Mars passes out of the field of view, the roll channel reverts to the cruise mode.

There are no obvious disadvantages to this method, but there are questions which have not been studied because of the lack of time. The primary question is what the size of the sensor field of view should be, and whether it can be a single fixed value, or whether it must be modified as the Canopus sensor field of view is stepped.

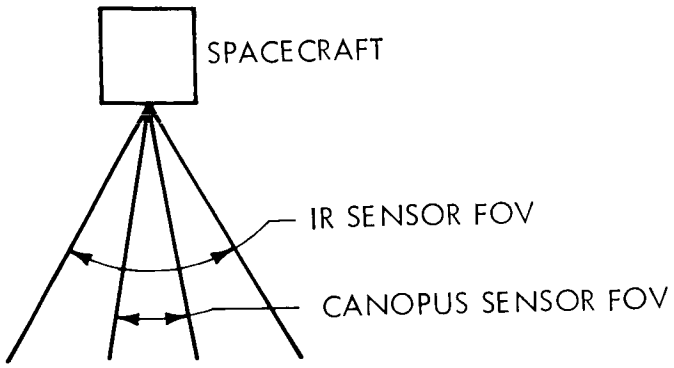

Figure 4. Alignment of IR Sensor to Detect Canopus Occultations

c. Inertial Control with Canopus Sensor Updating. The block diagram of this control loop is shown in Figure 5. The spacecraft is essentially in the inertial position control mode, but in addition, the low gain outer loop acts to correct for gyro drift, and thus maintain the inertial reference coordinate system aligned with the celestial reference coordinate system. The required outer loop gain is a function of the gyro drift rate. The lower the drift rate the lower the loop gain can be set. When a Canopus occultation occurs, the Canopus sensor output vanishes, and the spacecraft is under pure inertial control. At the end of the occultation, the Canopus sensor output returns and is used to torque the gyro.

Operation with this system is as follows. Prior to the start of the Canopus occultation period, the gyros are commanded on and remain on for the entire occultation period. The command enable Canopus occultation mode is sent, which places the roll channel in the configuration shown in Figure 5.

If the bright limb of Mars or one of the natural satellites were to pass through the sensor field of view, an erroneous error signal could be caused. However, with an outer loop gain sufficiently low, the spacecraft rotation in response to this erroneous signal would not be significant.

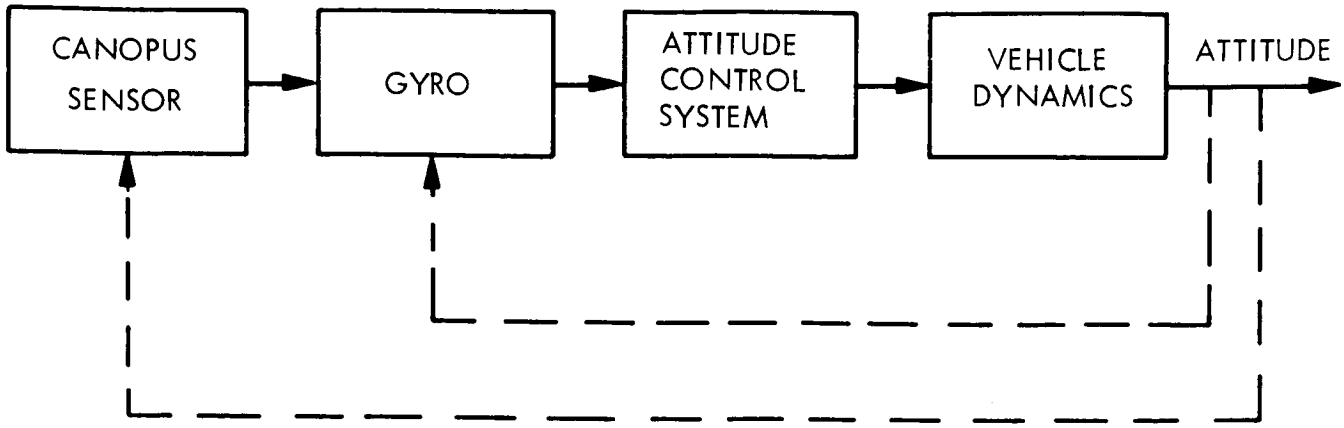

Figure 5. Inertial Position Control Loop with Canopus Sensor Updating

A numerical example best serves to illustrate this point. Assume a gyro drift rate of 0.25 deg/hr, and an allowable roll error in spacecraft attitude caused by Canopus sensor offset of 0.5 deg. It should be noted that because of the geometry involved the effect of this roll error on the high gain antenna pointing error is minor. This allows the use of an outer loop gain of:

$$\frac{0.25 \text{ deg/hr}}{0.5 \text{ deg}} = 0.5 \frac{\text{deg/hr.}}{\text{deg}}$$

Assume an interfering object with an intensity between the Canopus sensor high and low gates were to appear at the edge of the sensor field of view (±4 deg), and were to remain there for 15 minutes. This is a highly pessimistic case. If the sensor locked onto this object instead of Canopus, it would cause a roll error equal to:

$$4 \text{ deg} \times 0.5 \frac{\text{deg/hr.}}{\text{deg}} \times 1/4 \text{ hour} = 0.5 \text{ deg.}$$

This method has two important advantages:

a. No major additional equipment is required. It is only necessary to provide the switching to connect the Canopus sensor output to the gyro torquer.

b. It requires no sensing of when Canopus occultations begin and end, and no mode switching during the orbit.

The primary disadvantage is that low gyro drift is required. If the outer loop gain is chosen to correspond to a nominal gyro drift rate, and during the mission the drift rate increases, the result will be an increased offset error in roll attitude. This error will be present whenever the vehicle is in the Canopus Occultation Mode. Continuing the previous numerical example, if the gyro drift rate were to increase to 1 deg/hr from its nominal value of 0.25 deg/hr, it would cause a roll attitude error of:

$$\frac{1.0 \text{ deg/hr}}{0.5 \frac{\text{deg/hr}}{\text{deg}}} = 2 \text{ deg.}$$

A second disadvantage is that the primary roll control loop cannot recognize loss of Canopus. To offset this a fixed interval timer set to the maximum Canopus occultation time is used. The timer is started by the loss of the Canopus present signal from the sensor. If at the end of the interval the Canopus present signal has not reappeared, the control system is automatically switched to the acquisition mode.

2.2.5.3 System Selection

The use of roll inertial control with Canopus sensor updating is selected for system implementation at this time. However, the IR sensor method merits additional study, and a firm choice between these two methods should not be made until this is done.

The sun occultation mode remains unchanged from the Task B design. However, it also can be operated in the inertial mode with sun sensor updating.

2.2.5.4 Disable Pneumatics During Occultations

A brief analysis was conducted to consider the effect of disabling the pneumatics during occultations, allowing the vehicle to drift without control. This is not to be considered as a normal mode of operation, but only as an emergency measure.

There are two primary sources of attitude error during an uncontrolled drifting period. These errors are estimated for a single axis in the following paragraphs. The duration of the occultation period is assumed to be one hour.

a. Limit Cycle Rate. The nominal limit cycle rate is 0.0002 deg/sec. If the spacecraft is approaching the deadband limit (0.458 deg) when the pneumatics are disabled, the vehicle error after one hour is:

$$\theta = 0.458 \text{ deg} + 0.0002 \text{ deg/sec} \times 3600 \text{ sec}$$

$$= 1.15 \text{ deg}$$

b. Gravity Gradient Torque. The gravity gradient disturbance torques are a function of the mass distribution of the spacecraft, the orientation with respect to an orbital coordinate system, and the aerocentric radius. Maximum torques occur near periapsis. The maximum pitch gravity gradient torque has been estimated to be 2×10^{-4} lb-ft. If a one-hour occultation period were to coincide with the time of maximum gravity gradient torque, the resulting attitude error would be 32 degrees. However, at other portions of the orbit, the error is less than one degree. The evaluation of the actual error requires knowledge of the orbit and occultation times.

No attitude error results because of solar pressure forces. The primary effect of solar pressure force is to act upon the high gain antenna to produce a pitch disturbance torque. During a Canopus occultation pitch and yaw axis remain under control. During a solar occultation there is no disturbance torque.

The conclusion reached is that it may be possible to drift through an occultation period without requiring reacquisition at the end of the occultation. This is heavily dependent upon the gravity gradient disturbance torque and the duration of the occultation. These in turn are both a function of the orbit.

2.2.6 Two Level Acceleration System

Task Description: The present cold gas jet subsystem employs two thrust levels. High thrust is used prior to capsule separation after which low thrust is used. A study will be made to determine whether additional thrust levels or switching criteria should be used.

The present system employs a two-level thrust system that is designed to maintain an approximately constant control acceleration about all three axes throughout the entire mission. High thrust is used until capsule separation occurs. Following separation, a squib relay causes a switch from high to low thrust nozzles. The reduction in thrust level is proportional to the reduction in moments of inertia, thus maintaining a constant control acceleration. The moments of inertia are listed below in Table 2.

Table 2. Moments of Inertia

	Moments of Inertia ($slug\text{-}Ft^2$)		
	Transit	After capsule separation	Reduction
Roll	13084	5823	2.25
Yaw	18475	4026	4.58
Pitch	19016	5194	3.67

These are substantial changes, and obviously require the corresponding change in thrust level to maintain low limit cycle rates and gas consumption after capsule separation.

Thus, the questions to be answered are: (1) should an additional thrust level be provided, and (2) how should switching between thrust levels be done.

An additional thrust level would be a high thrust level. This could be used for the following purposes:

a. Performing maneuvers. In the present system, a combination of worst case conditions requires 6 degrees of gyro gimbal freedom to accommodate spacecraft overshoot without loss of gyro reference. This relatively large amount of gimbal freedom has proved to be a significant constraint on gyro selection. Increasing the thrust level during the maneuver mode would reduce the required gyro gimbal freedom. The reduction in gimbal angle freedom is directly proportional to the increase in thrust.

   The value of a high thrust mode for this purpose is difficult to evaluate. It allows more choice in gyro selection, and may permit a more accurate gyro to be chosen. However, a satisfactory gyro was selected during Task B, and it does not necessarily follow that a more accurate gyro will increase the probability of mission success. The disadvantages are severe. An additional set of solenoid valves and nozzles and provision for switching are required.

b. Limit attitude excursions upon separation from the launch vehicle. This requirement does not exist for the Voyager spacecraft.

   The problem of loss of references during capsule separation which existed during Task B is no longer present. This is true because: (1) the present capsule-spacecraft separation sequence causes no significant torques to be applied to the spacecraft (2) because of the reduction in spacecraft moments of inertia, the control accelerations are 1.7 to 3.8 times their nominal value.

The conclusion is that the advantages of an additional high thrust mode are not sufficient to warrant the additional weight and system complexity required.

It is possible to switch between the presently available high and low thrust modes during the mission. High thrust would be required during acquisition and maneuvers, and low thrust would be used for cruise and all modes following capsule separation. The advantage of this is a minor gas saving. Total impulse required for limit cycle operation prior to capsule separation is 96 lb-sec of a total of 2400 lb-sec total mission requirement.

Potential savings, using the reduction factors given in the table listing the moments of inertia, are 69 lb-sec. This is equivalent to approximately 1 pound of cold gas. The disadvantage of this system is that it requires the capability of continually switching between the high and low thrust modes. This is less reliable than the present system in which a squib relay is used to shift from high to low thrust following capsule separation. The minor weight-saving is not sufficient reason to change the present system.

2.2.7. Maneuver Mode

Task Description: In the present system maneuvers are performed by successively torquing each gyro at a precise rate for a commanded time. Other methods of performing maneuvers are compared to the present system.

Maneuvers are performed in the present system by a series of successive rotations about the spacecraft control axes. One, two or three rotations can be used. Each rotation is accomplished by torquing a particular gyro with a precision current for a commanded time. Because there is no direct measurement of the angular rotation, this method has been referred to as an open-loop system. This system is simple and straightforward, meets the accuracy requirements, and has been flight-proven on Mariner.

During this update it was felt that alternate approaches should be explored, particularly from the standpoint of reliability improvement. One idea that is intuitively appealing is to perform the maneuver in a closed-loop mode. Here, the spacecraft attitude is measured and compared to the commanded attitude. When these coincide, the maneuver is terminated. Unfortunately, there is no simple way to measure vehicle attitude during a maneuver. It is possible to calculate the angle. For example, the gyro can be operated in the rate mode, and its output integrated. This angle can be compared to the commanded angle. However, this too is an open-loop system. The only difference between it and the present system is where the angular rate is integrated. Here it is done by an electronic integrator, or if the system is implemented digitally, by a counter. In the present system, the integration is performed

by the combined actions of torquing the gyro, to yield a constant vehicle rate, and timing, in the C&S. One implementation of this type of system is shown in Figure 6. The maneuver is initiated by applying a slew voltage to the attitude control system. This commands a spacecraft rate. The gyro output is also applied to a voltage-to-frequency pulse converter. Each pulse corresponds to an increment of position. Pulses are counted, and when the sum is equal to that stored for the commanded maneuver, the slew voltage is removed and the gyro is switched to the rate integrating mode. It should be noted that this type of system has been used on Lunar Orbiter. Although this has been referred to in the literature as a closed-loop system, its fundamental operation is almost identical to the present system; there is no direct measurement of spacecraft attitude. This is derived from integrating spacecraft rate. Here the integration is performed by the voltage-to-frequency pulse converter and the counter.

The need to introduce digital circuitry for integration immediately suggests the possibility of incorporating digital circuitry within the gyro loop itself by using pulse rebalancing. Angle measurements can be made directly by counting gyro pulses in a bidirectional counter. Commanded slew rate can be achieved by introducing additional pulses into the rate output pulse train. Implementation details are significantly affected by the specific gyro design. Pulse rebalance techniques offer potential gyro drift reduction by reducing gimbal deflection. Torquer performance is improved by constant power operation, and by relieved linearity requirements.

However, the accuracy of the present system is satisfactory. Furthermore, gyro errors are not the principal contributors to maneuver mode pointing error. Motivation for change must rest on

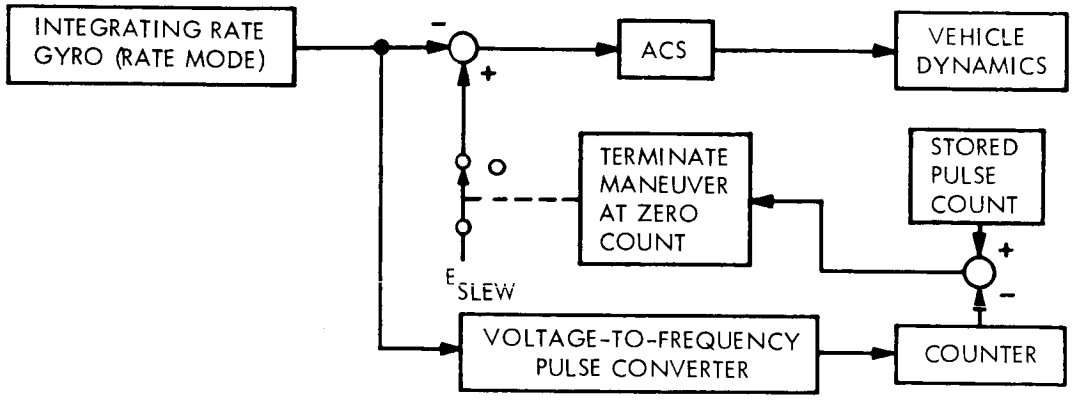

Figure 6. Vehicle Altitude Measurement System

reliability considerations. The present system appears to have the advantage here on the basis of simplicity. However, the opportunity exists with digital circuitry to enhance reliability with triple redundancy and voting logic, so that a clear-cut answer on reliability must rest with a detailed circuit analysis.

2.2.8. Gyro Evaluation

2.2.8.1. Summary

The gyro selected for the Voyager attitude control system is the Honeywell GG-334A. This is a single-degree-of-freedom, gas bearing rate integrating gyro. The primary reasons for switching to gas bearing gyro instead of continuing with the ball bearing gyro selected during Task B are:

a. Longer life.

b. Lower noise. This is of major importance to the autopilot design.

Gas bearing gyros have not yet been proven in space flight. However, they are scheduled to be used in space missions in the near future (Nimbus B in 1968, followed by MOL). This will provide space experience. If this experience reveals unexpected problems, it is possible to return to the use of ball bearing gyros.

System mechanization will employ single-degree-of-freedom gyros in an analog mode of operation. Two-degree-of-freedom gyros and digital operation were considered and eliminated.

Gyro motors will be operated from a single phase source using phase splitting capacitors. This provides a considerable improvement in power supply design. This change was made too late to be incorporated into the Task D design. For this reason the system descriptions still include a 3-phase, 400-cps power source for the gyro spin motors.

Additional study is required in the following areas:

a. Potential increase in reliability available from using the gyros in a digital mode. This offers the opportunity to use triple-redundant circuits and majority logic.

b. Information on some candidate gyros was unavailable.

c. Use of capacitor feedback around the gyros. This offers the possibility of eliminating the gyro heaters.

2.2.8.2. Gas versus Ball Bearings

Gyro bearing technology has advanced to the point where gas bearing gyros are beyond the development stage and are in production and operation. While always holding a theoretical advantage over the ball bearing, at least in operating life, the gas bearing gyro has been shunned by system designers because of a lack of flight experience. This is no longer the case. Numerous gas bearing gyros are now in use or are planned for use in the near future. Autonetics has used spherical gas bearing gyros in the Minuteman IGS for several years. Litton is using gas bearing gyros in aircraft navigation platforms. Nortronics has used single-degree-of-freedom (SDF) gas bearing gyros on Polaris and Minuteman and has one scheduled for use on the C-5A. Sperry has an SDF gas bearing gyro slated to fly on Nimbus B, and Honeywell has an SDF gas bearing gyro selected for a prime control system on MOL.

As far as space flight is concerned, the gas bearing gyro has not yet flown. The first space flight experience apparently will be provided by the Nimbus B flight in 1968. Following this will be MOL flights. Thus space flight experience will exist in a matter of several years. The ball bearing gyro, however, has proved itself in space many times, with the record to-date probably being set by Nimbus C which has had a Kearfott Alpha ball bearing gyro running continuously for over 11,000 hours, as of this writing.

The gas bearing gyro now appears to be fully competitive or better than the ball bearing gyro in all characteristics. A comparison of two hypothetical gyros having the same construction except for bearings would be as follows:

a. Drift - About the same. Contrary to early opinion, the gas bearing provides no edge in drift performance.

b. Noise - Output signal noise for the gas bearing gyro is lower by as much as an order of magnitude over its ball bearing counterpart.

c. Motor Power - The same.

d. Vibration/Acceleration Capability - A slight edge to the ball bearing gyro. The gas bearing is sufficiently rigid however to provide adequate capability even in the hard-mounted configuration.

e. Start-Stop Capability - Equally adequate. Gas bearing motors have demonstrated in excess of 20,000 start stops. A Honeywell gas bearing motor was subjected to 20,000 start-stop cycles (with cooldowns and position variations). At the end of this period the only noticeable change was an increase in the minimum starting voltage from 17 to 20 VAC. The motor was then installed in a gyro and is still operating.

f. Life - A definite edge to the gas bearing here. Demonstrated MTBF's for high-quality ball bearing motors are of the order of 15,000 to 20,000 hours. MTBF's for gas bearing motors have still not been well-determined, although vendors are willing to quote in excess of 40,000 hours. Honeywell has run four (4) gas bearing spin motors for over 42,000 hours each (with stops, starts, and cooldowns) as of September, 1967 and they are continuing to run properly. Autonetics is anticipating 1,000,000 hours MTBF for the G-10B gas bearing gyro.

The inherent long-life aspect of the gas bearing gyro coupled with the lower magnitude noise on the output signal are important advantages, and there are no significant disadvantages. It therefore must be concluded that, for Voyager, a gas bearing gyro should be selected over a ball bearing gyro-all other considerations being equal.

In the light of this decision, a new evaluation of SDF gas bearing gyros was made. (The evaluation of two-axis gyros is covered in Paragraph 2.2.8.3.) The gyros evaluated were:

AC Electronics	AC641G
Honeywell	GG334A
Kearfott	King II
Nortronics	GI-K7G
Nortronics	GI-T1-B
Sperry	SYG 4200
Sperry	SYG 1440

The latter five units were found to be unacceptable for Voyager for the following reasons:

2.2.8.2.1. Kearfott King II. This gyro represents Kearfott's early pioneering in gas bearing gyros. Although providing excellent performance, it has not reached the production stage. The main drawback is a susceptibility of its gas bearing to vibration in the 1400 to 1800 HZ range. A resonance in this area can cause bottoming at an acceleration level as low as 2-5 (g). This gyro must therefore be ruled out for Voyager application.

2.2.8.2.2. Nortronics GI-K7G. This unit, while in production, is a relatively low momentum (60,000 to 90,000 gm-cm^2/sec) device with resulting non-g sensititve drift rates approaching ± 1.0 degrees/hour. Thus, it is unacceptable based on performance.

2.2.8.2.3. Nortronics GI-T1-B. This unit is a large (3.5 lb; 1.8 x 10^6 gm-cm^2/sec) high-performance platform gyro used on Minuteman. With an input angle freedom of ± 1/60° and a maximum torquing rate capability of about 0.004 degrees/second, it cannot be used for Voyager - even in a pulse-rebalance strapdown system.

2.2.8.2.4. Sperry SYG-4200. The SYG 4200 weighs 1.4 pounds and has a wheel momentum of 136,000 gm-cm^2/sec. A unique feature of this gyro is an 8-wire ligament suspension system for the float. This gyro will be flown as part of an experiment on Nimbus B in 1968 as the first gas bearing gyro in space. Although its quoted performance is compatible with Voyager requirements, a developmental problem exists in the ligament suspension where creep of the wire material with time creates high disturbance torques on the float and results in high bias drifts. As a consequence, this gyro is being replaced by a ball bearing gyro for Nimbus D. This problem area makes this gyro unacceptable for Voyager.

2.2.8.2.5. Sperry SYG-14400. The SYG-1440 is a recently developed gyro designed primarily for strapdown system use requiring wide angles and high rates. The design incorporates features of the SYG-4200 and SYG-1000 (ball bearing) units. The gimbal suspension is the fundamental pivot and jewel, except that the pivots are spherical as opposed to the normal

cylindrical shaft design. The device weighs 1.2 pounds and has a wheel momentum of 100,000 gm-cm^2/sec. Like the Nortronics GI-K7G, the drift performance of this unit is too coarse for the Voyager application.

The Honeywell GG334A and the AC Electronics AC641G do stand out as potential units for Voyager. A listing of the characteristics of these two gyros is given in Table 3. Also shown in the table, for comparison purposes, is a listing of the characteristics of the Kearfott Alpha ball bearing gyro, which was the gyro previously selected by GE for Voyager.

The AC641G is a newly developed gyro which exhibits excellent performance. It incorporates several unique design features such as the magnetic suspension system utilizing a rotary transformer (which also provides spin motor power without the need for flexleads), the dual stator spin motor, and the Hall Cell-permanent magnet pickoff. The boldness of this design makes it desirable to accumulate adequate experience before selecting it for a program such as Voyager. This experience has not yet been accumulated.

The Honeywell GG-334A is a conventional design which is in production. It has been selected by GE for use in the MOL. A significant amount of test data exists to indicate that this unit can meet all of the Voyager requirements. The GG-334 would therefore be considered the optimum SDF gas bearing gyro for Voyager at this time.

2.2.8.3. Two-Axis Gyros

Two-axis gyros offer several features that are of interest to the Voyager mission. These are:

a. Redundant information. Because each gyro provides information about two axes, three gyros provide complete redundancy. This can be implemented so that on-board failure detection and correction is provided automatically.

b. Applicable two-axis gyros are operated in the rate mode. Position is generated by rate integration outside of the gyro. This type of operation eliminates the problem of loss of reference caused by limited gimbal freedom while performing maneuvers.

Table 3. Characteristics of SDF Gas Bearing Gyros

Characteristic	Kearfott ALPHA	Honeywell GG334A	AC Elec. AC 641G
Mech. and Dynamic Characteristics			
- Size (in.)	2.0 D x 2.8	2.3 D x 4.7	2.5 D x 4.5
- Wt. (lb.)	0.9	1.65	1.8
- Ang. Mom-H($G\text{-}CM^2/sec$)	2.27×10^5	2.0×10^5	5.6×10^5
- Output axis inertia ($G\text{-}CM^2$)	117	225	974
- Output axis damping	optional	optional	optional
- Angular Free. (Deg-IA)	$>\pm 6.0$ *	$>\pm 6.0$ *	$>\pm 6.0$ *
- Type suspension	pivot & jewel	pivot & jewel w/piezoelec. dither	Traixial magnetic using rotary XFMR
- Heater required	yes	yes	yes
Spin Motor			
- Type	hys. sync.	hys. sync.	(Dual-stator)
- Excitation	26 V, 3ø, 400HZ	26V, 2ø, 800HZ	25V, 2ø, 1200 HZ
- Starting Power (w)	4.5	8.0	14 (includes suspension)
- Running Power (w)	2.8	2.8	9.0 (includes suspension)
- Wheel Speed (RPM)	24,000	24,000	24,000
- Brg. material	SS	Steel-bonded carbide	
Pickoff			
- Type	Moving Coil XFMR	Inductosyn	Hall Cell-PM
- Sensitivity (MV/MR)	8.8	20	12.5
Torquer			
- Type	PM-Moving coil	PM-moving coil	PM-stationary coil
- Scale Factor (Deg/Hr/Ma)	70-134	120/1200 (2 windings)	3.1
- Max. Torq. rate (deg/sec)	5-9	10/100	0.34 (may be higher)
- Linearity (%)	0.05	0.01	>0.0001

* Dependent on damping coefficient chosen.

Table 3. Characteristics of SDF Gas Bearing Gyros (Cont.)

Characteristic	Kearfott ALPHA	Honeywell GG334A	AC Elec. AC 641G
Drift Performance (3σ)			
- g insens-random (deg/hr)	0.02	0.02	0.002
- g insens-stability (deg/hr) (for 1 yr-estimated)	0.20	0.20	0.10
- g sens. (deg/hr/g)	0.75	1.0	0.15
- g^2 sens. (deg/hr/g^2)	0.02	0.04	0.06
- restraint (deg/hr/deg OA)	0.2	0.5	0.16
- Temp Sens (deg/hr/^{o}f	0.025		0.003
Environmental Capability			
- Vibration-sine (g)	25	25	18 (limit at 200 HZ)
- Shock (g)	30 for 11 ms	50 for 10 ms	30 otherwise

c. Because the gyros are always operated in the rate mode, pulse rebalance is a natural choice. This lends itself to implementation of complete digital control loops in which reliability is increased through the use of triply redundant circuits and majority logic.

2.2.8.3.1. Automatic Failure Detection and Correction. Since each gyro provides two-axis information, a set of three two-axis gyros provides redundant information for on-board detection of a gyro failure. A generic three axis system is shown in Figure 7.

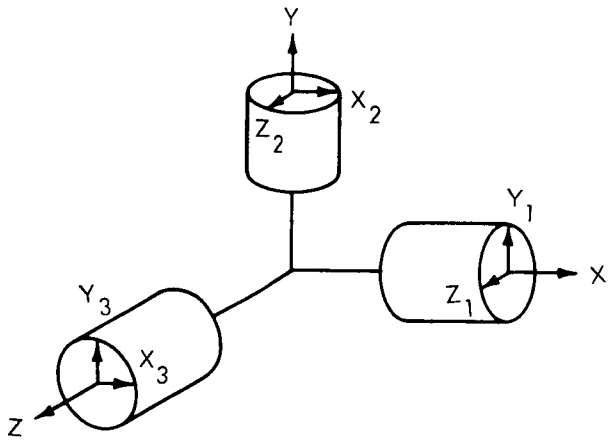

Figure 7. Generic 3-Axis System

Switching Logic for Gyro Malfunction

$$\left.\begin{array}{l}\text{if } x_3 - x_2 > \epsilon_x \\ \quad \text{and} \\ \text{if } x_3 - y_1 > \epsilon_y\end{array}\right\} \quad \bar{y} = y_1,\ \bar{x} = x_2,\ \bar{z} = \frac{z_1 + z_2}{2}$$

$$\left.\begin{array}{l}\text{if } z_2 - z_1 > \epsilon_z \\ \quad \text{and} \\ \text{if } x_3 - x_2 > \epsilon_x\end{array}\right\} \quad \bar{x} = x_3,\ \bar{z} = z_1,\ \bar{y} = \frac{y_1 + y_3}{2}$$

$$\left.\begin{array}{l}\text{if } y_3 - y_1 > \epsilon_y \\ \quad \text{and} \\ \text{if } z_2 - z_1 > \epsilon_z\end{array}\right\} \quad \bar{y} = y_3,\ \bar{z} = z_2,\ \bar{x} = \frac{x_2 + x_3}{2}$$

Use of redundancy to prevent gyro failure from causing mission failure

Figure 8 shows a block diagram of the switching logic.

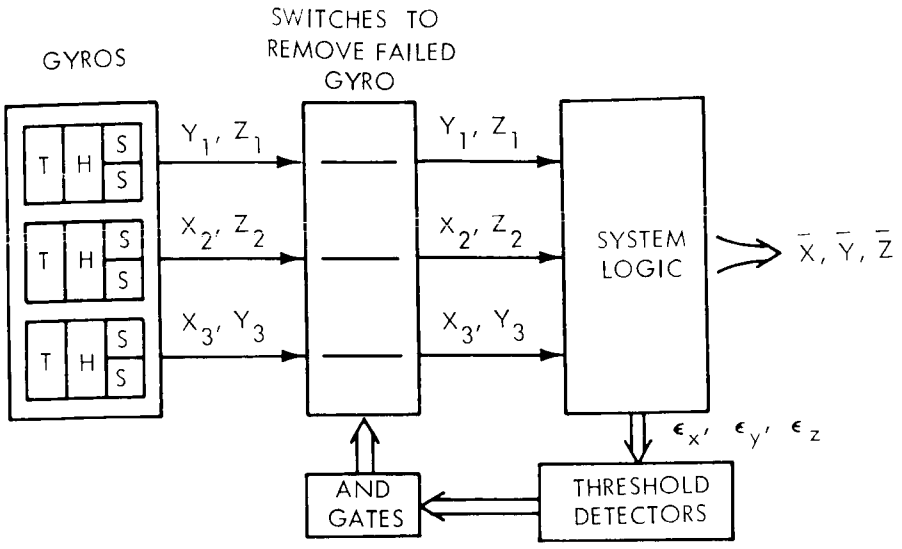

Figure 8. Switching Logic Block Diagram

The logic of Figures 7 and 8 replace the integrated gyro packages of the attitude control subsystem and its output is provided directly to the attitude control electronics.

2.2.8.3.2. Two-Axis Gyro Selection. A survey was made of the existing two-axis gyros that could be considered applicable to the Voyager mission. Gyros considered for evaluation were:

a. Arma G-16 Dynatune

b. Autonetics G-10B

c. GPI Gyroflex

d. Litton G-300 G2

e. Litton G-500-2 Vibrarotor

Table 4 summarizes various characteristics of the gyros, and the merits of each of the units are discussed individually below. Note that no data could be obtained relative to the GPI Gyroflex for the Voyager application. Also, note that Lear Sigler's two-axis unit was not

Table 4. Two-Axis Gyro Characteristics (Sheet 1 of 2)

Characteristic	ARMA G16 Dynatune	Autonetics G-10B	GPI Gyroflex	Litton G-300 G2	Litton G-500-2 Vibrarotor
Type	Non-float	Non-float	Non-float	Floated	Non-Float
Motor					
- Type		Induction		Hys. Sync	Hys. Sync.
- Brg. Type	Ball	Gas	Ball	Gas	Ball
- Exc. Freq (HZ)	400	400		800	1125
- Run Pwr (w)	4.0	0.7 @ 60RPS 6.0 @ 240RPS			
- Whl Speed (RPM)	12000	14400 Ascent 3600 Orbit		24000	22500
- Angular Mom.	0.6×10^6	0.2×10^6 @ 60 RPS		0.7×10^6	0.3×10^6
Size - (in.)	2 dia x 2.83	3.3 dia x 3.5		3.2 x 3.2 x 2.5	2.3 dia x 2.6
Weight - (lb)	1.4	1.65		1.0	1.0
Pickoff					
- Type		Capac.		Moving Coil Differ. XFMR	Perm Mag Voice Coil
- Excitation	Self Gener.	20V, 19.2KHZ		15V,4.8KHZ	Self Gener.
-Scale Factor (mv/mr)	4.5	500		135	90
Torquer					
- Type		Electro - Magnetic		Perm. Mag. Voice Coil	Perm. Mag. Voice Coil
- Scale Factor (o/hr/ma)	15			27	193
- Max Rate (o/hr)	3000	72000 @ 60RPS		—	720
- Linearity (%)				0.05	1.0
Angular Freedom (Deg)	±2.0	±0.17		±0.1	±0.25

Table 4. Two-Axis Gyro Characteristics (Sheet 2 of 2)

Characteristic	ARMA G16 Dynatune	Autonetics G-10B	GPI Gyroflex	Litton G-300 G2	Litton G-500-2 Vibrarotor
Heater					
- Req'd	Yes	No		Yes	Yes
- Max. Pwr. (w)		—		250	10
- Operate Temp (°F)	—	—		155	170
Drift (3σ)					
- g insens-random (°/hr)	0.003	0.1		0.015	0.3
- g insens-stability (°/hr)	0.1	0.9		0.015	1.6
- g sens (°/hr/g)	0.013	1.0		0.25	0.3
- g^2 sens (°/hr/g^2)	0.010	-3.0 ± 3.0		0.05	0.3
- Temp sens (°/hr/°F)	0.0003	0.005		0.01	0.1
- Restraint (°/hr/°)	9.0				
Accel. Capability					
A. Operating					
- Accel (steady-g)	100	22 @ 240RPS 6 @ 60 RPS		5	20
- Vibr (g)				2(5-500HZ)	10(5-500HZ)
B. Non-Operating					
- Accel (steady-g)				30	30
- Vibr (g)				10 (5-1000HZ)	5 (5-1000HZ)
Where Used	Arma Master Ref. Sys. (A Portable IGS Align. Unit)	IGS Platform for Elliott Bros.		Navigation Platforms	LT-300 Astro-Trkr
Life	40×10^3 Hrs Predicted for Brg Life	10^6 Hrs Predicted			

considered because of its very early stage of development. Likewise, electrostatic gyros were not considered because of their developmental status.

Arma G-16 Dynatune - This two-axis gyro is a non-floated, free-rotor unit which has an internal gimbal with two axes utilizing elastic pivots to support and rotate the inertial mass. Since the spin bearings are external to the gyro suspension system such that anisoelastic effects are not involved, the bearings can be operated at a low preload and can be adequately lubricated to provide potential long life.

Although this gyro has a relatively high angular freedom, it is nevertheless a platform type gyro; the high drift sensitivity to off-null displacement eliminates its use as an attitude reference at displacement offsets required for the Voyager control system. The gyro does lend itself, however, to a pulse rebalance mechanization in a strapdown system. For such a mechanization an overall drift accuracy approaching the Voyager requirement of 0.25 °/hr could be realized.

Since this gyro is still in the development stage, there is a lack of data to confirm long term drift stability, gyro life and environmental capability. It is therefore not a serious contender at this time.

Autonetics G-10B - This device is a two-degree-of-freedom, spherical gas bearing free rotor gyro designed for platform or pulse-rebalance strapdown system use. It is a miniature version of the G6B4 gyro used on Minuteman.

Autonetics has done a significant amount of work to analyze the performance of the G-10B in a pulse-rebalance strapdown system for a Voyager-type application. From their analyses it was concluded that a drift rate of 0.24°/hr could be obtained with in-flight updating of bias drift. That is, with drift rate measured and a new bias compensation set-in by commands, the drift rate would be less than 0.24°/hr (3σ) for a period of several days. Without in-flight bias drift compensation, drift rates of the order of 0.93°/hr (3σ) would result. This is mainly

caused by the high start-to-start bias drift shift and long term stability drift of 0.9°/hr. Schemes devised to get around the need for in-flight bias updating (such as allowing the gryo to run continuously after last trimming the bias drift prior to launch) do not provide drift accuracy within the Voyager requirements. It therefore must be concluded that in-flight bias drift updating is definitely required in order to meet mission requirements. This is undesirable from a mission complexity point of view and adds another failure mode to the gyro system.

Another undesirable characteristic of the Autonetics design is the requirement for a complex electronic servo to control wheel speed. This is necessary because the gyro uses an induction motor instead of a hysteresis synchronous motor.

GPI Gyroflex - This two-axis device is a non-floated instrument consiting of an inertial rim supported on a centrally located flexure joint which forms one end of a shaft. The other end of the shaft is driven through ball bearings by the spin motor. Like the Arma Dynatune, the location of the spin bearings external to the suspension system result in potentially long life bearings. Although Kearfott would not discuss the performance of the gyro, it is in production and is assumed to be comparable to the Arma Dynatune in performance. Since it is essentially a platform gyro with relatively low angular freedom it could only be considered for use in a pulse-rebalance strapdown system for the Voyager application.

Lack of essential data at this time eleminates it as a contender.

Litton G-300G2 - This two-axis unit is a gas bearing, floated gyro scaled down from the G-200 ball bearing gyro. While the unit provides very low drift, it is designed specifically for platform use. The torquer will not provide the torquing rate required for Voyager and hence cannot be used in a pulse-rebalance strapdown mode. In addition, it is not designed to survive the vibration environment of boost flight in a hard-mounted configuration.

Litton G-500-2 Vibrarotor - This two-axis non-floated device is somewhat similar to the GPI Gyroflex in concept inasmuch as it consists of a spinning mass supported by a torsion rod. It too is designed for platform use, although the torquer might be made large enough to provide operation in a pulse-rebalance strapdown system. The drift errors quoted for this device, however, are too high for the Voyager application.

2.2.8.3.3. Conclusions. Of the five precision two-axis gyros available today, the two Litton units are eliminated since they do not meet the program mission requirements.

The Arma Dynatune and the GPI Gyroflex could possibly meet the mission requirements if used in a pulse-rebalance strapdown system. Because of the relative newness of these designs, it would be risky to design a system based on these units at this time or in the near future. Both of these units offer simplicity with potential long-life and high reliability, however.

The Autonetics G-10B is considered to be a proven design offering long-life and high reliability. The requirement for in-flight updating of bias drift detracts from the attractiveness of this system as does the requirement for a speed control servo.

2.2.8.4. Gyro Mechanization Techniques

Three mechanization techniques have been considered for the Voyager gyro system. The first technique is the conventional analog system employing an inertial quality rate-integrating gyro operating in the attitude or open-loop mode, followed by a preamplifier and demodulator. Lead networks in series with the output signal provide rate information along with the attitude information. By feeding the output of the demodulator back into the gyro torquer through a torquer amplifier, the gyro can be electrically caged and the torquer current will provide an accurate rate indication for vehicle damping during initial acquisition. Maneuvers can be performed by timing a precise voltage into the torquer amplifier with the gyro system in the attitude mode. This system is shown in Figure 9 (system previously proposed by GE for Voyager).

A second scheme would utilize the same gyro in a pulse-rebalance strapdown mode as shown in Figure 10. In this mechanism the gyro float is continually torqued to null with a pulse rebalance technique. In this way spurious torques due to flex leads, pickoff and torquer reaction, and cross-coupled rates are minimized. The vehicle attitude is derived by integrating the rebalance pulses in a counter. Rate information can be obtained by either filtering the rebalance pulses or by differentiating the counter output. Since the counter is activated by the rebalance pulses, averaging of these pulses through a low pass filter is preferable to differentiating the counter output. Maneuvering can be performed by shifting the reference in the up/down counter by command inputs.

Examination of the two block diagrams will show that the pulse-rebalance strapdown scheme is somewhat more complex in mechanization, especially in the attitude mode. The advantage of the pulse-rebalance technique is the inherent improvement in attitude holding accuracy (drift). Ideally, the pulse-rebalance scheme approaches the basic random drift of the gyro - disregarding fixed torque stability drift.

A cursory look at the attitude drift error capability of the two systems would provide the following typical results. This analysis is based on a typical high-grade inertial-quality rate-integrating gyro such as the Kearfott Alpha or the Honeywell GG334.

	Attitude Drift Accuracy (3σ)	
	Open-loop analog	Pulse-rebalance strapdown
Without in-flight Bias drift update	0.25 deg/hr	0.20 deg/hr
With in-flight Bias drift update	0.10 deg/hr	0.05 deg/hr

The relatively high value of the drift error of the pulse-rebalance system without bias update is attributed to the long-term bias drift stability. The relatively high value of the drift error

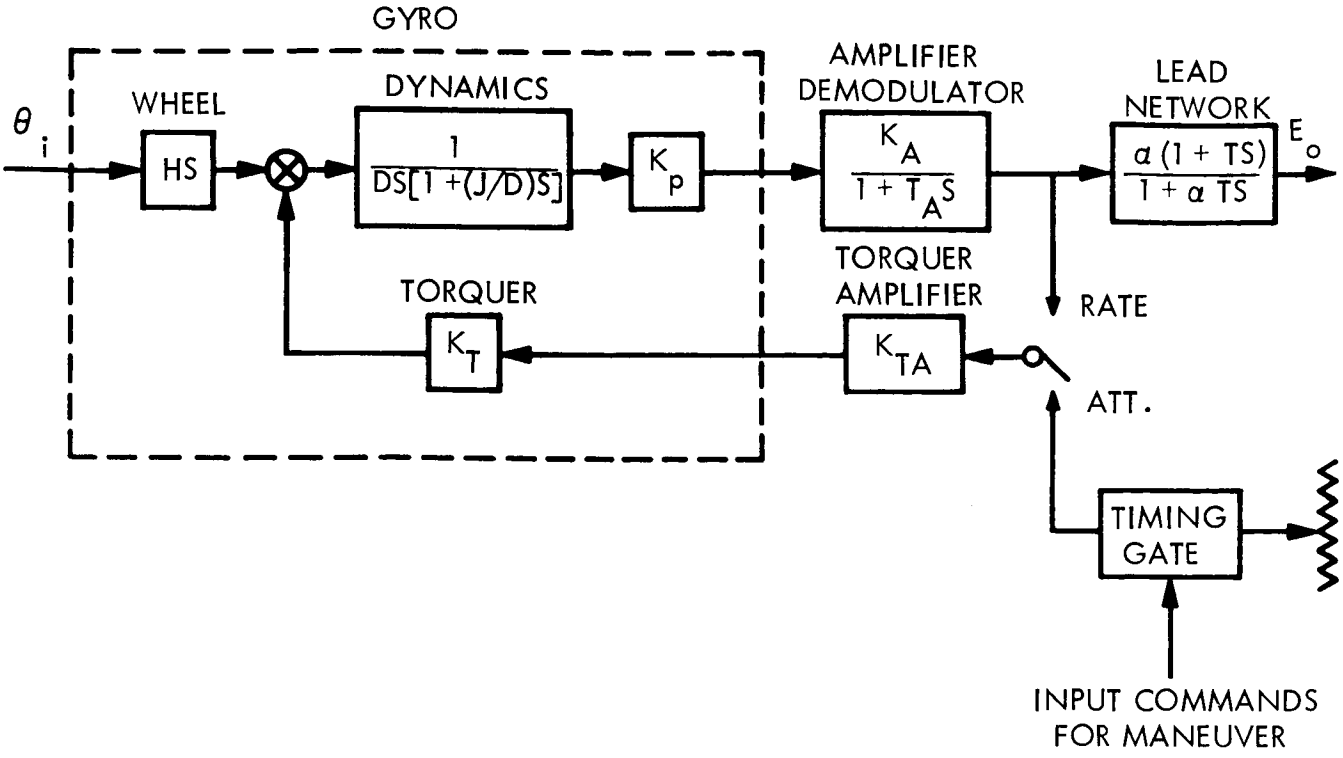

Figure 9. Block Diagram of Open-Loop Analog Mechanization

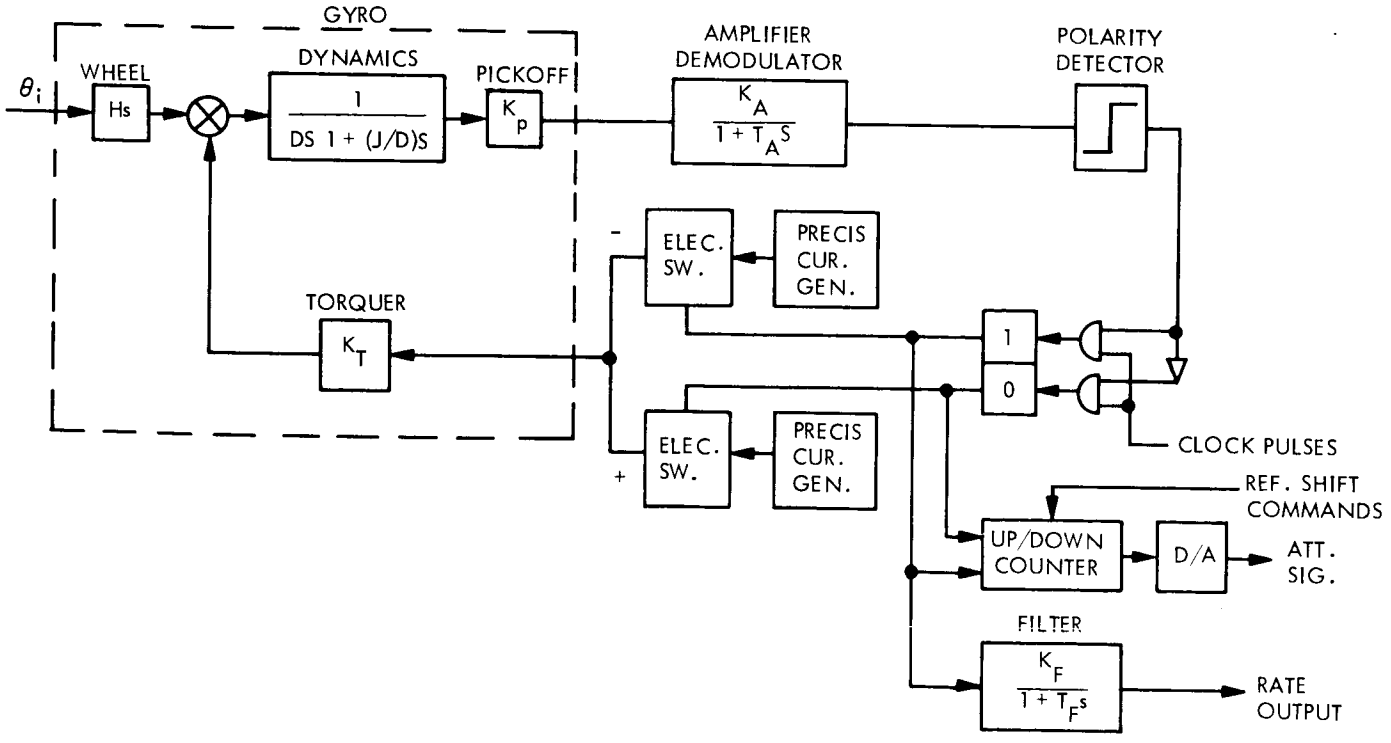

Figure 10. Block Diagram of Pulse-Rebalance Strapdown

of the open-loop analog system with bias update is attributed to the elastic restraint drift term caused by operating with an off-null attitude error.

Maneuvering accuracy of the two systems would compare as follows:

Open-loop analog:	±0.3 percent + cross-coupling due to off-null attitude error
Pulse-rebalance strapdown:	±0.1 percent

From these evaluations, it would be concluded that, if in-flight bias-drift updating is not utilized, and if the maneuver accuracy of the analog system is sufficient, there is no real advantage to utilizing the pulse-rebalance mechanization.

A third method of operating the gyro is in an analog feedback mode with a capacitor in the series feedback loop. This technique was used on Mariner. It has previously been shown that a rate plus attitude error indication is obtained with this scheme, and that the damping constant of the gyro does not enter into the transfer function of the DC gain. Thus, a perfect capacitor would allow operation of the gyro without a heater. The problem then becomes two-fold. Will drift effects due to large temperature variations contribute significantly to overall drift, and can capacitors be found with low enough leakage current such as not to contribute significantly to drift?

Discussions with gyro manufacturers indicate that the temperature sensitive drift coefficients for bias drift terms apply mainly to a gravity environment. For example, temperature gradients within the fluid must have g-forces to produce the disturbing convection currents. Likewise, forces on the float produced by non-perfect buoyancy of the fluid do not cause drift in a weightless environment. There are, of course, some drift effects which are present. One is change in flex lead restraint with temperature. Another is a change in the torquer scale factor, which would affect the bias trim compensation as well as the closed-loop current produced by rates into the spacecraft. Even so, these effects are felt to be second order.

Consequently, another review of capacitor characteristics was undertaken. Again it was found that the etched-foil tantalum capacitor provides the lowest leakage current per unit of capacitance. Extensive discussions were undertaken with the GE Capacitor Department, who furnished capacitors for the Mariner application. Tests were also performed by that Department to measure leakage current on a number of capacitors. The results of these tests are shown in Table 5. Some typical characteristics of the appropriate capacitor are shown in Table 6.

It is also seen from the manufacturers specification and test evaluations carried out by J.P.L. (Table 6) that the leakage currents vary greatly as functions of voltage and temperature. Capacitor selection obviously is a necessity.

At this point, it is interesting to take a quick look at the major contributions to the leakage current. It is well known from electrostatics that the dielectric displacement, $D = D(E, \theta)$ (E, θ), is a function of field, E, and temperature, θ. Thus, the change

$$dD = \frac{\partial D}{\partial E}\, dE + \frac{\partial D}{\partial \theta}\, d\theta$$

The displacement current $i = A\dot{D}$ is

$$i = A\epsilon_\theta \dot{E} + A\alpha_E \dot{\theta} \qquad \text{where} \qquad \epsilon_\theta = \left(\frac{\delta D}{\delta E}\right)_\theta$$

$$i = C_\theta \dot{V} + A\alpha_E \dot{\theta} \qquad \alpha_E = \left(\frac{\delta P}{\delta \theta}\right)_E$$

$$D = \theta_o E + P$$

$$E = V/d$$

Table 5. Tests on Engineering Samples

Capacitor Type 15K005BB

(Re-aged 12 hours, 35 volts at 25°C; off voltage 2 hours)

Leakage Current (μa)							
20 VDC Forward				Reverse			
Test No.	Serial No.	5 min	10 min	5 min	10 min	C	%D
1	52	0.6	0.3	0.9	0.3	882	6.2
2	51	0.6	0.4	1.1	0.4	996	9.0
3	50	0.3	0.2	1.2	0.5	1012	8.1
4	24	0.6	0.4	1.0	0.6	1015	7.3
5	20	0.6	0.4	0.9	0.5	1015	8.2
6	19	0.4	0.3	0.9	0.5	1027	8.2
7	15	0.8	0.3	1.2	0.6	981	6.9
8	63	1.0	0.6	1.1	0.6	1020	7.6
9	64	0.9	0.4	1.1	0.5		
10	68	0.7	0.6	1.1	0.6		
11	69	0.5	0.3	1.0	0.5		
12	71	0.6	0.5	1.1	0.6		
2 VDC							
	64	0.12	0.08	0.22	0.15	1039	9.4
	68	0.09	0.04	0.28	0.14	1079	11.3
	69	0.08	0.0.	0.25	0.10	1071	9.7
	71	0.04	0.02	0.08	0.07	1065	7.7
		0.33	0.18	0.83	0.46	1254	

Table 6. Type 15K005BB Capacitor Characteristics

Catalog Number	85°C	125C	Polarity	Foil	Capacitance μf: 25°C	Capacitance μf: Percent 25°C Cap. at Max. Rated Temp.	Capacitance μf: At 25°C percent 120 cps Cap. at 1000 cps	Capacitance μf: Capacitance tolerance at 120 cps, 25°C	DC leakage μamp: 25°C	DC leakage μamp: 85°C Rated Voltage	DC leakage μamp: 125°C Rated Voltage	Dissipation factor percent at 120 cps: 25°C	Dissipation factor percent at 120 cps: 125°C	Maximum impedance ohms at -55°C, 120 cps	Percent of 25C capacitance at -55C
* 15K005BB	30	20	N	E	1020	175	85	±20	14	105	70	20	50	4.5	5.0
** 15K005BB	30	20	N	E	1020	175	85	±20	5	12	-	20	50	1.6	50

* Spec.

** Jet Propulsion Lab data (1963)

Additionally, there is a residual polarization at zero applied potential (zero field) due to hysteresis in the dielectric.

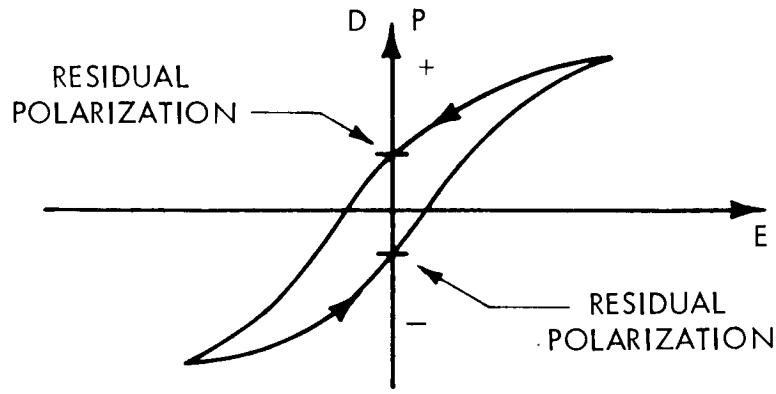

As seen in the hysteresis curve, at zero field E, the dielectric displacement, D, ($D = \epsilon_0 E + P$) is equal to the multi-valued residual polarization, $\pm P$. That is,

$$\pm P = (C/A)\ V'$$

where V' is the residual "battery voltage" due to the residual polarization changes in the dielectric to calculate the magnitude of the "battery voltage" would require knowledge of the polarization change density (or measurement) by a ballistic galvanometer) and the capacitance per unit area of the dielectric under specified conditions of temperature and voltage. This is beyond the scope of this report since this would require considerable laboratory evaluation.

On the practical side, impurities, voids and other defects in the oxide film can also cause a question of the leakage current. The performance of these high reliability capacitors has been improved by potting the sheets (that could rattle inside the can) and by hermetically sealing the leads.

An analysis of the data shown in the tables indicates that at low voltages where the system would normally operate, leakage values appear to be quite low. (The 2 vdc would be equivalent to an offset attitude error of 0.4 degrees in a system having a 5 VDC/DEG scale factor.) Calculations of system parameters indicate that a capacitive value of about 5000 μ f would be required. From the data it would appear that total leakage current for a bank of five, 1020 μ f capacitors would amount to about 0.6 μa. Temperature effects would probably be negligible for the predicted temperature range for the Voyager control equipment.

The 0.6 μa leakage current would contribute a drift of

$$\dot{\theta}_D = I_L \times K_T$$

where $\dot{\theta}$ = drift

I_L = leakage current

K_T = gyro torquer scale factor

For a gyro K_T of the order of 120 deg/hr/ma, a drift component of 0.072 deg/hr would result. This in itself is quite significant in a system which is already hard pressed to meet 0.25 deg/hr overall. This coupled with the fact that the capacitor requires a cycling circuit to reform the dielectric for minimizing the high leakage current after long periods of storage greatly detracts from this scheme. It would seem, however, that if the gyro heater power saving were a significant contribution to the success of the Voyager mission, then further analysis and testing should be performed to determine if a specific capacitor value could be used with a specific gyro to maintain the required performance accuracy.

2.2.8.5. Single Phase versus Polyphase Power Supply for Gyro Spin Motors

The results of the investigation of the gyros proposed for Voyager indicate that single phase power can be used for the gyro motors with no degredation of performance. However, a power penalty does result when the gyros are operated in this manner.

The industry standard motor in precision gyros in the hysteresis synchronous type since this type of motor is a constant speed device not sensitive to small variations in line voltage or load. A pure hysteresis synchronous motor has no special starting windings and is started by the hysteresis effects in the rotor caused by a rotating magnetic field. This rotating magnetic field can only be generated by a polyphase (either two or three phase) winding in the stator. A single phase winding will not generate a rotating magnetic field.

The standard method for operating either two or three phase motors from a single phase supply is to use a phase splitting capacitor to generate an approximate polyphase supply from the single phase source. This polyphase supply is then used to generate the required rotating magnetic field in the motor. Two and three phase gyro motors would be typically wired as shown in the sketch for operation from a single phase supply.

The efficiency of the gyro motor system is reduced when it is operated from a single phase supply. For typical two phase and three phase gyro motors of the type considered for Voyager, a power increase of approximately 0.5 watts is required per gyro for a total of 1.5

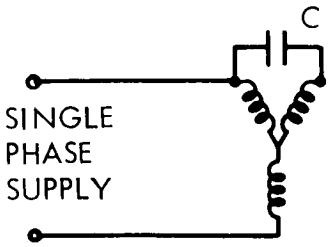

THREE PHASE MOTOR

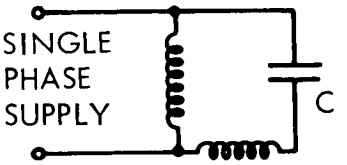

TWO PHASE MOTOR

watts per three-axis system. The required single phase input voltage must be nominally 30 volts, whereas a 26 volt source is used when the motors are operated directly from a poly-phase supply.

Standard three phase Kearfott Alpha gyros wired to a single phase source as shown in the sketch were successfully flown on the Lunar Orbiter program and will be flown in Nimbus D.

The use of single phase power instead of the two or three phase power presently required, depending upon the choice of gyros, would result in several improvements in the power sub-system. Assuming the power increase accompanying this change was slight, a decrease in system weight and power loss might be realized. System complexity would be considerably reduced since six power circuits would be eliminated. Fault sensing, fault removal, and free running capability are less difficult to implement on single phase systems.

A single phase gyro spin motor power supply is selected.

2.2.9. Digital/Analog Data Processing

As part of the redundancy phase of Task C, a study was made to determine the relative merits of analog and digital processing of attitude control data. Specifically, the advent of micro-electronics, the inherent reliability of digital circuitry, and the availability of digital sensors indicated the previous decision to use an analog processor in the G&C subsystem should be reviewed.

A presentation of the study results was made during the update period; the results were also recorded in Technical Memorandum VOY-C3-TM-33 dated March 15, 1967, which was part of the Task C Redundancy Study Report. A brief summary of this study is presented below.

The study reviewed both the functional requirements of the G&C subsystem and the analog design previously selected during Task 'B'. This design was then compared with several digital processing configurations to evaluate relative advantages. Since the availability of

analog sensors largely influenced the decision in favor of analog processing, digital and analog flight proven sensors were also reviewed.

The requirements for control signal data processing are relatively simple and straightforward. Each control loop operates in a null seeking mode, i.e. the pointing error to the celestial reference (sun or Canopus) is made to approach zero. There are no complex decisions to be made. For each axis, the decision is made to operate a solenoid, or not, by summing two signals and then detecting if a threshold value has been exceeded. Accuracy requirements are moderate and there are few modes of operation. Long life is a primary requirement. The conclusion reached was that either type of processor could meet all requirements, although the digital processor was potentially more versatile, e.g. in the ability to provide off axis pointing. Such versatility, however, is not needed.

A review of available sun sensors and gyros showed suitable digital and analog types were available. Pulse rebalancing techniques within the gyro loop could be used to provide a digital output from the inherently analog gyro. A simplified version of a digital sun sensor currently used by the C&S subsystem for maneuver attitude verification was deemed satisfactory. No digital Canopus sensor was found to be available, but the analog sensor followed by an analog/digital converter could be used. The analog sensors were in all cases much simpler devices than their digital counterparts. The digital sensors permit off axis pointing.

Several configurations for the subsystem were evaluated to determine their relative complexity. In configuration No. 1, all sensors were analog; the processing of their signal outputs was performed digitally. This necessitated analog/digital conversion of the sensor errors before processing could take place. In configuration No. 2, digital sun sensors and gyros were used with a digital processor. The analog Canopus sensor was retained. Configuration No. 3 was a hybrid subsystem in which analog processing was retained for the relatively short modes where large angles and rates occurred. During the long cruise and orbit operations modes, digital sun sensors and processor was used. It was planned to turn off the analog

equipment so that its expected life might be improved without the need for triple redundancy with its attendant costs in weight and power.

For each configuration, a block diagram was generated in sufficient detail so that its complexity could be evaluated and a preliminary parts count could be made. In each configuration, the digital processing was more complex and took more parts. In configuration No. 1, the A/D conversion equipment not only was an extra step with no apparent advantage, but the conversion required more analog equipment than it would replace. In configuration No. 2, the digital sun sensor was far more complex than the passive analog sensor. The pulse rebalance gyro contained analog electronics similar to the analog version plus more electronics to provide pulses with carefully controlled width and amplitude. The lack of an available digital Canopus sensor necessitated retention of the analog version with A/D conversion. In configuration No. 3, the digital sun sensor was again less reliable than the analog sensor. The digital processing could be applied effectively in only the pitch and yaw loops due to the lack of a Canopus sensor. In addition, there was a requirement to measure time in deadband for damping by derived rate, for which no proven technique was found to cover all cases of balanced and unbalanced limit cycles.

To summarize, the conclusions reached were as follows:

a. The subsystem requirements can be met by either analog or digital processing of the sensor data. The decision is not clear cut, and could be changed by having a digital computer on board for other reasons. Although the digital system is potentially more versatile, the analog system meets all requirements more simply.

b. Flight proven models of both types of sensors are available. Basically, all sensors are analog devices whose output is subsequently converted to a digital value. Consequently, those which use the analog output directly are simpler and more reliable than their digital counterparts.

c. The digital processor which includes required A/D conversion equipment is heavier, more complex and less reliable than the analog processor.

d. Analog processing should be retained for the G&C Subsystem.

3. FUNCTIONAL DESCRIPTION

3.1. ACS OPERATION

The mission requirements of the ACS are:

a. To acquire external attitude references

b. To stabilize the Planetary Vehicle and Flight Spacecraft to these references for the purposes of providing:

1. Efficient solar power conversion

2. Antenna Earth-pointing reference

3. Plant Scan Platform Mars-pointing reference

4. Coordinate reference for trajectory corrections

c. To maintain or modify the Planetary Vehicle and Flight Spacecraft attitude under control of inertial devices when required.

The external references chosen for the VOYAGER ACS are the sun and the star Canopus.

The following sections describe the mechanization of the ACS to fulfill these requirements, the pertinent subsystem performance characteristics, and the operational modes and sequences, and approaches to component designs.

3.2. MECHANIZATION

The external configuration of the Flight Spacecraft is illustrated in Figure 11. Solar panel orientation is accomplished by pointing the spacecraft negative roll axis at the Sun.

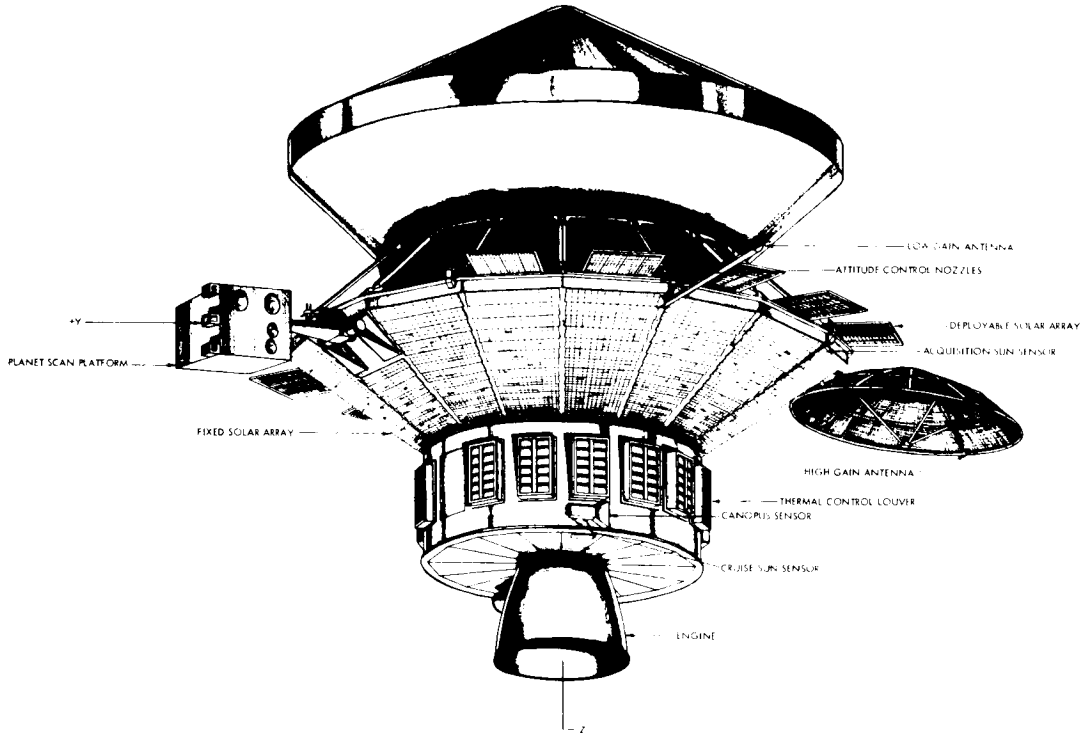

Figure 11. Voyager 1973 Spacecraft (External Configuration)

Holding a fixed orientation to the Sun and the star Canopus is accomplished by pointing the spacecraft roll-yaw plane so that Canopus lies in it. The capability of maneuvering the spacecraft to any orientation is provided by the use of three body-mounted gyros (aligned to the spacecraft pitch, yaw and roll axes) which can be switched by command to operate in a position mode and torqued at a precise rate for a precise time. The following is a description of the mechanization of the ACS.

3.2.1. Solar Orientation Loops

Solar orientation is accomplished by controlling the spacecraft motions about the pitch and yaw axes. Both control loops are identical except for the amounts of thrust provided by the cold gas jet subsystem which are sized in relation to the spacecraft moments of inertia to give equal control angular accelerations about both axes.

The basic components of each of the solar orientation loops are a sun sensor with a spherical field of view to provide an error signal and a cold gas jet subsystem to provide control torque. Auxiliary components to process the error signal and to provide loop compensation for control of the torque are the threshold detector, the rate gyroscope and the gas jet driver. Interconnection of these components is depicted in Figure 12 for the pitch and yaw loops.

3.2.2. Roll Orientation Loops

The roll-yaw plane orientation is accomplished by controlling spacecraft motion about the roll axis while the negative roll axis is pointed at the Sun.

The basic components of the roll axis control loop are a star sensor with a 9 degree by 36 degree total field of view (selectable in five steps of 9 by 11 degrees) which provides an error signal, a rate gyroscope for acquisition rate control, and a cold gas jet subsystem to provide control torque. A threshold detector and a gas jet driver process the error signal to control the torque. The control loop is shown in Figure 13. The spacecraft negative yaw axis will not necessarily point directly at the star because the spacecraft-Canopus line is not perpendicular

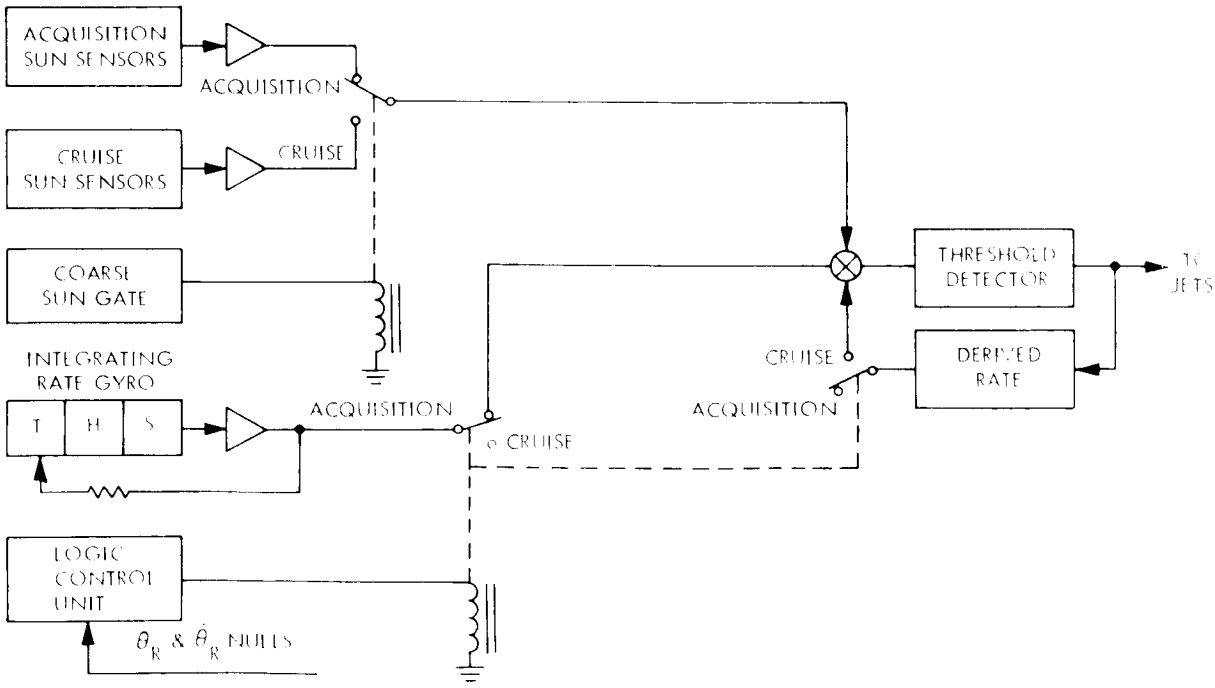

Figure 12. Pitch or Yaw Acquisition and Cruise Modes (Simplified Block Diagram)

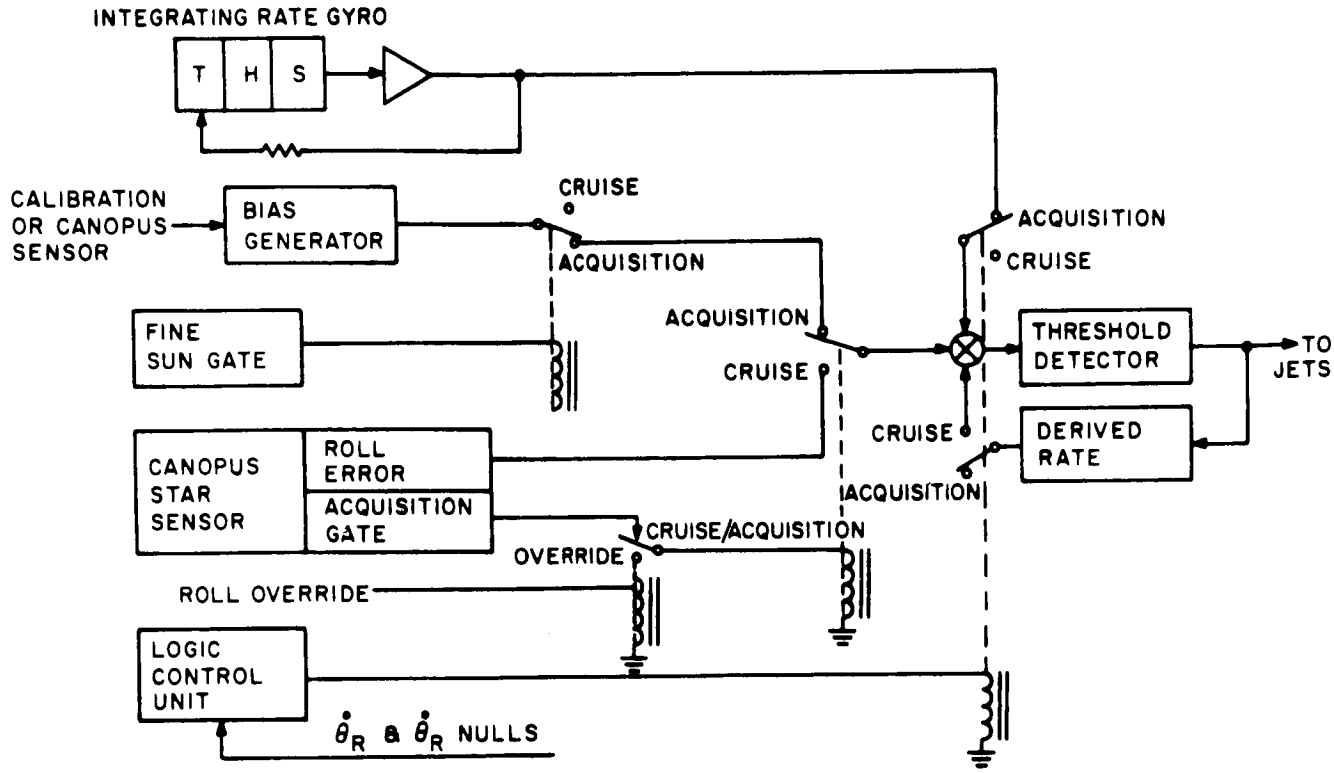

Figure 13. Roll or Yaw Acquisition and Cruise Modes (Simplified Block Diagram)

to the spacecraft-Sun line at all points along the heliocentric orbit. The negative yaw axis will be perpendicular to the spacecraft-Sun line, such that Canopus will lie in the spacecraft roll-yaw plane.

3.2.3. Commanded Orientation Loops

Maneuvering the spacecraft to any orientation is accomplished by switching the control loops to the gyros, which are placed in position mode, and then commanding a specific angle of turn for each axis sequentially. All the axes operate in the same manner.

The basic components of each of the commanded orientation loops are a gyro to provide an error signal referenced to the spacecraft's position at the time of switching and a Cold Gas Jet Subsystem to provide control torque. Auxiliary components to torque the gyro and process

the error signal are: (a) the torquer current generator; (b) the gyro output amplifier, demodulator and torquer amplifier; (c) the gyro buffer amplifier; (d) the threshold detector; and (e), the proportional plus lead network and the gas jet driver. The interconnection of these components is shown in Figure 14. By commanding rotations of the spacecraft through precalculated angles about any of the spacecraft axes, any desired spacecraft orientation can be obtained in an optimum sequence.

3.2.4. Complete Mechanization of the ACS

Figure 15 is a diagram of the complete ACS mechanization. The previous block diagrams are simplified descriptions of the individual control loops abstracted from Figure 15. All component assemblies depicted in this diagram are considered a part of the ACS except for the gas jet subsystem. The accelerometer and its associated electronics within the gyro and accelerometer package are also functionally a part of the autopilot subsystem. The accelerometer was packaged with the gyros because these components have similar mounting and alignment requirements and can possibly be obtained from one vendor source. Two Canopus Sensors are shown; the second one is used during the orbiting phases described in 3.4. Two

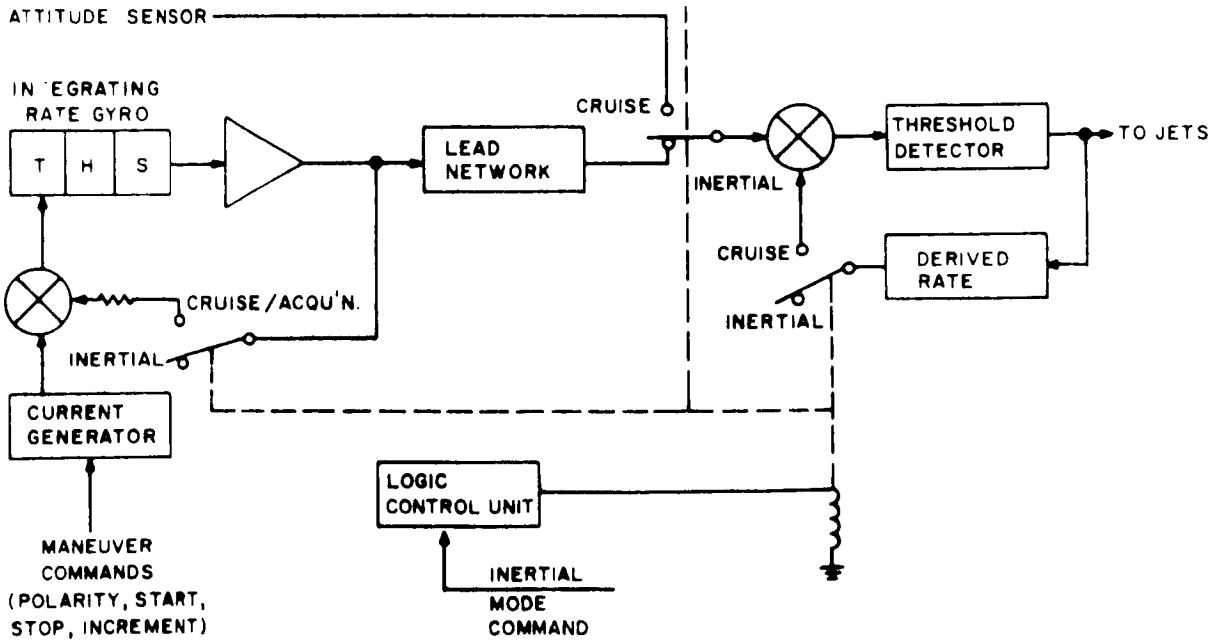

Figure 14. Typical Pitch, Yaw or Roll Inertial/Maneuver Modes (Simplified Block Diagram)

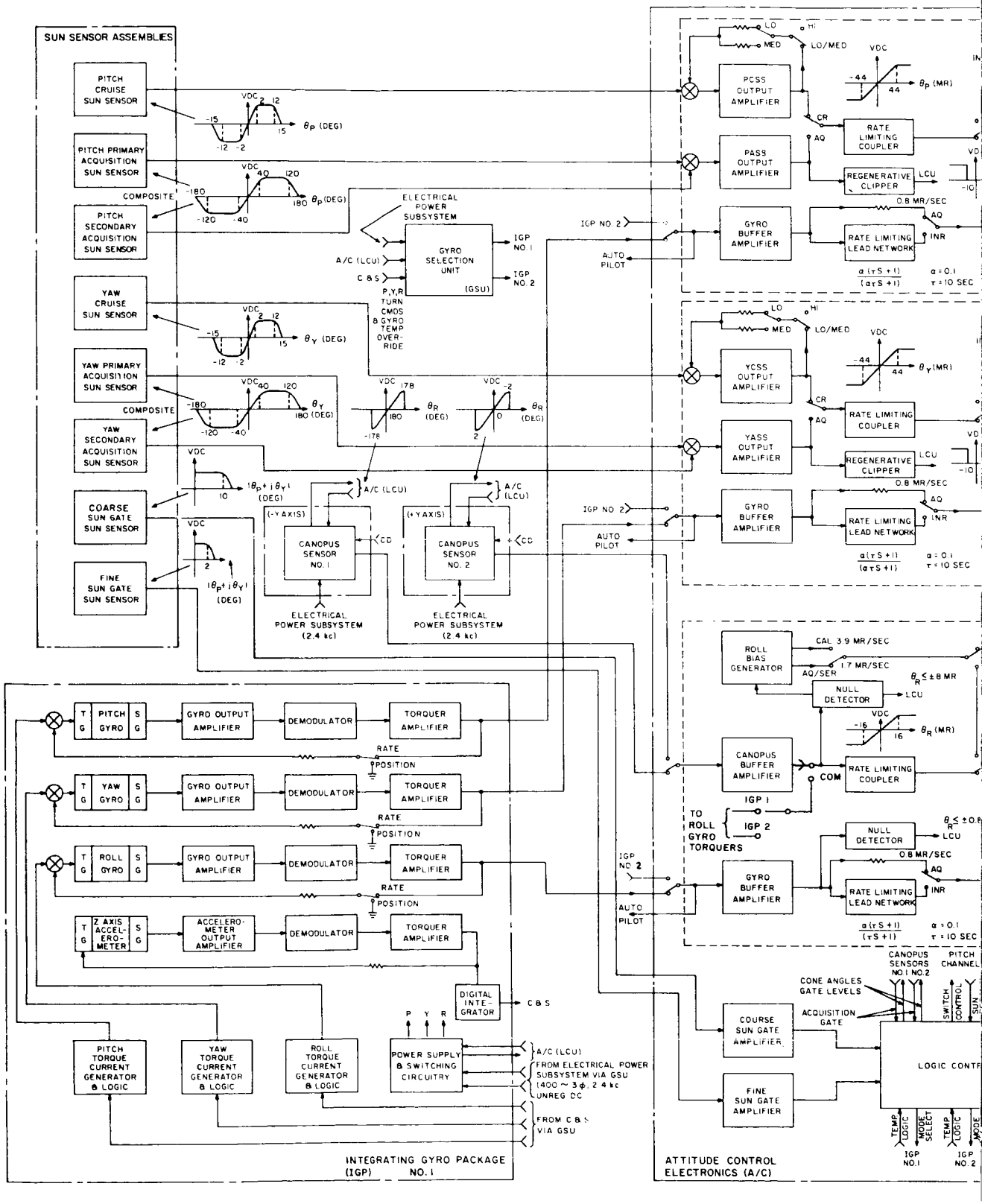

FOLDOUT FRAME

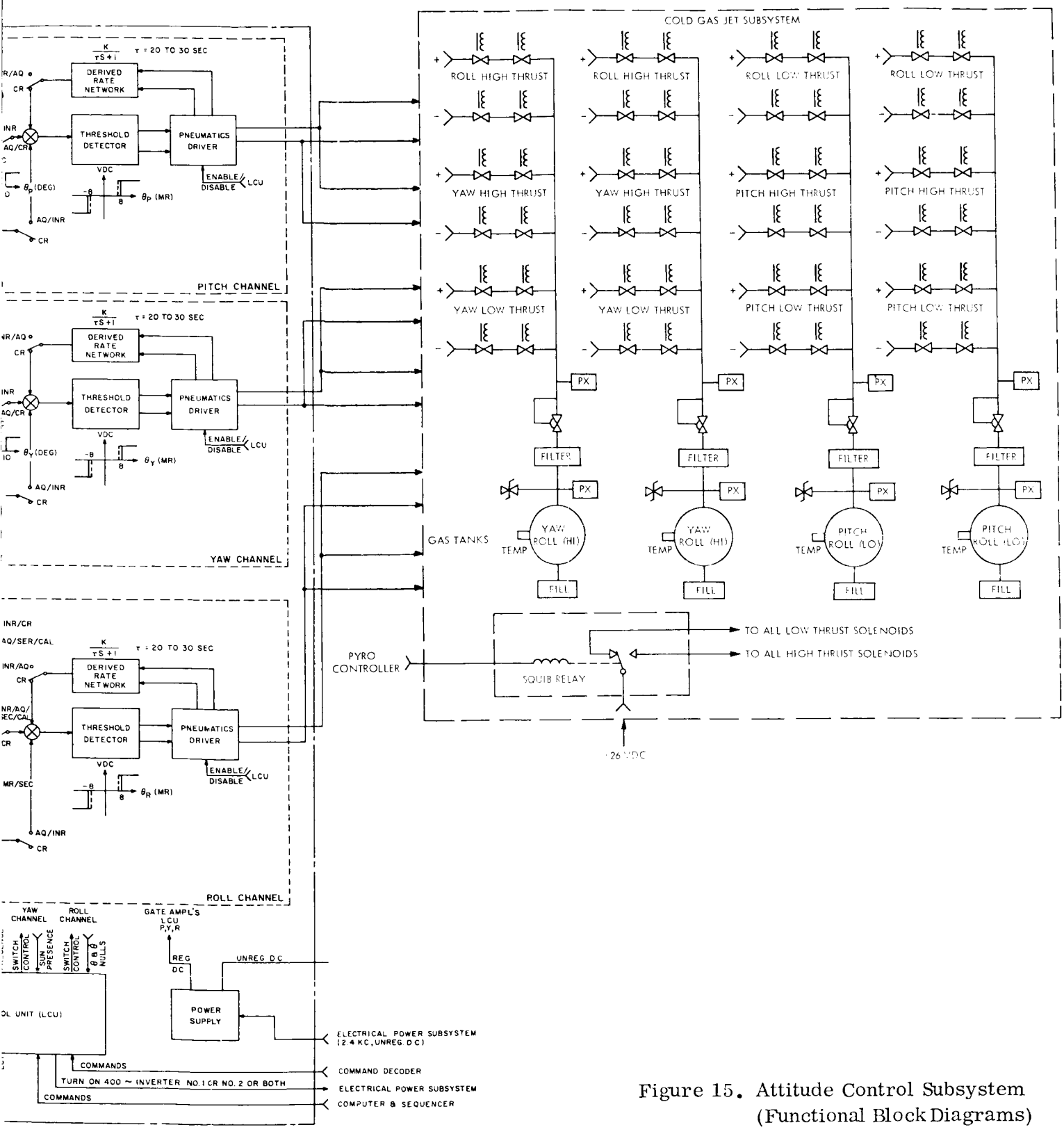

Figure 15. Attitude Control Subsystem (Functional Block Diagrams)

FOLDOUT FRAME

gyro packages are shown as discussed in 3.3. A two level thrust system is used to reduce gas consumption after capsule separation. The squib relay enables power to the low thrust jets by a signal from the gyro controller. All other significant components within the ACS which have not been discussed thus far, are covered in paragraphs 3.3, Modes and Sequences.

3.3. MODES AND SEQUENCES

The following is a description of the ACS in each of its modes of operation. The automatic sequencing of the ACS is controlled by the Logic Control Unit (LCU). Based on digital information received from the three control loops, the sun gate sensors, the Canopus sensor gate, the command decoder, and the computer and sequencer (C&S), the logic control unit makes decisions as to the ACS situations and sends digital signals to the loops to change component interconnections. The ACS is sequenced through the following modes of operation to fulfill its mission of controlling the angular orientation of the spacecarft:

a. Cruise mode

b. Pitch and yaw acquisition mode

c. Roll calibration mode

d. Roll acquisition mode

e. Reacquisitions

f. Maneuver mode

g. Occultations

3.3.1. Cruise Mode

This mode applies to the operation of the ACS when the components of the individual loops are interconnected as indicated in Figure 15. (Normally, this condition exists when the celestial references have been acquired.) When the cruise mode interconnections are changed, the ACS will be performing in either the acquisition, maneuver, or occultation mode. The roll

calibration and roll override situations are just particular phases of the acquisition mode. The cruise mode pertains to normal operating conditions of the spacecraft in orbit about Mars as well as during the interplanetary cruise phase.

3.3.2. Acquisition Mode

This mode is automatically introduced into the ACS logic whenever the Switch to Cruise Mode command is received. A special condition is mechanized following separation to result in the calibration of the magnetometer and the Canopus sensor. This condition is established prior to lift-off by commanding switch to cruise mode followed by the command to select roll calibration turn mode. The latter command inhibits the Canopus acquisition signal which is normally a part of the cruise mode.

For initial acquisition the components are interconnected as depicted in Figure 12 and 13 except that the Canopus acquisition gate signal is inhibited. The gyros are at operating temperature and the wheels at operating speed. The Canopus sensor is on, the pneumatic drivers are disabled and the roll calibration turn bias has been selected as the output of the roll bias generator. Upon receipt of a post separation command from the C&S to enable pneumatic drivers, the ACS will remove the initial angular rates and drive the negative roll axis toward the Sun.

When the negative roll axis is within ten degrees of the spacecraft/Sun line, the coarse sun gate signals the logic control unit and the acquisition sun sensors are switched out and the cruise sun sensors switched in the pitch and yaw control loops. When the negative roll axis is within two degrees of the spacecraft/Sun line, the fine sun gate signals the logic control unit that Sun acquisition is complete. The logic control unit then allows the roll axis to commence the controlled angular rate of turn of 3.9 milliradians per second to permit magnetometer/Canopus calibration. Previous to Sun acquisition, the roll loop has been receiving commands from the roll gate gyro to limit the angular rate to plus or minus 0.2 milliradians per second.

At the completion of the magnetometer/Canopus calibration period, the C&S will issue the switch to cruise mode command. The logic control unit will then enable the Canopus Acquisition Gate signal line and switch the roll bias generator to the Canopus search bias. In the absence of a Canopus acquisition gate signal, the roll bias generator is connected to the roll loop and the spacecraft commences a controlled roll turn of 1.7 milliradians per second. When the star Canopus comes within the star sensor's field of view, the Canopus acquisition gate signals the logic control unit, the roll bias is disconnected and the Canopus error signal is switched into the roll loop.

When the roll angular rate and position are within null detector limits, the logic control unit switches the gyros out of all three control loops, switches in the derived rate networks and enables turning off the gyros by the C&S. The ACS is now operating in the cruise mode. All subsequent commands to switch to cruise mode will result in those activities delineated above except for the magnetometer/Canopus calibration phase.

Confirmation that the star acquired by the Canopus sensor is indeed Canopus is not required during normal operation since the star sensor has a sufficiently narrow band of acceptable intensities that all stars but Canopus are rejected. However, verification may still be obtained by ascertaining proper performance of the articulation and communication subsystems in pointing the high gain antenna for peak performance. Star mapping is also a possible method of verification. If after the cruise mode has been established, it is desired to resume the roll search, a roll override command may be sent. Upon receipt of the command, the logic control unit will turn the gyros back on in the rate mode and connect them to their respective loops. At the same time all pneumatic drivers are disabled until the gyros come up to temperature and power is applied to their wheels. The search rate bias is applied to the roll loop and the remainder of the acquisition sequence takes place, terminating in the cruise mode.

3.3.3. Reacquisition Sequences

Part or all of the automatic acquisition sequence described above will occur in the following situations:

a. With the spacecraft stabilized to the Sun and Canopus, any non-catastrophic disturbance that results in the loss of either of these references will cause the logic control unit to automatically turn on the gyros in the rate mode and connect them to their respective loops. At the same time all pneumatic drivers are disabled until the gyros come up to temperature and power is applied to their wheels. The logic control unit then redirects the necessary portions of the acquisition sequence to return the ACS to the cruise mode.

b. With the spacecraft operating in the maneuver mode, the signal to switch to the cruise mode will cause the logic control unit to immediately redirect acquisition as the gyros will already be at their operating temperatures. This same condition applies to reacquisitions after occultations of the Sun or Canopus in orbit about Mars in the event that the spacecraft has experienced excessive drift during the inertial control period of occultation.

3.3.4. Maneuver Mode and Sequence

In this mode the C&S takes direct control of the attitude control logic functions to maneuver the spacecraft to a precalculated attitude in space for the purposes of trajectory corrections, orbit insertion or capsule separation.

Initially, the components are interconnected for cruise mode operation. Sixty minutes before the intended start of maneuvers, the gyros heaters are turned on to allow them to come up to operating termperature. Just prior to initiating the first turn, the three control loops are switched to inertial control (gyro in position mode as input to the loop). The C&S then signals the torquer current generators in the Integrating Gyro Package to torque their respective gyros for a predetermined time increment. This is done for one axis at a time in any combination of axes for one to three turns. At the completion of the final turn, 25 minutes are allowed for verifying the maneuver by telemetered information from the Solar Aspect Sensors. Then the intended event is performed while the spacecraft remains under inertial control in all three axes. At the completion of the event the C&S relinquishes control of the attitude control

logic functions to the logic control unit by the Switch to Cruise Mode command. At this point a complete reacquisition sequence takes place resulting in the cruise mode configuration.

3.3.5. Occultations During Orbit Mode

The following command sequences together with the automatic reacquisition sequence provide control during occultation periods. The gyros are commanded on before the onset of a Sun or Canopus occultation period and are kept on for the entire period. An occultation period is that period of the Mars orbit phase which contains an occultation of one of the references in each orbit of the spacecraft.

For a sun occultation, the Enable Sun Occultation Mode command is given anytime before the onset of the occultation period. The logic control unit then automatically switches the pitch and yaw loops to inertial position control at the start of an occultation which is determined by noting that all sun sensor outputs are below a threshold value. When the logic control unit determines that the Sun is present, it switches the pitch and yaw loops back into the cruise mode configuration. This sequence occurs once in each spacecraft orbit about Mars. If the Coarse Sun Gate signal is not present at this time, a complete reacquisition sequence is directed. This would not occur normally. If the Canopus acquisition gate is lost during the Sun occultation, the roll loop will automatically be switched to inertial position control rather than the Canopus search mode. At the conclusion of the last Sun occultation of an occultation period, the Switch to Cruise Mode command is given which cancels the previous Enable Sun Occultation Mode command.

For Canopus occultations the command enable canopus occultation mode is given prior to the start of the first occultation. This places the roll channel in the inertial position mode with the Canopus sensor output torquing the gyro. Thus, roll control is maintained with the roll gyro, and the Canopus sensor output acts to offset the gyro drift. When Canopus is occulted, the Canopus sensor output sensor output vanishes and the spacecraft is under gyro control only. This mode of operation requires no mode switching at the start and finish of Canopus occultations.

In this mode the roll channel cannot recognize loss of Canopus. To offset this a fixed interval timer is used,set to the maximum Canopus occultation time. The timer is started by the loss of the Canopus present signal from the sensor. If at the end of the interval the Canopus present signal has not reappeared, the control system is automatically switched to the acquisition mode.

If the fine sun gate signal is lost during a Canopus occultation, the logic control unit will switch all axes to the rate mode and reacquire the sun; it will then return the pitch and yaw loops to cruise mode and the roll loop to inertial control.

3.3.6. Mars Limb and Natural Satellite Interferences

The Canopus sensor may be caused to lose track of Canopus during Mars orbiting if either excessive light from the Mars limb enters the sensor shield or if one of Mars' natural satellites passes through the sensor's field of view. Since the orbits of the spacecraft and the natural satellites are known, possible interferences can be predicted and the ACS will be commanded to either a roll drift mode by disabling the roll pneumatic drivers or the Canopus occultation mode during those periods when such interference is anticipated.

3.4. FUNCTIONAL RELIABILITY

The following is a description of those items which contribute to the reliable performance of the ACS functions:

a. Attitude Control Gas Jet Subsystem - (See Figure 15.) Coupled pairs of gas jets are used on each axis with two valves controlling each jet. These valves are connected in parallel electrically and in series pneumatically. The jets of each couple are supplied from separate tanks and regulators. Two single, particular valves must fail in the primary failure mode (leakage) before excessive loss of gas occurs. In this case, control angular acceleration is cut to half its existing value. (See Section 3.4.4. for a description of redundant valve drivers.)

b. Integrating Gyro Package Back-up - (See Figure 15.) In case of a failure within Integrating Gyro Package No. 1 (IGP No. 1), a second identical package (IGP No. 2) may be brought into use by ground command. The capability of utilizing any combination of gyros and accelerometers in the two packages could be implemented; the present design, however, only allows for using one package or the other for inputs to the control loops. The second package will be turned on and temperature stabilized in a stand-by condition during those mission functions where time is critical in taking corrective measures due to malfunctions in IGP No. 1; (i.e. Mars orbit insertion).

c. Canopus Sensor No. 2 - This sensor is mounted on the spacecraft so that its field of view points in a direction 180 degrees away from that of Canopus Sensor No. 1. In all other respects, both sensors are identical.

d. Disabling of Pneumatic Drivers - The logic control unit will disable all pneumatic drivers whenever a celestial reference is lost and the gyros are not running. This automatic logic feature prevents wasting cold gas under those circumstances when the control system does not have adequate knowledge of the dynamic state of the spacecraft.

Two Canopus sensors are provided so that the mission can be continued if one sensor fails. Sensors are switched by ground command.

The second Canopus sensor is mounted so that the direction of its field of view is 180 degrees from the primary sensor. This is done because there are times in some missions, depending upon the orbit, in which the PSP field of view is blocked by the biological barrier if only one Canopus sensor is used. The diametrically opposed sensors provide for no interruption in PSP coverage of the planet during these periods.

3.5. COMPONENT DESCRIPTIONS

The following paragraphs present some approaches to component design which have been considered, and provide preliminary information on selection of vendor-supplied components. They are not intended to show results of formal design effort, or firm decisions on purchased parts and components.

3.5.1. Sun Sensors

3.5.1.1. Acquisition Sun Sensors

The acquisition sun sensors are used to provide intelligence to the control system to allow coarse acquisition of the spacecraft/sun line from any initial spacecraft orientation. Four of these sensors are used on each of the pitch and yaw axes thus providing 4π steradian field of view coverage. Some shading is required on the four anti-null sensors to prevent erroneous signals being generated by reflection from the capsule. The earth albedo will cause some null offset which is of no consequence if the shift to the cruise sun sensors can be made. This is done at approximately ten degrees from the spacecraft/sun line.

Table 7 describes acquisition sensor characteristics at one astronomical unit from the Sun.

Table 7. Acquisition Sensor Characteristics

Field of view	360 degrees
Linear range	$\pm 30^\circ$ (null) $\sim$ ± 15 deg (anti-null)
Accuracy	$\pm 1^\circ$
Peak output	0.75 ma
Sensitivity (linear range)	26 μ a/deg (null) $\sim$ 47.5 μ a/deg (anti-null)
Operating termperature	-20°C to 85°C

3.5.1.2. Cruise Sun Sensors

The cruise sun sensors are used for pitch and yaw attitude control whenever the control system is in the cruise mode. These sensors have a field of view of ± 15 degrees with a linear range of ± 1 degree. During the transit period when the earth is within 15 degrees of the spacecraft/Sun line, the earth's albedo illumination is approximately 2×10^{-8} of the Sun Illumination and therefore contributes negligible pointing error.

Table 8 describes cruise sensor characteristics for a distance from the Sun of one astronomical unit. The scale factor variation due to decreased radiation intensity is compensated by gain changes (3 increments) in the Attitude Control Electronics. These gain changes are commanded by the C&S.

Table 8. Cruise Sensor Characteristics

Field of view	±15 degrees
Linear range	±1 degree
Linearity	±5% of 1° output
Peak output	1.7 ma (at 2.5 degrees)
Sensitivity	900 μa per degree 0 → 1°
Null accuracy	0.05 degrees at 1 sigma
Operating temperature	-20° C to 85° C

3.5.1.3. Fine and Coarse Sun Gates

Two radially symmetrical field of view gating sensors are placed on the vehicle next to the cruise sun sensors and pointing in the same direction (-Z axis). The coarse sun gate (10 degree field of view) is used to switch control from the acquisition sun sensors to the cruise sun sensors. The fine sun gate (2 degree field of view) is used to signal the C&S that Sun acquisition is complete.

3.5.2. Canopus Sensor

The Canopus sensor is essentially that flown by JPL on the Mariner Spacecraft. The characteristics cited below are based on the "Mariner Mars 1969, Preliminary Design Review, Attitude Control Subsystem, Canopus Sensor," by the Honeywell Radiation Center.

3.5.2.1. Brief Description

This sensor incorporates an electrostatically focussed and deflected version of the image dissector tube. It has a slit aperture defining an instantaneous field of view which can be electronically scanned across the sensor view field. In operation, the slit view field is caused to oscillate or dither in short strokes in a direction orthogonal to the long axis of the slit. Also, by program or command, the slit field-of-view can be shifted along its long axis to any of a series of fixed, overlapping positions.

The sensor is mounted on the spacecraft so that the dither motion of the instantaneous field will detect Canopus direction changes due to roll, but the length of the slit permits up to 11 degree change in pitch. During the relatively long VOYAGER mission, however, Canopus will gradually appear to move toward the end of the slit field. Therefore, periodically the field is electronically stepped to the next fixed position, restoring Canopus near the center of the field.

A roll axis null error signal is generated by a phase sensitive demodulator and a DC bipolar output is supplied to the ACS.

3.5.2.2 Functional Details

To assure automatic unambiguous acquisition of Canopus during initial or subsequent search, the magnitude passband gates must be set much closer to Canopus than was the Mariner IV Canopus sensor. With careful determination of the magnitudes of Canopus and other potential targets plus a high degree of detector photocathode uniformity and control of sensor drift, it is believed possible to set the high and low gates so that no target other than Canopus will be acquired. The only exceptions are the two moons of Mars which may enter the brightness passband during Mars approach or during orbit. Since this is predictable, action can be taken to prevent undesirable control system activity; for example, switch to inertial control.

The high gate setting, used to discriminate against Sirius, Earth, the Moon, Mars and Jupiter will be set approximately 0.4 magnitude above Canopus. The low gate setting, discriminating

against Vega and all fainter stars, Saturn and all more distant planets will be set approximately 0.3 magnitude below Canopus. Because of their smaller orbits, the inner planets, Mercury and Venus, cannot lie in the field of view of the Canopus sensor during a Canopus acquisition roll about the Sun line.

Backup command modes will be available in the Canopus sensor to provide wider gates and permit operation as with Mariner IV in the event of failure in the automatic calibration function. The upper brightness gate will be removed after Canopus acquisition to prevent loss of star present signal cause by possible stray particles. Other modifications will be made where possible to improve over-all sensor reliability. Table 9 describes the Canopus sensor characteristics.

Table 9. Canopus Sensor Characteristics

S/N Canopus	Greater than 100/1
Field of View	±4.5 deg roll x ±35.8 deg pitch
Instantaneous Field of View	1.05 deg roll x 11 deg pitch
Optical Resolution	0.05 deg
Gimballing and Scan	All Electronic
Pitch Deflection	5 positions (4.8 deg overlap)
Star Acquisition	Between 1/4 and 4 times Canopus Brightness
Size	Approximately 4 x 5 x 11 in.
Weight	Approximately 6.25 lb
Power	Approximately 1.75 watts

3.5.3. Integrating Gyro Package

The package contains three rate integrating gyroscopes, one force balance accelerometer, gyro and accelerometer loop electronics, gyro temperature controls, torque current generators (precision current supplies), logic circuitry, relays, relay drivers and a regulated DC power supply.

Upon receipt of a Gyro On command, unregulated DC and 400 cycle power is applied to the temperature controller. The 400 cycle power sets the nominal frequency of the pulse width modulated temperature controller.

When the gyro reaches temperature, a signal from the temperature controller supplies 400 cps 3ϕ power to the gyro wheel and 2400 cycle power to the gyro, gyro electronics and the regulated DC power supply, and a signal to the logic control unit (LCU) indicating that the gyro wheel has been actuated. Integrating Gyro Package No. 2 will have a ground command override feature to allow the thermal switching logic to be bypassed in the event that an emergency necessitates use of the gyros before they attain operating temperature. The gyro portion of the package is now ready for operation and is capable of furnishing rate or position information in accordance with the gyro mode selection signal from the LCU.

When a command is received for autopilot mode, 2400 cycle and regulated DC power is applied to the accelerometer and accelerometer electronics. The accelerometer power switches are in series, because the gyros are on in either autopilot or attitude control, but the accelerometer is only in the autopilot mode. The analog output is converted to digital information which is sent to the C&S where it is processed to provide velocity information. Since the normal failure mode of the accelerometer loop is an open circuit, time can serve as a velocity control back-up.

Each gyro loop in the position mode is capable of being torqued by the C&S through receipt of positive on, negative on, and off commands via the Gyro Selection Unit and the torque current generators and logic circuits. These circuits then apply a precision current to the gyro torque motors to obtain a new vehicle position.

All three gyros and the accelerometer are thermally connected. Each gyro has an individual temperature control which has the capability to control the temperature of the entire sensor block. This capability adds redundancy, in that the package can operate without degradation after loss of two temperature controls. In addition, each gyro contains an over-heat

thermostat to prevent temperature run-away in case of a full-on controller failure. The accelerometer does not have a heater or temperature controller, but because of thermal connection to the gyros, it is thermally stabilized.

It is presently planned to operate the gyros at approximately 40°C. This will tend to minimize operating heater power and warm-up time as well as not causing any great difficulty in selecting the proper thermal resistances.

3.5.3.1. Digital Integrator

It is necessary to employ digital integration to supply velocity information. The device is an integrator that is reset by a capacitance discharge. The input is integrated by a Miller integrator. When the output of the integrator reaches a prescribed level, it triggers a delay multivibrator that resets the integrator and delivers an output pulse. Thus, the device is a voltage-to-frequency converter whose sum of output pulses is the integral of the input voltage. This device has the capability to deliver 10,000 pulses per second, which is equivalent to an acceleration of 100 ft/sec^2.

3.5.3.2. Gyro Selection

The Honeywell GG-334A Gas Bearing Gyro has been selected for the VOYAGER spacecraft control system although other gyros also meet the requirements. The details of the selection are reported elsewhere.

3.5.3.3. Accelerometer Selection

The Bell VII B Force Balance Accelerometer has been chosen for use in VOYAGER. Since all accelerometers investigated met the accuracy required, full selection was based on smallest size, least weight and input power. The details of the selection are reported in the Phase IA Task A study.

3.5.4. Attitude Control Electronics

3.5.4.1. Pitch and Yaw Loops

Circuitry for the pitch and yaw axes is identical. Inputs are provided by the acquisition and cruise sun sensors, and the rate gyros. Separate amplifiers are employed for the acquisition and cruise sun sensors, with gains controlled by signals from the Logic Control Unit (LCU) to adjust for decreasing Sun intensity as the vehicle-Sun distance increases. The LCU passes control from the acquisition to the cruise sun sensor, upon receipt of a signal from the coarse sun gate sun sensor. This prevents reflections from the vehicle or the albedo on Earth, Moon, or Mars from producing null offsets.

A buffer amplifier is provided in the rate gyro signal path to split the input signals into redundant paths and to allow switching in a proportional plus lead network during slewing maneuvers.

The outputs of the gyro amplifier and the sun sensor amplifiers are summed by a third amplifier. The sun error signal is coupled to the summing amplifier through a resistor network which limits the position signal at a desired level. Following the summing amplifier are threshold detectors, which are triggered when the output of the summing amplifier exceeds the limits defined by the switching line equations. The amplifier output is used to energize the solenoid valves via the majority voters and pneumatic drivers.

The derived rate network functions only during the cruise mode with the charge and discharge time constants set to different values. The charge time constant is 20 to 30 seconds.

3.5.4.2. Roll Loop

The inputs of the roll channel are the Canopus sensor signal, the gyro, and the roll bias which generates the roll search after Sun acquisition. Triply redundant null detectors are employed to generate logic signals for use in the logic control unit. The outputs of plus and minus threshold level detectors are combined in a NOR circuit to produce the LCU null signal.

In addition, the outputs of the threshold detectors are sent separately to the roll bias generator, in order to set and reset a flip-flop which determines the polarity of the roll bias. This search polarity switching is used to drive the vehicle toward Canopus null in the absence of a true error signal. Without this circuitry search through 360° would result in instances of abnormal overshoot. Normal overshoot even at half-torque levels does not exceed the sensor field of view. This polarity switching occurs well within the error saturation limits of the Canopus sensor, and therefore, the LCU is still receiving the acquisition signal from the sensor. The output of the roll bias generator is not connected to the threshold detector unless the Canopus acquisition signal is lost. The remaining portions of this axis are identical to the pitch and yaw axes.

3.5.4.3. Logic Control Unit

The logic control unit (LCU) processes commands from the Computer and Sequencer (C&S) and the Command Decoder, and handles the automatic sequencing of the control subsystem logic. Among the specific functions performed are:

a. Indicate Sun presence by monitoring the pitch and yaw regenerative clippers and the sun gate amplifiers.

b. Indicate Sun acquisition by monitoring fine sun gate amplifier.

c. Indicate star acquisition when roll rate and position signals are nulled.

d. Provide signals to turn on the 400 cycle inverters and all primary gyros in the rate mode when an attitude reference is lost.

e. Provide signals to enable or disable the pneumatic drivers as a function of signals from the gyro temperature logic which indicate whether the gyro wheels are energized.

3.5.4.4. Power Supply

Power at several voltage levels at one percent and three percent regulation is required. These voltages are obtained by transforming the 2400 cps, 50 volt input, rectifying, filtering,

and in some cases regulating the filtered output. The voltage levels are ±15 volts and ±4 volts. The use of a transformer-rectifier-regulator supply within the Attitude Control Electronics provides isolation of the circuitry from disturbances emanating from other subsystems. Conversely, transients generated within the Attitude Control Electronics will be attenuated. Two independent transformer-rectifier filter systems are provided in the power supply to permit redundant operation.

3.6. ATTITUDE CONTROL IMPULSE REQUIREMENT ANALYSES

An estimate of the total impulse requirement has been made for the VOYAGER vehicle. Table 10 gives a breakdown of the calculated impulse requirement. The estimate is conservative but does not include any safety factors; these are included in the design of the gas jet system.

Table 10. Impulse Requirements

Source	Impulse Required (lb-sec)			
	Pitch	Yaw	Roll	Total
Initial stabilization	192	190	25	407
Maneuvers	240	236	142	618
Orbit insertion	79	79	47	205
Reacquisition	50	50	33	133
Cruise - transit	40	39	27	106
Cruise - orbit	16	9	15	40
Gravity gradient	17	22	16	55
Orbit trim	110	100	56	266
Fuel slosh effects	190	180	90	485
Roll control during thrusting	--	--	100	100
Total	934	905	551	2390

The moment of inertial in slug-ft^2 are:

Transit		Orbit	
I_{xx}	= 19016	I_{xx}	= 6282
I_{yy}	= 18475	I_{yy}	= 3612
I_{zz}	= 13084	I_{zz}	= 6578

These values may not correspond precisely with those published in the section on mass properties of the vehicle since the impulse requirements were being calculated at the same time that the final mass properties were evaluated.

The estimates are based on the following assumptions:

a. Initial Stabilization

Removal of pitch and yaw separation rates of 50 mr/sec (2.86 deg/sec). Zero roll rate at separation.

Attitude stabilization in pitch and yaw, rate limiting = 4.4 mr/sec (0.25 deg/sec)

Magnetometer calibration roll at 3.9 mr/sec (0.22 deg/sec)

Roll search for Canopus at 1.7 mr/sec (0.1 deg/sec)

b. Maneuvers (3)

Yaw, pitch maneuver sequence assumed
Re-stabilization in pitch and yaw after completion of the maneuver
Roll search for Canopus

c. Re-acquisitions - Required after accidental loss of references

Solar re-acquisitions (2 assumed)
Canopus re-acquisitions (6 assumed)

d. Limit Cycle Operation

Symmetrical limit cycle operation assumed

e. Gravity Gradient

Orbit assumed is 1000 x 10,000 Km, 60 degree inclination

f. Mission Life

170 day transit
180 day Mars orbit time

g. Fuel Slosh

Fuel slosh impulse requirements are approximately 25% of total impulse.

The parameters of the system are:

a. Control acceleration 0.225 mr/sec^2

b. Dual thrust level system (i.e., control acceleration remains essentially constant throughout the mission)

c. Valve on-time during limit cycle operation 30 ms

d. Position deadbands ±8 mr

e. Maneuver rates 3.14 mr/sec

f. Roll calibration rate 3.9 mr/sec

g. Roll search rate 1.7 mr/sec

3.6.1. Gyroscopic Coupling Effects

The high separation rates and differences in moments of inertia assumed give rise to relatively large cross-coupling torques. Since the vehicle is essentially under rate control during initial stabilization, the control torques are acting to reduce the rates and the system energy is decreasing. The net effect of the cross-coupling torques is to increase the settling time of the system.

Several digital computer runs were made with separation rates of 50 mr/sec about each axis and products of inertia as large as 8000 slug-ft^2. It was found that in the worst case, the settling time was increased by approximately one-third over the single axis case. Since the largest products of inertia are 283 slug-ft^2 before capsule separation and 556 slug-ft^2 after separation, it is believed that the gyroscopic coupling effects do not present a stability problem. However, a slight penalty is incurred in gas expenditure. This penalty has been conservatively estimated to be 50 percent greater than that calculated on a single axis basis. After capsule separation, the principal moments of inertia are decreased such that this value of product of inertia is approximately 10 percent of the principal moments. Then firing of a pitch or yaw nozzle induces a rate of 0.7×10^{-6} radians/sec in the opposite axis. This is about 20 percent of the nominal limit cycle rate of 3.375×10^{-6} rad/sec and of arbitrary sign depending on the polarity of the torque. Thus no gas penalty should be assessed due to the effects of products of inertia.

3.6.2. Micrometeroid Impact

The effect of micrometeroid impact during the transit and orbit stages has been evaluated. It has been found that there will be negligible expenditure of gas due to this effect.

3.6.3. Gravity Gradient Effects in Orbit

A digital computer program has been utilized to assess the effects of the gravity gradient torques. The peak torques have been found to be several orders of magnitude below the control torques. The accumulated momentum has been evaluated and entered into the estimated fuel requirements.

3.6.4. Effect of HGA and PSP Gimbal Motion

The stepping motors advance the gimbals of the HGA and PSP in 3/16 degree increments throughout the life of the mission. The effect of this step is to move the vehicle as the ratio of the inertias, i.e., no net change in rate occurs after the step is completed. The largest moment of inertia of the antenna is forty-three slug-ft^2. The minimum spacecraft moment of

inertia is 3612 slug-ft^2. The maximum change in position of the spacecraft is then 3/16 x 43/3612, or 0.002 degrees.

The maximum PSP moment of inertia is 154 slug-ft^2, resulting in an attitude change of 0.008 degrees.

3.6.5. Roll Nozzle Failure

In the event of failure of a single roll nozzle, each firing of the remaining roll nozzle will cause a torque about the pitch axis. The distance from the plane containing all of the attitude control nozzles to the center of mass is 4 inches during transit and 20 inches during orbit after capsule separation. For a roll nozzle thrust of 0.15 pound, the torque about the pitch axis is 0.05 ft-lb. The momentum imparted to the pitch axis is $0.633 \times 30 \times 10^{-3} = 0.0015$ ft-lb sec per valve operation. For an expected 3270 operations during transit, the induced momentum is 4.9 ft-lb second. Since the thrust of this nozzle is reduced to 0.08 pound after capsule separation, the induced torque about the pitch axis is 0.08 x 20/12 = 0.13 ft lb. This corresponds to a momentum of 0.0041 ft-lb-sec per valve operation. For an expected 3270 operations during orbit, the induced momentum is 13.4 ft-lb seconds. This momentum must be removed by the pitch nozzles. The additional gas consumption is 0.028 pound.

The PSP outboard gimbal is driven continuously to track the local vertical. Because of the elliptical orbit, this requires a range in angular velocity between 0.05 and 0.005 deg/sec. The effect of this PSP momentum change is to impart a velocity to the spacecraft. The maximum velocity is 3.6×10^{-6} rad/sec. This is approximately equal to the nominal limit cycle rate, and is developed over half the orbit period, approximately four hours. Therefore, there is no measurable effect on gas consumption.

For PSP unwinding the travel is approximately 300 degrees. The moment of inertia about the outboard gimbal is 15 slug-ft^2. The resulting spacecraft attitude change is 300 x 15/3612 or 1.25 degrees. This will cause an additional two or three valve firings. Assuming 540

orbits in 180 days and 0.0014 lb-sec impulse per firing, the additional impulse is 2 x 3 x 540 x 0.0028 = 9 lb-seconds. This is a negligible amount.

These figures assume the same number of valve operations after failure of a nozzle as before. Actually the limit cycle rate and, thus, the number of operations will be reduced so that the penalty is less than that calculated.

3.6.6. Solar Balance Vane

With the high gain antenna mounted on the nominal Y_V axis, a continuous disturbance torque will appear about the vehicle X_V axis due to solar pressure. For the vehicles presently under consideration, the peak value of this torque is not sufficient to require compensation, such as by the use of a solar pressure balance vane. This is shown in Figure 16 which was developed and explained in more detail in 234AA102, Appendix I of the Task A study.

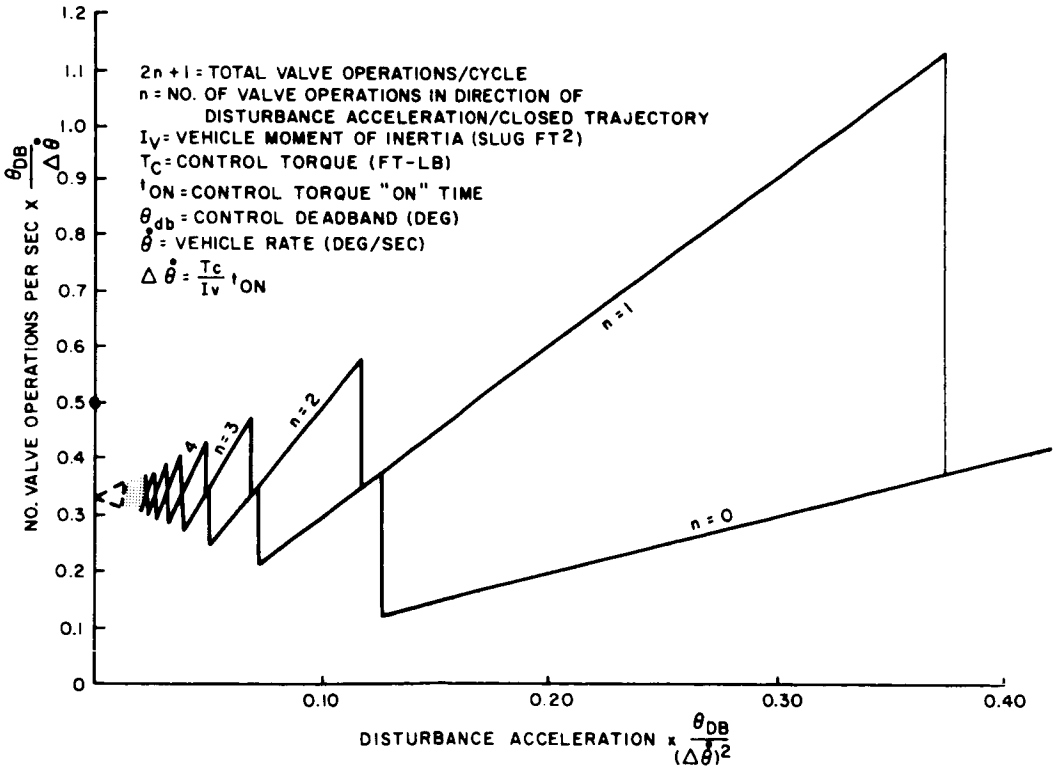

Figure 16. Number of Valve Operations versus Disturbance Acceleration for Limit Cycle Systems

Figure 16 gives the total number of valve operations of a limit cycle system as a function of the disturbance acceleration. The dimensionless parameters used are functions of the pneumatic deadband θ_{DB} and the velocity increment $\Delta\dot{\theta}$ imparted to the vehicle by the gas jets.

The number of valve operations is generally a double-valued function. The applicable value depends only on the initial conditions. For symmetrical operation in the absence of a disturbance acceleration the number of operations per unit time is shown as the singular point at $N = 0.5\,\Delta\dot{\theta}/\theta_{DB}$. The following analysis shows that, for the uncompensated system, the worst case number of value operations (and thus gas consumption) is approximately equal to that of the compensated system (i.e., symmetrical operation).

The vehicle parameters are:

Deadband $\theta_{DB} = 8 \times 10^{-3}$ radians
Control acceleration $\alpha_c = 0.225 \times 10^{-3}$ rad/sec^2
Diameter of high gain mesh antenna, A = 9.5 ft
Equivalent solid area = 30% of antenna area
Moment arm of solar pressure torque, ℓ = 14.75 ft
Pitch moment of inertia, I_x 19016 slug-ft.^{2}
Solar pressure, $P_o = 9.7 \times 10^{-8}$ lb per ft^2
Minimum valve on-time 0.03 sec

The disturbance acceleration at 1AU is:

$$\alpha_D = \frac{P_o A \ell}{I_x}$$

$$= 16 \times 10^{-10} \text{ rad/sec}^2$$

Since

$$\theta_{DB} = 16 \times 10^{-3} \text{ rad and}$$

$$\Delta\dot{\theta} = 6.75 \times 10^{-6} \text{ rad/sec}$$

the non-dimensional factor along the abscissa is

$$\alpha_D \left(\frac{\theta_{DB}}{\Delta \dot{\theta}^2} \right) = 0.563$$

From the graph, the number of valve operations N per unit time is:

$$N \left(\frac{\theta_{DB}}{\Delta \dot{\theta}} \right) = (2n + 1) \left[\alpha \frac{\theta_{DB}}{\Delta \dot{\theta}^2} \right]$$

$$\therefore \quad N = (2n + 1)(0.563) \left(\frac{\Delta \dot{\theta}}{\theta_{DB}} \right) \text{ operations/sec}$$

The single type of operation which can occur is for n=0 (i.e., one-sided operation).

Thus

$$N = 0.563 \frac{\Delta \dot{\theta}}{\theta_{DB}} \text{ operations/sec}$$

which is only slightly greater than that for symmetrical operation which is

$$N = 0.5 \frac{\Delta \dot{\theta}}{\theta_{DB}} \text{ operations/sec}$$

For a 170-day transit time 3480 valve operations are required, compared to 3100 for the symmetrical case. The additional impulse required is 4.6 lb-sec.

After the capsule separation, the pitch moment of inertia is reduced to 6571 slug-ft^2. Since the numerical value of the solar radiation pressure varies inversely with the square of the distance from the Sun, at Mars this value is approximately

$$P_o = 4.3 \times 10^{-8} \text{ lb/ft}^2$$

The disturbance acceleration is

$$\alpha_D = 2.05 \times 10^{-9} \text{ rad/sec}^2$$

Thrust level is reduced after capsule separation to maintain the same rate increment. Thus the non-dimensional factor along the abscissa becomes

$$\alpha_D \left[\frac{\theta_{DB}}{(\Delta\dot{\theta})^2}\right] = (0.563)\ \frac{2.05 \times 10^{-9}}{16 \times 10^{-10}} = .721$$

From the curve the only type of operation which can occur is one-sided (n = 0). The number of valve operations per unit time is

$$N \quad 0.721\ \frac{\Delta\dot{\theta}}{\theta_{DB}}$$

Again all the valve firings are by the same nozzle. For a 180-day orbit period 4730 valve operations are required, compared to 3280 for the symmetrical case. The additional impulse required is 2.0 lb-sec.

Thus the total gas saving that will result from the use of a solar pressure balance vane is $\frac{4.6 + 2.0}{65}$ or approximately 0.1 lb. The valve firings would be distributed more equally through use of a balance vane but, since the total number of operations is relatively low, this is of minor importance. Therefore, the use of a solar pressure balance vane is not justified.

This example was done assuming complete absorption of solar energy. Pure specular reflection would cause the gas consumption to double. The amount is still negligible.

3.6.7 Two-Level Torque System

Table 11 gives a comparison of the effects of a single thrust level system vs a two-level system. The impulse required due to limit cycling and total number of valve operations per axis are given. Since the thrust level affects only the impulse requirement for limit cycling, only that impulse which is due to limit cycling is shown. The single thrust level system is sized for the inertias during transit.

Table 11. Single Thrust Level Versus Two-Level Comparison

Axis	Single Thrust Level		Two Thrust Level	
	Impulse Required (lb-sec)	No. of Operations	Impulse Required (lb-sec)	No. of Operations
Roll	76	9170	42	6540
Pitch	157	12800	56	6540
Yaw	217	18170	48	6540
Total	450		146	

The additional impulse required for a single level system is 304 lb sec, or about 4.7 pounds of gas before the inclusion of safety factors. Also, the number of valve operations triples in the yaw axis with the resultant decrease in reliability. Also of concern is the effect of the increase in the yaw limit cycle rate in orbit from a nominal 3.375×10^{-6} rad/sec to 1.55×10^{-5} rad/sec. The actual rate about a given axis may approach twice the nominal symmetrical limit cycle value. This rate alone can exceed the maximum permissible rate of approximately 10^{-5} rad/sec set by the photo experiments.

3.7 INTERFACE DEFINITIONS

The overall functional boundaries of the ACS are the radiation inputs to the celestial sensors and spacecraft motion to the inertial sensors, and the output torques applied to the spacecraft by the gas jets. In addition to these functional boundaries, mechanical and electrical interfaces with other subsystems exist. The various interfaces are defined below, with sources and destinations identified.

3.7.1 Inputs to ACS

Directly Sensed Inputs

a. Solar radiation to the acquisition, cruise and sun gate sun sensors. Solar intensity varies as the square of distance to Sun (1 to 1.67 AU when the entire Mars orbit is considered).

b. Canopus radiation to the Canopus sensors.

c. Spacecraft body rates about the three control axes as inputs to the Gyro and Accelerometer Package.

d. Simulated inputs are provided by OSE for each of the six gyros, the 14 Sun sensors, and the two Canopus sensors.

e. The OSE provides simulated Computer and Sequencer and Command Decoder interfaces, as well as necessary power during subsystem test.

Inputs from Other Subsystems

a. Power Subsystem - The ACS receives power from three power sources: a) 2400 cps square wave, 50 V RMS, b) 400 cps square wave, 3 phase, and c) Unregulated DC, 30-44 VDC.

b. Command Sources - The ACS receives commands from the Command Decoder and the Computer and Sequencer. These specific commands can be found in the Flight Sequence Document. Initialization commands are received from the launch complex equipment and these are covered in Document.

3.7.2 Outputs of the ACS

ACS outputs include driver signals to the 48 cold gas jet solenoid valves, telemetry, test points and thermal outputs.

Driver Signals. The ACS generates appropriate signals which drive the redundant, coupled cold gas jet subsystem solenoid valves as required to perform the specified control functions.

Telemetry. Various points in the ACS will deliver information for telemetering to Earth for operational and diagnostic purposes. The telemetered points are listed in the Telemetry Channel Assignments.

Operational Support Equipment. Table 12 lists those test points which will be available by direct access for system testing after assembly of the spacecraft.

Table 12. ACS-OSE Test Points

Unit	Quantity
Transformer/rectifier outputs	5
Gyro torquer signals	6
Gyro amplifier outputs	6
Acquisition sun sensor outputs	12
Cruise sun sensor	6
Threshold detectors	9
Solenoid valve commands	24
Cruise sun sensor amplifier gain control	6
Command detector	1

Thermal Outputs. The thermal interfaces of the various components will be designed to remove the heat in excess of that required for proper temperature control; or will (in the case of several of the pneumatics components) provide additional heat inputs to components where required. (See Spacecraft Component Design Parameters.)

3.8 ATTITUDE CONTROL PERFORMANCE PARAMETERS

3.8.1 Control Angular Acceleration

The nominal value of the control angular acceleration at booster separation will be 0.225 mr/sec^2 (.0129 deg/sec^2) about each axis. Use of this value of acceleration in conjunction with the derived rate network enables the spacecraft to maintain its attitude with a minimum of gas usage and number of valve operations. In addition, adequate control torque is available to ensure Canopus acquisition within the field of view of the sensor even in the event of failure of a single nozzle of the roll couple. Failure of a single nozzle of a couple reduces this value to 0.1125 mr/sec^2 (.0645 deg/sec^2). A dual level pneumatic control system is utilized to provide similar acceleration levels during the Mars orbit phase when the moments of inertia have been reduced because of retro fuel usage and capsule separation.

3.8.2 Limit Cycle Rate

The nominal limit cycle rate for both the transit phase and the orbit phase is 3.375×10^{-6} rad/sec (.000193 deg/sec). This angular rate is well below the random angular rate of 10^{-5} rad/sec permissible during a photo imaging experiment exposure.

3.8.3 Maneuver Slewing Rate

The slewing rate during an inertial maneuver is ±3.14 mr/sec (.18 deg/sec) for each control axis. This rate provides for a 50% margin of safety in the gyro input angular freedom of 105 mr (6 degrees) in the event of failure of a single nozzle.

3.8.4 Acquisition Angular Rates

The pitch and yaw angular rates during Sun acquisition are limited to a nominal value of +4.4 mr/sec (.25 deg/sec). This value provides for Sun acquisition in a reasonable time and limits the cross-coupling torques to approximately 5% of the control torques. Roll rate during Sun acquisition is limited to approximately ±0.2 mr/sec (.011 deg/sec). During magnetometer calibration, the commanded roll angular rate is 3.9 mr/sec (.22 deg/sec) with

a rate deadband of 0.4 mr/sec (.023 deg/sec). During Canopus search, the roll angular rate is 1.7 mr/sec (.1 deg/sec) with a deadband of 0.4 mr/sec (.023 deg/sec). Use of this roll search rate is compatible with the roll control torque and field of view of the Canopus sensor.

3.8.5 Pointing Accuracy

The nominal control deadband is ±8 mr (.458 deg) about a null which will be less than 4 mr (.229 deg) off from the vehicle axes, in all modes of control. An error analysis of the PSP and HGA shows this to be compatible with the allowable system errors. Total system pointing errors are reported in VOY-D-260.

3.8.6 Maneuver Accuracy

The accuracy of any maneuver varies as a function of the specific maneuvers involved and the total time interval. There is also some, as yet unassessed, variation due to the nature of the coupling torques. The error analysis for the worst case maneuver assuming an uncoupled vehicle indicates that the final pointing error will be less than 2 degrees. For details, VOY-D-260, Trajectory and Guidance Analysis.

3.8.7 Acquisition Time

It takes no longer than 20 minutes to stabilize to the Sun and no longer than 70 minutes to stabilize to Canopus after the Sun has been acquired.

3.9 ACS PHYSICAL CHARACTERISTICS AND OPERATIONAL CONSTRAINTS

The first part of this section defines the physical characteristics of the complete ACS, which is composed of the component assemblies as previously defined and depicted in the ACS Functional Block Diagram, Figure 3-5. The second part of this section defines the operational constraints.

3.9.1 ACS Physical Characteristics

The estimated weight, power input and power dissipation for the various ACS components are indicated in Table 13.

Table 13. ACS Component Physical Characteristics

Component	Weight (lb)	Power (W avg)
Secondary sun sensors	1.2	
Primary sun sensors	1.2	
Canopus sensor No. 1	6.3	1.8
Canopus sensor No. 2	6.3	
Gyro/accelerometer Pkg No. 1	14.5	26
Gyro/accelerometer Pkg No. 2	14.5	
AC electronics	8.6	25
Totals	52.6	52.8

3.9.2 ACS Operational Constraints

The following operational constraints are derived from consideration of the selected ACS performance parameters and sensors.

Maneuvers. In normal operation, the orientation of the spacecraft roll axis for rocket thrusting will be accomplished by a pitch-yaw or a yaw-pitch maneuver. The capability for slewing the roll axis inertially is also provided for in the ACS. Sixty minutes prior to a maneuver, the gyros must be turned on to allow sufficient warm-up time.

Time-To-Complete Stabilization. Initial acquisition of the Sun will be accomplished within 20 minutes after initiation, including reduction of initial rates as high as 3 degrees per second about each control axis. Subsequent Sun acquisitions will be accomplished in less than 15 minutes.

Automatic Canopus acquisition will require at most 70 minutes following Sun acquisition if the cruise mode is commanded.

The initial magnetometer and Canopus calibration is accomplished by a roll maneuver requring 27 minutes for a 360 degree rotation.

Environmental Conditions. Canopus sensor - This sensor must be mounted in the vehicle, and vehicle structure; appendages must be located so that no light is reflected into the shield of the sensor.

Sun sensor - Reflected light impingement on the solar sensors must be prevented. Albedo inputs to the acquisition sensors have not been determined, but are estimated to be such that on the order of 8 degrees pointing error will be introduced until the acquisition sensors are switched out. The alignment of the various acquisition sensors must be such as to minimize the effect of albedo.

VOY-D-321
APPENDIX A

ON MOTION OF A CAVITY IN A SPHERICAL OR CIRCULAR CYLINDRICAL TANK AT VERY LOW GRAVITY

The behavior of propellant sloshing has to be included in any guidance and control analysis. A great deal of work on liquid sloshing has been done for the case of high gravity (References 1, 2, 5, 6). During the flight of the Voyager Planetary Vehicle, very low gravity is exerted on the propellant. In this case, only scattered works on sloshing problem have been carried out (References 1, 2, 3). For the Voyager vehicle, spherical tanks are used. Such a case is therefore of practical importance.

In this report, a mathematical formulation for the general case of a tank of arbitrary shape with a cavity filled up with gas of any equilibrium shape under a gravitational field is first discussed. Then the shape of the equilibrium (quiescent) gas-liquid interface in a spherical tank is determined for small Bond numbers*. The problem of free and forced small oscillations can therefore be formulated in terms of the (radial) displacement.

Finally, the frequency of small free oscillation for the limiting case of $\alpha \to 0$ (zero gravity) of a spherical cavity at any location in a spherical tank is obtained. The simple case of a spherical cavity at the center was solved before (Reference 2). The forced oscillation is also investigated. The two-dimensional case of a circular cavity in a circular tank is considered first as a mathematical guidance to obtain the solution for the other case.

---

* Higher order terms in Bond can thus be computed.

A.1 GENERAL MATHEMATICAL FORMULATION

Consider that* the rigid wall is moving with respect to a fixed frame of references a velocity $\bar{V}(t)$. The propellant is assumed to be incompressible, inviscid and thus irrotational (as it starts from rest). With respect to the fixed frame, let

$\bar{q}^*$ = Velocity Vector

P Pressure

ρ Density

We have $\bar{q}^* = \nabla^* \phi^*$, when $\phi^* = \phi^*(\bar{r}^*, t^*)$. Thus the equation of continuity gives

$$\Delta \phi^* = 0 \tag{1}$$

From the equation of motion

$$\rho \frac{d\bar{q}^*}{dt^*} = \rho \frac{\delta \bar{q}^*}{\delta t^*} + (q^* \cdot \nabla^*)\, \bar{q}^*$$

$$- \nabla^* P + \rho\, \bar{V}(t^*) + \rho\, g\bar{a}$$

$$- \nabla^* (P + \rho\Omega)$$

where

$$\nabla^* \Omega = -\dot{\bar{V}} - g\bar{a}$$

We have the Bernoulli's equation

$$\phi_{t^*}^* + \frac{1}{2} (\nabla^* \phi^* \cdot \nabla^* \phi^*) + \frac{P}{\rho} - (g\bar{a} + \dot{\bar{V}}) \cdot \bar{r}^* = c(t) \tag{2}$$

---

* Elasticity of the wall has not been considered. A coupled oscillation can be formulated.

Now we change the coordinates

$$\bar{r}^{*} = \bar{r} + \int_{t_o}^{t} \bar{V}(t)\, dt, \quad t^{*} = t$$

and set $\phi^{*}(\bar{r}^{*}, t^{*}) = \phi(\bar{r}, t) + \bar{V}.\bar{r}.$

By the chain rule of differentiation, it is easily seen that

$$\nabla^{*} \phi^{*} = \nabla \phi + \bar{V}$$

and

$$\phi_{t}^{*} = \dot{\bar{V}} \cdot \bar{r} + \phi_{t} - \bar{V} \cdot \nabla \phi - \bar{V} \cdot \bar{V}$$

Then the equation (2) becomes

$$\phi_{t} + \frac{\nabla \phi \cdot \nabla \phi}{2} + \frac{P}{\rho} - g\bar{\alpha} \cdot \bar{r} = c_1(t) \tag{2a}$$

The equation (1) reduces to

$$\nabla \phi = 0 \tag{1a}$$

a. The boundary condition at the wetted part B_2 of the wall of the tank as shown in Figure A-1

$$\bar{N} \cdot \nabla^{*} \phi^{*} = \bar{N} \cdot \bar{V}$$

Hence

$$\bar{N} \cdot \nabla \phi = 0 \text{ on } B_2 \tag{3}$$

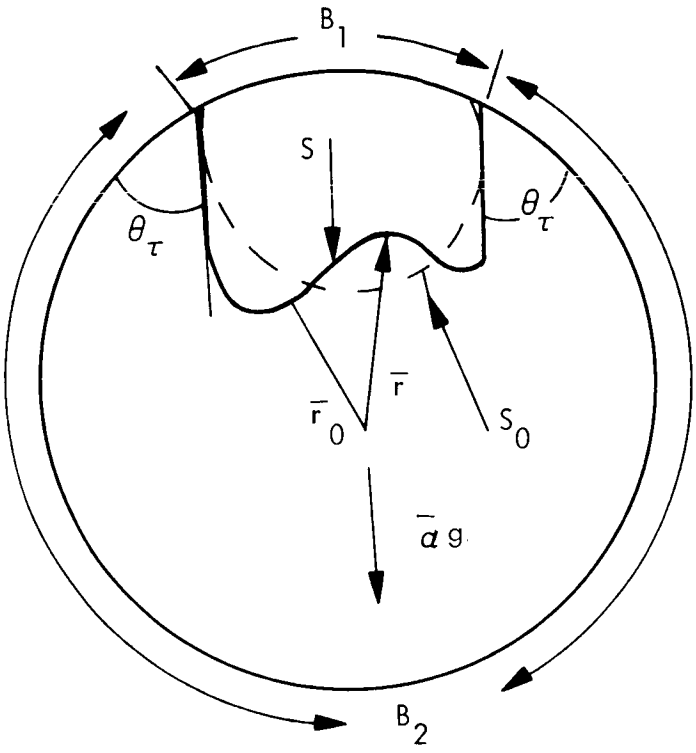

Figure A-1. Equilibrium Interface Configuration

Where $B = B_1 + B_2$ the Wall of the Tank

$\bar{N}$ = the unit vector along the outward normal at B

b. On the free boundary S, which is interface of the liquid and the gas cavity at the time t,

$$p + 2\sigma J = p_{gas}, \quad p = P + \rho \dot{\bar{V}} (\bar{r}_1 - \bar{r}) \tag{3a}$$

where p_{gas} the pressure of the gas.

$\bar{r}_1$ a fixed point on the wall of the tank in the cavity.

J the mean curvature of S.

The increase of the pressure in the gas due to the acceleration $\dot{\bar{V}}$ can be neglected as its density is small as compared to P. When $|\bar{\alpha} g| << g$, $p = p_0$. The surface with the mean curvature equal to a constant is a sphere. Thus the equilibrium surface of the cavity for the case of zero-g is a sphere. For small Bond number (in the case of $|\bar{\alpha} g| << g$) the quiescent liquid-vapor interface is expected to be close to a sphere. However, the surface is not determined unless the angle θ_τ of contact of the liquid with the tank wall is given.

If the surface S is represented parametrically as $\bar{r} = \bar{h}(u, v, t)$, then from the theory of Surface S in the classical differential geometry (Reference 4), we can find the mean curvature in terms of h from the following formula:

$$\frac{1}{R_1} + \frac{1}{R_2} = \frac{Eg - 2Ff + Ge}{EG - F^2} \tag{4}$$

where $ds^2 = d\bar{r} \cdot d\bar{r} = E\,du^2 + 2F\,du\,dv + G\,du^2$ (5)

$$E = \left(\frac{\delta}{\delta u}\bar{r}\right)^2 = \bar{r}_u \cdot \bar{r}_u \text{ and etc.}$$

$$e = -\bar{r}_{uu} \cdot (\bar{r}_u \times \bar{r}_v)/\sqrt{EG - F^2} \tag{6a}$$

$$f = -\bar{r}_{uv} \cdot (\bar{r}_u \times \bar{r}_v)/\sqrt{EG - F^2} \tag{6b}$$

$$g = -\bar{r}_{uv} (\bar{r}_u \times \bar{r}_v)/\sqrt{EG - F^2} \tag{6c}$$

A.2 THE QUIESCENT GAS-LIQUID INTERFACE IN A SPHERICAL TANK (OR A TANK WITH ROTATION SYMMETRY) AT VERY LOW GRAVITY

Let the origin be chosen at P as indicated in the Figure A-2. In spherical coordinates,

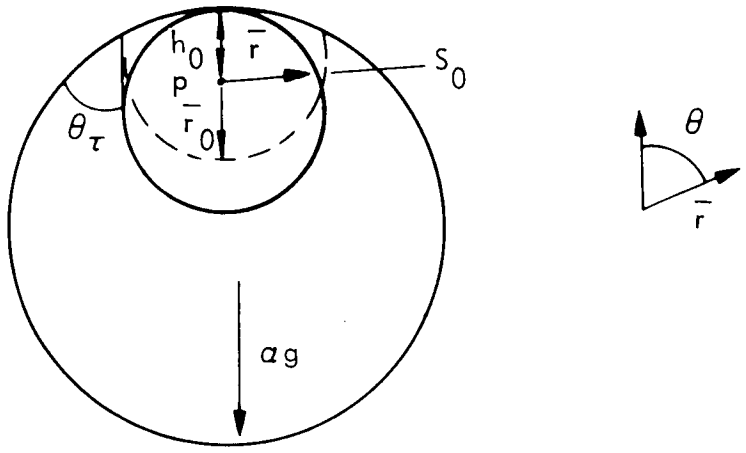

Figure A-2. Spherical Bubble and Tank Coordinate System

let the quiescent interface S_0 be:

$$r = h(\theta)$$

Or,

$$\bar{r} = h(\theta)\,\bar{K}_1 \tag{7}$$

From the Appendix I (3.1), the mean curvature J is given by

$$2J = \frac{1}{R_1} + \frac{1}{R_2}$$

$$\frac{1}{h\sqrt{h^2 + h'^2}}\left(2h + \frac{hh'^2 - h^2h''}{h^2 + h'^2} - h' \cot\theta\right)$$

$$\frac{p_{gas} - p}{\sigma} = \frac{p_{gas} - p_0}{\sigma} + \frac{\rho \alpha g}{\sigma}(h\cos\theta + r_0) \tag{8}$$

Let $2 h_0^{-1} = \frac{p_{gas} - p_0}{\sigma} + \frac{\rho \alpha g}{\sigma} r_0$. We rewrite (8) in the following form

$$\frac{d}{d\theta} (\tan^{-1} \frac{h'}{h}) + \frac{h'}{h} \cot\theta = 2 - (2 + B \frac{h}{h_0} \cos\theta) \frac{h}{h_0} \sqrt{1 + (\frac{h'}{h})^2} \qquad (9)$$

where $B = \frac{h_0^2 \rho \alpha g}{\sigma}$

For very small B, it is expected that $\frac{h'}{h} \sim 0(1)$. Thus, $(\frac{h'}{h})^2$ can be neglected against 1. Hence, we have

$$\frac{d}{d\theta} (\frac{h'}{h}) + \frac{h'}{h} \cot\theta = 2 - (2 + B \frac{h}{h_0} \cos\theta) \frac{h}{h_0}$$

Now, let* $h = h_0 e^{U(\theta)}$. U is small when B is. We have $\frac{h'}{h} = U'(\theta)$.

Consequently,

$$U'' + U' \cot\theta = 2 (1 - e^U) - B e^{2U} \cos\theta) \qquad (9'')$$

Write $U = U_1 B + U_2 B^2 + \text{----------}$

We have

$$U_1'' + U_1' \cot\theta + 2 U_1 = -B \cos\theta \qquad (9''a)$$

One particular solution* of (9''a) is

$$\frac{1}{2} + \frac{1}{3} \cos\theta \log (1 - \cos\theta)$$

---

* Direct perturbation on B for h does not yield reasonable result.

Hence,

$$U_1 = A_1 P_1(\theta) + A_2 Q_2(\theta) + \frac{1}{2} + \frac{1}{3} \cos\theta \log(1 - \cos\theta)$$

where

$$P_1(\theta) = \cos\theta$$

$$Q_1(\theta) = \frac{1}{2} \cos\theta \log \frac{1 + \cos\theta}{1 - \cos\theta}$$

Since the solution should be regular at $\theta = \pi$, $A_2 = 0$. The singularity at $\theta = 0$ of the particular solution is allowed, because the neighborhood of this point is in the cavity, not on the interface S_0. Thus, up to the first power of B,

$$h = h_0 e^{BU_1} = h_0(1-\cos\theta)^{\frac{1}{3}B\cos\theta} e^{B(\frac{1}{2} + A_1 \cos\theta)} \tag{10}$$

There are four parameters, p_0, r_0, h_0, and A_1. They are to be determined by the following four conditions:

(a) $$\frac{2}{h_0} = \frac{p_{gas} - p_0}{\sigma} + \frac{\rho a g}{\sigma} r_0 \tag{11a}$$

(b) Let the interface S_0 intersect the wall of the tank at θ_1 as shown in Figure A-3.

Then,

$$p_0 = \rho a g (h(\theta_1) \cos\theta_1 + r_0) \tag{11b}$$

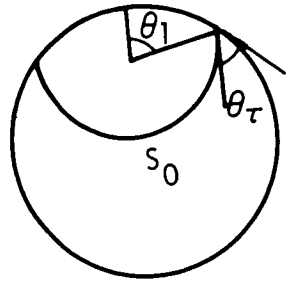

Figure A-3. Liquid Surface - Tank Interface

(c) $r_0 = h\ (\theta = \pi)$ (12)

(d) The angle of contact between the liquid-vapor interface and the wall of the tank is θ_τ.

The horizontal curve $r = \theta_1$ of the contact of the interface with the tank is determined by

$$h^2(\theta_1) + 2(1-h_0)\, h(\theta_1) \cos\theta_1 + (1-h_0^2) - 1 = 0 \tag{13}$$

Then

$$r_0 = h(\pi)$$

$$p_0 = p_{gas} + \rho\, a\, g\, r_0 - \frac{2\sigma}{h_0} \tag{11a}$$

$$= \rho\, a\, g\, (r_0 + h_1(\theta_1) \cos\theta_1) \tag{11b}$$

Eq. (13) yields $h(\theta_1) = -(1-h_0)\cos\theta_1 + \sqrt{1 + (1-h_0)^2\,(\cos^2\theta_1 - 1)}$

So far, this is perfectly general. Now, for small values of $B = \frac{\rho a g h_0^2}{\sigma}$, we have

$$h(\theta) = h_0(1-\cos\theta)^{\frac{1}{3}\, B\cos\theta}\, e^{B(\frac{1}{2} + A_1\cos\theta)} \tag{10}$$

The equation for the determination of θ_1 is

$$F(\chi) \quad h_0 e^{B(\frac{1}{3}\chi \log(1-\chi) + \frac{1}{2} + A_1\chi)} + (1-h_0)\chi - \sqrt{1 + (1-h_0)^2(\chi^2-1)} = 0$$

Where $\chi = \cos\theta_1$, set $\chi = 1-\epsilon$, $A_1 = \frac{-1}{3}\log\epsilon + A$

Then

$$h_0 e^{B\left[A(1-\epsilon) + \frac{1}{2}\right]} + (1-h_0)(1-\epsilon) - 1 - \frac{1}{2}(1-h_0)^2(-2\epsilon + \epsilon^2) = 0$$

Linearizing with respect to ϵ,

$$e^{B(\frac{1}{2} + A)} - 1 - (1-h_0)\epsilon \qquad 0 \tag{14}$$

or

$$\epsilon \quad \frac{(\frac{1}{2} + A)\ B}{1 - h_0} + 0(B^2) \tag{14a}$$

From (11a) and (11b),

$$p^* - \frac{2\sigma}{h_0} \qquad \rho\alpha g h_0 (1-h_0\epsilon) + 0\left((1-h_0)^2\epsilon^2\right)$$

$$\rho\alpha g h_0 - \frac{\rho^2\alpha^2 g^2 h_0^3}{\sigma} \frac{(\frac{1}{2} + A)}{1 - h_0} \tag{15}$$

where $p^* \qquad p_{gas}$

or

$$h_0 \qquad \frac{2\sigma}{p^*}\left(1 + \frac{1}{2}B - B^2 \frac{(\frac{1}{2} + A)}{2(1 - h_0)}\right) \tag{16}$$

where $\frac{2\sigma}{p^*} = R_0$ = the radius of the spherical cavity when $x = 0$. For small α, one may take $B = B_0 = \frac{\alpha g \rho R_0^2}{\sigma}$. The angle of contact θ_τ has to tend zero as $\alpha \to 0$. Let

$$-\gamma^* = -\tan\theta_\tau = \left[\frac{h'(\theta_1)}{h(\theta_1)} - \frac{r'(\theta_1)}{r(\theta_1)}\right] \Big/ \left(1 + \frac{h'(\theta_1)\, r'(\theta_1)}{h(\theta_1)\, r(\theta_1)}\right) \tag{17}$$

where $r^2(\theta) + 2(1-h_0)\, r(\theta)\cos\theta + (1-h_0)^2 - 1 = 0$

and $r(\theta) = h(\theta_1)$

Let $\gamma^* = \sqrt{2B}$. Hence from (17), we have

$$\gamma = \sqrt{(1-h_0)/\left(\frac{1}{2} + A\right)}\left(\frac{1}{6} + A\right) \tag{18}$$

The equation (18) and (15) determine A and h_0. Equations (11a) and (12) then yield r_0 and p_0.

A.3 FORCED AND FREE OSCILLATIONS OF THE VAPOR-LIQUID INTERFACE

Since Φ^* is determined up to an arbitrary function of t, one may absorb any function of t in Φ in the Bernoulli's equation (2a):

$$\Phi_t + \frac{\nabla\phi \cdot \nabla\phi}{2} + \frac{p-p_0}{\sigma} - g\bar{\alpha} \cdot (\bar{r}-\bar{r}_0) + \dot{\bar{V}} \cdot (\bar{r}-\bar{r}_0) = 0 \tag{2b}$$

where

$$p = P - \dot{\bar{V}}(\bar{r} - \bar{r}_1) = 2\sigma J + p_{gas}$$

on the interface S. Let S be represented as

$$r = h(\theta, \phi, t) = H(\theta) + w(\theta, \phi, t)$$

---

* the notation ϕ is changed to Φ.

where

$$w(\theta, \phi, t) << H(\theta).$$

Let

$$g\bar{\alpha} \cdot (\bar{r} - \bar{r}_0) = -g\bar{\alpha}(h\cos\theta + r_0) \tag{19}$$

$$(\bar{r} - \bar{r}_0) \cdot \dot{\bar{V}} = -\ddot{x}(t)\, h \sin\theta \cos\phi \tag{20}$$

Write

$$h = e^{u} = e^{U+\lambda} = e^{U}(1 + \lambda + \ldots) \tag{21}$$

On the linearized expression, we have

$$H(\theta) = e^{U(\theta)} \cdot e^{U}\lambda = w \tag{22}$$

From the Attachment I, (41), we have

$$J = \frac{1}{h}\left[\frac{2}{\sqrt{1+U'^2}} - \frac{1}{\sin\theta}\frac{\delta}{\delta\theta}\left(\frac{U'\sin\theta}{\sqrt{1+U'^2}}\right) - \frac{1}{\sin\theta}\frac{\delta}{\delta\theta}\frac{(\sin^{\theta}\lambda_{\theta})}{(1+U'^2)^{2/3}} - \frac{\sin^{-2}\theta}{\sqrt{1+U'^2}}\lambda_{\phi\phi}\right] \tag{23}$$

Since on S_0,

$$2\sigma J_0 = p_{gas} - \left(p_0 + \sigma g\bar{\alpha}\cdot(\bar{r} - \bar{r}_0)\right)$$

$$p_{gas} - p_0 + \rho g \alpha (e^{U(\theta)}\cos\theta + r_0)$$

$$\frac{\sigma}{e^{U}}\left[\frac{2}{\sqrt{1+U'^2}} - \frac{1}{\sin\theta}\frac{\delta}{\delta\theta}\frac{U'\sin\theta}{\sqrt{1+U'^2}}\right] \tag{24}$$

We have the Bernoulli's equation on S (linearized on S_0 and linearized in ϕ):

$$\Phi_t + \lambda \left[e^{U(\theta)} 2g\alpha\cos\theta + \frac{2\sigma}{\rho h_0} \right] + \frac{\sigma}{\rho e^{U(\theta)}} \left[\frac{1}{\sin\theta} \frac{\delta}{\delta\theta} \left(\frac{\sin\theta \lambda_\theta}{(1+U'^2)^{3/2}} \right) + \frac{\sin^{-2}\theta}{\sqrt{1+U'^2}} \lambda_{\phi\phi} \right] = -\ddot{x} e^{U(\theta)} \sin\theta \cos\phi \qquad (25)$$

On the other hand, if a point (r, θ, ϕ) on the surface $r - h(\theta, \phi, t) = 0$ at instant t is moved to (r_1, θ_1, ϕ_1) on the surface

$$r_1 - h(\theta_1, \phi, t + dt) = 0$$

at the instant t + dt, where

$$r_1 = r + dr = r + \frac{dn}{A}$$

$$\theta_1 = \theta + d\theta = \theta + \frac{1}{h} \frac{dn}{A} \frac{-h_\theta}{h}$$

$$\phi_1 = \phi + d\phi = \phi + \frac{1}{h \sin\theta} \frac{dn}{A} - \frac{h_\phi}{h \sin\theta}$$

then

$$r_1 - r - h(\theta_1, \phi_1, t + dt) - h(\theta, \phi, t) = 0,$$

or

$$\frac{dn}{A} \left(1 + \frac{h_\theta^2}{h^2} + \frac{h_\phi^2}{h^2 \sin^2\phi}\right) - h_t dt = 0$$

Thus,

$\frac{dn}{dt} = \frac{h_t}{A}$ = the normal component of velocity (relative to the wall) on S. This should equal to the fluid velocity relative to the wall on S. Hence,

$$\frac{h_t}{A} = \frac{1}{A}\left(\Phi_r - \Phi_\theta \frac{h_\theta}{h^2} - \Phi_\phi \frac{h_\phi}{h^2 \sin^2\theta}\right)$$

We obtain the linearized relation:

$$h_t = \Phi_r - \frac{U'\Phi_\theta}{e^U} \tag{26}$$

Thus, the boundary condition for ϕ on S_0:

$$\Phi_{tt} + \left[2 g \alpha \cos\theta + \frac{2\sigma}{\rho h_0} \frac{1}{H(\theta)}\right]\left(\Phi_r - \frac{H'}{H^2}\Phi_\theta\right)$$

$$+ \frac{\sigma}{\rho H(\theta)}\left[\frac{1}{\sin\theta} \frac{\delta}{\delta\theta}\left(\frac{\sin\theta H^2}{(H^2 + H'^2)^{3/2}} \cdot \left(\Phi_r - \frac{H'}{H^2}\Phi_\theta\right)_\theta\right)\right.$$

$$\left. + \frac{\sin^{-2}\theta}{\sqrt{H^2 + H'^2}}\left(\Phi_r - \frac{H'}{H^2}\Phi_\theta\right)_{\phi\phi}\right] = -\ddot{x} H(\theta) \sin\theta \cos\phi \tag{27}$$

where S_0 is the surface

$r = H(\theta)$

The linearized problem of liquid sloshing problem of a vapor cavity in a spherical tank is now completely formulated as to find the solution $\phi(r, \theta, \phi, t)$ of the Laplace equation

$$\Phi_{rr} + \frac{2}{r}\Phi_r + \frac{1}{r^2 \sin^2\theta}\Phi_{\phi\phi} + \frac{1}{r^2 \sin\theta} \frac{\delta}{\delta\theta}(\sin\theta \Phi_\theta) = 0$$

with the boundary conditions which are satisfied for all values of t, θ, and ϕ.

(a) $\Phi_r = 0$ $\qquad r = 1,\ \pi > \theta \geq \theta_1$

(b) The equation (27) on $\qquad r = H(\theta)\ (\theta_1 \leq 0 \leq \pi)$

(c) The angle θ_τ of contact is given*. This yields

$$\lambda_\theta = \Gamma\ \lambda \quad \text{at} \quad \theta = \theta_1$$

where $^*\Gamma$ can be calculated if θ_τ is given.

A.4 OSCILLATIONS OF INTERFACE AT ZERO-GRAVITY IN A SPHERICAL TANK

When $\alpha = 0$, the quiescent interface reduces to $r = h_0$, where

$$h_0 = \left(\frac{K}{1+K}\right)^{1/3} = (1 - \text{Fill})^{1/3}$$

$$K = \frac{\upsilon\ \text{gas}}{\upsilon_{\text{Liquid}}} \quad - \text{ the gas-liquid volume ratio}$$

Hence, $U' = 0$, $H = e^U = h_0$. Then, we have

$$\Delta\Phi = 0 \tag{1a}$$

The location of the center of the spherical cavity could be any place in the tank as shown in Figure A-4. In this case, let the origin be chosen at the center of the cavity. Let the radius of the tank be normalized as 1. Hence, the boundary conditions are:

(a) $\Phi_n = 0$ $\qquad$ on B

or

$$\Phi_r - \frac{G'(\theta)}{G^2(\theta)}\Phi_\theta = 0 \text{ on } r = G(\theta) = -\delta\cos\theta + \sqrt{1+\delta^2(\cos^2\theta - 1)} \tag{28}$$

---

* Attachment III

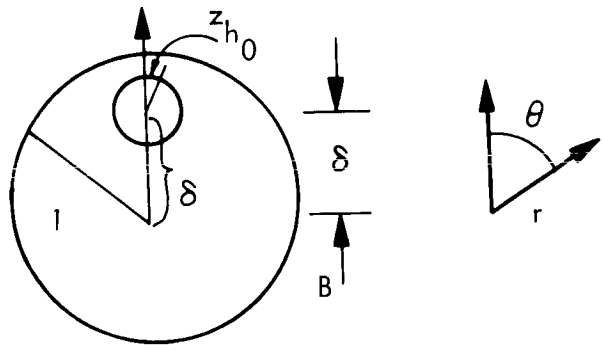

Figure A-4. Tank - Bubble Symbol Definition

$$\text{(b)}\ \Phi_{tt} + \frac{2\sigma}{\rho h_0^2}\left[\Phi_r + \frac{1}{\sin\theta}\frac{\partial}{\partial\theta}(\sin\theta\Phi_{r\theta}) + \frac{1}{\sin^2\theta}\Phi_{r\phi\phi}\right] = -\ddot{x}\cos\theta\cos\phi\, H(\theta) \text{ on } r = h_0 \tag{29}$$

Since $\Delta\phi = 0$

$$\frac{1}{\sin\theta}\frac{\partial}{\partial\theta}(\sin\theta\,\phi_{r\theta}) + \frac{1}{\sin^2\theta}\phi_{r\phi\phi} - \frac{\partial}{\partial r}\left|r^2\phi_{rr} + 2r\phi_r\right| = \frac{-1}{r}(D^3+D^2)\Phi, \text{ where } D = r\frac{\partial}{\partial r}$$

Consequently, the condition (b) can be rewritten in the following form

$$\phi_{tt} + \frac{2\sigma}{\rho h_0^3}\left[-D^3 - D^2 + 2D\right]\phi = -\ddot{x}\cos\theta\cos\phi\, h_0 \text{ on } r = h_0 \tag{29a}$$

When $\delta < 1 - h_0$, no condition as (c) is necessary. When $\delta = 1 - h_0$, if $\theta_\tau = 0$ and $\lambda_\theta(0,\Phi,t) = 0^*$, then $k(\Phi) = 0$. The condition (c) in this case corresponds to $\lambda = 0$ or $\Gamma = +\infty$, the stuck-edge condition.

* If the solution $F'(z)$ is a single valued function in the domain, it turns out that F is of this form because of the conditions (30) and (31).

A.4.1 THE TWO-DIMENSIONAL PROBLEM

The corresponding two-dimensional problem is that

$$\Delta\Phi = \Phi_{rr} + \frac{1}{r}\Phi_r + \frac{1}{r^2}\Phi_{\theta\theta} = 0$$

with boundary condition

(a) $\Phi_n = 0$ on B

or

$$\Phi_r - \frac{G'(\theta)}{G^2(\theta)}\Phi_\theta = 0 \text{ on } r = G(\theta)$$

where

$$G(\theta) = -\delta\cos\theta + \sqrt{1 + \delta^2(\cos^2\theta - 1)}$$

(b) $$\Phi_{tt} + \frac{\sigma}{\rho h_0^3}\left[D - D^3\right]\Phi = -\dddot{x}\cos\theta\, h_0$$

A.4.1.1 Free Oscillation of a Circular Cavity

Let $\dddot{x} = 0$, $\phi = \Phi_1(r,\theta)\cos\omega t$, $re^{i\theta} = z$, and $F(z) = \Phi_1 + i\Psi$, where Ψ is the harmonic conjugate of Φ_1. The condition (a) yields

$$\text{Re}\left[F'(z)\,(z+\delta)\right] = 0 \text{ on } z + \delta = e^{i\theta} \tag{30}$$

The condition (b) yields

$$\text{Re}\left[-\frac{\omega^2}{a}F(z) + DF(z) - D^3F(z)\right] = 0 \text{ on } z = h_0 e^{i\theta} \tag{31}$$

where

$$D = z\frac{d}{dz}, \quad a = \frac{\sigma}{\rho h_0^3}$$

Although a conformal mapping can be readily found such that the two circles are transformed into the two concentric circles, and one of the boundary conditions can be immediately satisfied by expressing F as an infinite series of positive and negative powers of the transformed variable, the other condition yields a system of infinitely many linear equations involving the undetermined coefficients. This resembles the problem of finding a periodic solution of the Mathieu equation by a Fourier series. Because of this difficulty, we employ the following alternative method working directly with the boundary conditions (30) and (31). The solution obtained corresponds to the "Stuck edge" condition, when $\delta = 1 - h_0$.

$$\text{Let}^* \quad F(z) = \sum_{n\ 1}^{\infty} A_n z^n + B_n z^{-n}$$

The stuck-edge condition corresponds to a solution that Φ involves only $\cos\theta$ terms, thus both A_n and B_n are real.

Let $\nu = \frac{\omega^2}{a}$. The condition (31) yields

$$\text{and:} \quad \nu = \frac{\omega^2 \rho h_0^3}{\sigma}$$

$$\upsilon \left(A_n h_0^n + B_n \frac{1}{h_0^n}\right) = -(n^3 - n)\left(A_n h_0^n - B_n \frac{1}{h_0^n}\right) \tag{31a}$$

For the condition (30), we have

$$\text{Re}\left[F'(\lambda - \delta)\lambda\right] = 0 \quad \text{on} \quad \lambda = e^{i\theta *}$$

Now apply the conformal mapping

$$\lambda = \frac{h + \delta}{\delta h + 1}$$

and

$$\lambda - \delta = \frac{(1-\delta^2)\, h}{1 + \delta h}$$

it follows that

$$\text{Re}\left[(\lambda - \delta)\, F'(\lambda - \delta)\, (1 + \delta h^{-1}) \right] = 0$$

or

$$\text{Re}\left[\sum_{n=1}^{\infty} \left\{ n\alpha_n h^n (1+\delta h)^{-n} - n\beta_n h^{-n} (1+\delta h)^n \ (1+\delta h)^n \right\} (1+\delta h^{-1}) \right] = 0 \qquad (30a)$$

$$\text{on } h = e^{i\theta} \text{ for all } 0 \leq \theta \leq 2\pi.$$

Where

$$\alpha_n = A_n(1-\delta^2)^n, \quad \beta_n = \frac{B_n}{(1-\delta^2)^n} .$$

Now we write (31a) in the form

$$\nu(\alpha_n h_1^n + \beta_n \frac{1}{h_1^n}) = -(n^3 - n)(\alpha_n h_1^n - \beta_n \frac{1}{h_1^n})$$

where

$$h_1 = \frac{h_0}{1-\delta^2} .$$

The condition (30a) reduces to a Fourier series in σ with coefficients which are functions of δ. Write

$$\alpha_n = \sum_{j=0}^{\infty} \alpha_{nj} \delta^j , \qquad \beta_n = \sum_{j=0}^{\infty} \beta_{nj} \delta^j$$

and

$$\nu = \sum_{j=0}^{\infty} \nu_j \delta^j$$

Then, we have, from (31a), the coefficients of δ^0, δ, $\delta^2 \ldots$ respectively:

$$(\nu_0 + n^3 - n)\, h_1^n \alpha_{n,0} + (\nu_0 - n^3 + n)\, \frac{\beta_{n,0}}{h_1^n} = 0 \tag{31.1}$$

$$\nu_1(\alpha_{n,0} h_1^n + \beta_{n,0} h_1^{-n}) + (\nu_0 + n^3 - n)\, h_1^n \alpha_{n,1} + (\nu_0 - n^3 + n)\, \frac{1}{h_1^n} \beta_{n,1} = 0 \tag{31.2}$$

$$\nu_2(\alpha_{n,0} h_1^n + \beta_{n,0} h_1^{-n}) + \nu_1(\alpha_{n,1} h_1^n + \beta_{n,1} h_1^{-n})$$

$$+ (\nu_0 + n^3 - n)\, h_1^n \alpha_{n,2} + (\nu_0 - n^3 + n)\, \frac{1}{h_1^n} \beta_{n,2} = 0 \tag{31.3}$$

and so on, for all $n \geq 1$.

The various coefficients of δ-power in (30a) are Fourier series which vanishes for all σ. Consequently, we have

$$\alpha_{n,0} - \beta_{n,0} = 0 \tag{30.1}$$

$$-(n-1)^2 \alpha_{n-1,0} + n\alpha_{n,1} - \beta_{n+1,0}(n+1)^2 - n\beta_{n,1} + (n+1)\alpha_{n+1,0} - (n-1)\beta_{n-1,0} = 0 \tag{30.2}$$

$$\frac{(n-2)^2(n-1)}{2} \alpha_{n-2,0} - (n+1)^2 \alpha_{n-1,1} + n\alpha_{n,2} - n^2 \alpha_{n,0} + (n+1)\alpha_{n+1,1}$$

$$- \frac{(n+2)^2(n+1)}{2} \beta_{n+2,0} - (n+1)^2 \beta_{n+1,1} - \beta_{n,0} n^2 - (n-1)\beta_{n-1,1} - n\beta_{n,2} = 0 \tag{30.3}$$

and so on, for all $n \geq 1$.

Equations (30.1) and (31.1) yield the solution:

$$\alpha_{n,0} = \beta_{n,0} = 0 \quad \text{for all } n \neq k$$

where k is a fixed integer $k \geq 2$, and $\alpha_{k,0} = \beta_{k,0} \neq 0$. This determines also

$$\nu_0 = (k^3 - k)\,\frac{1-h_1^{2k}}{h_1^{2k+1}}$$

$$h_1 \equiv \frac{h_0}{1-\delta^2}$$

$$\omega^2 \quad \frac{\sigma\, v}{\rho h_0^3}$$

This result agrees* with the previously obtained one for the simple case $\delta = 0$. Equations (30.2) and (31.2) yield the following solution:

$$\nu_1 = 0$$

and

$$\beta_{k-1,1}\left[\left(\nu_0+f(k-1)\right)h_1^{k+1} + \left(\nu_0-f(k-1)\right)\frac{1}{h_1^{k-1}}\right] = -kh_1^{k-1}\left(\nu_0+f(k-1)\right)\alpha_{k,0}$$

$$\beta_{k+1,1}\left[\left(\nu_0+f(k+1)\right)h_1^{k+1} + \left(\nu_0-f(k+1)\right)\frac{1}{h_1^{k+1}}\right] = -k\left(\nu_0+f(k+1)\right)h_1^{k+1}\alpha_{k,0}$$

where $f(n) = n^3-n$.

$\alpha_{k-1,1}$ and $\alpha_{k+1,1}$ are obtained from (31.2). $\alpha_{n,1} = \beta_{n1} = 0$ for $n \neq k-1$ or $k+1$.

Finally, (30.3) and (31.3) yield the expression

---

* (2), p. 35, Note that a factor b is missed there, perhaps due to a misprint.

$$\nu_2 = \frac{h_1^{2k}}{1+h_1^{2k}} (\nu_0+k^3-k) \left[\frac{k(k-1)h_1^{k-1}(\nu_0+f(k-1))}{S(k-1)} + \frac{k(k+1)\left(\nu_0+f(k+1)\, h_1^{k+1}\right)}{S(k+1)} - k(k-1) \right]$$

where

$$S(n) = \left[\left(\nu_0 + f(n)\right) h_1^n + \left(\nu_0 - f(n)\right) \frac{1}{h_1^n} \right]$$

$$f(n) = n^3 - n$$

$$\nu_2 = \frac{2h_1^{2k}}{(1+h_1^{2k})^2} (k^3 - k) \left[\frac{k(k-1)h_1^{k-1}\left(\nu_0+(k-1)^3-k+1\right)}{S(k-1)} + \frac{k(k+1)h_1^{k+1}\left(\nu_0+(k+1)^3 k-1\right)}{S(k+1)} - k(k-1) \right] \quad (35)$$

Where $S(n) = (\nu_0 + n^3-n)\, h_1^n + (\nu_0 - n^3 + n) \frac{1}{h_1^n}$ (36)

Consequently,

$$\nu = \nu_0 + \nu_2 \delta$$

In the case where the cavity oscillates at the wall

$$\delta = 1-h_0, \quad h_1 = \frac{1}{2-h_0}$$

$$\nu_0 = (k^3 - k) \frac{(2-h_0)^{2k} - 1}{(2-h_0)^{2k} + 1}$$

$$\nu = \nu_0 + \nu_2 (1-h_0)^2 \text{ , } \nu_2 \text{ is given by (35).}$$

$$\omega^2 = \frac{\sigma \nu}{\rho h_0^3}$$

A.5 FREE OSCILLATION OF A SPHERICAL CAVITY IN A SPHERICAL TANK* AT ZERO GRAVITY

Let $\Phi(r, \theta, \phi, t) = \Psi(r, \theta, \phi) \cos \omega t$.

The problem is then reduced to find a harmonic function Ψ such that

(a) $\Psi_n = 0$ on the wall of the tank.

With the origin at the center of the spherical cavity of the radius h_0, this condition is

$$\Psi_r - \frac{G'(\theta)}{G^2(\theta)} \Psi_\theta = 0 \quad \text{on } r = G(\theta), \tag{37}$$

where

$$G(\theta) = -\delta \cos \theta + \sqrt{1-\delta^2 \sin^2 \theta}$$

δ = the distance between the center of the cavity and that of the tank.

(b) On $r = h_0$, $-\frac{\omega^2}{a} \Psi + (2D - D^2 - D^3) \psi = 0$

where

$$D = r \frac{\partial}{\partial r} \text{ , } a = \frac{\partial}{\rho h_0^3} .$$

* The "stuck-edge" condition is assumed when the cavity is attached to the wall of the tank.

Let* $$\Psi = \sum_{n=0}^{\infty} \left(A_n r^n + B_n \frac{1}{r^{n+1}}\right) P_n^m(x) \cos m\phi$$

where

$$P_n^m(x) = (-1)^m (1-x^2)^{m/2} \frac{d^m}{dx^m} P_n(x)$$

$P_n(x)$ = the Legendre polynomial

and

$x = \cos\theta$

For the sake of simplicity, we are only considering the fundamental modes m = 0. Hence

$$\Psi = \sum_{n=0}^{\infty} \left(A_n r^n + B_n \frac{1}{r^{n+1}}\right) P_n(x)$$

The condition (b) yields

$$A_n h_0^n \left(\nu + n^3 + n^2 - 2n\right) + B_n \frac{1}{h_0^n} \left(\nu - (n+1)^3 + (n+1)^2 + 2(n+1)\right) = 0$$

where

$$\nu = \frac{\omega^2}{a} .$$

The condition (a) can be rewritten in the form

$$\phi_r (r+\delta\zeta) - \frac{\delta \sin\theta}{r} \phi_\theta = 0 \qquad (39)$$

on B: $r^2 + 2\delta r \cos\theta + \delta^2 - 1 = 0$

---

* The following investigation is for the case m = 0. The method is perfectly valid for the case m > 0.

Thus, we have

$$\sum_{n=1}^{\infty} P_n(x) \left[\left\{ nA_n + \delta(n+1)\, A_{n+1} \right\} r^n - \left\{ (n+1)\, B_n + \delta n B_{n-1} \right\} r^{-n-1} \right] = 0 \quad \text{on B} \qquad (39a)$$

$$r = -\delta\chi + \sqrt{1+\delta^2(\chi^2-1)}$$

$$= \frac{1-\delta^2}{\delta\chi + \sqrt{1+\delta^2(\chi^2-1)}} = \frac{1-\delta^2}{1+\delta\chi\,\frac{1}{2}\,\delta^2(\chi^2-1)+\ldots.}$$

Let $\alpha_n = A_n(1-\delta^2)^n$, $\beta_n = \dfrac{B_n}{(1-\delta^2)^{n+1}}$

Now write $\alpha_n = \alpha_{n0} + \alpha_{n1}\,\delta + \alpha_{n,2}\,\delta^2 + \ldots$

$$\beta_n = \beta_{n0} + \beta_{n1}\,\delta + \beta_{n,2}\,\delta^2 + \ldots$$

$$\nu = \nu_0 + \nu_1\,\delta + \nu_2\,\delta^2 + \ldots,$$

(38) yields

$$\alpha_{n,0} h_1^n (\nu_0 + n(n-1)\,(n-2)) + \beta_{n,0}\,\frac{1}{h_1^{n+1}} \left(\nu_0 - (n^2-1)(n+2) \right) = 0 \quad (n \geq 0) \qquad (38.1)$$

and similar expressions for $\alpha_{n1}, \beta_{n,1}$, and etc.

where $h_1 = \dfrac{h_0}{1-\delta^2}$. Thus (39a) yields

$$n\alpha_{n,0} - (n+1)\,\beta_{n,0} = 0 \quad (n \geq 0) \qquad (39.1)$$

and other expressions for $\alpha_{n,1}, \beta_{n,1}$, etc. These relations, in turn, determine successively

(1) $\alpha_{n,0} = \beta_{n,0}$ for $n \neq k$ (a fixed integer)

$$\nu_0 = (k(k^2-1)(k+2) \frac{1-h_1^{2k+1}}{k+(k+1)h^{2K+1}} \tag{40}$$

which reduces to a known result* for the case $\delta = 0$. (Bubble at the tank center.)

(2) $\nu_1 = 0$

$$\alpha_{n,1} = \beta_{n,1} = 0 \text{ for } n \neq k-1 \text{ or } k+1$$

and

$$\alpha_{k-1,1} = \frac{k(k-1)}{h_1^k} \left(\nu_0 - k(k-2)(k+1)\right) \frac{\alpha_{k,0}}{S(k-1)},$$

$$\beta_{k-1,1} = -\frac{k(k-1)}{S(k+1)} \left(\nu_0 + (k^2-1)(k-2)\right) h_1^{k-1} \alpha_{k,0},$$

$$\alpha_{k+1,1} = \frac{k(k+2)}{h_1^{k+2}} \left(\nu_0 - k(k+2)(k+3)\right) \frac{\alpha_{k,0}}{S(k+1)},$$

and

$$\beta_{k+1,1} = -\frac{k(k+2)}{S(k+1)} \left(\nu_0 + k(k+1)(k+s)\right) h_1^{k+1} \alpha_{k,0}$$

where

$$S(n) \quad (n+1)\left(\nu_0 + (n-1)n(n+2)\right) h_1^n + n\left(\nu_0 - (n-1)(n+1)(n+2)\right) \frac{1}{h_1^{n+1}} \tag{41}$$

(3) Finally, we have

$$\nu = \nu_0 + \nu_2 \delta^2, \qquad \omega^2 = \frac{\sigma \nu}{\rho h_0^3}$$

---

* (2), p. 40

where

$$\nu_2 = \frac{(k+1)h_1^{2k+1}\left(\nu_0+k(k-1)(k+2)\right)}{k\left(k+(k+1)h_1^{2k+1}\right)} \left[\frac{-(2k^4+3k^3-k^2-k)}{(2k-1)(2k+3)} + \right.$$

$$\frac{k^2(k-1)}{h_1^k(2k-1)S(k-1)}\left\{(k-1)^2\left(-\nu_0+k(k-2)(k+1)\right) + (k^2+2k-1)\left(\nu_0+(k^2-1)(k-2)\right)h_1^{2k-1}\right\}$$

$$\left. + \frac{k(k+1)(k-2)}{h_1^{k+2}(2k+3)\,S(k+1)}\left\{(k^2-2)\left(-\nu_0+k(k+2)(k+3)\right) + (k+2)^2\left(\nu_0+k(k+1)(k+3)\right)h_1^{2k+3}\right\}\right] \tag{42}$$

where

$$h_1 = \frac{h_0}{1-\delta^2}$$

$$\nu_0 = k(k^2-1)(k+2)\,\frac{1-h_1^{2k+1}}{1+h_1^{2k+1}}$$

$$h_0 = \left(\frac{K}{1+K}\right)^{1/3}$$

K = The gas-liquid volume ratio

and S(n) is given by the expression (41). When the gas cavity is attached to the wall,

$$\delta = 1-h_0.$$

k is any integer ≥ 2. When k = 2, it gives the fundamental mode of the free oscillation.

A.6 FORCED OSCILLATION OF A SPHERICAL CAVITY IN A SPHERICAL TANK $\alpha \to 0$

Let $\chi = \chi_0 \cos \omega t$ and $\phi = \chi_0 \sin \omega t \psi(r, \theta, \phi)$. Then the condition (27) reduces to

$$-\frac{\omega^2}{a}\psi + (2D - D^2 - D^3)\psi = b \sin\theta \cos\phi, \text{ on } r = h_0 \tag{43}$$

where

$$a = \frac{\sigma}{\rho h_0^3}, \quad D = r\frac{d}{dr}$$

and

$$b = -\omega^3 h_0$$

Now write

$$\psi = \left[\sum_{n=0}^{\infty} \left(A_n r^n + B_n \frac{1}{r^{n+1}}\right) P_n^1(\cos\theta)\right] \cos\phi$$

where

$$P_n^1(\zeta) = -(1-\zeta^2)^{1/2}\frac{d}{d\zeta} P_n(\zeta)$$

Let

$$\nu = \frac{\omega^2}{a}.$$

It follows that

$$\nu\left(A_1 h_0 + B_1 \frac{1}{h_0^2}\right) = b \tag{44a}$$

$$(\nu + n^3 + n^2 - 2n) A_n h_0^n + B_n \frac{1}{h_0^{n+1}} \left(\nu - (n^2-1)(n+2)\right) = 0 \tag{44b}$$

for all $n \neq 1$.

The condition on the wall yields

$$(r+\delta\cos\theta)\psi_r - \frac{\delta\sin\theta}{r}\psi_\theta = 0 \quad \text{on } r = -\delta\cos\theta + \sqrt{1-\delta^2\sin^2\theta}$$

Employing the relations (Reference 5)

$$\zeta P_n^1(\zeta) = \frac{nP_{n+1}^1(\zeta) + (n+1)P_{n-1}^1(\zeta)}{2n+1}$$

and

$$(1-\zeta^2)\frac{d}{d\zeta}P_n^1(\zeta) = \frac{n^2 P_{n+1}^1(\zeta) + (n+1)^2 P_{n-1}^1(\zeta)}{2n+1}$$

we have

$$\sum_{n=0}^{\infty}\left[\left(nA_n + (n+2)\delta A_{n+1}\right)r^n - \left((n+1)B_n + (n-1)\delta\right)\frac{1}{r^{n+1}}\right]P_n^1(\zeta) = 0 \text{ on } B \qquad (45)$$

Now, as before, we set

$$\alpha_n = A_n(1-\delta^2)^n = \sum_{j=0}^{\infty}\alpha_{nj}\delta^j$$

and

$$\beta_n = \sum_{j=0}^{\beta}\beta_{nj}\delta^j$$

The equations (44) and (45) yield successively

(a) $\alpha_{1,0} = 2\beta_{1,0} = \dfrac{bh_1}{\nu(1+2h_1^2)}$, where $h_1 = \dfrac{h_0}{1-\delta^2}$

$$\alpha_{n,0} = \beta_{n,0} = 0 \text{ for } n \neq 1$$

(b) $$\alpha_{2,1} = \frac{\frac{3}{2}(\nu-1,2)\alpha_{1,0}}{2\nu-24+(3\nu+24)h_1^5}$$

$$\beta_{2,1} = \frac{-\frac{3}{2}(\nu+\delta)\,h_1^5}{(2\nu-24)+(3\nu+24)h_1^5}\ \alpha_{1,0}$$

$$\alpha_{n,1} = \beta_{n,1} = 0 \quad \text{for } n \neq 2$$

The higher order terms can be worked out successively. After finding these coefficients, the force exerted on the wall in the x-direction is computed by the following formula

$$F_x = \int_{\phi=0}^{\phi=2} \left[-\rho\Phi_t - \rho\,\ddot{\chi}\, r \sin\theta\cos\phi\right] G^2 \sin\theta \left[\sin\theta\cos\phi - \cos\theta\cos\phi\,\frac{G'(\theta)}{G(\theta)}\right] d\theta\, d\phi$$

where

$$r = G(\theta) = -\delta\cos\theta + \sqrt{1-\delta^2\sin^2\theta}$$

VOY-D-321
ATTACHMENT I

THE MEAN CURVATURE IN SPHERICAL COORDINATES

1. The infinitesimal rotation of the local frame of references due to the increment of general orthogonal coordinates is developed as follows:

Let the general orthogonal coordinates be $\alpha_1, \alpha_2, \alpha_3$, and

$$dS^2 = h_1^2 d\alpha_1^2 + h_2^2 d\alpha_2^2 + h_3^2 d\alpha_3^2$$

The infinitesimal rotation referred to the local frame of references $(\bar{K}_1, \bar{K}_2, \bar{K}_3)$ is, symbolically,

$$d\bar{\omega} = \begin{vmatrix} \bar{K}_1, & \bar{K}_2, & \bar{K}_3, \\ \frac{1}{h_1}\frac{\partial}{\partial\alpha_1}, & \frac{1}{h_2}\frac{\partial}{\partial\alpha_2}, & \frac{1}{h_3}\frac{\partial}{\partial\alpha_3}, \\ h_1 d\alpha_1, & h_2 d\alpha_2, & \frac{1}{h_3} d\alpha_3, \end{vmatrix} \tag{1.1}$$

This can be derived as follows: and is shown in Figure A-5.

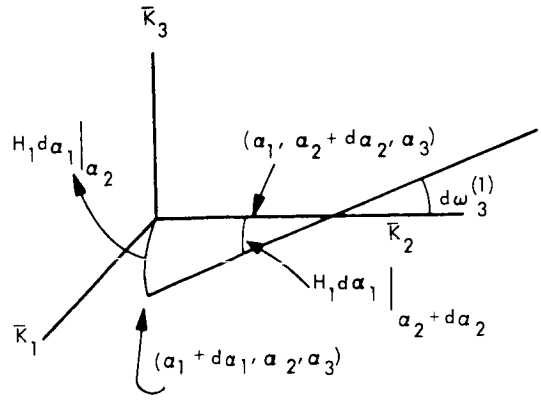

Figure A-5. Coordinate System

$d\omega_3^{(1)}$ = the infinitesimal rotation about $\bar{K}_3$ due to the increment of $d\alpha_1$

$$= \frac{h_1(\alpha_1, \alpha_2, \alpha_3)\, d\alpha_1 - h_1(\alpha_1, \alpha_2, + d\alpha_2, \alpha_3)\, d\alpha_1}{h_2(\alpha_1 + d\alpha_1, \alpha_2, \alpha_3)\, d\alpha_2}$$

$$- \frac{1}{h_2} \frac{\partial h_1}{\partial \alpha_2} d\alpha_1$$

For the spherical coordinates, $\alpha_1 = r, \alpha_2 = \theta, \alpha_3 = \phi$; $h_1 = 1$, $h_2 = r$, $h_3 = r \sin\theta$

$$d\bar{\omega} \quad \cos\theta\, d\phi \bar{K}_1 - \sin\theta\, d\phi \bar{K}_2 + d\theta \bar{K}_3 \tag{1.2}$$

$$d\bar{K}_1 \quad d\theta \bar{K}_2 + \sin\theta\, d\phi \bar{K}_3$$

$$d\bar{K}_2 \quad -d\theta \bar{K}_1 + \cos\theta\, d\phi \bar{K}_3$$

$$d\bar{K}_3 \quad -\sin\theta\, d\phi \bar{K}_1 - \cos\theta\, d\phi \bar{K}_3$$

2. THE FIRST AND SECOND FUNDAMENTAL FORMS

Now, let the surface be represented by

$$r \quad h(\theta, \phi),$$

or

$$\bar{r} \quad h(\theta, \phi)\, \bar{K}_1$$

$$d\bar{r} \quad (h_\theta d\theta + h_\phi d\phi)\, \bar{K}_1 + h\, d\theta \bar{K}_2 + h \sin\theta d\phi \bar{K}_3$$

From

$$ds^2 \quad d\bar{r} \cdot d\bar{r}$$

we have

$$E \quad h^2 + h_\theta^2, \quad F \quad h_\theta h_\phi, \quad G \quad h_\phi^2 + h^2 \sin^2\theta \tag{2.1}$$

where

$$h_\theta = \frac{\partial h}{\partial \theta}, \quad h_\phi = \frac{\partial h}{\partial \phi}$$

Now

$$\bar{r}_\theta \times \bar{r}_\phi = h^2 \sin\theta \, \bar{K}_1 - h h_\theta \sin\theta \, \bar{K}_2 - h h_\phi \, \bar{K}_3$$

$$\bar{r}_{\theta\theta} = \frac{\partial^2}{\partial \theta^2} \bar{r} = (h_{\theta\theta} - h) \bar{K}_1 + 2 h_\theta \bar{K}_2$$

$$r_{\theta\phi} = h_{\theta\phi} \bar{K}_1 + h_\phi \bar{K}_2 + (h \cos\theta + h_\theta \sin\theta) \bar{K}_3$$

and

$$r_{\phi\phi} = (h_{\phi\phi} - h \sin^2\theta) \bar{K}_1 - h \sin\theta \cos\theta \, \bar{K}_2 + 2 h_\phi \sin\theta \, \bar{K}_3$$

Consequently, we have

$$(EG-F^2)^{1/2} e = (h^3 - h^2 h_{\theta\theta} + 2 h h_\theta^2) \sin\theta$$

$$(EG-F^2)^{1/2} f = (-h^2 h_{\theta\phi} + 2 h h_\theta h_\phi + h^2 h_\phi \cot\theta) \sin \tag{2.2}$$

$$(EG-F^2)^{1/2} g = (h^3 \sin^2\theta - h^2 h_{\phi\phi} - h^2 h_\theta \sin\theta \cos\theta + 2 h h_\phi^2) \sin\theta$$

In this case, it can be directly * verified that the mean curvature for the surface:

$$r = h(\theta, \phi)$$

in spherical coordinates is

$$2J = \left(\frac{1}{R_1} + \frac{1}{R_2}\right) = \frac{Eg - 2Ff + Ge}{EG - F^2}$$

$$= \frac{2h \sin}{\sqrt{EG-F^2}} - \frac{1}{h \sin\theta} \left[\frac{\partial}{\partial \theta} \left(\frac{h h_\theta \sin^2\theta}{\sqrt{EG-F^2}} \right) + \frac{\partial}{\partial \theta} \left(\frac{h h_\phi \sin^{-1}\theta}{\sqrt{EG-F^2}} \right) \right] \tag{2.3}$$

* The cumbersome calculations are omitted here.

where

$$E = h^2 + h_\theta^2, \quad F = h_\theta h_\phi, \quad G = h^2 \sin^2\theta + h_\phi^2$$

This is a very useful formula.

3. THE SPECIAL CASE $h_\phi = 0$

$$F = 0, \quad E = h^2 + h'^2, \quad G = h^2 \sin^2\theta$$

$$2J = \frac{1}{\sqrt{h^2 + h'^2}} \left[\frac{2}{h} - \frac{d}{d\theta} \left(\tan^{-1} \frac{h'}{h} \right) - \frac{h'}{h} \cot\theta \right] \tag{3.1}$$

4. LINEARIZED EXPRESSION FOR J

Let $h = H(\theta) + \omega(\theta, \phi)$

where

$$\omega(\theta, \phi) << H(\theta)$$

set

$$h = e^u, \quad u = \log H + \frac{\omega}{H}$$

$$\log H = \bar{U}$$

$$\frac{\omega}{H} = \lambda$$

Neglecting the square and higher order terms in λ, we have

$$2J = \frac{1}{h} \left[\frac{2}{\sqrt{1 + \bar{U}'^2}} - \frac{1}{\sin\theta} \frac{\partial}{\partial\theta} \frac{\bar{U}' \sin\theta}{1 + \bar{U}'^2} - \frac{1}{\sin\theta} \frac{\partial}{\partial\theta} \left(\sin\theta \frac{\lambda_\theta}{(1+\bar{U}'^2)^{3/2}} \right) - \frac{\sin^{-2}\theta}{\sqrt{1 + U'^2}} \lambda_{\phi\phi} \right] \tag{4.1}$$

VOY-D-321
ATTACHMENT II

METHOD OF FINDING A PARTICULAR SOLUTION BY INTEGRATION IN SERIES

Consider the equation

$$(1-\chi^2)\,\omega'' = 2\chi\omega' + 2\omega = -1-\chi$$

We are looking for a solution which is regular at $\chi = -1$.

Set $\chi + 1 = y$

Then (1) becomes

$$L(\omega) \equiv y(2-y)\frac{d^2\omega}{dy^2} - 2(y-1)\frac{d\omega}{dy} + 2 = -y$$

$$L(y^m) \equiv (-m+1)(m+2)\,y^m + 2m^2\,y^{m-1}$$

Hence, if

$$\omega = \sum_{m=2}^{\infty} A_m y^m$$

$$L(\omega) \equiv \sum_{m=2}^{\infty} (-m+1)(m+2)\,A_m y^m + \sum_{m=1}^{\infty} 2(m+1)\,A_{m+1} y^m = n$$

Hence

$$8A_2 = -1$$

and

$$A_{m+1} = \frac{(m-1)(m+2)}{2(m+1)^2} A_m, \qquad m \geq 2$$

Thus,

$$A_m = \frac{(m-2)!\,(m+1)!\,2^2}{6(m!)^2\,2^{m-2}}\,A_2$$

$$= \frac{2}{3}\,\frac{(m+1)}{m(m-1)}\,\frac{1}{2^{m-2}}\,A_2,\quad (m \geq 2)$$

and

$$\omega = \frac{8}{3}\,A_2\,z^2 \sum_{m=2}^{\infty} \frac{(m+1)}{m(m-1)}\,z^{m-2},\ \text{where } z = \frac{y}{2}$$

This infinite series can, however, be summed up in a closed form as follows:

$$\frac{m+1}{m(m-1)} = \frac{-1}{m} + \frac{2}{m-1}$$

$$\sum_{m=2}^{\infty} \frac{2}{m-1}\,z^m = -z\log(1-z)$$

$$\sum_{m=2}^{\infty} \frac{-1}{m}\,z^m = \log(1-z)$$

Finally,

$$\omega = -\frac{1}{3}(1-y)\log\left(1-\frac{y}{2}\right)$$

$$+\frac{1}{3}\chi\log\frac{1-\chi}{2}$$

Since χ is a solution of the homogeneous equation, one particular is

$$\frac{1}{3}\chi\log(1-\chi)$$

VOY-D-321
ATTACHMENT III

THE ANGLE OF CONTACT BETWEEN THE INTERFACE AND THE WALL OF THE SPHERICAL TANK

The curve of the intersection of the interface S with the wall of the tank is given by the following equation:

$$H(\theta, \phi, t) = H(\theta)\, e^{\lambda(\theta,\phi,t)}$$

$$= \underbrace{-(1-h_0)\cos\theta + \sqrt{1 + (\cos^2\theta - 1)(1-h_0)^2}}_{r(\theta)} \qquad (1)$$

This determines θ as a function of ϕ. In the linearized theory, we have

$$H(\theta)\left(1 + \lambda(\theta, \phi, t)\right) = r(\theta) \qquad (1a)$$

Let θ_1 be the solution of the equation

$$H(\theta_1) = r(\theta_1)$$

Let the solution of (1a) be

$$\theta = \theta_1 + \Delta\theta$$

Then, up to the first power of $\Delta\theta$, we have

$$\left[r(\theta_1) - H'(\theta_1)\right] \Delta\theta = H(\theta_1)\, \lambda(\theta_1, \phi, t)$$

$$\Delta\theta = \frac{H(\theta_1)}{r(\theta_1) - H'(\theta_1)}\, \lambda(\theta_1, \phi, t) = k(\phi) \qquad (2)$$

Let $R(\theta) = \log r(\theta)$, $h = e^{U + \lambda(\theta, \phi, t)}$

The condition that the angle of contact is θ_τ, yields

$$\tan\theta_\tau = \left[R'(\theta) - (U' + \lambda_\theta) \right] / \left[1 + R'(U' + \lambda_\theta) \right]$$

at $\theta = \theta_1 + k(\phi)$

Since $\tan\theta_\tau = \dfrac{R'(\theta) - U'}{1 + R'U'}$, we have, after the linearization with respect to λ,

$$\tan\theta_\tau \left[\lambda(\theta, \phi, t) + \left\{ R''(\theta_1)\, U'(\theta_1) + R'(\theta_1)\, U''(\theta_1) \right\} k(\phi) \right]$$

$$\left[R''(\theta_1) - U''(\theta_1) \right] k(\phi) + \lambda_\theta(\theta_1, \phi, t) \qquad (3)$$

From (2) and (3), it follows that

$$\lambda_\theta = \Gamma\lambda \quad \text{at} \quad \theta \quad \theta_1$$

REFERENCES

1. H.N. Abramson, Editor, The Dynamic Behavior of Liquids in Moving Containers, NASA SP-106 1966

2. Voyager Support Study, Propellant Hydrodynamics Studies, TRW Report 04480-6006-R000 February 1967

3. (a) Gordon, C. K. Yeh, "Free And Forced Oscillation of a Liquid in an Axisymmetric Tank at Low-Gravity Environments" pp. 23-28 Journal of Applied Mechanics, March, 1967.

   (b) H.M. Satterlee and W. C. Reynolds, "The Dynamics of the Free Liquid Surface in Cylindrical Containers Under Strong Capillary and Weak Gravity Conditions" T. Rep. No. LG-2, Department of Mech. Engineering, Stanford University, May 1, 1964.

4. D.J. Struik, Classical Differential Geometry, Addison-Wesley, 1957.

REFERENCES (Cont.)

5. B. Budiansky, "Sloshing of Liquids in Circular Canal and Spherical Tanks," J. Aerospace Sciences, pp. 161-173, vol. 27, No. 2, 1960.

6. J.D. Riley, and N.W. Trembloth, "Sloshing of Liquids in Spherical Tanks," J. Aerospace Sciences, Vol. 28, No. 3, 1961.

7. W. Magnus and F. Oberhettinger, Formulas and Theorems for Special Functions of Mathematical Physics, Chelsea, 1949.

VOY-D-321
APPENDIX B

MULTIMASS MODEL OF ZERO G FLUID DYNAMICS

B.1 INTRODUCTION

The following development defines a simple, consistent model for studying the propellant motion at near zero bond numbers in a spherical tank.

The model is limited to perfectly wetting liquids (hydrazine and nitrogen tetroxide), the ullage bubble may be taken to be spherical at "zero g". For g/g_o (g_o = 32.2 ft/sec^2) of the order of 10^{-8}, the bubble should, however, rise at the top of the tank when the liquid is at rest. When the liquid is in motion, the bubble will remain near-spherical. It is also predicted that it will not disintegrate. This assumption may be substantiated.

The geometry of the problem is defined in Figure B-1.

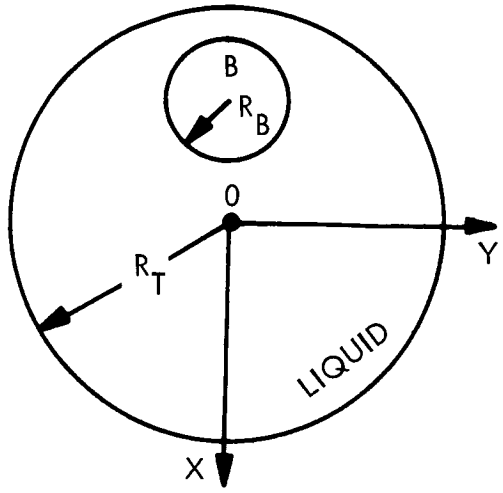

R_T IS THE RADIUS OF THE TANK, TO WHICH ALL OTHER LENGTHS OF THE PROBLEM WILL BE NORMALIZED.

R_B IS THE RADIUS OF THE BUBBLE (WHICH IS MASSLESS), NORMALIZED TO R_T.

M_T THE MASS OF THE FULL TANK IS TAKEN AS THE NORM FOR THE MASSES.

Figure B-1. Geometry of System

The following relations hold, F being defined as the fill ratio

$$F \equiv \frac{V_{liq}}{V_{tank}} = \frac{V_{full} - V_{bubble}}{V_{full}} = 1 - \left(\frac{R_B}{R_T}\right)^3 = 1 - R_B^3 \text{ (normalized)} \qquad (1)$$

F is taken as the independent variable. Then

$$R_B = (1-F)^{1/3} \qquad (2)$$

When the bubble is "at the top", the coordinate of the center of the bubble is

$$X_B = -(1 - R_B) = -\left[1 - (1-F)^{1/3}\right] \qquad (3)$$

($x > o$ downwards) Then the center of mass has abscissa

$$X_{cg} = \frac{m_B}{m_{liq}} X_B = \frac{1-F}{F}(1-R_B) = \frac{1-F}{F}\left[1 - (1-F)^{1/3}\right] \qquad (4)$$

in which m_B is the mass of liquid that would occupy the volume of the bubble.

B.2 DEVELOPMENT OF A MULTI-MASS MODEL

The model should be "equivalent" to the true physical system from several viewpoints. We shall require the invariance of the total mass and the duplication of the center of mass -- which may be labeled "translation" properties. Of equal importance are the inertias in spin about the center of the tank; or "rotation" characteristics.

Consider first that the system of Figure B-1 is represented by one single moving mass (pendulum of variable length) as on Figure B-2. This mass represents the sloshing liquid, while the part of the liquid "behaving like a solid" is represented by m_o, mass at rest*. The latter is located at the geometrical center of the tank.

* SWRI: Reference cited.

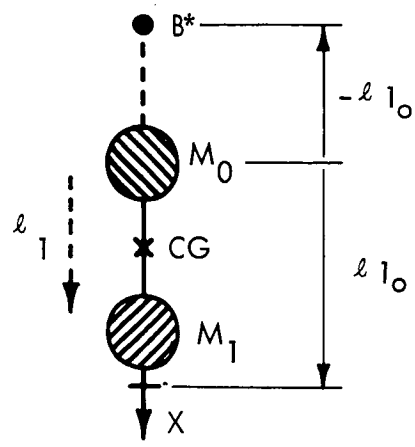

Figure B-2. One Slosh - Mass Model

Conservation of mass requires: $m_o + m_1 = m_{liq}$ (5)

and duplication of the center of mass is expressed by

$$m_1 l_1 = m_{liq} X_c \quad (6)$$

In order to reproduce the properties of the system when the bubble is wall-bound (Figure B-3), and undergoing small oscillations about its equilibrium position (at the "top" of the tank), m_1 is taken as the low-g slosh mass for a spherical tank. This is assumed to be a fraction, $\zeta(m_1)_{g<<}$, of $(m_1)_{g>>}$, the high-g slosh mass for spherical tanks, that is the "flat gas-liquid interface" value. This is given elsewhere**, and $\zeta \approx 0.85$, the value of ζ if the low-g and high-g cases are compared for cylindrical tanks*. m_1, as obtained from the theory***,

---

**F. T. Dodge, L. R. Garza: Experimental and Theoretical Studies of Liquid Sloshing at Simulated Low Gravity. Journal of Applied Mechanics. Paper No. 67-APM14 June 1967.

***F. T. Dodge: "Analytical Representation of Lateral Sloshing by Equivalent Mechanical Models" Chapter 6 in the Dynamic Behaviour of Liquids in Moving Containers, Abramson, H. N. ed. NASA Special Publications SP-106.

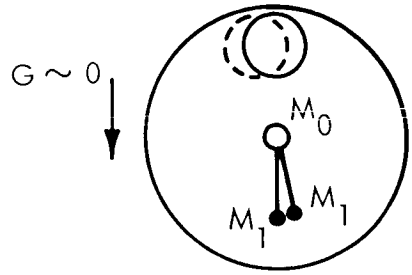

Figure B-3. Low-g Slosh Mass

and ℓ_1 as computed from equation (6) are plotted on Figures B-4 and B-5 for the wall-bound bubble. In this model, the wall condition (the bubble may not cross the wall) is expressed by

$$0 \leq \ell \leq (\ell_1)_{max} \quad \ell_{1_o}$$

where $(\ell_1)_{max}$ is the value of ℓ_1 for the wall-bound bubble. (X_{cg} is then the largest, for given F.)

In spite of its simplicity, this model, however, leads to an inconsistency. If a spin motion about axis Z exists, centrifugal action will cause the bubble to move inwards ($X_B \rightarrow o$). As is shown by equation (4), if $X_B \rightarrow o$, $X_{cg} \rightarrow o$. This would not be realized by this model. Even if the bubble is represented by a massless geometrical point B* (see Figure B-2) rigidly fixed on the pendulum arm, of abscissa

$$X \quad -\ell_{1_o}$$

when the bubble is wall-bound, if $B^* \rightarrow 0$, $\ell_1 \rightarrow 2\ \ell_{1_o}$ and one would find

$$X_{cg} \quad 2\ (X_{cg})_{wall\text{-}bound} \quad 2\ \frac{m_l}{m_{liq}}\ \ell_{1_o}$$

instead of the actual value $X_{cg} \quad 0$.

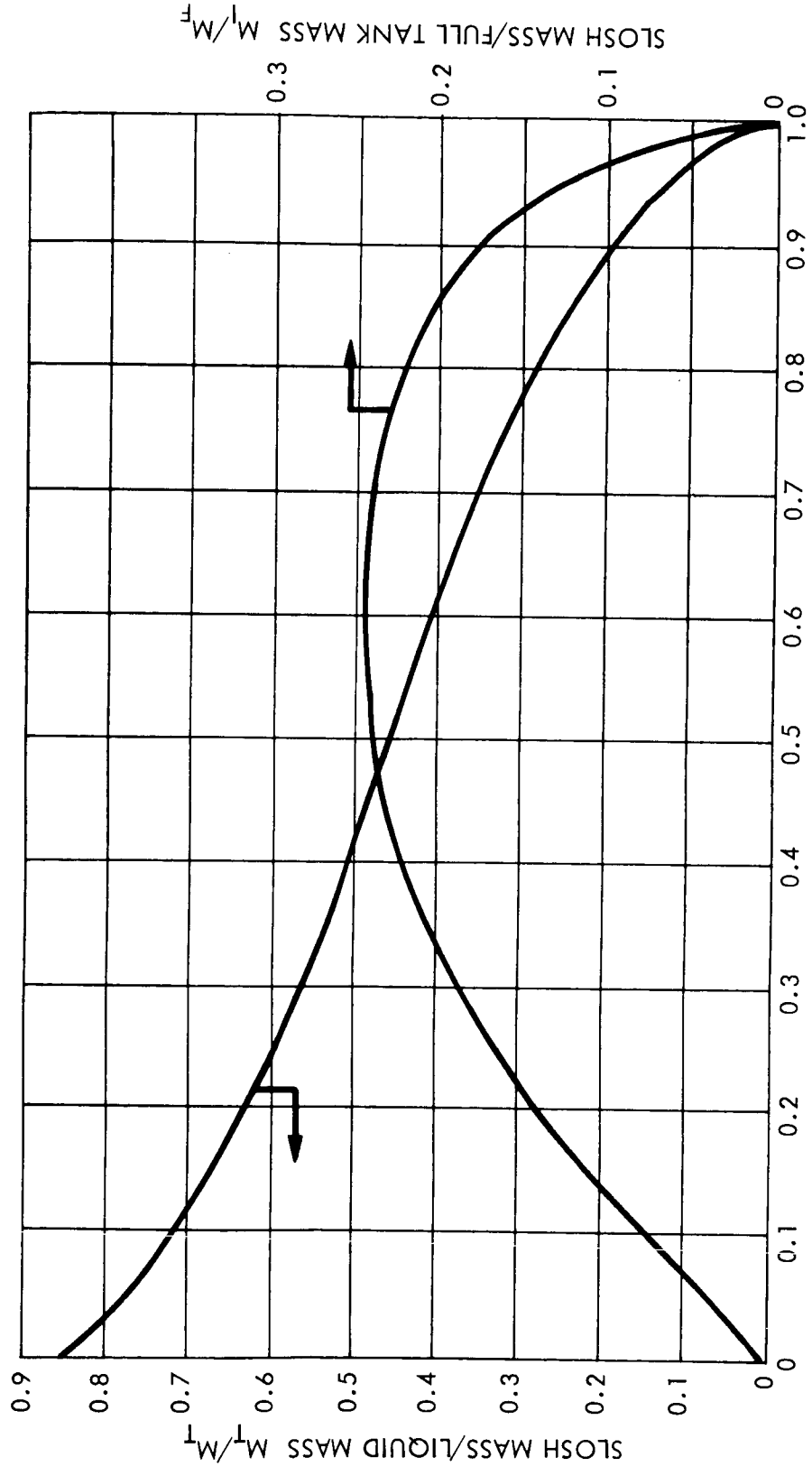

Figure B-4. Zero-G Slosh Mass

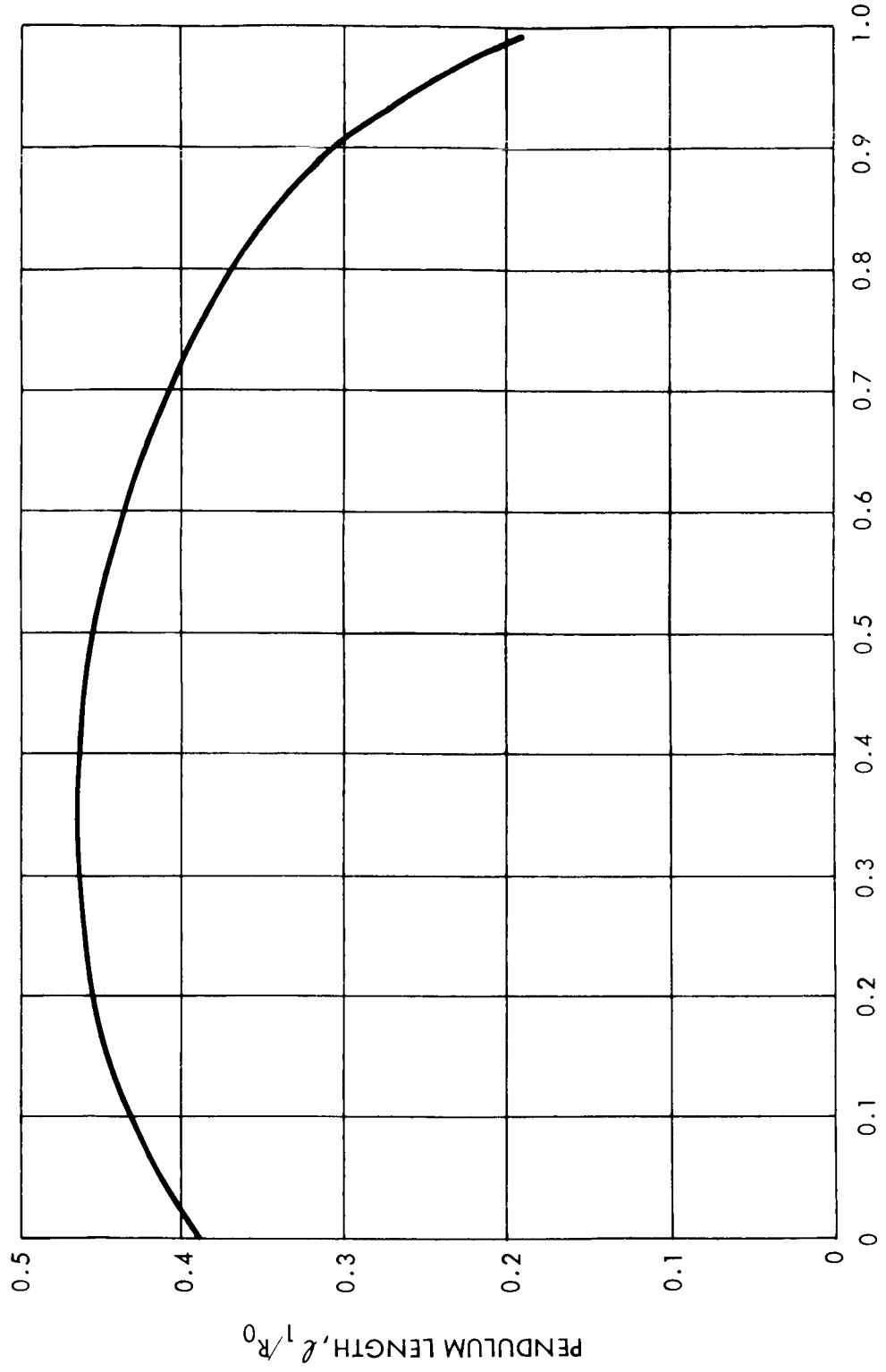

Figure B-5. Zero-G Slosh Model Pendulum Length

To alleviate these difficulties, a multi-mass model is proposed here which is believed to represent the actual phenomenon more faithfully by giving more attention to the physical picture. First we shall accept that Figure B-3 represents the infinitesimal oscillations of the liquid when the bubble is wall-bound and the liquid at rest. The sloshing mass is m_1 of Figure B-4, and the mass at rest located in 0, geometrical center of the tank, is given by

$$m_0 + m_1 = m_{liq} \tag{7}$$

As represented on Figure B-6, we discretize a continuum (the liquid) into a finite number of masses. One mass is the coarsest modeling that can be considered. It could account for the translational aspects of the motion of the bubble, but could never describe the "splashing out" of the liquid mass when the tank is spinning about 0_z.

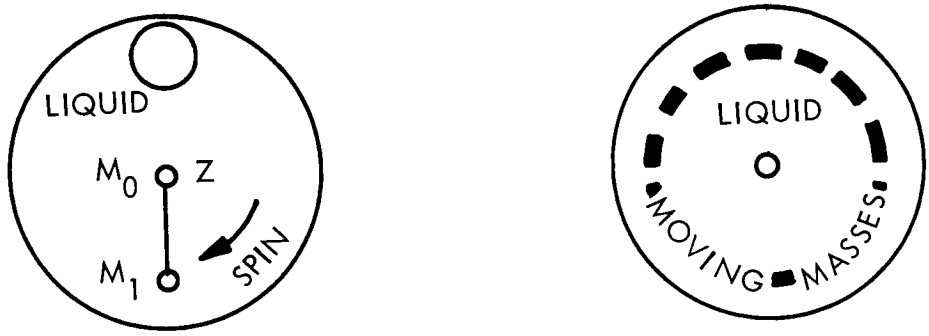

Figure B-6. Continuous and Single Discrete Systems

This will not be true for a three-mass model (or more generally a 2 N+1 mass model, N integer) as illustrated in Figure B-7. If the bubble is translated radially in the physical system, part of the fluid will undergo the translation, and two other parts will also "flow" aound the bubble (symmetrical motion); if a spin about axis Z exists, the bubble will migrate to the center, and the "unbalanced" masses should move to the periphery of the tank. This is reproduced qualitatively by the mechanical model in which C is the (massless) hinge of

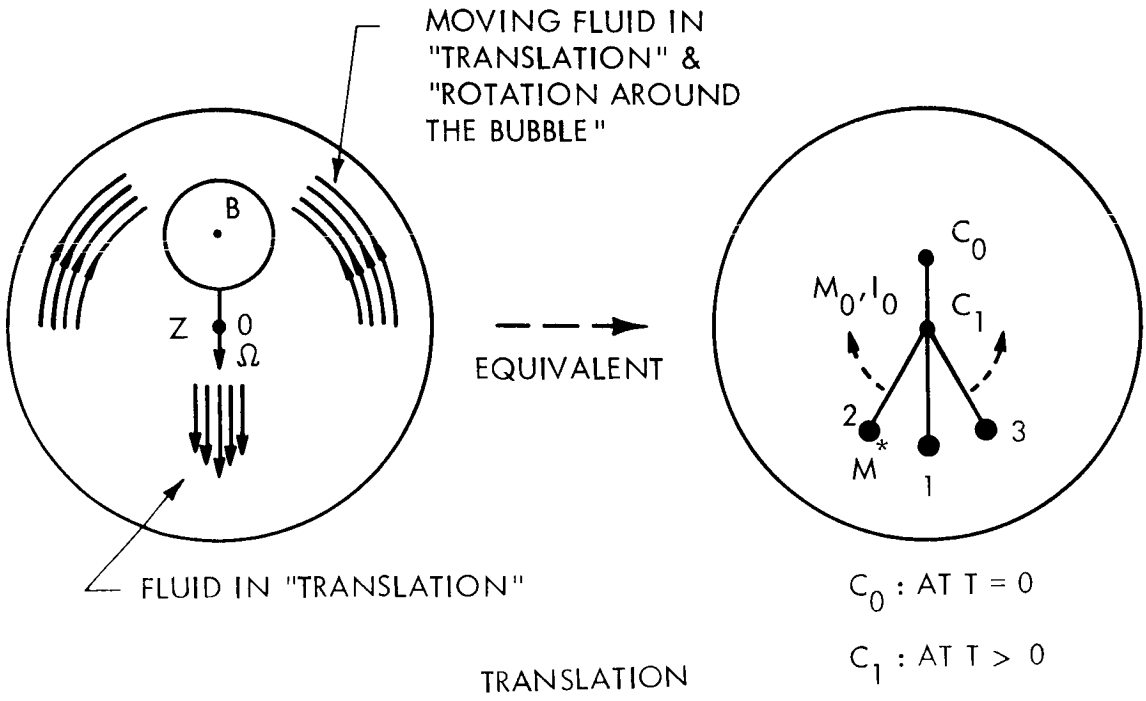

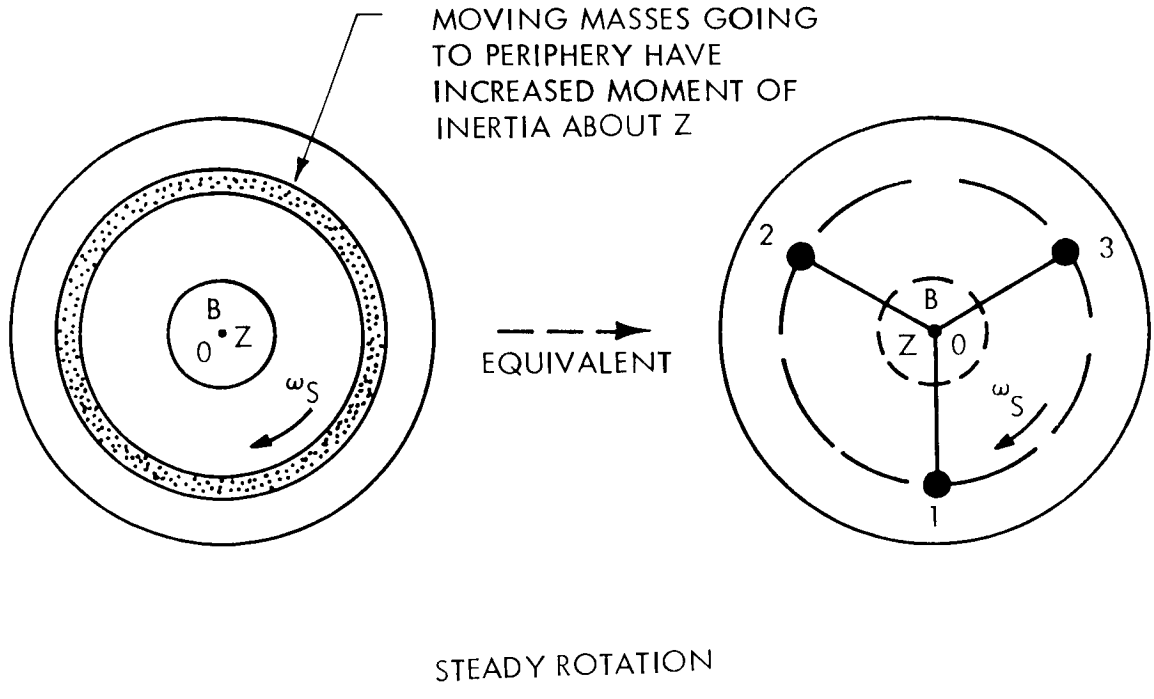

Figure B-7. Equivalence of Motions in the 3-Mass Model

the lever arms ℓ, and "represents" the radial position of the bubble (but $X_c \neq X_B$). I_o is the massless moment of inertia of the inert masses.

We now define the model quantitatively.

a. Duplication of behavior for small oscillations of wall-bound bubble - Thus, m_1 being given by Figure B-4, as explained above, when B describes a circle about 0, so does C_o in Figure B-7. The mass of the pendulum attached in 0 is 3m* or m_1, thus

$$m^* = \frac{m_1}{3} \tag{8}$$

then

$$m_o = m_{liq} - 3m^* \tag{9}$$

b. Duplication of center of mass with wall-bound bubble -

$$3m^* X^* = m_{liq} X_{cg}.$$

or under normalized form, (m_1 normalized to mass of full tank)

$$X^* = \frac{1-F}{3m^*} \left[1 - (1-F)^{1/3}\right] \tag{10}$$

X* is plotted vs. F on Figure B-8.

c. Duplication of spin moment of inertia with wall-bound bubble - If the bubble is prevented from moving from the wall, the moment of inertia, I_{BW}, of the liquid rotating as a solid body, is related to I_o, m*, and ℓ^* through

$$I_o + 3m^* X^{*2} = I_{BW} \tag{11}$$

d. Duplication of spin moment of inertia with bubble in the center - If the bubble is in the center and the liquid rotating like a solid, then (Figure B-7)

$$I_o + 3m^* \ell^2 = I_{BC} = \frac{2}{5}\left[m_T R_o^2 - m_B R_B^2\right] \tag{12}$$

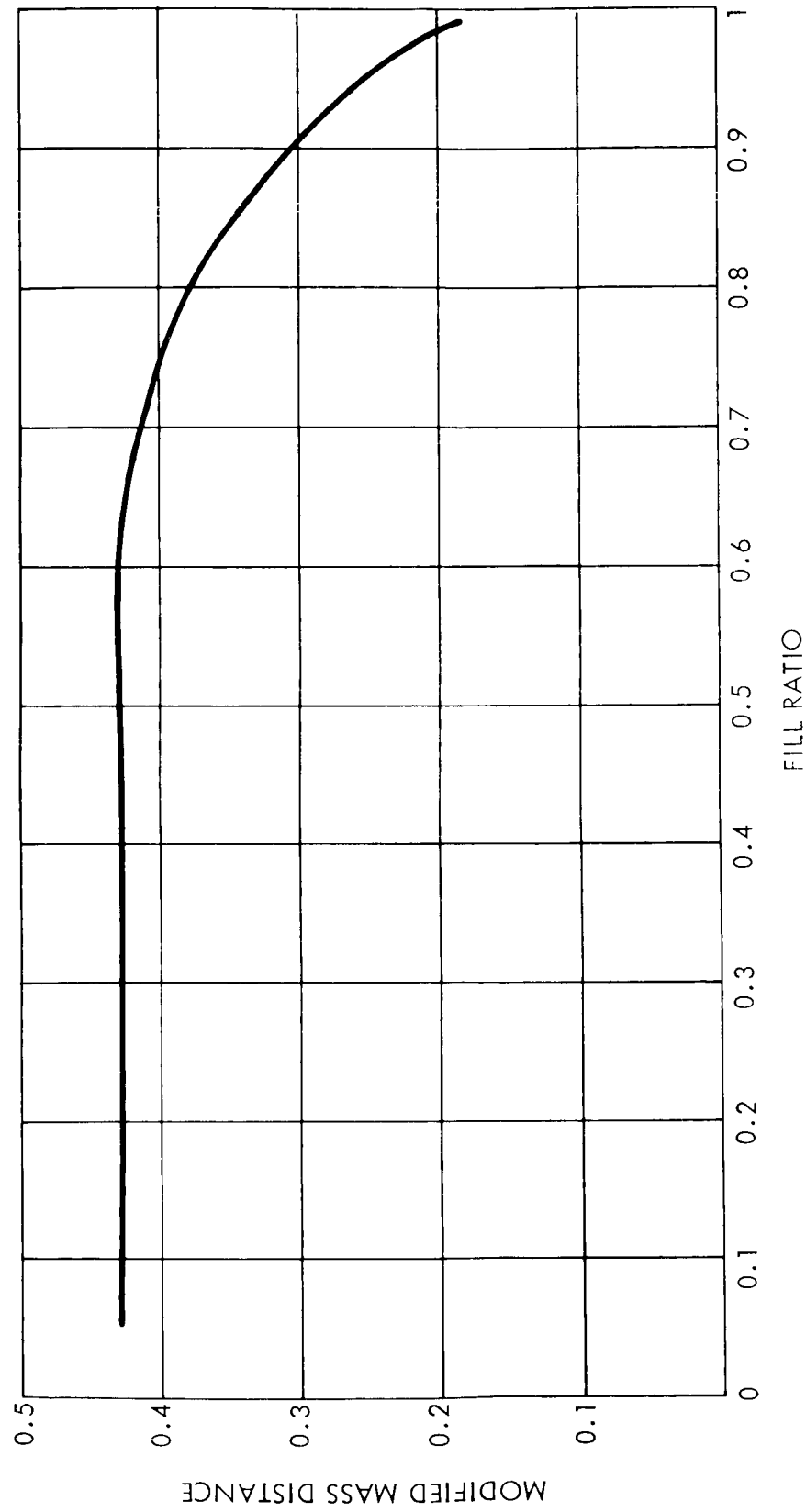

Figure B-8. Modified Mass Distance vs Fill Ratio

Under normalized form,

$$I_o + 3m^* \ell^2 = I_{BC} = \frac{2}{5}\left[1 - (1-F)^{5/3}\right]$$

Continuing c) and d), ℓ is given by

$$\ell^2 = \frac{\Delta I}{3m^*} + (X^*)^2 \qquad (13)$$

with

$$\Delta I = I_{BC} - I_{BW} = m_B X_B^2$$

Therefrom, the abscissa of the hinge point, X_C, and the moment of inertia of the mass at rest

$$X_C = X^* - \ell \qquad (14)$$

$$I_o = I_{BC} - 3m^* \ell^2 \qquad (15)$$

In Figures B-9, B-10, and B-11 the quantities ℓ, X_c and I_o are plotted vs. F

Comments

Knowing m^*, m_o, ℓ, X_c, X^*, I_o, the model is completely determined statically. It is interesting to note that if we imagine the bubble to be wall-bound, and the surrounding liquid spinning with it at rate ω, the (centripetal) force exerted on the bubble would be

$$F = m_B |X_B| \omega^2 \qquad (16)$$

Since $3m^* X^* = m_{liq} X_{cg} = m_B |X_B|$, from equation (10) and (4) the physical force existing on the model is equal to F. The hinge point C, "representing" the bubble is acted upon by F and will move inwards.

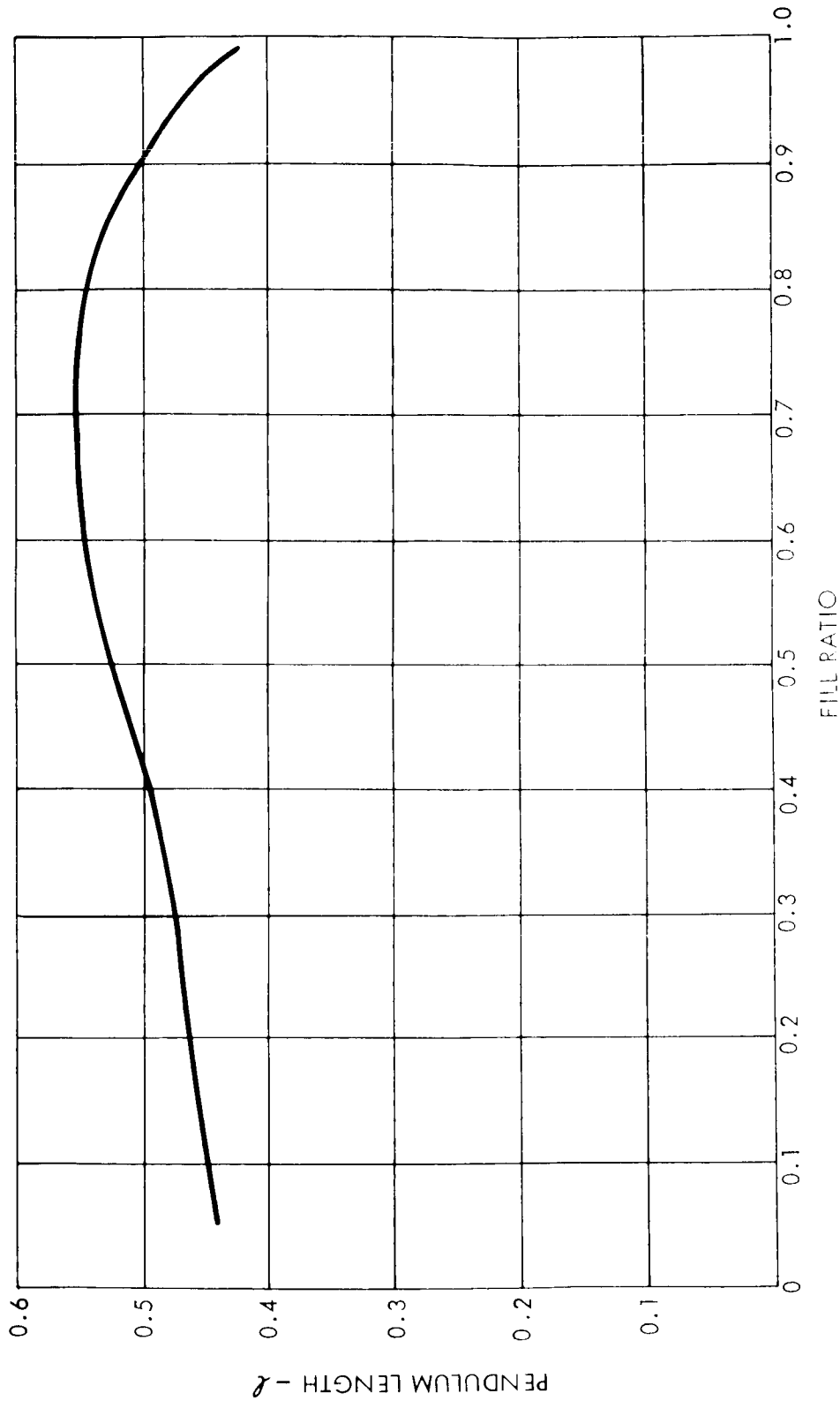

Figure B-9. Pendulum Length vs. Fill Ratio

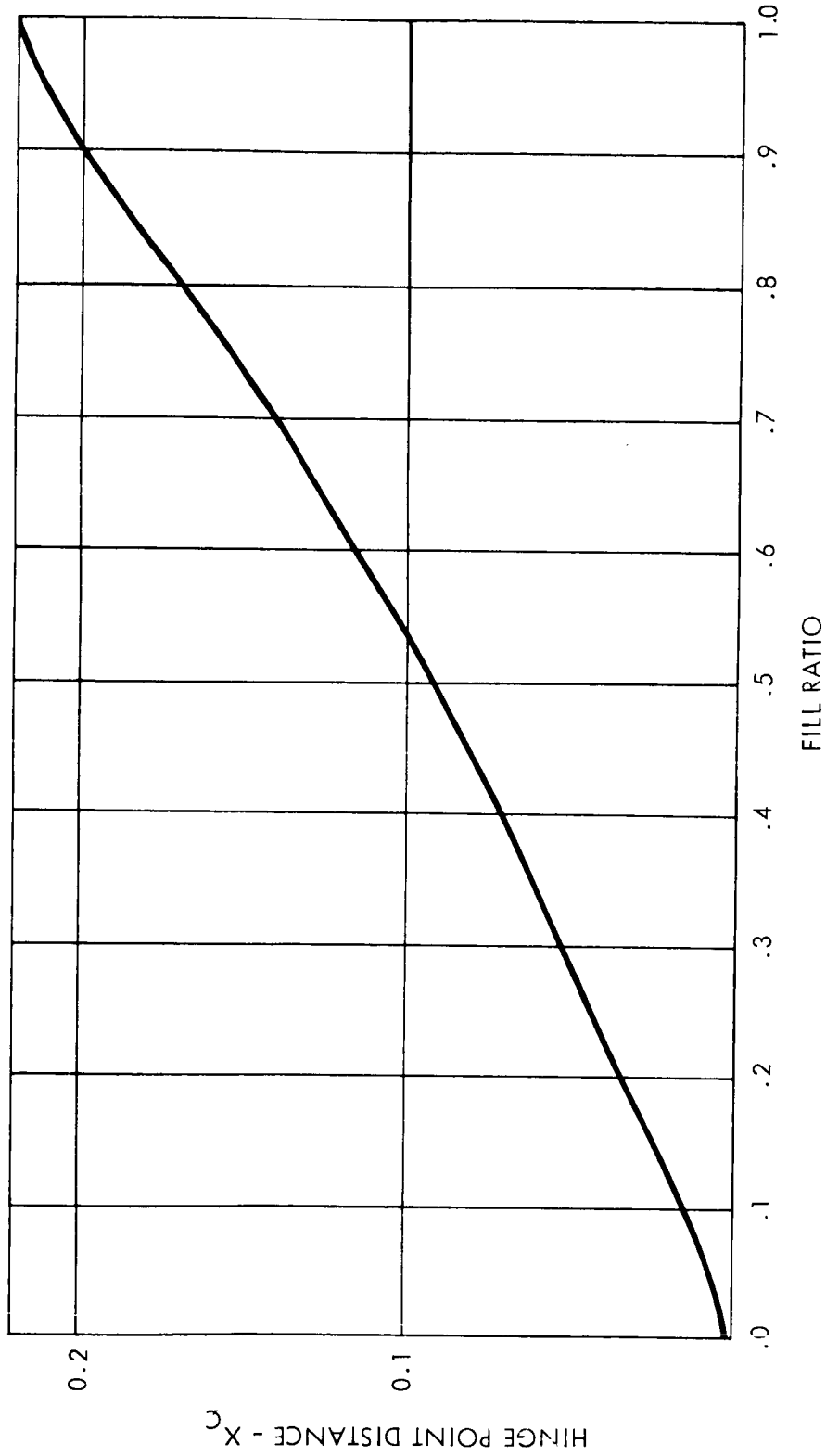

Figure B-10. Hinge Point Distance vs Fill Ratio

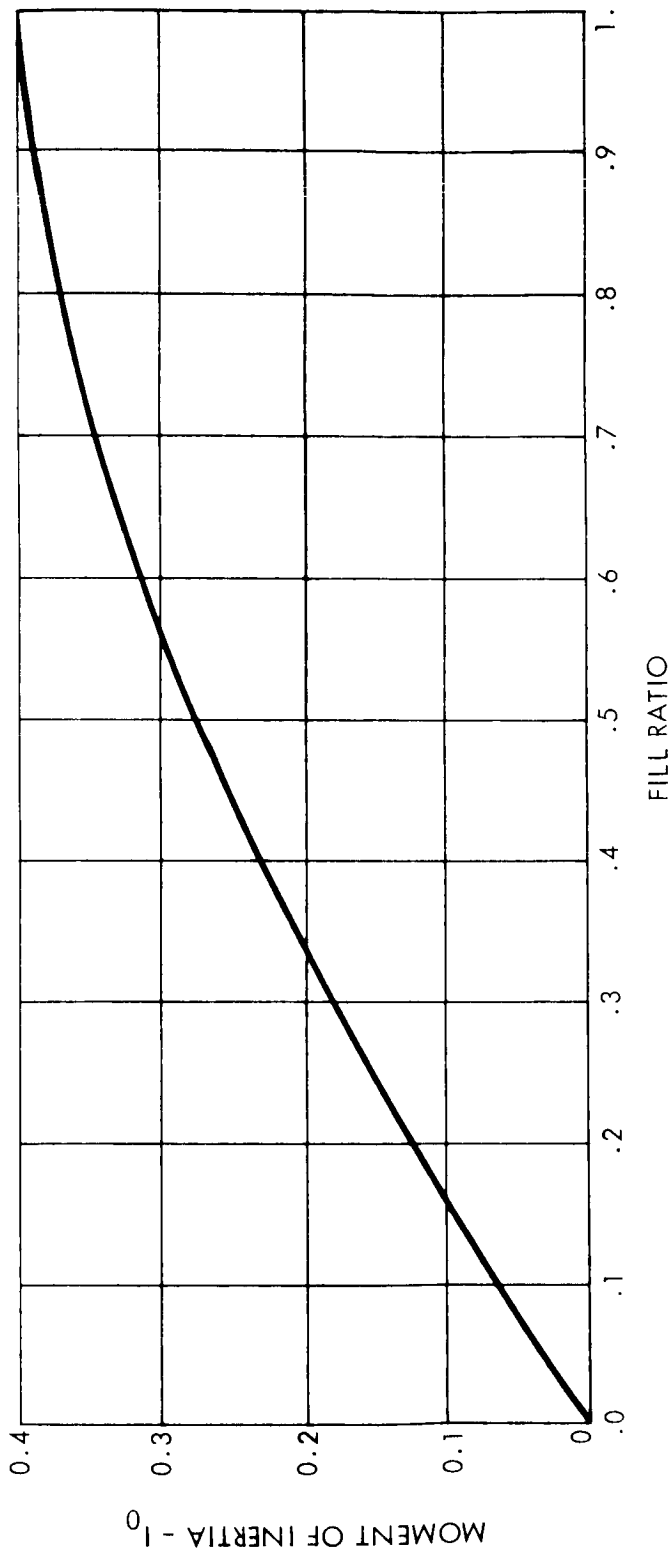

Figure B-11. Moment of Inertia vs Fill Ratio

Considering an arbitrary motion of the tank, masses 2 and 3 need not be always symmetric with respect to the radial direction (Figure B-12). The model is dynamically determined if:

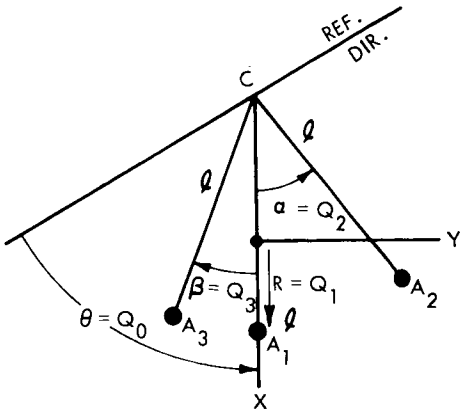

-THE DIRECTION OF $\overrightarrow{OA_1}$, IS KNOWN (GENERALIZED COORDINATE $\theta = Q_0$)

-THE MAGNITUDE OF $\overrightarrow{OA_1}$, IS KNOWN (GENERALIZED COORDINATE $R = Q_1$)

-THE ANGULAR POSITION OF $\overrightarrow{CA_2}$ IS KNOWN (GENERALIZED COORDINATE $\alpha = Q_2$)

-THE ANGULAR POSITION OF $\overrightarrow{CA_3}$ IS KNOWN (GENERALIZED COORDINATE $\beta = Q_3$)

Figure B-12. Non-Symmetric Condition

In axes (X, Y), known with q_o, the position of the c-g and of the bubble will be given by

$$X_{cg} = -\frac{1-F}{F} X_B = \frac{m^*}{F}\left[q_1 + (\ell \cos q_2 + q_1 - \ell) + (\ell \cos q_3 + q_1 - \ell)\right] \tag{16a}$$

$$Y_{cg} = \frac{m^*}{F}\left[\ell \sin q_2 + \ell \sin q_3\right] \tag{16b}$$

VOY-D-322
REACTION CONTROL SUBSYSTEM

VOY-D-322
REACTION CONTROL SUBSYSTEM

1. SCOPE

The Reaction Control Subsystem is a mass expulsion system which applies torques to the spacecraft upon demand of the attitude control system. The system which is believed to best satisfy the Voyager requirements, and is therefore selected, employs nitrogen gas as the propellant. The equipment is comprised of storage tanks, filters, regulators, valves and nozzles.

Other propellants such as freon, ammonia, propane, hydrazine and others can also be used for this application. The principal effort of this study has been to evaluate the state of development of these alternate propellant systems, to assess their suitability to Voyager, and to select the best of them from the standpoint of reliability and weight savings.

2. TRADE STUDIES

2.1. INTRODUCTION

A trade study was made of various alternative reaction control systems. These are categorized by the propellant used. The characteristics of the systems were evaluated in relation to the requirements of the Voyager mission. Reliability was felt to be by far the most important characteristic and it is predominantly because of reliability that the nitrogen cold gas system was chosen.

Other systems such as hydrazine certainly offer the prospect of significant weight savings. It is felt, however, that considerably more development and demonstration is needed with these systems before they become truly competitive. Selecting them at this time would entail an unjustifiable degree of risk.

2.2. PRELIMINARY SYSTEMS EVALUATION

The following systems were evaluated:

a. Cold Gas Systems
   - Freon - 14
   - Gaseous Nitrogen
   - Ammonia
   - Propane
   - Helium

b. Hot Gas Systems
   - Bipropellants. Nitrogen Tetroxide, Hydrazine
   - Monopropellants:
     - Hydrazine catalyzed thruster
     - Hydrazine gas generator system

c. Subliming Solids

d. Incremental Solids (cap pistol)

e. Ion and Plasma Jets

A number of these systems have obvious significant drawbacks and were, therefore, eliminated quickly. This elimination is summarized below.

a. Bipropellant Systems - These systems are the highest energy systems considered. However, the development status is limited to systems above 2 pounds of thrust, which is significantly higher than the requirement for Voyager. Reliability of bipropellant systems is lower than that of cold gas because the former require dual feed systems, positive propellant expulsion, and very small diameter orifices.

b. Monopropellant, Hydrogen Peroxide - Hydrogen Peroxide systems provide no performance advantage over hydrazine. Their added disadvantage of propellant instability, which causes long term decomposition, requires a pressure relief and phase separation venting for long-term storage.

c. Heated Gas Systems - In these, an inert propellant such as nitrogen is heated to increase its energy. Two methods of heating are generally considered;

1. Electrical heating is achieved by employing spacecraft power. During periods of excess supply such power is "free" and the heating is effective. At other times, additional power must be carried just for this purpose and little is gained. Excess power may be available during transit from earth to Mars when the spacecraft is stabilized to the sun. At other times, such as during maneuvers or in Mars orbit, the supply is limited to the demand. A review of table 1 reveals that only 100 lb-sec or 4 percent of the total impulse is used during periods of excess power when gas heating would be advantageous. Hence, even if half this amount is saved, only 2 percent of the gas weight or about 1.2 pounds is saved. This is hardly worth the added complexity.

Table 1. Total Impulse for Various Phases (lb-sec)*

	Pitch	Yaw	Roll	Total
Initial Stabilization	192	190	25	407
Maneuvers (3)	240	236	142	618
Orbit Insertion	79	79	47	205
Reacquisitions (2 Sun, 6 Canopus)	50	50	33	133
Limit Cycle				146
Before Capsule Separation	40	39	27	
After Capsule Separation	16	9	15	
Gravity Gradient	17	22	16	55
Orbit Trims (2)	110	100	56	266
Subtotal	744	725	361	1830
Fuel Slosh Effects 25 percent of Above (estimated)	190	180	90	460
Roll Control During Thrusting			100	100
Total	934	905	551	2390

*Moment Arm (Center of Mass to Jet) is 10 feet

Note: The conditions used in determining these impulses are summarized in Section VOY-D-321, Attitude Control Subsystem

2. Radioisotope heating is achieved by placing the isotope at the thrusting nozzle. Although such a system could provide heat, and therefore an increase of gas specific impulse during all mission phases, it has two classes of limitations precluding its use on Voyager. These are:

   (a) Safety Considerations:

   - Personnel radiation exposure during prelaunch operations.
   - Isotope contamination and recovery in event of mission abort.

   (b) Science Instrument Interference:

   - The following listed instruments are radiation detecting devices that could experience interference with the radioisotope thrusters:
     - Gamma ray spectrometer
     - Trapped radiation detector
     - Ion Chamber
     - Cosmic Ray Telescope
     - Plasma Probe

d. Incremental Solids - These systems are under development by USAF Rocket Propulsion Laboratory. Current laboratory models show that these systems may be heavier than cold nitrogen systems for the required impulses.

e. Ion and Plasma Engines - These systems, although providing high specific impulse, are limited to micropound thrust applications.

f. Subliming Solids - These systems are designed for micropound thrust operation and low duty cycle. Higher average impulse demands will require significant heat addition to maintain sublimation (10 watts per millipound).

g. Helium Stored Gas System - The helium systems, although providing a high specific impulse (172 sec), are approximately 20 percent heavier than nitrogen systems. This is a result of a low bulk density which requires large and consequently heavy tankage.

2.3. DETAILED EVALUATION

The following systems are potentially attractive and were investigated in some detail:

a. Stored cold gas systems; Nitrogen, Freon

b. Vaporizing liquid systems: Ammonia, Propane

c. Hydrazine Systems: Catalyzed Thrusters, Gas Generator

These systems are shown in schematic form in Figures 1 and 2.

2.3.1. Weight

Figure 3 shows the weights of the systems studied as a function of the total impulse stored. Table 1 indicates that about 2400 lb-sec are required to perform a nominal mission. To

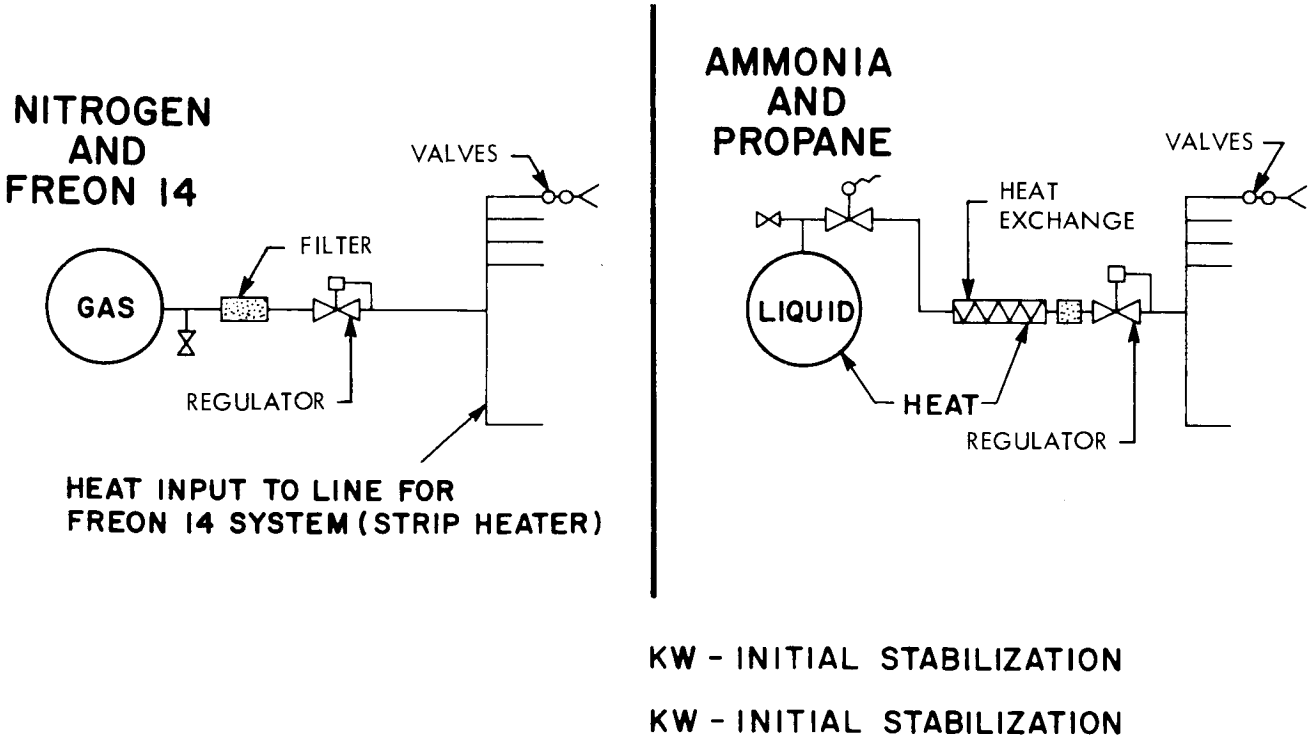

Figure 1. Cold Gas Systems

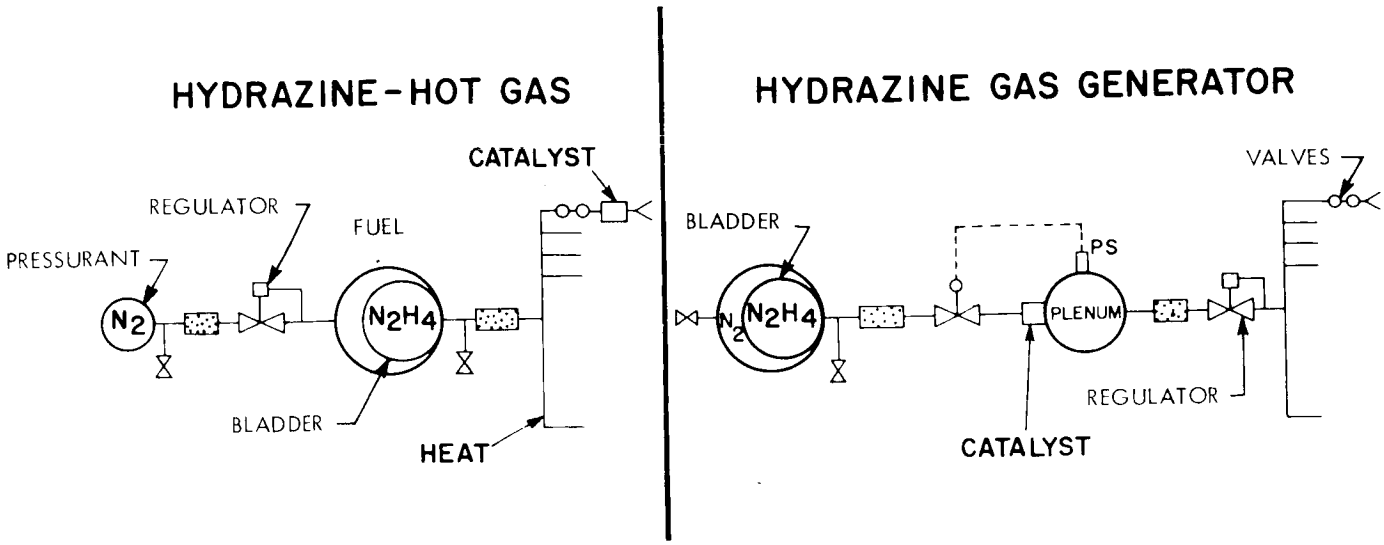

Figure 2. Decomposition System

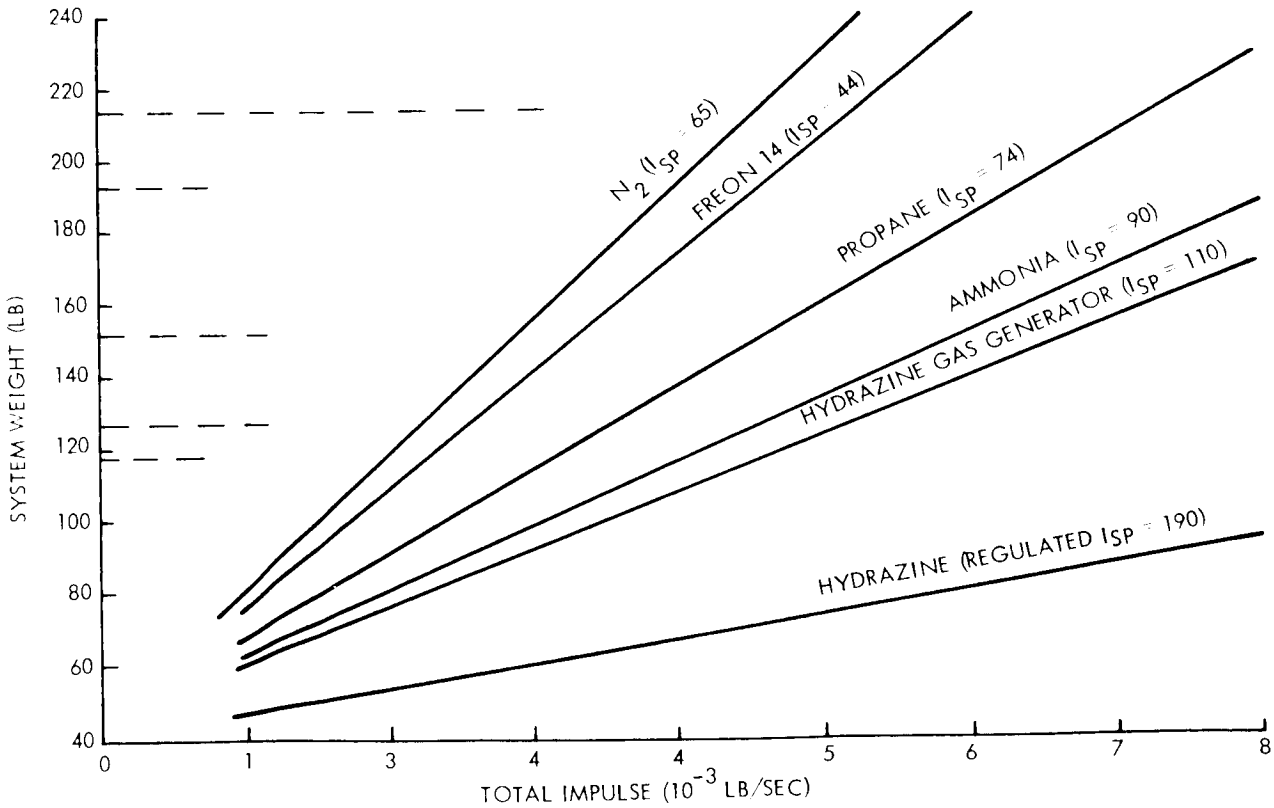

Figure 3. Reaction Control System Weights

provide redundancy the amount of gas carried will be increased. As demonstrated in 2.4 a reasonable level of redundancy is provided by about 4000 lb/sec. Hence, a nitrogen system which is the heaviest, will weigh from 135 pounds to 190 pounds, depending on the gas redundancy desired. A hydrazine system on the other hand weighs from 55 pounds to 65 pounds for the same redundancy. The other systems evaluated fall between these two extremes. Selecting a hydrazine system would result in about a 100-pound weight saving, which is certainly attractive. When viewed as a percentage of total dry spacecraft weight, however, it represents only 2 percent. It was decided to pay this weight penalty for the proven reliability which a nitrogen system is felt to offer.

A compromise approach of selecting one of the intermediate systems was not believed warranted since their state of development is less advanced than that of hydrazine systems. The only exception to this is freon, which is as simple as a nitrogen system and has been flight proven. Its weight advantage though not as great as the other candidates may nevertheless be desirable. It was not chosen for the following reason. In the Voyager configuration the nozzles, valves and lines of the reaction system are at the extremes of the fixed solar array. During periods of solar eclipse in Mars orbit these equipments and the propellant in them will become very cold.

Since freon is a vapor, it may condense. This will result in wastage of propellants. Other effects may also result but are not as well understood. This condition can, of course, be prevented by using heaters but this complicates the system slightly. A detailed study of operation in eclipse may reveal acceptable performance. In this case freon would be chosen and would yield a 20-pound savings in a 4000 lb-sec impulse system.

The weight of the hydrazine system is based on an average specific impulse of 190 seconds. This value may be questionable in pulsed mode operation and at the low (fractional pound) thrust levels required. Figure 4 shows the expected performance of a pulsed hydrazine system. This figure shows that the specific impulse is reduced to 70 seconds for very infrequent short pulses such as exist during transit or in orbit limit cycling. Table 1 shows

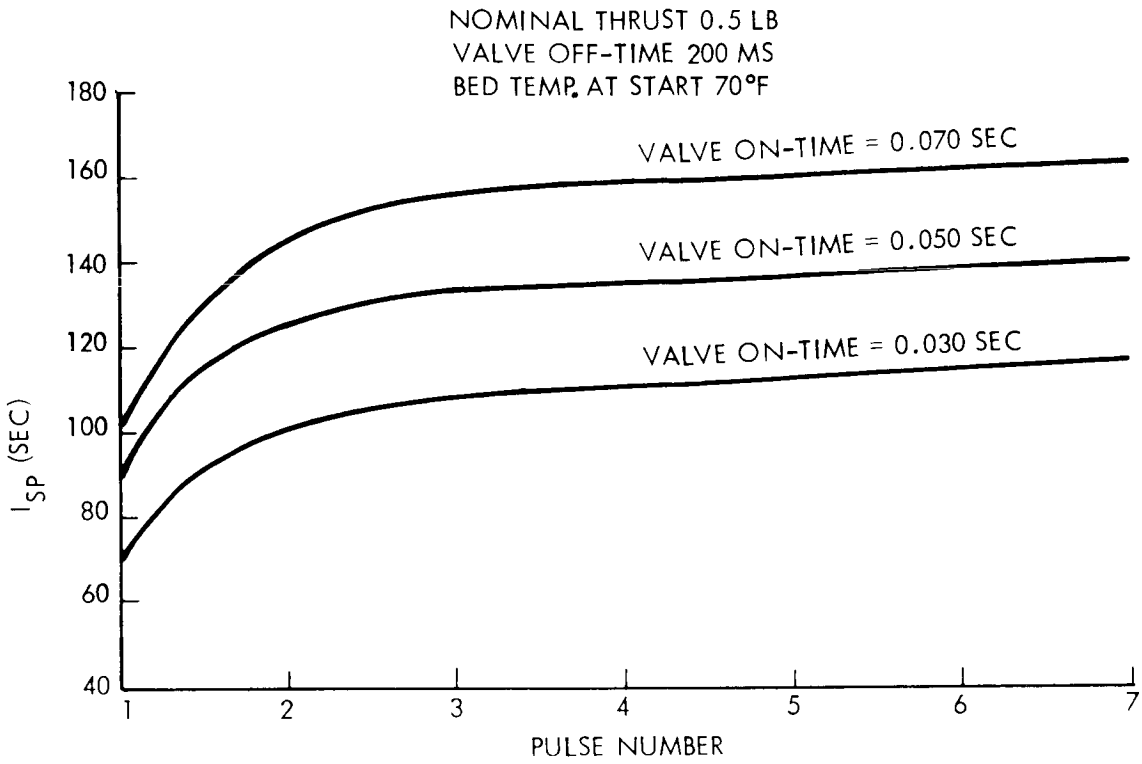

Figure 4. Cyclic Operation Effect on Hydrazine Specific Impulse

that about 200 lb-sec or 8 percent of the impulse is used in this mode, while about 2200 lb-sec are used in other modes. For these other modes of operation the on-time exceeds one second so that the steady state specific impulse value is achieved. Figure 4 implies that a continued increase in on-time will result in a continued increase in specific impulse. Such an increase would be expected until a value somewhat below the theoretical value is reached. The steady state value was assumed to be 210 seconds. Using these values, the average specific impulse for the mission was found to be about 190 seconds.

There is little question that a specific impulse of 210 seconds or greater can be achieved with motors of one-pound thrust or greater. For motors of fractional pound thrust the performance figure is not as well established. Experimental data is scarce. Data which was available for the present study was all manufacturer-originated. Significant differences were noted in the claims made by the several suppliers. If the steady state performance were to be 180 lb-sec, the average specific impulse would be 168 lb-sec and the weight advantage of a hydrazine system would be significantly reduced.

Since the performance of hydrazine rockets at thrusts of a pound or more is high and has been demonstrated, the following question must be answered. Can the attitude control system operate with thrusters of one pound when requirements appear to call for thrust levels of 0.2 lb and less? This question is discussed in the next section.

2.3.2. Control System Compatibility

The control system demands that the reaction control system deliver a certain torque impulse to the spacecraft. This corresponds to a thrust level and response time requirement for the reaction control system.

Conservative design calls for low thrust levels, short pulses and sharp thrust rise times. To achieve the control system parameters described in VOY-D-321, the reaction control system must have the following general characteristics:

a. Time response: 30 milliseconds or less

b. Pulse shape: rectangular

c. Thrust level: 0.05 to 0.20 pounds depending on the inertia of the axis being torqued.

These values are easily achieved by all the systems which use the propellant in a cold form. These are the cold gas, the vapor and the gas generator systems. The hydrazine system which requires a chemical decomposition to occur at the time of thrust demand, cannot meet these requirements. It was of interest to determine if a control system could be designed employing a torquing system which violates these requirements.

Specifically, the effects of the relatively long rise and delay times of a thrust pulse in a low level hydrazine thruster on the attitude control system were studied.

Low level hydrazine gas systems produce thrust pulses with relatively long rise and decay times. A representative pulse is shown in figure 5. In nominal limit cycle operation, the

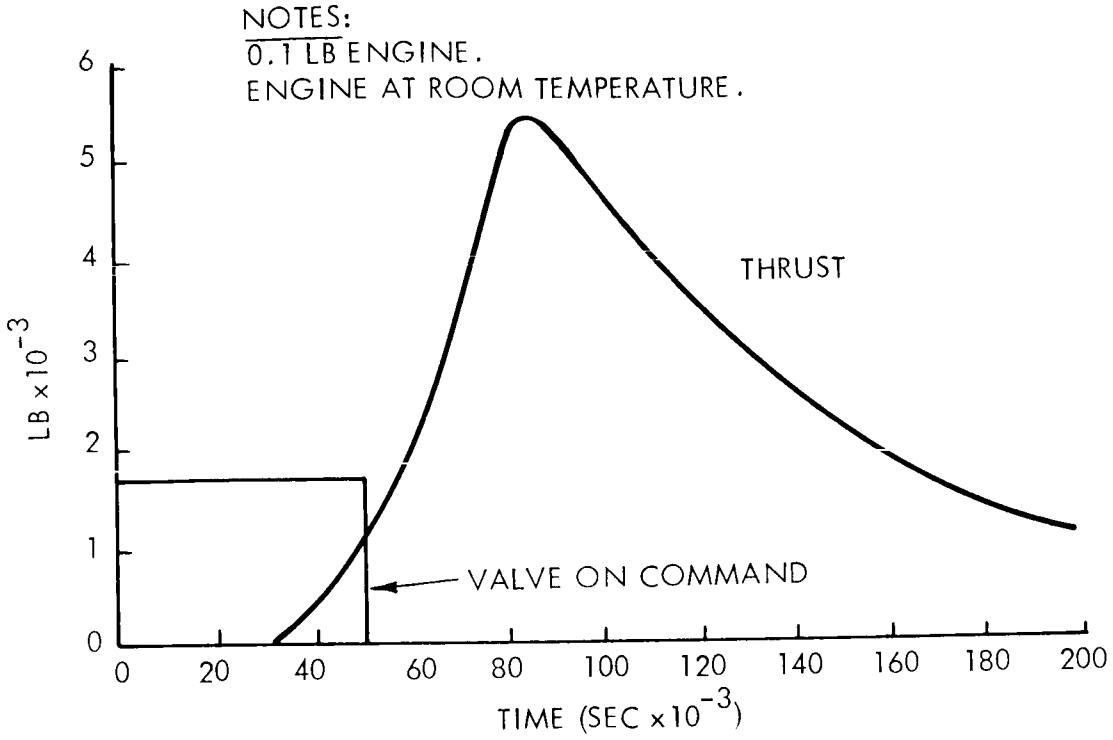

Figure 5. Hydrazine Engine Thrust Profile

important parameter is the impulse produced by the thruster. This is the integral of the thrust-time curve, and is not dependent upon the pulse shape. The delay in producing full thrust causes some deadband overshoot, but at the low limit cycle rate of Voyager (0.0002 deg/sec) this is insignificant. Furthermore, the long time duration between firings of a particular valve (2.5 hours) acts to minimize thrust variations caused by valve temperature changes.

It is difficult to perform an exact analysis of system performance. Phase plane analysis is greatly complicated if thrust is assumed to have an exponential rise or decay. This leads to equations of motion in which time appears explicitly. However, a good approximation which leads to conservative results for fuel consumption and system damping is to assume full thrust occurs after a pure time delay. The effect of the time delay is to change the slope of the switching lines on the phase plane in the destabilizing direction.

In the present system design, the reciprocal of the switching line slope is 9 seconds. The time delay is subtracted from this value. As long as the time delay is much less than 9 seconds, system performance should not be greatly affected. This is the case here where the time delay is estimated to be 0.2 seconds. Therefore, the hydrazine engine pulse shape appears to have no significant effect on the attitude control system performance. It must be recognized that this analysis is quite simplified. Before such a system could be recomended confidently, a more rigorous study must be performed. Non bang-bang systems are known to have been designed for operation on the transient portion of the thrust curve. It should also be noted that the performance must be reasonably repeatable. Since operation is on the transient, the repeatability is in question.

To avoid this transient and possibly non-repeatable operation, it is possible to place a lower limit on the thruster on-time. This would assure that steady state operation is reached and that the pulse is repeatable. Such an approach would yield considerably larger impulse bits than necessary during limit cycle operation. The limit cycle rate would increase and the period decrease for a given deadband. The ultimate effect is to increase net impulse requirements. The degree of increase is of course a function of the choice of thrust level and on-time. If demonstrated state-of-the-art equipment is used, such as one-pound thrusters with 50-millisecond on-times, the impulse increase results in the hydrazine system being significantly heavier than a nitrogen gas system.

2.3.3. Reliability

A comparison of the candidate design approaches relative to reliability potential must, at this time, be qualitative rather than quantitative. For some of the approaches, such as the approach using hydrazine as a monopropellant, there is not yet sufficient realistic experience to justify assignment of even approximate values to the failure rates needed for quantitative comparison. In fact, a quantitative comparison can be dangerously misleading unless the failure data are numerous and strictly comparable.

The systems are then evaluated by considering their physical characteristics, complexity, development status and experience.

a. System Experience and Development Status - One of the most significant factors in the reliability prediction of a system is the development status and experience with the system. The nitrogen and freon 14 stored cold gas systems are the most highly developed. These cold gas systems have been extensively used and consequently have a large history of quantitative data that can be used for estimating system reliability. Particularly pertinent is the very favorable experience on Nimbus, Mariner, Ranger and numerous military programs.

   Hydrazine rocket systems at low thrust levels have undergone rapid development over the past several years, but are still in the developmental or experimental stages. At thrust levels above one pound, which are believed too high, more experience exists, but even here it is much sparser than with cold gas systems.

   The hydrazine gas generator systems and the vapor systems are also in early stages of development.

b. Complexity and Physical Characteristics - The systems being evaluated were shown schematically in figures 1 and 2. These reveal that the difference in complexity between the systems is not extreme. Nevertheless, increased complexity, no matter how small, is believed undesirable when high demands for reliable performance are made. In addition to the equipment needed by the nitrogen system, the ammonia or propane systems require a heat exchanger and significant heat input. The hydrazine systems on the other hand require, in addition to a pressurant system, a propellant tank with expulsion bladder, and catalyzing decomposition beds.

   Unlike the cold gas systems, the hydrazine systems have two unfavorable characteristics. The first is the temperature cycling which is inherent. Temperature cycling through stressing of materials is a potential cause of failures. It is recognized that large cycling operations have been demonstrated on hydrazine systems. The significant point however is that cold gas systems do not have to undergo this cycling. The second point concerns the small orifice size required in hydrazine rockets of fractional pound thrust. The size of these vary depending on the specific design. Typically, they can be about 0.007 inch diameter. The smallest orifice in a nitrogen system is about 0.025 inch diameter. The areas therefore differ by about an order of magnitude. The small orifices in hydrazine systems are much more likely to change in dimension than those of the gas systems.

2.3.4. Quarantine

A complete assay of propulsion systems biological contamination potential was conducted during the General Electric Task C effort, and was reported in detail in Phase 1A Task C Final Report, Volume III, Planetary Quarantine Study. The investigation evaluated the ejecta of nitrogen cold gas, hydrazine and bipropellant systems. From the knowledge gained in the planetary quarantine program, all the candidate systems, with the exception of propane, could be decontaminated to the extent suitable to meet planetary quarantine requirements. The propane system, being a hydrocarbon, may be conducive to support of bacterial growth, and therefore would need to be evaluated before known techniques could be applied to maintain the system within quarantine boundaries. Of all the systems tested, the catalyzed hydrazine thruster system provided the least probability of ejecting viable organisms since it is sporicidal. The cold stored nitrogen systems, under current assembly and cleaning techniques, is marginal in meeting the quarantine constraints. Several techniques are available for reducing this potential biological load to acceptable levels:

a. Reduce the total amount of gas in tanks that is carried into orbit. By placing emphasis on design against leakages, both slow and sudden, less gas need be carried which eventually is released in orbit. For example, in the Task A and B designs, two separate tank systems were employed such that each half of the three couples was supplied with gas from a separate gas tank system. Then if a valve were to remain open, one tank system would be drained, but the other would lose only the gas required to overcome half the disturbance caused by the leak since the other half of the corrective impulse would be provided by the operable valve fed from the "leaky tank system." The tanks were loaded such that after a leak occurred enough gas remained in the healthy tank to complete the mission. Total gas carried to satisfy this concept was three times the nominal mission requirements. Now if a leak did not occur early in the mission, about 3/4 of the nominal mission impulse would be used prior to orbit insertion, and about 2-1/4 times would be carried into orbit. Over a period of time, this gas would leave the tanks through usage or leakage. By employing techniques such as series valves to reduce the leakage probability, only the nominal mission impulse (plus small safety factor), rather than three times need be carried. In this case, only about 1/9 of the nominal initial gas would be carried into orbit, reducing significantly the biological load. Reliability considerations, however, call for a compromise. The choice of how much gas to carry is discussed in paragraph 2.4.

b. Filters may be employed. To be effective, however, these must filter particles less than 5 microns, probably 3 microns would be satisfactory. No experience is known to exist with filters of this fineness in cold gas systems. Moreover, to prevent filter clogging, the entire system must be cleaned down to this level. This in itself is a task of major magnitude. There have been attempts to build gas jet systems which are clean to 5 microns, but the success of these endeavors is yet to be proven. Though filters can alleviate the biological problem in principle, the method is anything but state-of-the-art.

c. A nitrogen reaction control system can be purged with sporicidal material. Certainly, ethylene oxide would more than adequately reduce the bioload, but its effect on materials may be undesirable. Other less drastic agents, such as isopropyl-alcohol appear adequate.

d. Sterilization can, of course, reduce all biological load. The ease of sterilizing the gas jet system is a function of its assembly design and tank weight penalty. For example, the assemblies chosen for Task A and B studies did not lend themselves to sterilization. The modular assembly chosen for the present system on the other hand is most amenable to sterilization.

2.3.5. Power

The systems were also evaluated on the basis of electrical power demands. All systems require power for operating valves. Although this may amount to 24 watts depending on how many valves are operated, the on-pulses are of short duration so that energy usage is low. The nitrogen and hydrazine systems require no other power. The vaporizing liquid systems need additional energy for vaporization. During sun-Canopus stabilized cruise mode, impulse rate requirement is low, and heat of vaporization may be provided adequately from spacecraft waste heat dissipated in electronics. During peak demands this waste is inadequate and additional heat must be provided through electrical heaters. Since these peak demands occur when the spacecraft is not stabilized to the sun, the energy must come from batteries. Because the battery system is designed for these periods, any additional requirements imposed for vaporization is a net addition. This penalty is estimated to be 5 pounds of battery for the ammonia system and 3 pounds for the propane system. These weights are included in the system weights given.

Finally, some small level of heat, about 5 watts, is required at times to insure that propellants do not liquify or freeze in the lines. In the nitrogen system this is not mandatory, but keeping the temperature above the dew point is desirable. In the vapor systems, liquification can occur. The effect of this event has not been fully evaluated, but is felt to be undesirable. As a minimum effect, liquid will be expelled. In the case of hydrazine, which has a high freezing point, line heating is mandatory to prevent clogging the lines with frozen hydrazine.

2.3.6. Growth Capability

The systems were compared from the standpoint of their ability to support a Voyager mission growth. The higher energy systems such as hydrazine would appear to have a significant edge over the cold gas systems. This, however, is not the case.

Growth in a Voyager mission generally means an extension of the orbit operations beyond the initially planned six months. This will not require a significant increase in the number of maneuvers. In fact, it is rather unlikely that the total maneuvers will increase at all. Impulse demands in an extended mission are then predominantly for limit cycle operation and gravity gradient disturbance. The rate of pulsing is low and the specific impulse of hydrazine, as shown in Figure 4, is essentially that of nitrogen.

2.4. GAS STORAGE REDUNDANCY

Quarantine constraints and system weight allocations require that the reaction control gas weight be kept to a minimum. Maximizing the probability of mission success requires that sufficient gas be carried to cope with a reasonable number of failures. The selection of a compromise value is described in this section.

The first step is to provide series solenoid valves at each nozzle. For a tank system to develop a catastrophic leak then requires a double failure at a single nozzle. In addition to this, each thruster of a couple is supplied from an independent tank as shown in Figure 6.

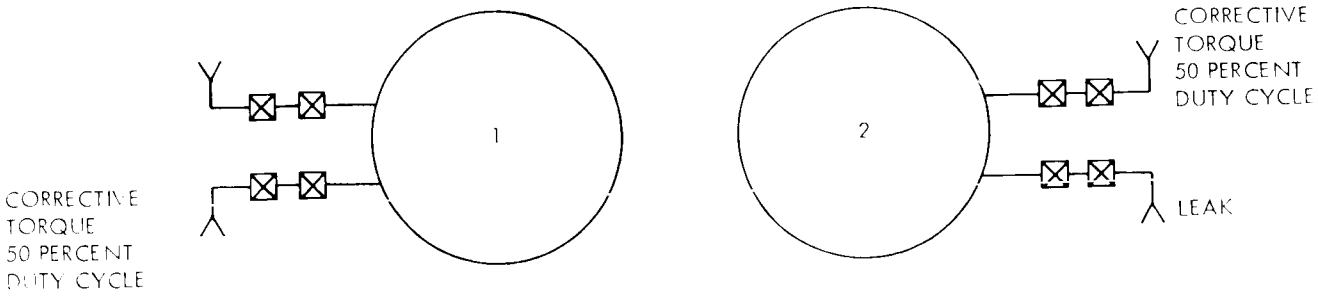

Figure 6. Independent Tank System

This figure also demonstrates the effect of a leak at one nozzle. As a result of a leak, tank 2 is completely depeleted while tank 1 loses one-third of its gas. The remaining gas in tank 1 is available for the continuation of the mission. It is desirable to size the system such that the remaining gas is sufficient to complete a reasonable mission.

Figure 7 shows the profile of the impulse usage in the pitch axis. The mission is started with the nominal impulse requirement, one-half of which is stored in each tank. The upper line shows the nominal mission while the lower line the effect of a leak. The loss of gas is assumed to occur soon after the first midcourse maneuver. As can be seen, enough impulse remains to perform a second midcourse maneuver and the transit phase but not enough to perform the orbit insertion maneuver. If the leak were to occur prior to the first maneuver, then the mission would be shortened even further. It is concluded that storing just the nominal impulse is inadequate.

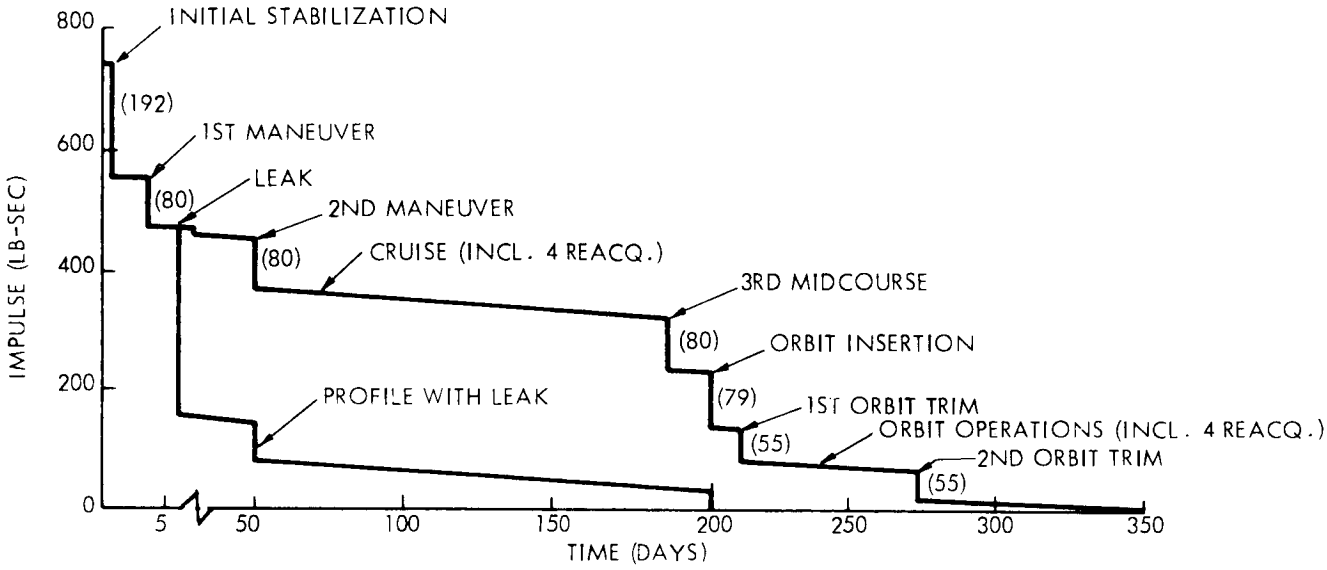

Figure 7. Profile of Pitch Impulse Usage (Nominal Charge)

Figure 8 illustrates an alternate plan. The total gas stored was increased from 37 pounds to 60 pounds. Apportioning this to each axis provided pitch with 1350 lb-sec at start of mission. The leak was assumed to occur after initial stabilization but before any maneuver. Even with a leak occurring as early as this, an attractive mission can be accomplished: two midcourse maneuvers, orbit insertion, one orbit trim and over three months of orbiting. If the leak had occured later, mission capability would be reduced by even a lesser degree.

It should be pointed out that the impulse requirements listed in Table I are conservative. In performing the calculations worst case conditions were assumed to exist at each maneuver. Since this is not likely, the more probable situation will yield a more favorable impulse profile than shown in Figure 8.

It has therefore been decided to carry 60 pounds of nitrogen gas for control requirements.

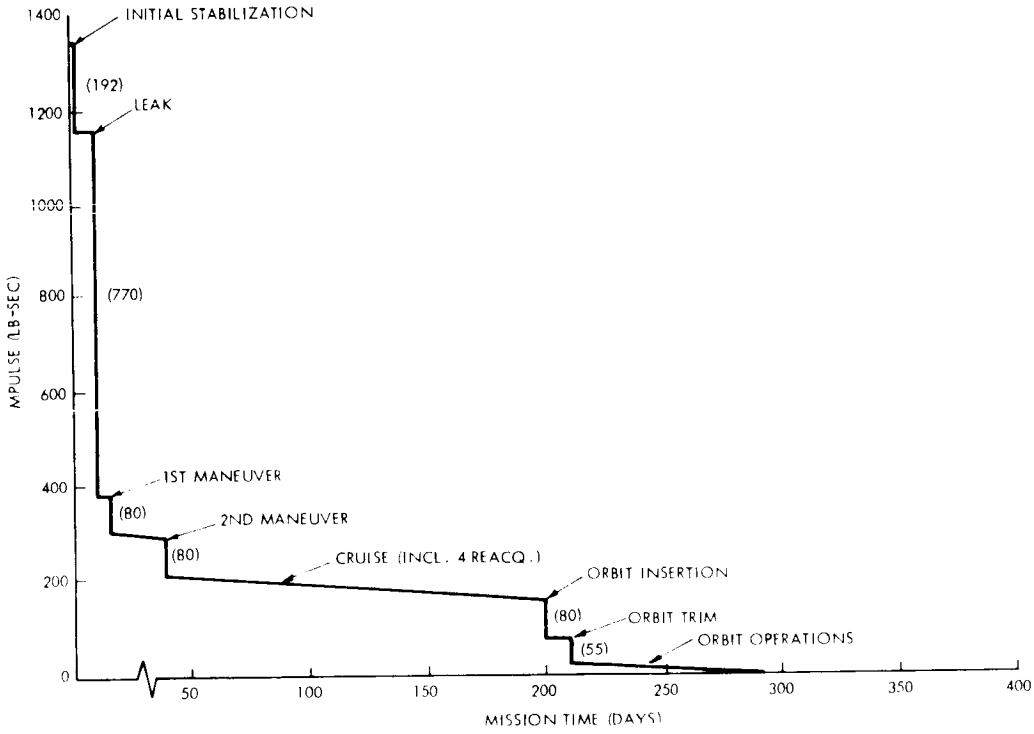

Figure 8. Profile of Pitch Impulse Usage (Assuming Leak) - Alternate Gas Charge

3. FUNCTION DESCRIPTION

3.1. SYSTEM DESCRIPTION

The Reaction Control Subsystem consists of four functionally identical but separate gas systems, each constructed in a modular form. The subsystem supplies two levels of thrust to the spacecraft on 10 foot moment arms. The generated torques maintain a nearly constant angular acceleration of the spacecraft under all mass conditions.

Thrust Levels	High Thrust	Low Thrust
Pitch	0.20	0.075
Yaw	0.20	0.045
Roll	0.15	0.08

The gas distribution for the modules are as follows:

a. Two modules, each containing 12 pounds of gas for pitch and low thrust roll functions.

b. Two modules, each containing 18 pounds of gas for yaw and high thrust roll functions.

The total gas quantity is 60 pounds.

The typical modular system schematic is shown in Figure 9.

Pure couples are generated by the thrusters in all three axes. Each couple is produced by the activation of a pair of thrusters from complementary modules.

3.2. COMPONENT DESCRIPTION

A survey was made of the currently state-of-the-art components available in the industry. The study showed that hardware components for the selected system can be chosen from many generic types of flight-proven hardware.

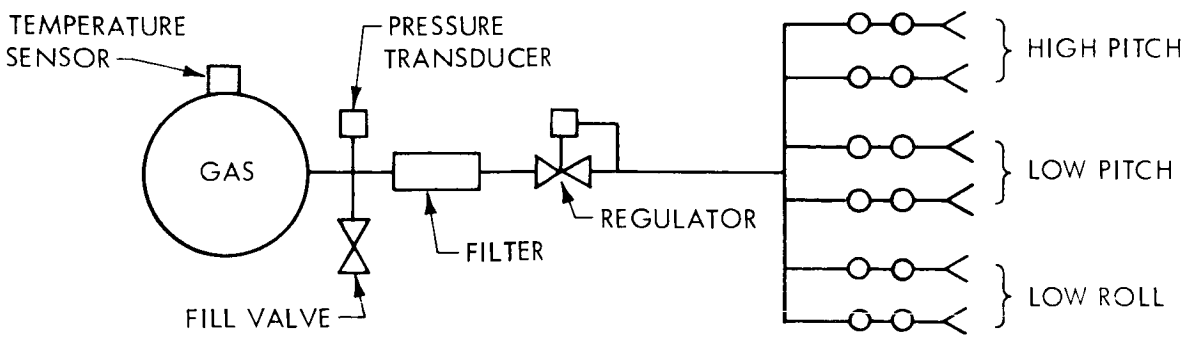

Figure 9. Typical Modular System Schematic

3.2.1. Gas Storage Tank

The gas storage tanks are to be made from 6A1-4V titanium in spherical configuration. The tanks will be for 3000 psi service, sized at $100^{o}F$, and will have a burst-to-operating-pressure ratio of 2.

3.2.2. Fill Valve

The fill and vent valve will contain a positive shutoff integral with a check valve. This unit will provide positive sealing with disconnect capability following charging.

3.2.3. Temperature Sensors

The sensor will incorporate a platinum resistance element.

3.2.4. Pressure Transducers

Pressure transducers will be of the potentiometer type.

3.2.5. Filters

A 10-micron filter is selected for this application. The filter will be a stacked disk type. These filters have the advantage of being completely cleanable with no media or entrapped manufacturing contamination to migrate during cyclic function or vibration environment.

3.2.6. Regulators

The selected regulator will be a single-stage spring-loaded unit with two control seats in series. The regulated output pressure will vary 1 psi for an inlet pressure variation from 3000 to 150 psi. The spring-loaded regulators were selected over pilot operated or dual-stage regulators because of simplicity, greater reliability and lower weight.

3.2.7. Relief Valves

The relief valve is a type that maintains nearly constant seat load up to the instant of opening. Anti-reaction fittings are used at the output to avoid torque generation should the relief valve open. The relief valve is set 100 percent above the regulated pressure to insure that pressure surges or temporary gas pressure rises will not break the valve seal. A filter and a burst disc protect the relief valve seat from contamination and leakage.

3.2.8. Solenoid Valves

The valves are of the direct-acting co-axial type.

3.2.9. Nozzles

The nozzles are made from titanium, having an area ratio of 100:1, with a 30-degree straight exit cone.

3.3. MANUFACTURING

3.3.1. Assembly

To minimize leakage potential, the hardware components are to be assembled into a system with welded joints. Each gas system is assembled into a compact self-contained module on a mounting platform which can be located and aligned in any one of the four prescribed locations on the spacecraft structure. Each component of the module will be tested separately, then assembled into the module. All environmental tests will be performed on the complete module. Repairs will not be made to modules on the spacecraft, instead a complete module change will be made. In this fashion, all disassembly and work can be done in a clean area. The system can be sealed and charged in this area.

3.3.2. Cleanliness

Foreign particles are a prime hazard to the successful performance of a cold gas system, and biological contamination presents the possibility of violating planetary quarantine constraints. To control contamination, care must be taken in every phase of manufacturing and assembly.

It was found that cleaning techniques provide low particulate contamination levels also result in low bacterial contamination. These processes include:

a. Disassembly of all components and ultrasonic cleaning in freon.

b. Purge with dry biofiltered (0.45 microns) nitrogen for particulate count.

c. Work "clean area" to conform to class 10,000 minimum.

d. Perform assembly and teardown of components on class 100 laminar flow benches.

e. System module assembly on class 100 laminar flow bench.

f. System pressurized with dry nitrogen through redundant 0.45 micron membrane filters adjacent to fill connector.

3.4. PHYSICAL CHARACTERISTICS

3.4.1. Weight

The total loaded gas subsystem will weigh approximately 188 lb without mounting structure or micrometeoroid shield. Structural weight and micrometeoroid shield would weigh approximately 5 and 4 pounds respectively, for each module, for a total weight of 36 pounds. System weight breakdown by component is as follows:

Component	Weight (lb)
gas weight	60.0
tank weight	84.0
hardware (tubing and fittings)	2.0
heaters	.5
fill valves (4)	1.0
temperature sensors (4)	1.0
pressure transducers (8)	4.0
filters (4)	1.0
pressure regulators (4)	8.0
solenoid valves (48)	24.0
nozzles (24)	2.4
	187.9

3.4.2. Power Consumption

The average power consumption is negligible. Peak power when three couples are commanded is 24 watts.

VOY-D-323
AUTOPILOT

AUTOPILOT

LIST OF SYMBOLS

Symbol	Definition	Units
A_X, A_y, A_Z	Inertial acceleration of reduced center of gravity measured along X, Y, Z axis.	ft. sec^2
F_x, F_y, F_Z	Forces along X, Y, Z axis	lb
I_{yy_o}, I_{xx_o}	Moments of inertia about a point on the vehicle centerline that is the instantaneous longitudinal center of mass when the engine angle is zero.	slug-ft^2
$I_{R_{yy}}, I_{R_{xx}}$	Moments of inertia of engine about gimbal	slug-ft^2
T_y, T_x	Torques about Y, X axis	ft-lb
L_{po_n}	Oxidizer pendulum length	ft
L_{pfn}	Fuel pendulum length	ft
ℓ_c	Distance along vehicle Z axis from reduced center of mass to engine gimbal	ft
ℓ_x	Distance of propellant tank center from vehicle centerline	ft
ℓ_o	Length from reduced center of mass to pendulum hinge point measured along the Z axis	ft
ℓ_R	Distance from engine gimbal to engine center of mass	ft
M_{po_n}	Oxidizer pendulum mass	slugs
M_{pf_n}	Fuel pendulum mass	slugs
M_o	Mass of vehicle excluding sloshing pendulum masses	slugs
M_R	Engine mass	slugs
M_T	Total mass of vehicle	slugs
$\dot{\theta}, \dot{\phi}$	Angular velocity of vehicle about Y, X axis	rad/sec

Symbol	Definition	Units
$\Delta X_o, \Delta Y_o$	Offset of M_o from vehicle center line in X and Y direction	ft
β_{on}	Oxidizer yaw pendulum angle	rad
β_{fn}	Fuel yaw pendulum angle	rad
Δ	Angular offset of engine center of mass from the engine centerline	rad
∇	Thrust misalignment angle from the engine centerline	rad
ξ	Yaw engine gimbal angle	rad
ϵ	Thrust offset	rad
ω_{on}	Oxidizer sloshing natural frequency	rad/sec
ω_{fn}	Fuel sloshing natural frequency	rad/sec
ζ_{on}	Oxidizer sloshing damping ratio	
ζ_{fn}	Fuel sloshing damping ratio	
F_c	Engine thrust	lb
Σ	Inertially referenced thrust pointing error	rad
δ	Damping factor, or logarithmic decrement	
V_R	Propellant fill ratio, or % propellant remaining	
η_g	Gyro noise power spectral density	deg^2/cps
$\Delta X, \Delta Z$	Offsets of M, the instantaneous center of total vehicle mass, from the vehicle centerline, in the X and Z directions.	ft
$(\ )_n$	denotes particular tank of oxidizer or fuel tank pair	ft

VOY-D-323
AUTOPILOT

1. INTRODUCTION

The autopilot is the spacecraft control system mode employed to hold a spacecraft inertial position during rocket engine thrusting. The system consists of body fixed rate integrating gyros, electronic signal processors and electromechanical rocket engine gimbal actuators.

The emphasis of the present study has been on stability analyses and the determination of required system parameters rather than on detailed equipment designs.

The basic autopilot system has been found through digital simulation to have completely adequate performance. The propellant tanks, however, must have some propellant slosh control, preferably ring baffles.

Use of the Lunar Module Descent Engine (LEMDE) propulsion system has associated with it some major vehicle-autopilot interactions compared to a rigid body vehicle. The uncertainty of the lateral center of mass position which is larger in a system containing liquid propellants than one with solids, combined with a short gimbal point to center of mass distance may dictate a pointing error loop which will aggravate the control system dynamics. The presence of large unrestrained liquid masses and their location aft of the rigid body mass center complicates the system dynamics. The gimballing of a large engine imposes response difficulties on an electromechanical actuator, and introduces the destabilizing "tail-wags-dog" effect. The use of a hydraulic gimbal actuator system has the disadvantage of potential leakage. The coupled roll disturbance torques may require additional higher level thrusters in the ACS system. The large lateral center of mass shift during orbit trim caused by PSP extension may be beyond the LEMDE gimballing capability, requiring either PSP retraction or auxiliary engines with greater control authority. These qualitatively discussed design problems are the subject of the autopilot analysis which has a primary goal of promoting simplicity and reliability.

The velocity magnitude control does not appear to have significantly changed in difficulty or complexity.

2. AUTOPILOT REQUIREMENTS

The thrust vector accuracy requirements are best expressed by Table 1 and Figure 1 (the allowable velocity magnitude error and allowable pointing error, respectively) as a function of velocity increment for the particular type maneuver.

Table 1. Allowable Velocity Magnitude Error (Meters/Sec)

Allowable Error	Requirement	Goal
3σ Error for 0.3 m/s ΔV Goal Midcourse	-	0.03 m/s
3σ Error for 1 m/s ΔV Midcourse	0.1 m/s	0.03 m/s
3σ Error for 200 m/s ΔV Midcourse	6.0 m/s	4.0 m/s
3σ Error for 2000 m/s Orbit Insertion	60 m/s	30 m/s
3σ Error for 1.5 m/s ΔV Orbit trim	0.5 m/s	0.2 m/s
3σ Error for 150 m/s ΔV Orbit trim	7.5 m/s	4.5 m/s

Section VOY-D-260 Trajectories and Guidance presents an error analysis for various contributions to pointing error during maneuvers. This budget indicates that the Autopilot contribution to thrust pointing uncertainty can be as large as 0.43 deg (3σ) per axis, for midcourse maneuvers, and as large as 1.08 deg (3σ) per axis for orbit insertion and orbit adjust. The terminal vehicle rates following engine shutdown must be within 1 deg/sec to be compatible with the ACS impulse capability. The autopilot must meet the above requirements in the presence of the following disturbance effects:

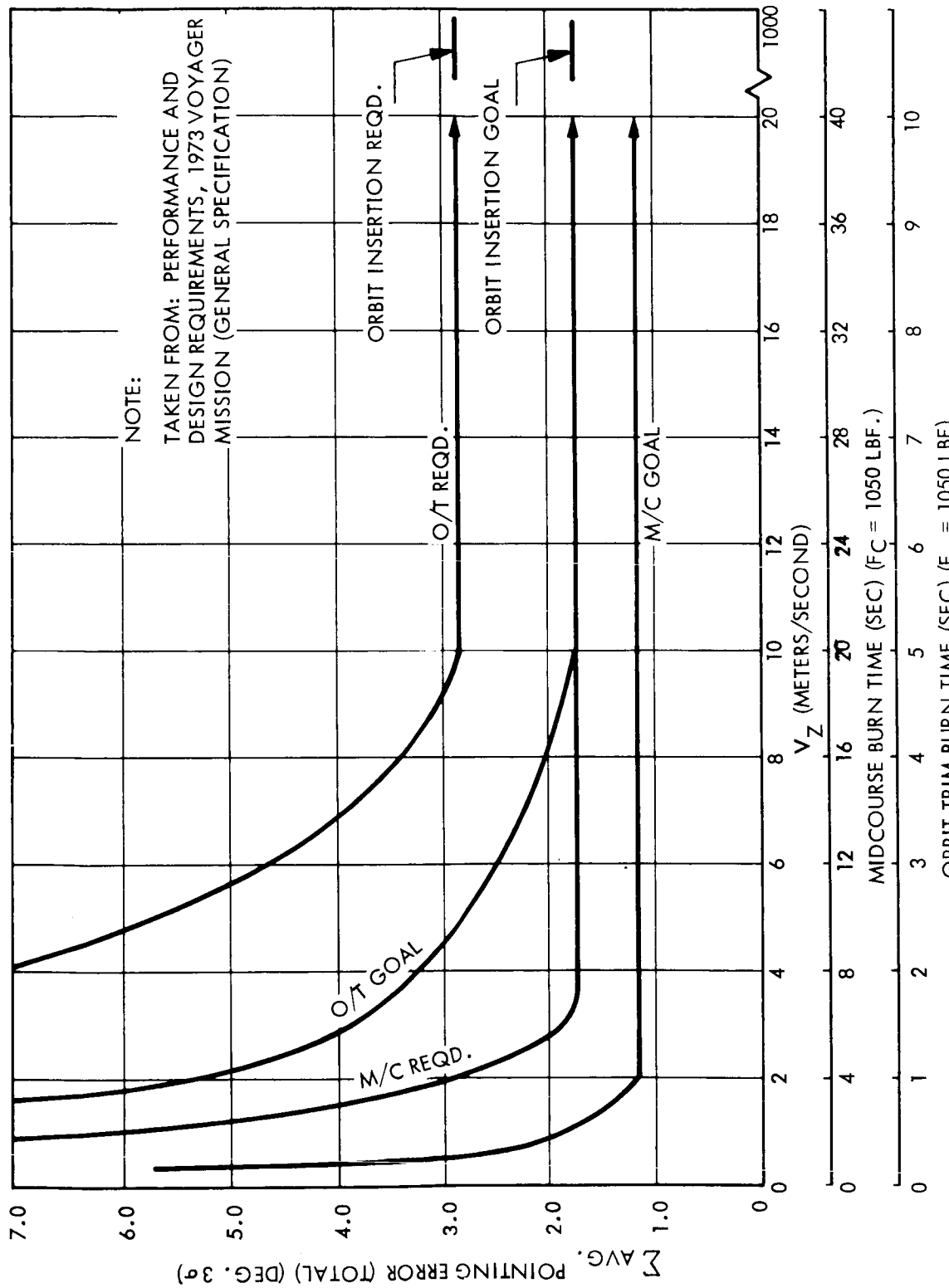

Figure 1. Total Thrust Vector Pointing Errors for Pitch or Yaw Axis

a. Thrust vector angular misalignment relative to the vehicle roll axis and thrust angular misalignment relative to the engine centerline, (∇), which is 0.30 deg (3σ).

b. Thrust vector lateral displacement from the vehicle center of total mass. This includes:

1. Lateral engine misalignment relative to the vehicle, and lateral thrust axis misalignment relative to the engine thrust centerline (ϵ), which is 0.125 inches.

2. The lateral displacement of the total vehicle center of mass is ΔX_T. This is comprised of a nominal value and an uncertainty. The uncertainty contributes fully to the pointing error. The angular error caused by the nominal portion of ΔX_T is corrected by modifying the maneuver rotations. Despite the correction, error results because of transients and gain dispersions. The magnitude of this error is estimated to be 40 percent of the correction. The root sum square combined displacement uncertainty is:

$$\left[(0.4\,\Delta X_T)^2 + (3\sigma\,\Delta X_T)^2 + \epsilon^2\right]^{1/2}$$

Using the moment arms of Table 2, these displacement uncertainties are converted to angular errors, δ, as follows:

Midcourse	Lateral Offset (in.)	Angle Offset (degrees)
Nominal	0.302	0.24
3σ Uncertainty, δ	0.214	0.16
Orbit Insertion, Capsule On		
Nominal	0.47	0.345
3σ Uncertainty, δ	0.615	0.45
Orbit Adjust, Capsule Off, PSP Stowed		
Nominal	0.74	0.93
3σ Uncertainty, δ	0.863	1.08
Orbit Adjust, Capsule Off		
PSP Deployed	5.4	6.8
Nominal		

The LEMDE gimballing capability is exceeded for the orbit adjust maneuver with the PSP deployed, requiring one or a combination of the following alternatives:

1. Large angle gimballed auxiliary thrusters.

2. Retraction of the PSP.

3. Increasing the gimballing capability of the LEMDE.

4. Using auxiliary thrusters in a pulsed or throttled mode.

c. Propellant sloshing effects will appear only in the transient behaviour of the system. Propellant unbalance between tanks, due to unequal flow rates or migration during the coast periods, will result in a thrust vector pointing error because of CM motion. The unbalance due to unequal flow rates from each of the pair of oxidizer and fuel tanks is nullified by interconnecting tank balance lines. These lines should be viewed with some care, since they result in a second order manometer system, the damping ratio of which should be no less than unity. The "propellant migration" through the tank balance lines will be negligible for "zero-g" cruise prior to midcourse and orbit insertion maneuvers. This is caused by the solar pressure resultant acceleration vector being along the roll axis, thereby keeping the propellant balanced in each tank pair. There may be some migration during the Mars orbiting phase depending on the relative magnitudes of the gravity gradient and solar pressure induced accelerations.

   This analysis was not performed in this study since the balance lines can be closed after the orbit insertion maneuver, thereby eliminating the problem; they do not appear necessary for the orbit adjust maneuver because of the reduced mass of remaining propellant. The propellant sloshing effect will be analyzed in the performance analysis section.

d. The roll disturbance torques are not completely defined because propellant slosh coupling requires a three-axis analysis. The roll attitude error is constrained by the earth-pointing antenna requirement to be no greater than ±10 degrees. The present ACS high-thrust control is felt to have adequate margin over the maximum rigid body vehicle roll disturbance occurring during the orbit insertion maneuver. Incorporation of gimballed auxiliary thrusters would be more than adequate.

3. SYSTEM STEADY STATE PERFORMANCE

The analysis of the autopilot performance is separated into its steady state and transient performance, including the propellant slosh effects. Assuming for now that the simple

autopilot configuration of TASK B will be adequate for acceptable transient performance, the steady state performance will be studied.

3.1 THRUST POINTING ERROR

Figure 2 is a simplified single-axis diagram of the Autopilot used in Task B for either the pitch or yaw axes. As in Task B, the thrust vector pointing is given by:

$$\Sigma = \xi + \nabla - \theta$$

with the sign conventions as shown in Figure 3.

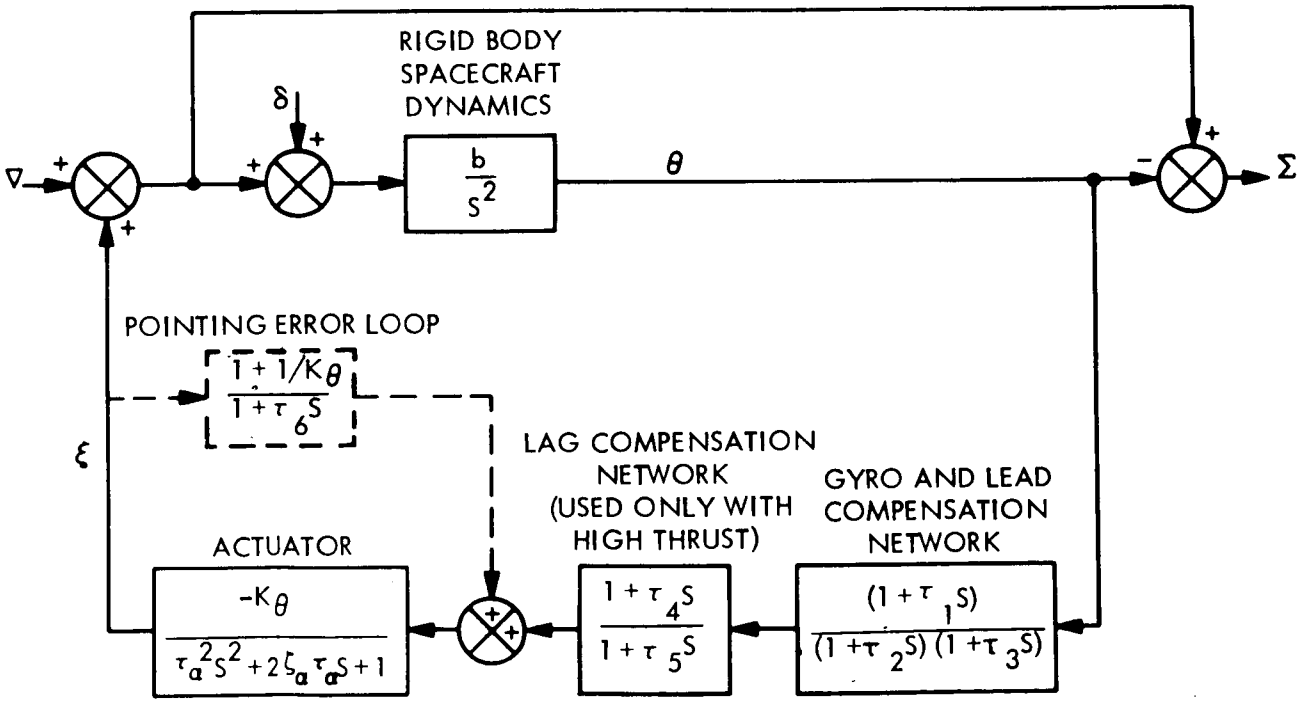

Figure 2. Autopilot Servo Diagram

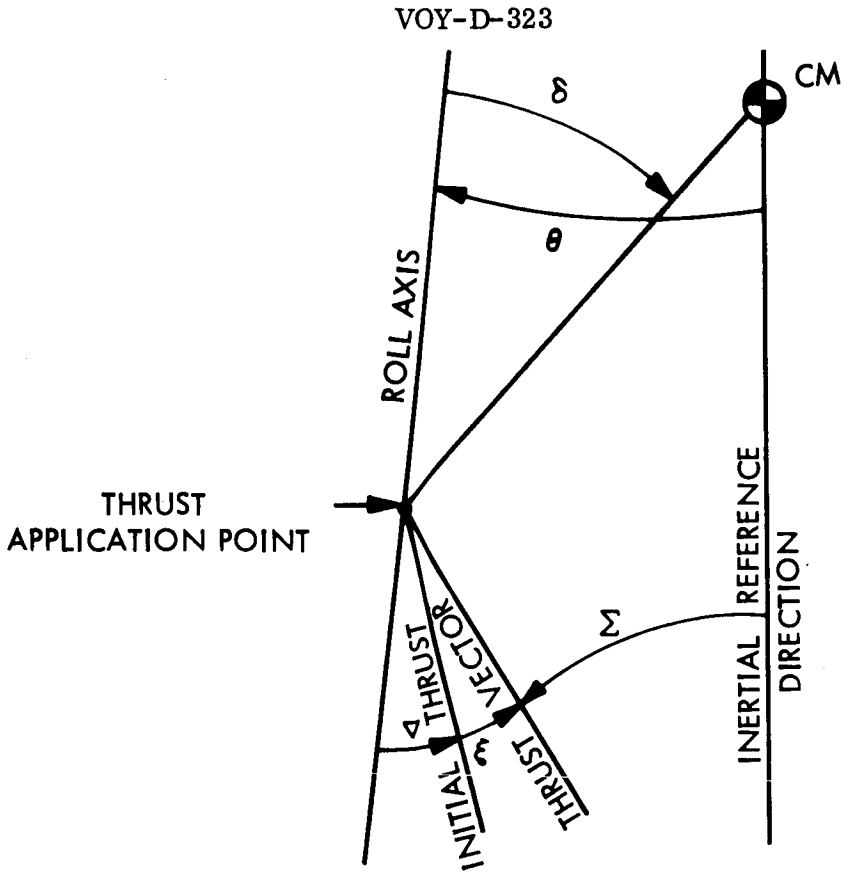

Figure 3. Autopilot Angular Relations

The angles are defined as follows:

Σ, is the thrust pointing error with respect to the inertial reference coordinate system.

θ, is the spacecraft attitude with respect to the inertial reference coordinate system.

ξ, is the angle through which the thrust vector is deflected, measured from its initial position (gimbal angle).

∇, is the thrust misalignment angle; i.e., the angle between the initial thrust vector position and the spacecraft roll axis.

δ, is the uncertainty component of angular offset of the spacecraft center of mass from the nominal thrusting axis. The steady-state error due to the corresponding predictable component is compensated for by appropriately modifying the commanded angular turns.

The feedback gain, K_θ, includes the dc gain of all the elements in the feedback loop; i.e., the gyro, compensation network, and actuator. The vehicle gain, b, is given in Table 2 for

Table 2. Vehicle Characteristics

MISSION PHASE	Total Mass Slug M_T	Pitch Or Yaw Inertia Total Rigid Slug/Ft^2 I_{yyo}	Total Body Control Arm ℓ_T Ft.	Slosh Pendulum Length L_p Ft.	Axial Distance From Rigid C-M To Slosh Pendulum Hinge Pt. ℓ_o Ft.	Total Body Vehicle Gain Factor, b $\frac{F_c \ell_T}{I_{yyo}}$ sec^{-2}
Before Orbit Insertion Capsule On	620	18300	6.0	0.7	-1.7	0.35 LoF_c 3.3 HiF_c
Before Orbit Insertion Capsule Off	460	5700	4.0	0.7	0.3	0.74 LoF_c 6.9
Midway Through Orbit Insertion Capsule On	490	14800	6.5	1.3	-3.2	5.0 HiF_c
Midway Through Orbit Insertion Capsule Off	354	5000	3.9	1.3	0.3	7.9 HiF_c
After Orbit Insertion Capsule On	385	15300	7.1	1.8	-2.8	4.6 HiF_c 0.49 LoF_c
After Orbit Insertion Capsule Off	250	3800	3.8	1.8	0.5	9.85 HiF_c 1.2 LoF_c

the various phases of the mission. There may be some minor discrepancies between these mass properties and those of section VOY-D-220, Spacecraft Configuration; these are not significant enough to affect the autopilot system analysis. The steady state pointing error equation of the current design is identical to the Task B expression, or:

$$\Sigma_{ss} = -\delta - \left(\frac{\delta+\nabla}{K_\theta}\right)$$

where δ is the equivalent angular offset uncertainty of the total center of vehicle mass. This uncertainty is greater in a spacecraft employing a liquid propulsion system than one employing a solid.

As before the steady state pointing error is acceptable if K_θ is greater than about 2 for all maneuvers. However, there being no great difficulty in having a higher feedback gain ($K_\theta \cong 5$), the 3σ steady state pointing errors are estimated to be:

Midcourse:	0.25 deg. (0.0044 rad)
Orbit Insertion, Capsule On:	0.60 deg. (0.0105 rad)
Orbit Trim-Capsule Off:	1.36 deg. (0.0241 rad)

For small ΔV maneuvers, the steady state pointing error may never be attained. The pointing error for these cases is studied in the transient analysis section.

The known lateral displacement error, ΔX_T, will be compensated for by modifying the commanded angular turns so that the combination of commanded angles and the steady state thrust pointing offset, yields the desired pointing direction in inertial space. The steady state pointing errors, as estimated, do meet the requirement, but if the uncertainty in the vehicle center of mass becomes greater, the alternative system configuration, incorporating a pointing error loop may be required as shown dashed in Figure 2. This "c-m bias" compensation loop has some significant disadvantages, as detailed in Task B:

a. It cannot be tested in combination with the gimbal actuator servo loop since it results in an unstable system.

b. The pointing error is very sensitive to the pointing error loop gain, $1 + 1/K\theta$, thereby degrading the system reliability.

c. The vehicle transient performance is aggravated by the addition of this loop.

3.2 VELOCITY MAGNITUDE CONTROL

The autopilot must control the magnitude of velocity increment to within 3 percent (3σ) or 0.1 meters/second (3σ), whichever is larger for midcourse maneuver ΔV's ranging from 1 meter/sec to 100 meters/sec.* The requirements for orbit insertion and orbit trim maneuvers are listed in Table 3. To attain this accuracy, a roll axis accelerometer and integrator are used to control engine on-time. The integration is performed by the accelerometer generating a pulse for every 0.01 ft/sec of ΔV; the Controller and Sequencer (C&S) counts these pulses and compares the sum to a preloaded desired ΔV. When the desired velocity is attained, the C&S commands engine shutdown. A timer circuit will be used as a backup to the accelerometer and integrator. In the case of auxiliary thrusters for the smaller ΔV maneuvers, the backup timer time-to-go (TTG) register counting rate can be changed in the event of a pair-out situation, thereby keeping the cutoff backup signal valid. Sources of error in the accelerometer technique of engine shutdown are:

a. Engine uncertainties

   1. Uncertainties in the delay between a shutdown command and actual valve closure.

   2. Engine tail-off dispersion, i.e., deviation from the nominal thrust vector decay profile.

These uncertainties, determined by static test firing, are 155 lb-sec for high thrust, and 25 lb-sec for low thrust.

*Table 3.3.3-1, "Performance and Design Requirements for the 1973 Voyager Mission, General Specification for, Jan. 1, 1967, Jet Propulsion Laboratory.

Table 3. Thrust Termination Errors (meters/second)

Error	Predicted	Requirement	Goal
Minimum ΔV 3σ Error Midcourse	0.04 m/s	0.1 m/s	0.03 m/s
3σ Error for 1 m/s ΔV Midcourse	0.04 m/s	0.1 m/s	0.03 m/s
3σ Error for 200 m/s ΔV Midcourse	0.6 m/s or 0.3%	6.0 m/s	4.0 m/s
3σ Error for 2000 m/s Orbit Insertion	6.1 m/s or 0.3%	60 m/s	30 m/s
Minimum ΔV 3σ Error Orbit trim	0.05 m/s	0.5 m/s	0.2 m/s
3σ Error for 1.5 m/s ΔV Orbit trim	0.051 m/s	0.5 m/s	0.2 m/s
3σ Error for 150 m/s ΔV Orbit trim	0.46 m/s or 0.3%	7.5 m/s	4.5 m/s

b. Accelerometer - integrator uncertainties [(significant contributors only)] (3σ):

1. Accelerometer scale factor error (9×10^{-5}) (g) (t)
2. Integrator error (3×10^{-5}) (g) (t)
3. Integrator bias ($0.003 \Delta V$)
4. Integration granularity (0.0009) meters/sec)

Where:

g is the acceleration level in g's

t is the engine on-time in seconds

Errors in termination of the thrust are root-sum-squared with the velocimeter errors. In the values listed in Table 3 the LEMDE high thrust was used only for the orbit insertion maneuver.

In summary, the LEMDE with the two-thrust mode capability adequately meets the velocity magnitude control requirements.

4. DYNAMIC MODEL DEFINITION

The mathematical model used to describe the vehicle dynamics is defined by the equations in Appendix A with the coordinates and sign conventions of Figure 4. It incorporates three degrees of vehicle freedeom (1 rotation, 2 translation), propellant sloshing in the four tanks, and engine inertial (tail-wags-dog) effect. The propellant sloshing is treated by the well known pendulum analogy, to duplicate the forces and moments produced by the first slosh modes in each tank.

The normally used slosh pendulum has been expanded to large angles in order to bound the initial thrust transient; the zero-g propellant motion work indicates that the vehicle will slew about the propellant slosh mass. Since the initial sloshing mass position may be predictable due to solar pressure exerted acceleration, the angular position from the roll axis will be determined by the maneuver rotations. Even if the above argument is not correct, the initial slosh mass angular position will probably not be along the thrust vector axis at maneuver commencement. It is recognized that the pendulum analogy is most precise for small angles, $\lesssim 15$ degrees. Also at the time of thrust commencement, the propellant surface tends to be concave spherical. If the initial pendulum angle is large breakup of the liquid surface will occur. Much of the propellant potential energy is expected to be dissipated in the ensuing turbulence. Restricting the study to initial pendulum angles of 30 degrees which reduces non-linearities, and keeping the sloshing mass concentrated at the pendulum bob, a conservative result should be obtained. It is the intent in additional work to introduce amplitude dependent damping and sloshing mass, in order to improve the model.

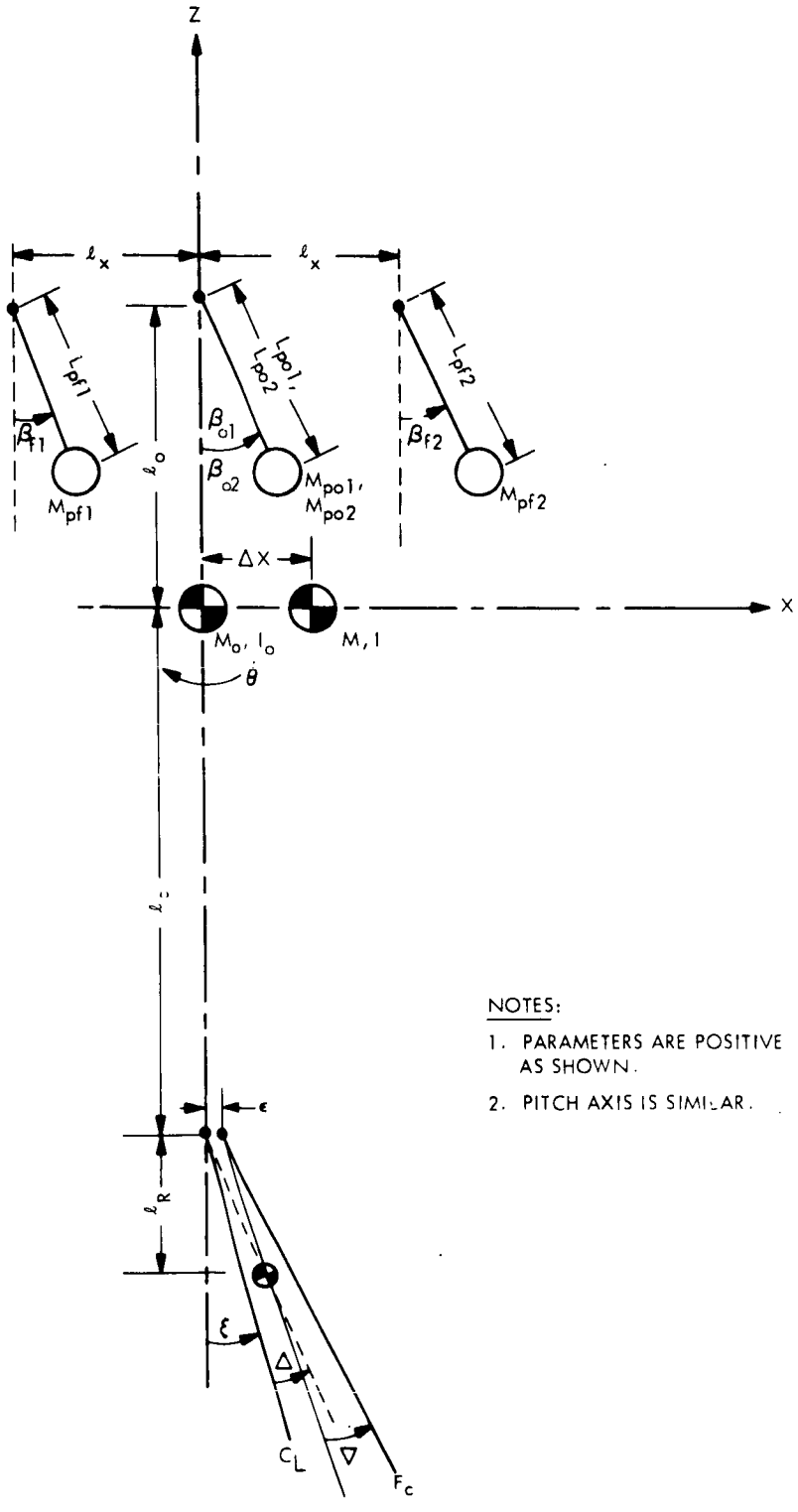

Figure 4. Yaw Axis Vehicle Coordinate System

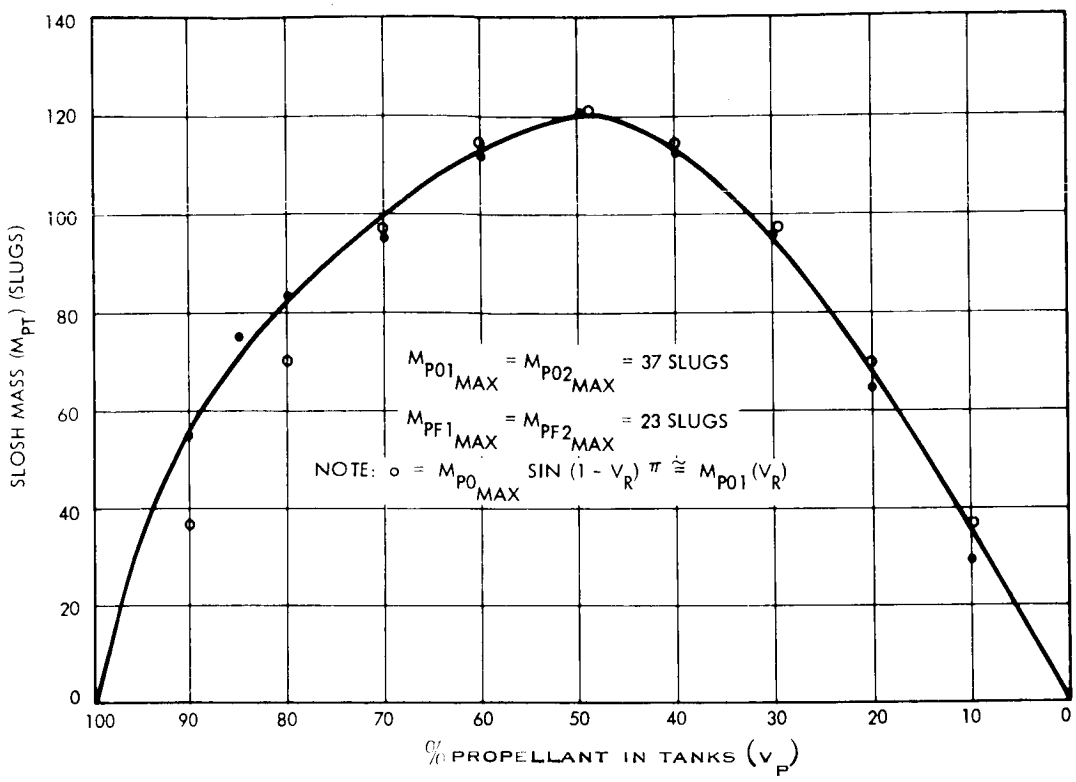

Figure 5. Sloshing Mass

The high Bond number sloshing mass as a function of propellant fill ratio, V_R, is approximately that of Figure 5. All four tank sloshing masses have been summed but individual slosh masses can be derived by the use of the density ratio of 1.6:1 (oxidizer: fuel). The sloshing pendulum length as a function of fill ratio is shown in Figure 6. The basic fundamental uncoupled sloshing frequency as a function of the propellant remaining is shown in Figure 7. The frequency parameter is relatively constant during any particular thrusting maneuver, thereby reducing the chance of increasing propellant sloshing-autopilot coupling during the total time span of a maneuver. The remaining factor of importance in the liquid behaviour is the damping ratio. Shown in Figure 8 are the relations between the dimensionless viscosity parameter and axial acceleration, and the logarithmic decrement, δ, versus propellant fill ratio. The damping ratio, ζ, must be derived from the logarithmic decrement. The effect on damping factor (logarithmic decrement) and slosh mass due to rigid or flexible baffles has been theorized and experimentally determined for spherical tanks in the literature, and so is not presented here; however, the effect on sloshing frequency will be taken for this study to be inconsequential.

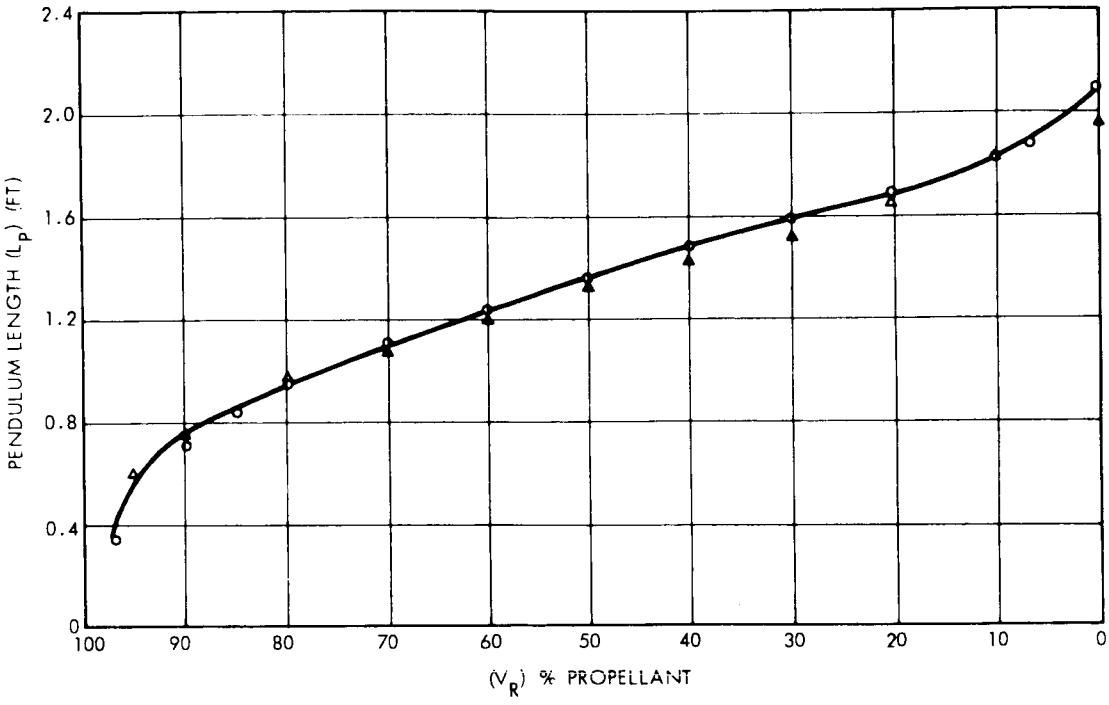

Figure 6. Sloshing Pendulum Length vs Propellant Fill Ratio

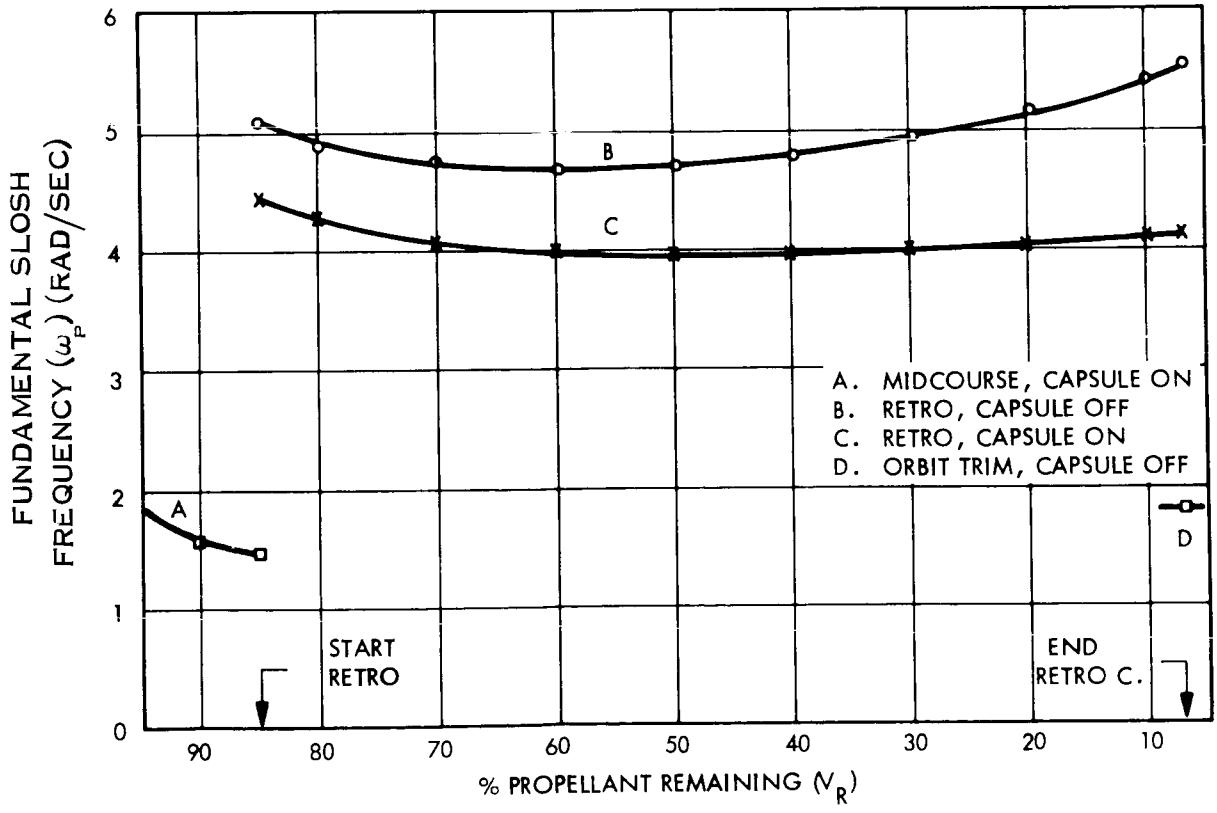

Figure 7. Fundamental Slosh Frequency vs Percent Propellant Remaining

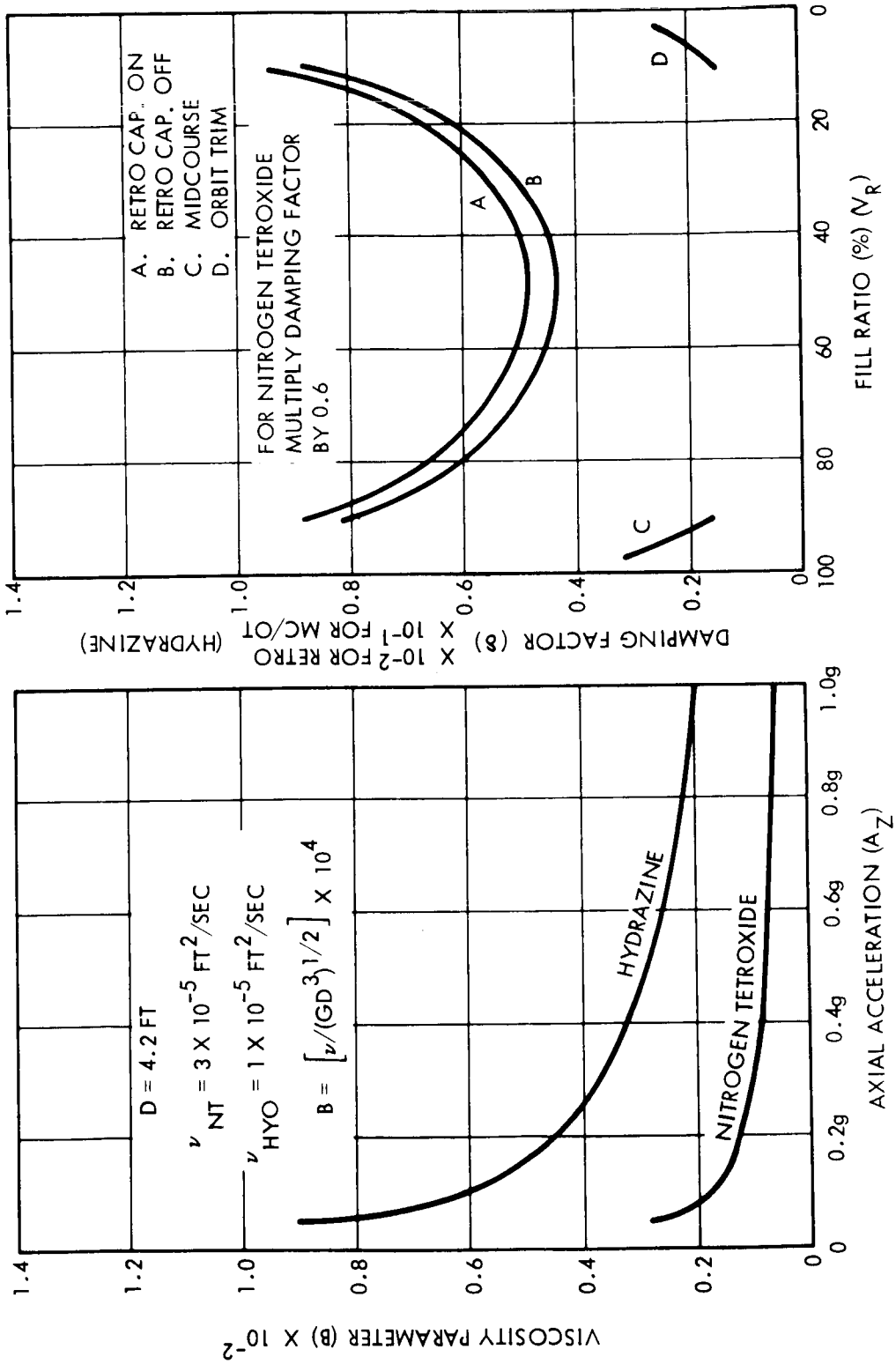

Figure 8. Propellant Damping Characteristics

5. RIGID BODY/PROPELLANT SLOSHING STABILITY

The rigid body/propellant sloshing stability is analyzed in both the complex frequency and time domains. The complex frequency domain studies are carried out with fixed-time root locus plots, while the time domain solutions are generated by a digital computer simulation. The "time sliced" root-locus plots provide valuable insight into the linear, small perturbation stability characteristics. An extension of the work performed is to combine the actuator non-linear describing function with the linear root-locus. The time domain studies were carried out on a planar time varying digital computer simulation, but with constant vehicle parameters. This simulation presently has the capability of incorporating all the significant non-linearities of the system except the slosh amplitude dependent damping. The end result is a quantitative description of the expected system response, power consumption, limit cycle, as well as verification of the root-locus analysis.

5.1. ROOT LOCUS STABILITY ANALYSIS

The root locus analysis uses the equations of Appendix A of VOY-D-323 in simplified form by neglecting the engine inertial reaction (which is small) and by lumping the four individual slosh masses into one pendulum mass, hinged on the roll axis. A linear transfer function between the actuator command signal and the actual thrust vector angle is used in place of the equations of motion of the engine. This transfer function is described in Paragraph 5.1.2. The equations are written as perturbations about the vehicle and engine nominal trim positions. Engine deflections and thrust deflection are assumed to be identical. With these assumptions the following set of equations for the yaw axis results:

Rotational $$\ddot{\theta} I_{yyo} = F_c \ell_c \xi + \beta_p A_z M_p L_p$$

Axial $$A_z M_T = F_c$$

Lateral $$A_x M_o = - F_c \xi + \beta_p A_z M_p$$

Pendulum Acceleration

$$\ddot{\beta}_p = -2\zeta_p \omega_p \dot{\beta}_p - \beta_p \omega_p^2 - \left[\frac{\ddot{\theta}(\ell_o - L_p) + A_x}{L_p}\right]$$

Pendulum Frequency

$$\omega_p = \left[\frac{A_z}{L_p}\right]^{1/2}$$

After combining:

$$\frac{\ddot{\theta}(S)}{\xi(S)} = \left[\frac{F_c \ell_c}{I_{yyo}}\right] \left\{ \frac{\left[S^2 + 2\zeta_p \left(\frac{F_c}{M_T L_p}\right)^{1/2} S + \frac{F_c}{M_T}\left(\frac{M_p}{M_o L_p} + \frac{1}{L_p} + \frac{M_p}{M_o \ell_c}\right)\right]}{\left[S^2 + 2\zeta_p \left(\frac{F_c}{M_T L_p}\right)^{1/2} S + \frac{F_c}{M_T}\left(\frac{M_p}{M_o L_p} + \frac{1}{L_p} + \frac{M_p\{\ell_o - L_{p_o}\}}{I_{yyo}}\right)\right]} \right\}$$

The engine-actuator transfer function is:

$$\frac{\xi(S)}{\epsilon_g(S)} = \frac{K_A}{1 + 2\zeta_A \tau_A S + \tau_A^2 S^2}$$

and the gyro plus compensation network transfer function is:

$$\frac{\xi_g(S)}{\ddot{\theta}(S)} = \frac{K_s (1 + \alpha\tau_1 S)(1 + \beta\tau_2 S)}{S^2 (1 + \tau_1 S)(1 + \tau_2 S)(1 + \tau_3 S)(1 + \tau_g S)}$$

The system open-loop transfer function is then the product of the three transfer functions above.

Figures 9 through 12 depict the root locus of the Voyager Spacecraft for the nominal mission profile: midcourse with lander, orbit insertion with lander, orbit insertion without lander, and orbit trim without lander. The root locus for the orbit insertion maneuver is for the

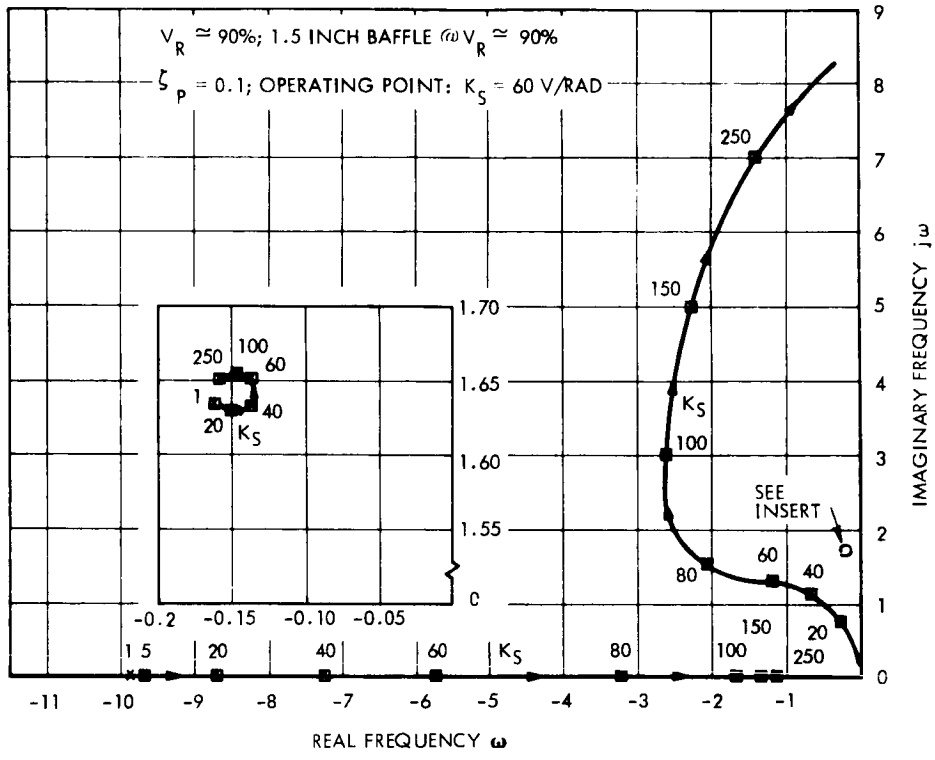

Figure 9. Root Locus Plot of Start of Last Midcourse Maneuver (Capsule ON)

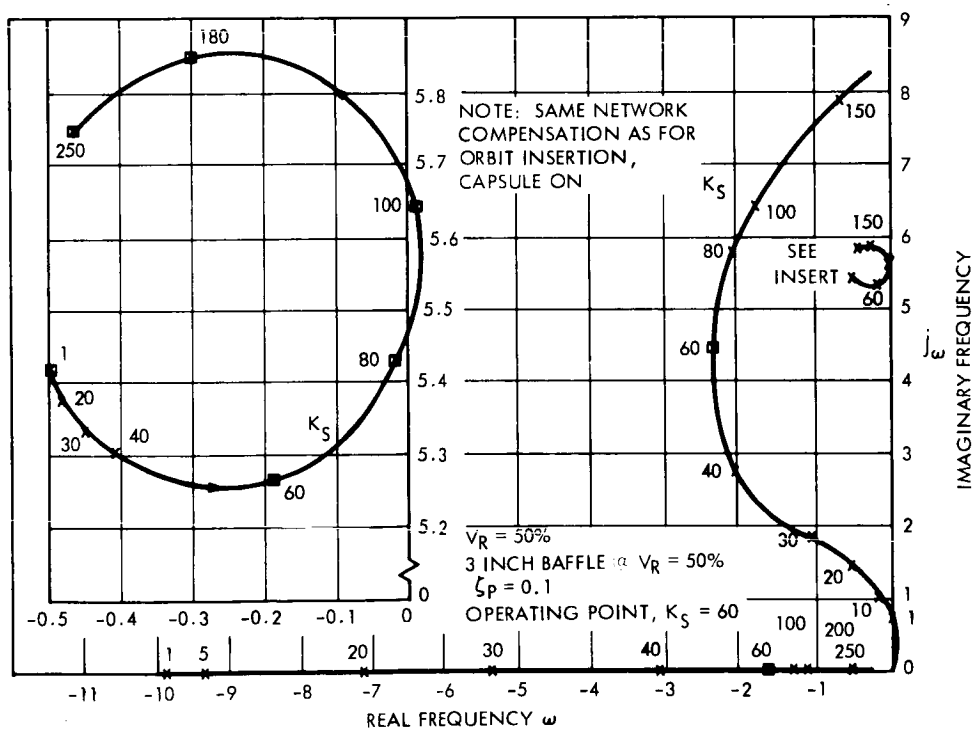

Figure 10. Root Locus Plot Midway Through Orbit Insertion (Capsule OFF)

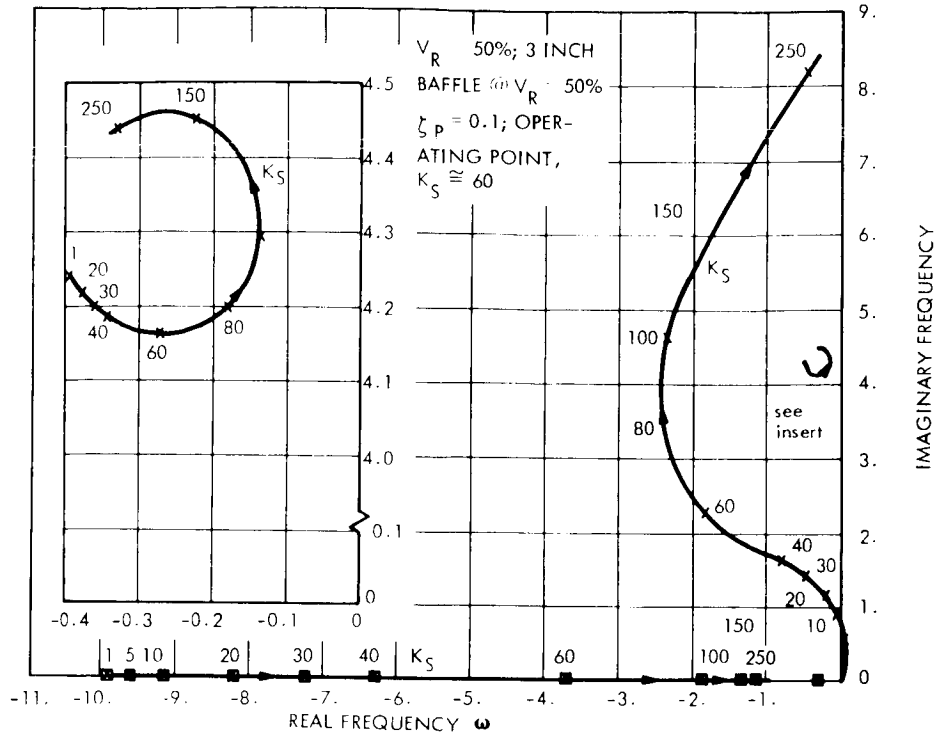

Figure 11. Root Locus Plot Midway Through Orbit Insertion (Capsule ON)

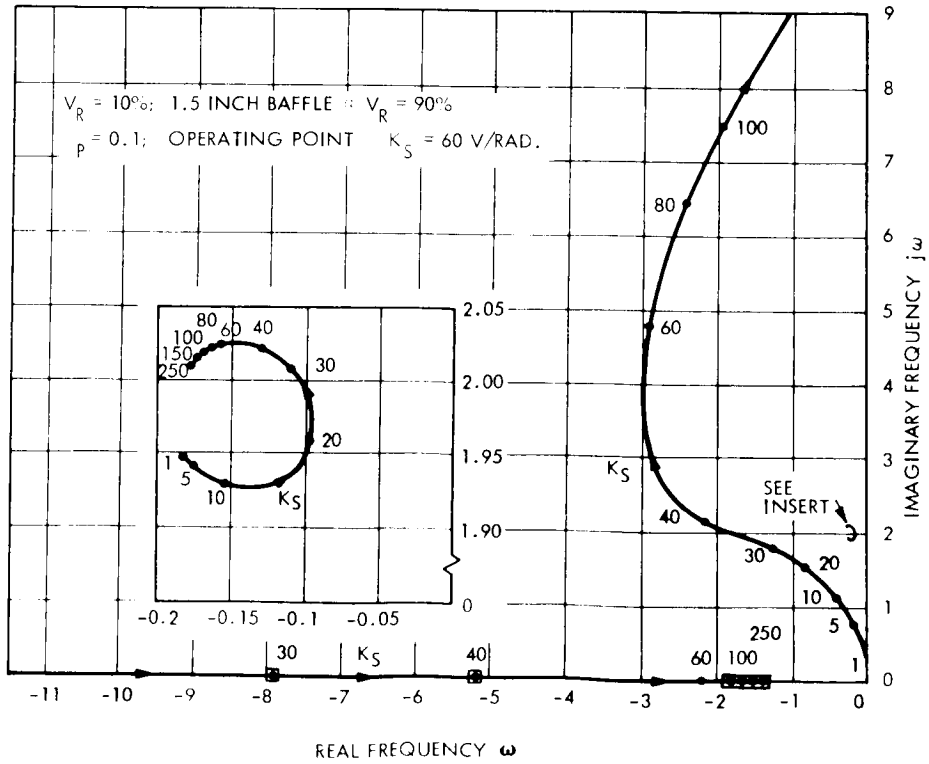

Figure 12. Root Locus Plot for Start of Orbit Trim Maneuver (Capsule OFF)

time approximately halfway through the maneuver. The unbaffled sloshing mass, (maximum at this time) leads to conservative stability prediction results. The actual ignition transient and terminal phase have a substantially reduced sloshing mass, thereby reducing the coupling with the rigid body. As expected, the slosh dipole is in a potentially unstable configuration due to the sloshing mass being located aft of the reduced (rigid) center of mass. The significance of this is that for practically any system gain, the coupled slosh locus crosses into the right half of the plane. This occurs because the unbaffled damping ratio $\zeta_{ox} \approx 0.01$ places the slosh dipole immediately adjacent to the imaginary axis. The magnitude of coupling is dependent essentially on the rigid body response, and the ratio of sloshing mass to vehicle rigid body principal moments of inertia. Since the orbit insertion maneuver with the capsule off has smaller rigid body moments of inertia, the coupling will be increased as is shown in Figure 10.

5.1.1. Propellant Slosh Control

In summary, the root locus stability analysis dictates the incorporation of increased slosh damping and reduced sloshing mass. Assuming the choice of ring baffles (because they yield the desired changes in the slosh parameters), an estimate of baffle width can be made. Figures 13 and 14, which show the relationships between normalized sloshing force and damping factor versus baffle width and ratio of propellant fill ratio to baffle location, are used in conjunction with the root locus to arrive at an adequately stable "linear" system. As can be seen from the stable system root locus plots of Figures 9, 11 and 12, a 3-inch ring baffle results in the desired damping ratio, $\zeta = 0.1$ over a small range of depth ratio. Equally significant is the decrease in sloshing mass which decreases the movement of the coupled locus towards the imaginary axis. The performance shown in Figure 10 for the degraded mission phase (orbit insertion with capsule off) may be acceptable. However, it is marginal in its slosh damping sensitivity to system gain. It would seem advisable for this degraded mission phase to reduce the system gain to $K_s = 40$ volt/radian. The normal orbit insertion maneuver, with the capsule on could also have a reduced gain without seriously increasing the steady-state pointing error. Exact parameter selections are not the intent of this study, however.

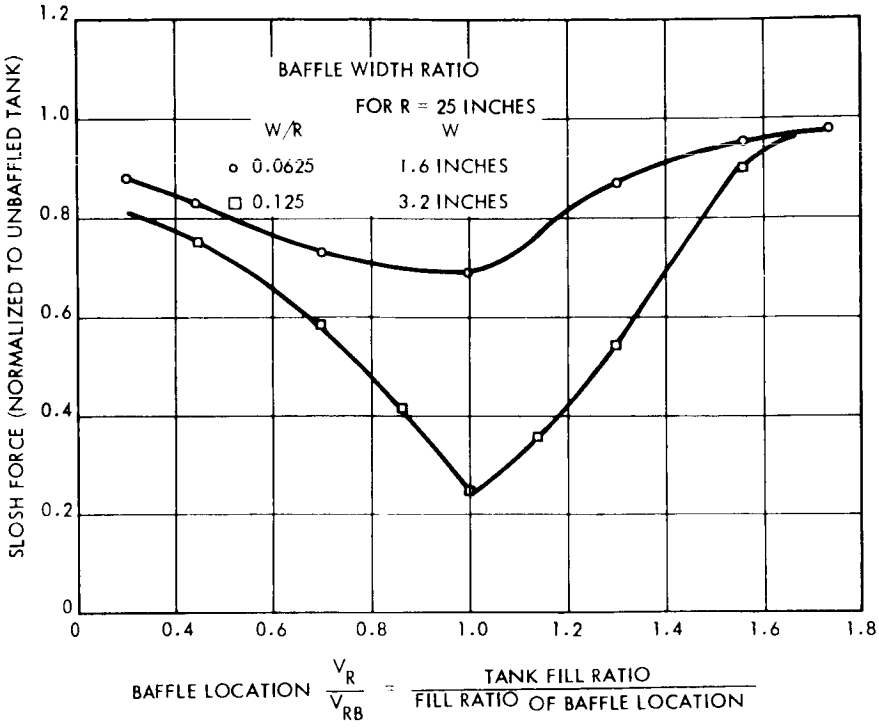

Figure 13. Slosh Force vs Baffle Size and Fill Ratio

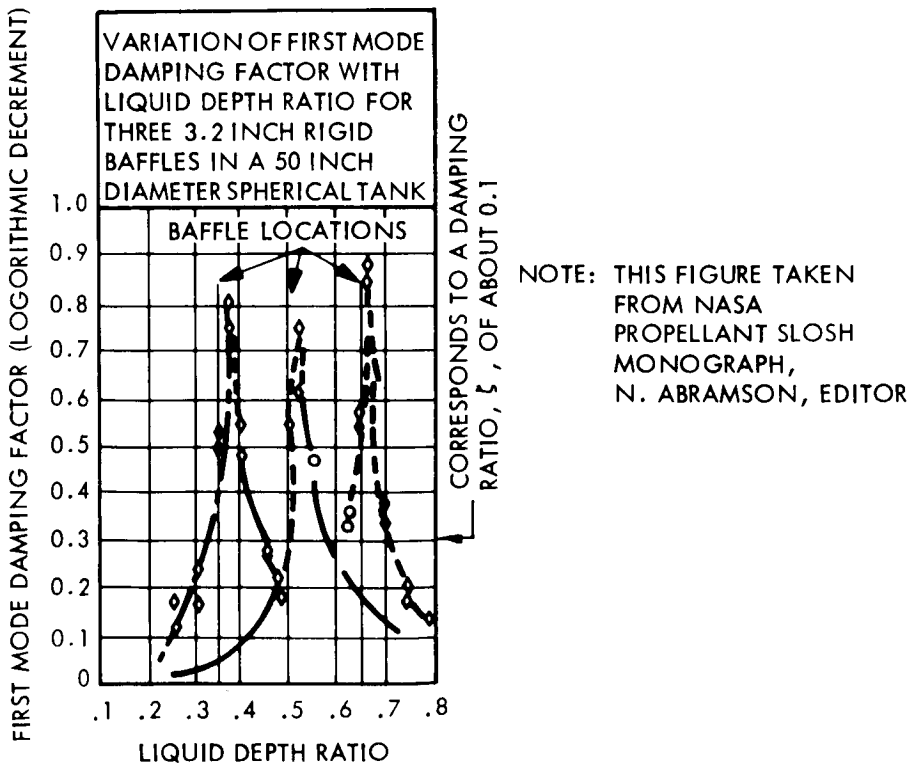

Figure 14. Damping Factor vs Baffle Size and Fill Ratio

It is felt that three 3-inch baffles per tank are adequate for a normal mission phase. However, to accommodate the orbit insertion maneuver without the capsule, four baffles per tank may be required. The location of these baffles has not been analyzed in detail. An estimate of location and corresponding propellant fill ratio (V_r where d = 50 inches corresponds to the tank top) is:

	d	V_R
Baffle No. 1:	35 in.	80%
Baffle No. 2:	28 in.	60%
Baffle No. 3:	20 in.	35%
Baffle No. 4:	10 in.	10%

It is also to be noted from the root locus plots that flexibility in system gain may be desirable to achieve higher slosh damping, thereby reducing the limit cycle power consumption.

5.1.2 Electro-Mechanical Gimbal Actuator Analysis

The actuator considered for the system root locus studies has a no-load linear transfer function

$$\frac{K_A}{1 + 2\zeta_A \tau_a S + \tau_a^2 S^2}$$

where

$K_A = 0.0877$ rad/volt

$\zeta_A = 0.8$

$\omega_A = \frac{1}{\tau_a} = 22$ rad/sec

The effect of the engine load torques is to reduce the actuator performance. Since the actuator design is quite simple, and its performance easily increased by the amount of the load torque, no problem is anticipated. Even so, a reduced performance actuator having a linear response of 15 rad/sec at $\zeta_A = 0.8$ was included in some root locus studies which are not presented here. The autopilot system was not affected appreciably. Future work will, as mentioned previously, include the system sensitivity to the non-linear assymetrical and linear actuator performance.

The gimbal actuator transfer function is derived in the following analysis. A preliminary estimate at the beginning of the study, based on Task A and B work, was that the actuator-engine should have a minimum response of 15 rad/sec at an amplitude of 0.05 radians. The preliminary actuator selection was a 7 ft-lb dc torquer with a 1-inch lead screw driving the LEMDE engine at the 19-inch attachment point. The performance of this actuator does not meet these preliminary requirements, but because of its simplicity, ease of incorporating redundancy, and the fact that the requirements were only estimated, it was felt to be highly desirable. One conclusion of these studies, however, is that this actuator does meet the autopilot requirements. In other words, the preliminary requirements were set too high. A motor-clutch actuator will be compatible with the initial requirement. However, from the autopilot standpoint, the large clutch hysteresis is extremely undesirable. A hydraulic system will easily meet the autopilot performance requirements.

Figure 15 is the servo diagram of the actuator loop including the gyro compensation network which is included in the digital computer simulation. The vehicle structural compliance at the point of actuator support was found to be negligible. The pitch and yaw actuators will be identical.

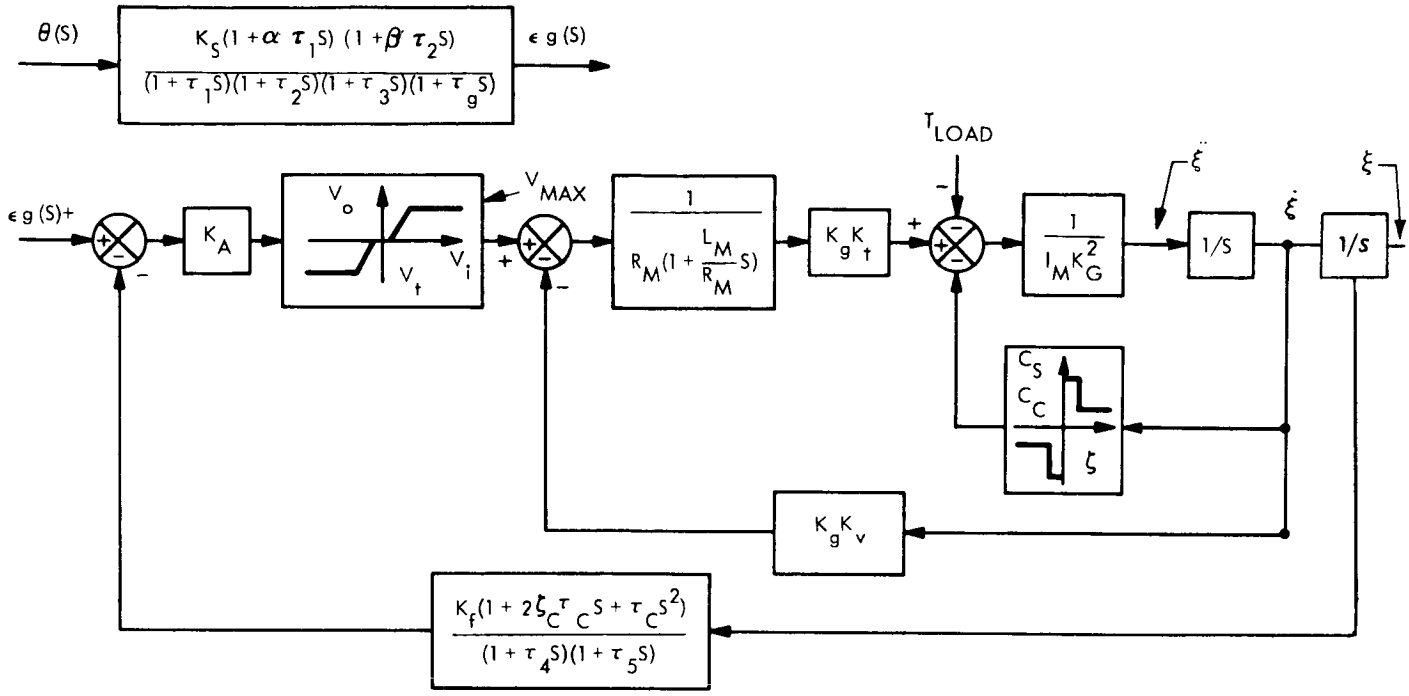

where: $T_L = M_R \ell_R A_Z(\xi+\Delta) + M_R \ell_R(A_x - \ddot{\theta}\ell_C) + I_{R_{YY}}(\ddot{\xi}-\ddot{\theta}) - F_C \epsilon$

Figure 15. Servo Diagram of Actuator Loop

Writing the linear open loop transfer function neglecting the load torque except for the engine inertial reaction:

$$G(S)\,H(S) = \left[\frac{K_A K_f}{K_G K_V}\right]\left[\frac{1+2\zeta_c\tau_c S+\tau_c^2 S^2}{S\left(1+\frac{R_m J}{K_g^2 K_v K_t}S+\frac{L_m J}{K_g^2 K_v K_t}S^2\right)(1+\tau_4 S)(1+\tau_5 S)}\right]$$

where J is the total inertia reflected to the engine gimbal and is

$$J = I_m K_g^2 + I_{ryy}$$

and K_g is the ratio of engine angular velocity to motor angular velocity, with the 1-inch lead screw at the 19-inch distant attachment point from the engine gimbal point.

The parameters for the Inland Motor Corporation (Type T-5730) 7ft-lb torquer with the 1-inch lead screw are:

$K_t = 0.57$ ft-lb/amperc

$I_m = 5 \times 10^{-3}$ slug-ft^2

$K_v = 0.7$ volts/rad/sec @ zero source impedance

$R_m = 1.5$ ohms

$L_m = 5 \times 10^{-3}$ henries

$K_g \simeq 120$

$K_f = 0.0877$ volts/rad

$I_{ryy} = 47$ flug-ft^2

The feedback compensation network, because of its necessarily high bandwidth which results in increased noise, is not particularly desirable. It was found not to be required (except as a controlling influence on motor and amplifier parameters for reliability purposes). The actuator-engine root locus, shown in Figure 16, shows that for an amplifier gain of 100 v/v, the actuator has the desired damping ration of 0.8 (with an ω_A of about 22).

The estimated maximum static load torque occurring during the orbit insertion maneuver is 140 ft-lb. During the low thrust mode, it is approximately 20 ft-lb. This torque results from effects such as the thrust offset from the gimbal axis. The continuous power consumption due to this load will be approximately 55 watts per axis during orbit insertion and 8 watts per axis during low thrust maneuvers.

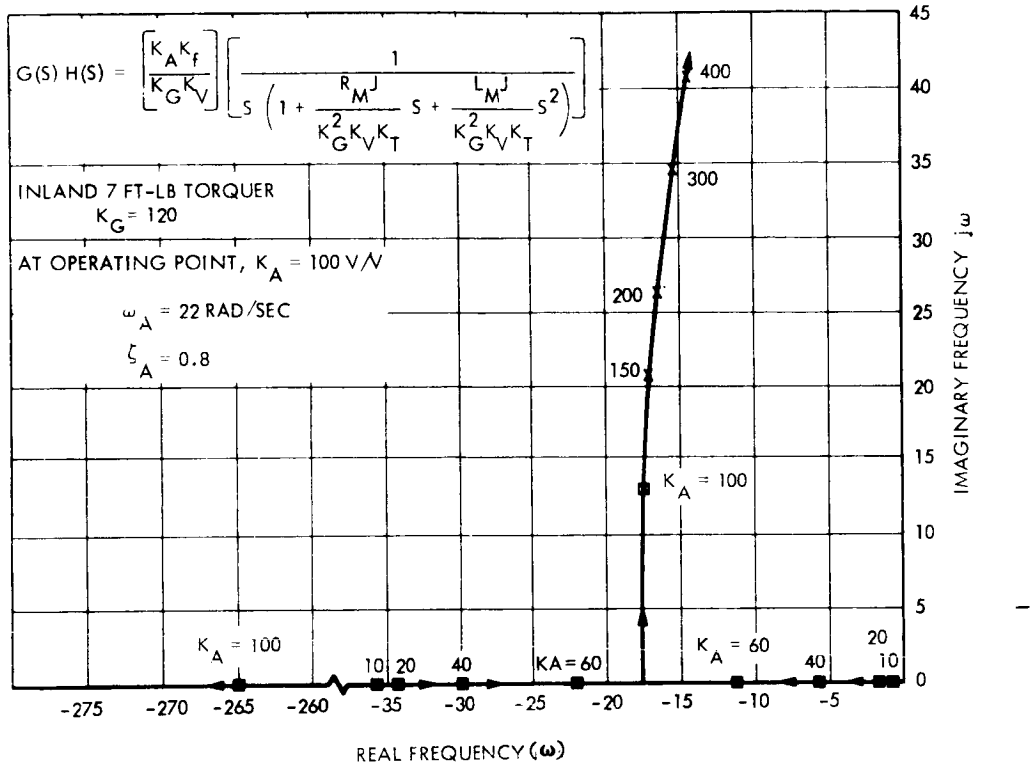

Figure 16. Linear Actuator Root Locus

The implementation of the power amplifier is of concern because of the high current output required (13 amp) for peak motor torque. Use of a pulsed-width modulation scheme reduces the semiconductor load current requirement and also presents a constant low source impedance to the motor, thereby maintaining a predictable K_V. Use of redundant "stacked" torque motors for each axis plus parallel redundant amplifiers also alleviates the individual amplifier power level requirement. Should the K_V with a non-zero source impedance be affected enough to result in oscillatory response (inner loop), a tachometer loop can be added quite easily.

As mentioned before, the noise input to the actuator servo-amplifier may be critical in the selection of the dc torquer, since it may cause significant power consumption throughout the maneuver. Using specifications for gyro output signal noise for the Orbiting Astronomical Observatory (OAO) spacecraft guidance and control system, the gyro output signal noise power

spectral density (η_g) including preamplifier is 7×10^{-9} deg^2/cps. The gas bearing gyros selected for Voyager should have substantially lower noise. The mean squared noise expressed at the output of the selected low thrust gyro compensation network is:

$$N_s^2 = \eta_g \left\{ \frac{a^2 \tau_1^2 + \left[\tau_1 \tau_3 + \tau_g (\tau_1 + \tau_3)\right]}{2\left[\tau_1 + \tau_3 + \tau_g\right]\left[\tau_1 \tau_3 + \tau_g (\tau_1 + \tau_3)\right] - 2\tau_1 \tau_3 \tau_g} \right\}$$

Using the parameters:

$a = 10$

$\tau_1 = 0.1$

$\tau_3 = 0.0125$

$\tau_g = 0.003$

$N_s = 4.4 \times 10^{-3}$ volts rms

At the output of the servo amplifier ($K_A = 100$ v/v) the actuator input noise is 0.44 VRMS. Since this is low frequency noise, the power dissipation and the noise factor contributing towards the limit cycle will be equivalent to the 2 σ 0 to peak noise level (or about double the RMS level). This is acceptable in relation to the expected 2 volt equivalent 3σ frictional torque, and the 3.5 volt equivalent 3σ load torque.

5.1.3 Gyro Signal Compensation

The compensation network parameters were, in keeping with the philosophy of minimizing switching, compromised in terms of yielding best system response for each of the mission phases. The midcourse maneuver with capsule on or off, and the orbit trim maneuver with capsule on or off, are adequately stabilized with the same simple lead-lag network

parameters. These maneuvers were studied for both capsule on and capsule off cases to include modes in which failures have occured. The orbit insertion maneuver incorporates a lag-lead network in addition to the low thrust compensation network.

It is noticed that the locus for this network compensation (Figure 11) leaves the open loop double pole at the origin and crosses into the right half plane. This is due to restricting the parameter α to not greater than 10, for acceptable actuator signal noise level. Methods considered for correcting this are:

(1) to increase α to 40 increasing the noise problem

(2) require the addition of rate gyros to provide damping, increasing system complexity.

(3) increase the system bandwidth by reducing the lag-lead network effect, increasing the noise problem and the amount of coupling or excitation of the elastic vehicle modes (i.e., high-gain antenna).

(4) Require a lower noise gyro, such as a gas bearing gyro, thereby permitting a large value of α.

The second filter (τ_3) in addition to the pure lead-lag for low thrust, or the double lead-lag, for high thrust, is desirable to reduce the gyro signal noise. This is described more fully in the actuator analysis, Paragraph 5.1.2.

The operating point on the root locus is at K_s = 57.3 volt/rad. This in conjunction with the actuator dc gain of 0.0877 rad/volt yields the desired autopilot feedback gain of 5.

The parameters used in the transient study are:

Figure No.	α	β	Time Constants (Sec) τ_1	τ_2	τ_3	τ_g
9	10	0	0.07	0	0.012	0.003
17	10	0	0.07	0	0.012	0.003
10 and 11	10	0.1	1.0	20	0.012	0.003
18 and 19	10	0.1	1.0	20	0.012	0.003
12	10	0	0.07	0	0.012	0.003
20	10	0	0.07	0	0.012	0.003

5.2 TRANSIENT ANALYSIS

The primary purposes of the transient study are to determine actuator performance, including non-linearities, determine prior propellant settling requirements, if any, and to verify the root locus analysis.

The equations written in Appendix A in conjunction with the root locus derived compensation network parameters, and non-linear gimbal actuator, were programmed for digital simulation. Four vehicle-mission phase conditions have presently been considered, correlating with the selected root locus plots. They are:

a. Midcourse Maneuver with capsule ON (Figure 17)

1. Propellant fill ratio of 90%
2. 3-inch baffle located at a fill ratio of about 85% to define damping but having slosh mass equivalent to a 1.5 inch baffle (conservative)
3. Thrust buildup to 1050 lb. having about a 0.5 second time constant.
4. Nonlinearities included only servo-amplifier saturation and gimbal limits.

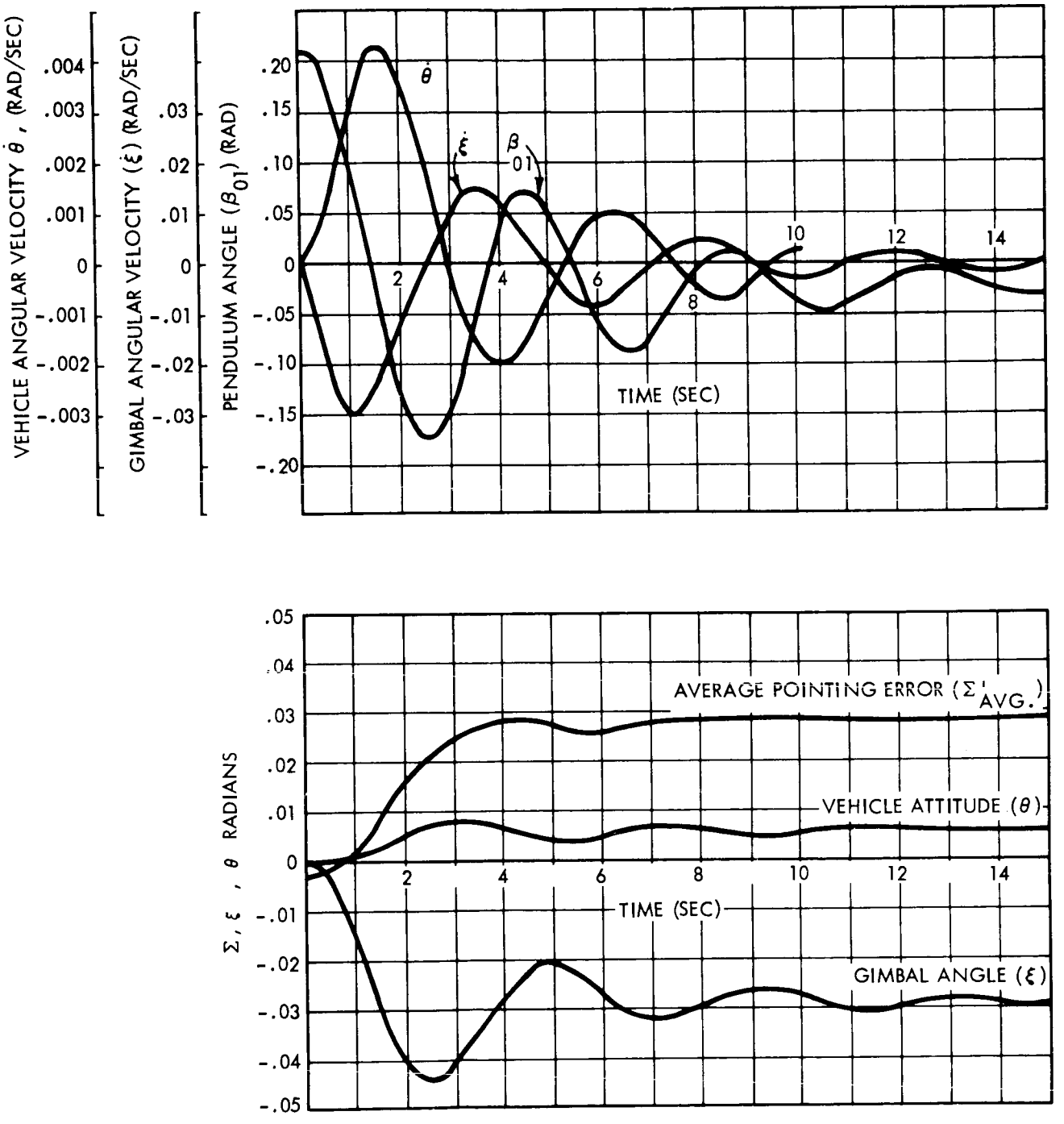

Figure 17. Midcourse with Capsule ON (3-inch Baffle)

5. Engine misalignment angle (∇) of 0.25 degrees.

6. C-M lateral offset (δ) of 1.41 degrees.

7. $\Sigma_{ss} = 0.03$ radians

b. Orbit Insertion Maneuver with Capsule ON (Figure 18)

1. Propellant fill ratio $\simeq$ 50%.

2. 3-inch baffle located at a fill ratio of about 50%.

3. Thrust buildup to 9850 lb-f with a time constant of 0.1 seconds.

4. Engine misalignment angle (∇) of 0.25 degrees.

5. C-M_o lateral offset (δ) of 1.14 degrees.

6. $\Sigma_{ss} = 0.0245$ radians

c. Orbit Insertion Maneuver with Capsule OFF (Figure 19)

Same conditions as with capsule on except δ = 2.13 degrees and $\Sigma_{ss} = 0.0455$ radians.

d. Orbit Trim Maneuver with Capsule OFF (Figure 20)

1. Propellant fill ratio $\simeq$ 10%.

2. 3-inch baffle located at a fill ratio of $\simeq$ 15%.

3. Thrust buildup to 1050 lb-f. with time constant to 0.5 sec.

4. Engine misalignment ∇ of 0.25 degrees.

5. C-M_o offset (δ) = 2.19 degrees.

6. $\Sigma_{ss} = 0.0468$ radians.

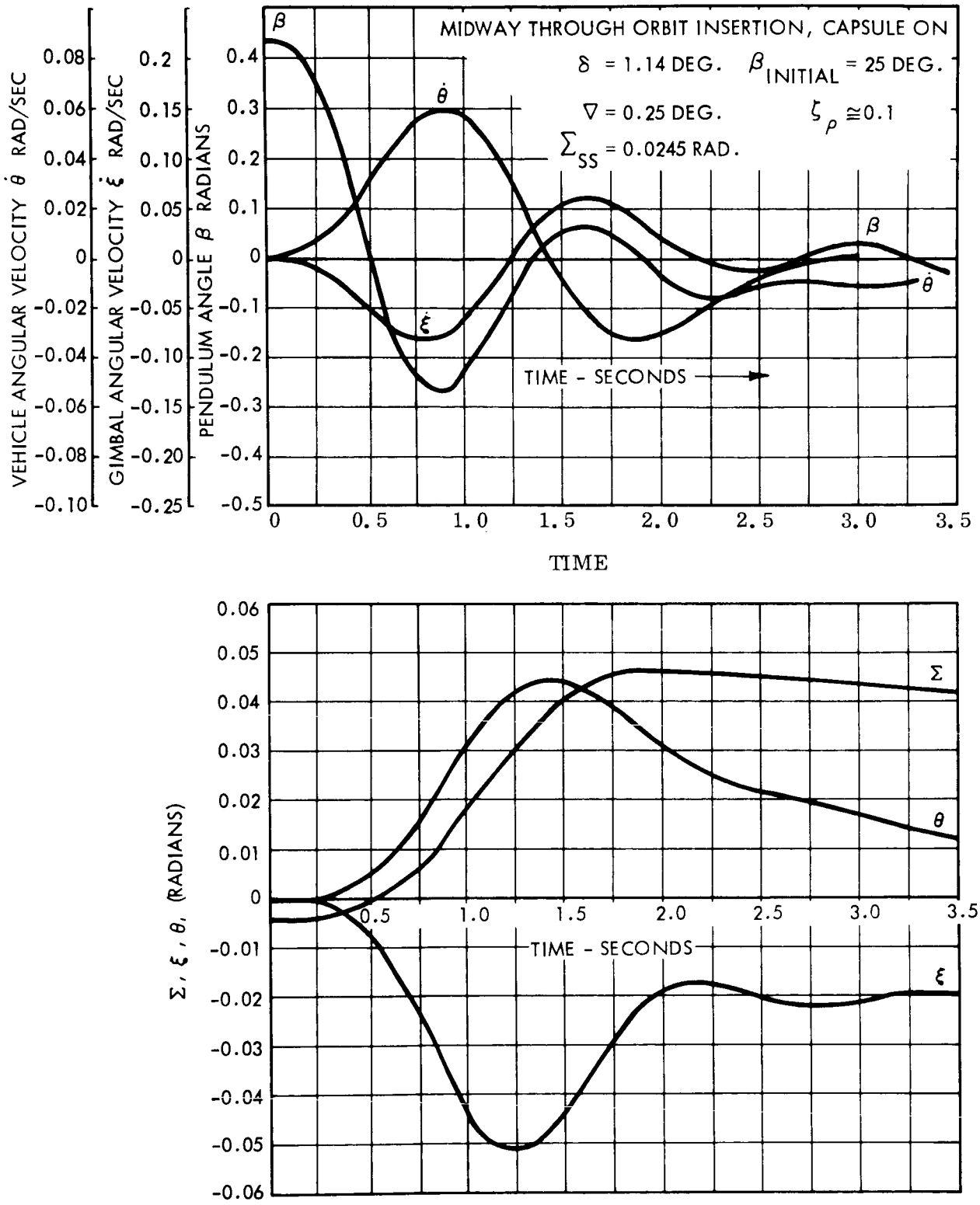

Figure 18. Midway Through Orbit Insertion (Capsule ON)

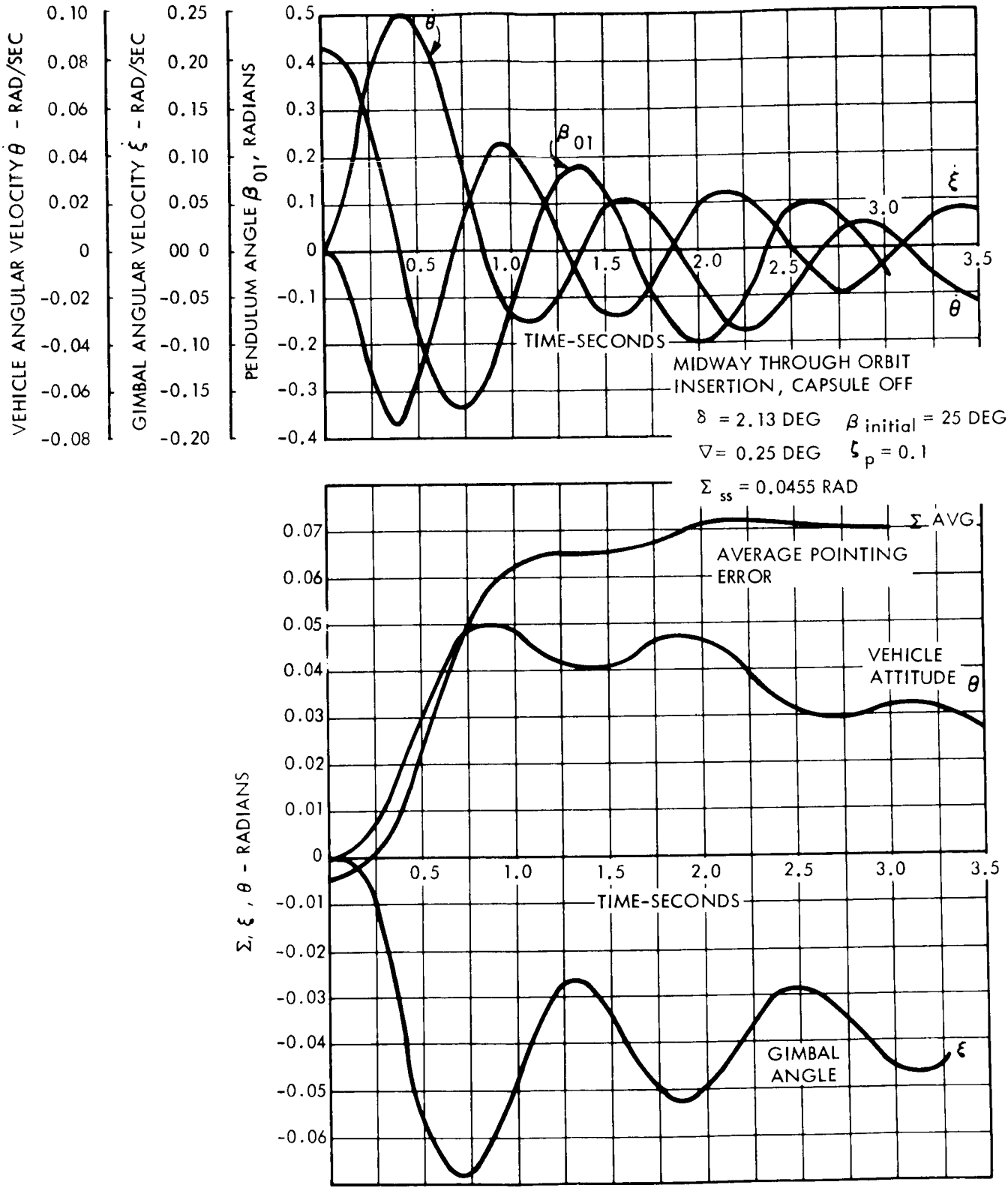

Figure 19. Midway Through Orbit Insertion (Capsule OFF)

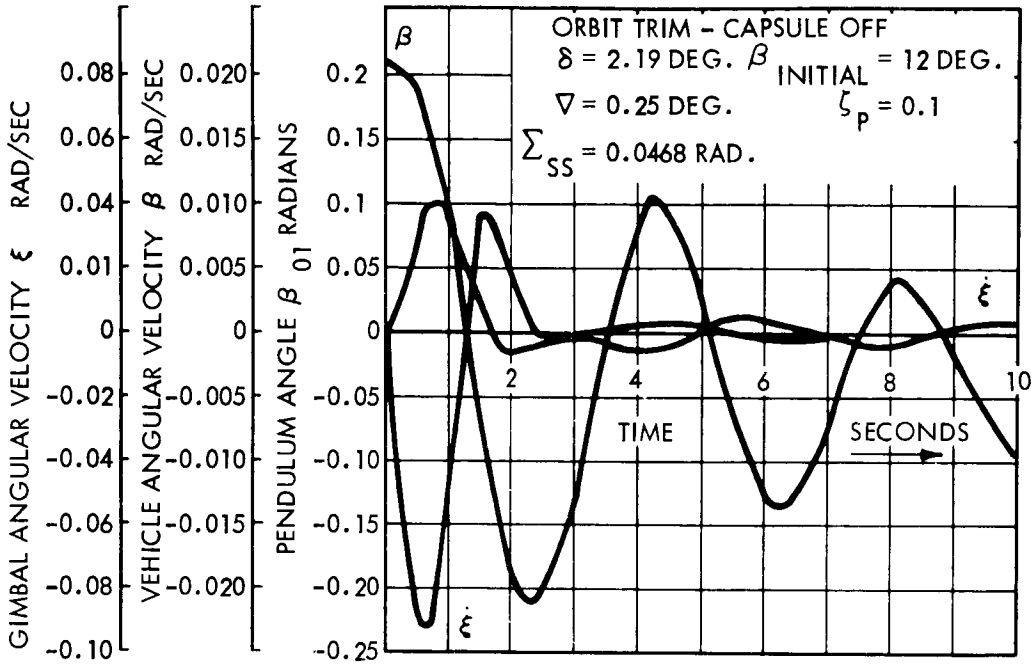

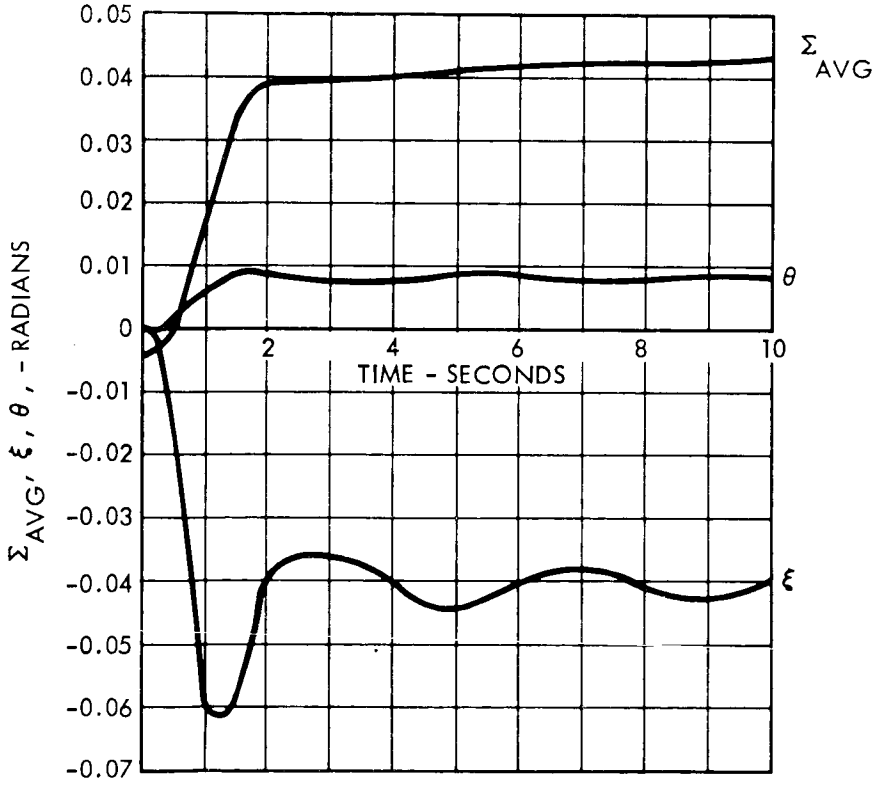

Figure 20. Orbit Trim (Capsule OFF)

The results are felt to be somewhat conservative. Two cases studied the startup transient with the worst dynamic properties that occur which is about midway through the orbit insertion both with the capsule off and on. These, shown in Figure 18 and 19, were the most severe of those studied.

The orbit insertion maneuver with the capsule off was predicted by the root locus plot to have significantly more rigid body-slosh coupling. This effect in addition to having the large initial rigid body transient, and the use of compensation network parameters designed for the orbit insertion capsule on, makes this case the most severe for required actuator performance. The actuator torque required was 75 percent of the torque saturation limit. This verifies the linear analysis up to this severe disturbance level. As expected, the midcourse maneuver was the least severe. The orbit trim maneuver with the capsule off did have low propellant damping as predicted. However, there was little effect on the vehicle because of the reduced sloshing mass. As stated previously, the orbit trim phase should be baffled sufficiently to prevent the propellant from uncovering the engine inlet.

The midcourse and orbit trim average thrust vector pointing errors were within the predicted steady-state value. The transient of Σ_{avg} is felt to be adequately predictable for the small Δ V maneuvers; however, until an extensive parametric study and comprehensive error analysis is made, it is not certain. The orbit insertion maneuver and large ΔV low thrust maneuvers are adequate in relation to pointing error when the nominal portion of the rigid center of mass offset is removed, and the transient effect is averaged over the total burn time.

In all cases studied the average thrust vector pointing error meets the performance requirements when the nominal portion of the rigid center of mass offset is removed. This removal is justified because the maneuver rotations performed to establish the velocity change orientation can be adjusted appropriately to account for the known nominal CM offset.

In summary, the transient study has thus far confirmed:

a. The linearized root locus study with respect to system gain limiting.

b. The system adequacy with regard to the linear stability criteria.

c. The electromechanical gimbal actuator adequacy.

d. The system adequacy with respect to starting the maneuver with an initial pendulum angle of 30 degrees thus far, and satisfactory propellant damping.

e. The requirement for propellant damping greater than the wall-wiping value (i.e., the need of baffles).

f. The average thrust vector pointing is not significantly affected by propellant sloshing.

5.3 SUMMARY OF STUDY RESULTS

- The system meets the performance requirement on thrust vector pointing error with the basic LEMDE gimballed engine driven by electromechanical actuators and with four 3-inch ring baffles located in each tank.

- Prepositioning of the LEMDE thrust through the nominal c.m. is not necessary for the center of mass offsets studied (2.5 degrees).

- Auxiliary thrusters are not required for stability.

- The orbit trim maneuver with the PSP deployed, due to the excessive vehicle center of mass offset, can not be performed with the basic LEMDE (6 degree gimbal) system.

- The engine inertial reaction ("tail-wags-dog") effect is small.

- Gyro signal compensation networks are adequate but parameters must be switched for the different thrust levels.

- Rate gyros or accelerometers are not required for stability.

- Commencing the orbit insertion maneuver in the low thrust mode is not required. However, it will reduce the peak vehicle attitude excursion (θ peak).

- Roll control by the ACS appears to be adequate without considering propellant slosh coupling. A complete 3-axis study is necessary to define the roll control requirements completely.

- Terminal vehicle rates are expected to be less than the required 1 degree/second for all maneuvers. The exact limit cycle value is primarily dependent on slosh damping, gimbal friction, and gyro noise. These were not yet included in the simulation.

- The gyro input angle will be less than the required ±6 degree for all maneuvers, being actually less than ±3 degree.

5.4. FUTURE WORK

As stated previously, the results of this study are based on a single-axis model. Also the performance up to now is based on discrete "time slice" analysis and ignition transient; the control system parameters selected are the first synthesis iteration, and are not implied to be optimum values.

A continuation of the autopilot study would include the following:

a. Development of the three-axis dynamic model including the conical pendulums with the primary purpose of defining the roll control system, and three-axis coupled stability.

b. Continuation of the single-axis study with the primary objectives of

   1. Detailed determination of tank baffle requirements.

   2. Completion of the digital simulation including time varying vehicle parameters, amplitude dependent damping and sloshing mass, time varying tank baffle effects-including sloshing frequency, limit cycle amplitudes, and high-gain antenna coupling (or excitation) effects.

   3. Extending the root-locus analysis to include (a) the basic non linear gimbal actuator, (b) "time slices" corresponding to liquid depth farther between baffles, (c) parameter sensitivity analysis and optimization.

   4. Comprehensive pointing error analysis, in conjunction with the above studies.

c. More detailed investigation of the control of slosh characteristics by baffling or other techniques.

d. An investigation of the autopilot performance with amplitude-dependent slosh damping to determine damping required to prevent slosh motions from uncovering the tank outlets. Low fill ratios would probably require baffling to keep sloshing amplitudes low.

6. FUNCTIONAL DESCRIPTION

The function of the autopilot is to maintain the orientation of the thrust vector in inertial space and to command engine shutdown when the required ΔV has been delivered during trajectory maneuvers. Acquisition of the proper attitude is accomplished by the attitude control subsystem, so that thrust vector control is primarily one of attitude hold during the propulsion phase.

The autopilot subsystem employs body-mounted rate-integrating gyros for attitude sensing, and processes this information by means of appropriate compensation networks and amplifiers to control the pitch and yaw gimbal actuators. These actuators are physically part of the propulsion system. Roll control torque is supplied by the attitude control subsystem. Velocity magnitude control is obtained by an accelerometer-integrator which dictates the cutoff signal with a back-up timed signal.

Figure 21 is a functional diagram of the LEMDE autopilot without auxiliary thrusters. The auxiliary thrusters would have separate amplifiers and compensation networks in order to fully utilize their capabilities. The LEMDE itself has variable thrust capability; however it is used in a discrete two-thrust mode. High thrust is 9,850 pound for orbit insertion, while low thrust is 1,050 pound for the midcourse and orbit trim maneuvers.

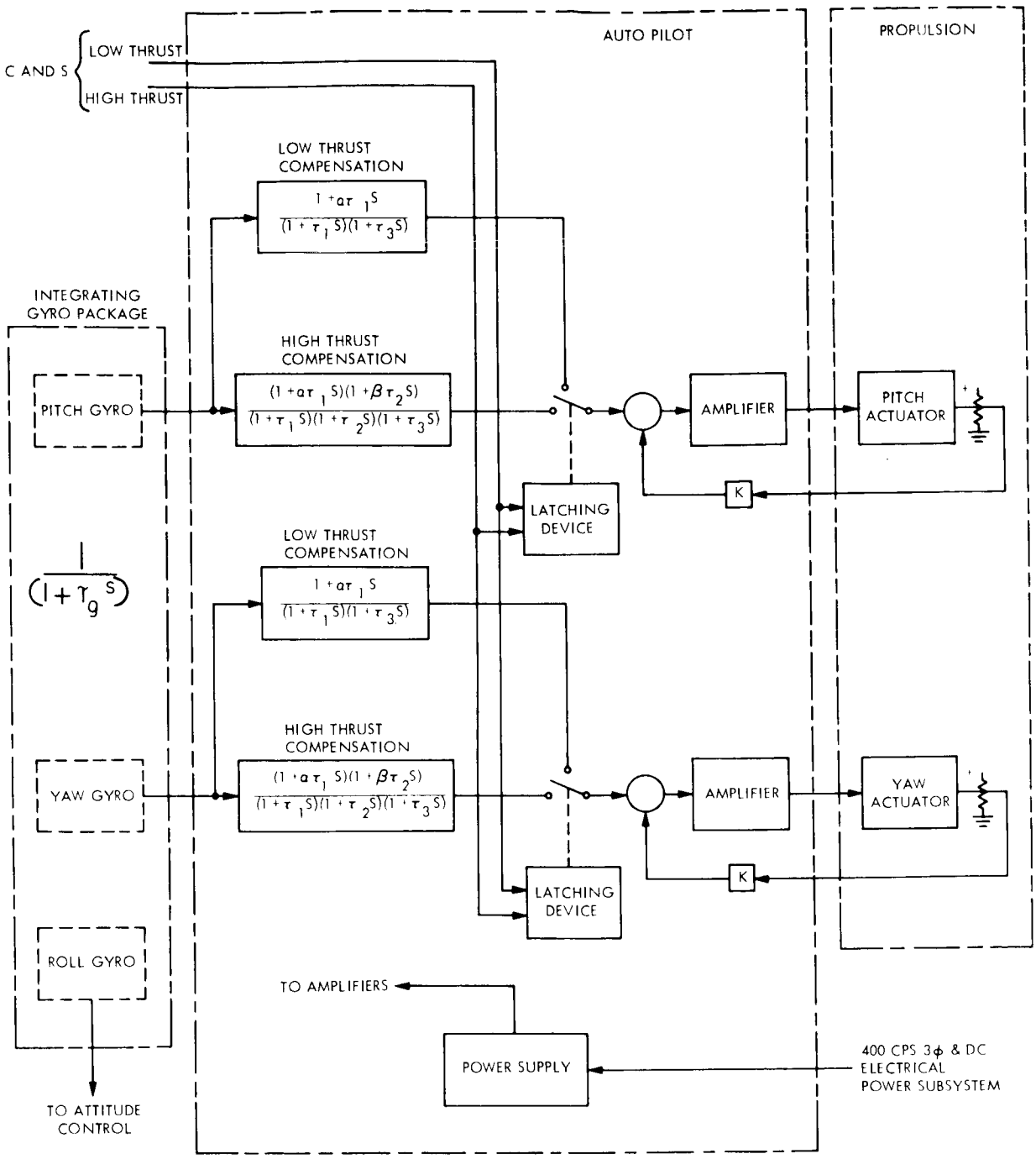

PARAMETER VALUES

	α	β	τ_1 (SEC)	τ_2 (SEC)	τ_3 (SEC)	τ_g (SEC)
HIGH THRUST	10	0.1	1.0	20	0.012	0.003
LOW THRUST	10	0	0.07	0	0.012	0.003

Figure 21. LEMDE Functional Diagram

APPENDIX A

This section presents the single axis equations of motion for a rigid vehicle with propellant sloshing in four tanks, a gimballed engine, and generalized external forces. The equations of motion for the vehicle, excluding vehicle structural elasticity, are derived by writing equations for the energy of the vehicle and propellants with respect to a vehicle-fixed coordinate system shown in Figure 4, and repeated in Figure 22 for convenience. The equations for the inertia torques and forces on the vehicle, engine, and slosh pendulums can then be derived from Lagrange's equation. Because of physical restraints on the variables, the equations can be reduced to those following. The assumptions made in obtaining the equations are:

a. Small angle approximations are made for all angles excepting the sloshing pendulums.

b. The time rates of change of the mass and inertia are assumed to be insignificant so that that their derivatives are zero.

c. Reduced mass and inertia properties are defined based on the total mass of the vehicle (including engines) less the sloshing mass of the propellants. The moments of inertia are summed and written as a reduced moment of inertia about the reduced center of gravity. This is the point where all terms containing ΔX and ΔZ vanish.

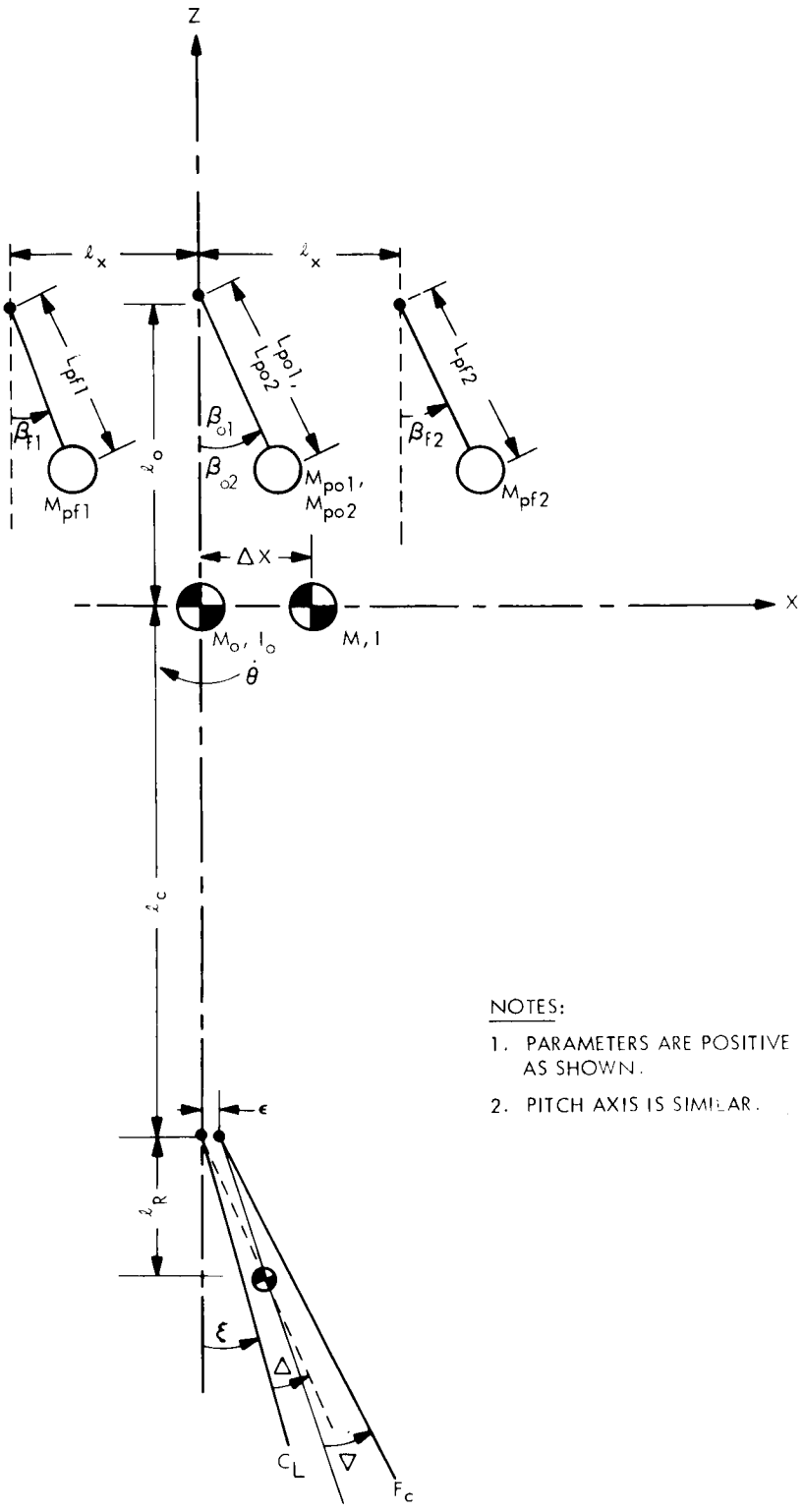

Figure 22. Yaw Axis Vehicle Coordinate System

$$T_{cr} = -\ddot{\theta}\Big[I_{yyo} + M_{po1}\,(\ell_o^{\,2} + L_{po1}^{\,2}) - 2\,M_{po1}\,\ell_o\,L_{po1}\cos\beta_{o1} + M_{po2}\,(\ell_o^{\,2} + L_{po2}^{\,2})$$

$$-2M_{po2}\,\ell_o\,L_{po2}\cos\beta_{02} + M_{pf2}\,(\ell_o^{\,2} + \ell_x^{\,2} + L_{pf2}^{\,2})$$

$$-2M_{pf2}\,(\ell_o^{\,2} + \ell_x^{\,2})^{1/2}\,L_{pf2}\cos\left(\beta_{f2} + \frac{\pi}{2} - \tan^{-1}\frac{\ell_o}{\ell_x}\right) + M_{pf1}\,(\ell_o^{\,2} + \ell_x^{\,2} + L_{pf1}^{\,2})$$

$$-2\,M_{pf1}\,(\ell_o^{\,2} + \ell_x^{\,2})^{1/2}\,L_{pf1}\cos\left(\frac{\pi}{2} - \beta_{f1} - \tan^{-1}\frac{\ell_o}{\ell_x}\right)\Big]$$

$$+\ddot{\xi}\left[I_{R_{yy}} + M_R\,\ell_R\,\ell_c\right] - \ddot{\beta}_{o1}\left[M_{po1}\,L_{po1}\,(\ell_o\cos\beta_{o1} - L_{po1})\right]$$

$$-\ddot{\beta}_{o2}\left[M_{po2}\,L_{po2}\,(\ell_o\cos\beta_{o2} - L_{po2})\right]$$

$$-\ddot{\beta}_{f2}\left[M_{pf2}\,L_{pf2}\left\{(\ell_o^{\,2} + \ell_x^{\,2})^{1/2}\cos\left(\beta_{f2} + \frac{\pi}{2} - \tan^{-1}\frac{\ell_o}{\ell_x}\right) - L_{pf2}\right\}\right]$$

$$-\ddot{\beta}_{f1}\left[M_{pf1}\,L_{pf1}\left\{(\ell_o^{\,2} + \ell_x^{\,2})^{1/2}\cos\left(\frac{\pi}{2} - \beta_{f1} - \tan^{-1}\frac{\ell_o}{\ell_x}\right) - L_{pf1}\right\}\right]$$

$$+A_x\Big[M_{po1}\,(L_{po1}\cos\beta_{o1} - \ell_o) + M_{po2}\,(L_{po2}\cos\beta_{2} - \ell_o) + M_{pf2}\,(L_{pf2}\cos\beta_{f2} - \ell_o)$$

$$+M_{pf1}\,(L_{pf1}\cos\beta_{f1} - \ell_o)\Big] + A_z\left[M_{po1}\,L_{po1}\sin\beta_{o1} + M_{po2}\,L_{po2}\sin\beta_{o2}\right]$$

$$+M_{pf2}\ (L_{pf2}\ \sin\beta_{f2}\ +\ell_x)\ +\ M_{pf1}\ (L_{pf1}\ \sin\beta_{f1}\ -\ell_x)\ +\ M_o\Delta X_o\Big]$$

$$T_{CE}=\ -F_c\left[\ell_c\ (\xi+\nabla)\ -\ \epsilon\right]-2\dot{\beta}_{o1}\,\zeta_{o1}\ M_{po1}\ (A_z\ L_{po1})^{1/2}\ (\ell_o\ \cos\beta_{o1}\ -\ L_{po1})$$

$$-2\dot{\beta}_{o2}\,\zeta_{o2}\ M_{po2}\ (A_z\ L_{po2})^{1/2}\ (\ell_o\ \cos\beta_{o2}\ -\ L_{po2})$$

$$-2\dot{\beta}_{f1}\,\zeta_{f1}\ M_{pf1}\ (A_z\ L_{pf1})^{1/2}\left[(\ell_o^{\,2}+\ell_x^{\,2})^{1/2}\ \cos\ (\tan^{-1}\ \frac{\ell_x}{\ell_o}\ -\beta_{f1})\ -\ L_{pf1}\right]$$

$$-2\dot{\beta}_{f2}\,\zeta_{f2}\ M_{pf2}\ (A_z\ L_{pf2})^{1/2}\left[(\ell_o^{\,2}\ +\ell_x^{\,2})^{1/2}\ \cos\ (\beta_{f2}\ +\ \tan^{-1}\ \frac{\ell_x}{\ell_o})\ -\ L_{pf2}\right]$$

TRANSLATIONAL DYNAMICS

$$F_{zR} = A_z M_T - M_o \ddot{\theta}\Delta X_o + M_R \ell_R \left[\ddot{\xi}\ (\xi+\Delta) + \dot{\xi}^2 - 2\dot{\theta}\dot{\xi}\right] + M_{po1}\left[\ddot{\beta}_{o1} L_{po1} \sin\beta_{o1}\right.$$

$$\left. + \dot{\beta}_{o1}^2 L_{po1} \cos\beta_{o1} - \ddot{\theta} b_{o1} \sin\gamma_{o1} - \dot{\theta}^2 b_{o1} \cos\gamma_{o1} - 2\dot{\theta}\dot{\beta}_{o1} L_{po1} \cos\beta_{o1}\right]$$

$$+ M_{po2}\left[\ddot{\beta}_{o2} L_{po2} \sin\beta_{o2} + \dot{\beta}_{o2}^2 L_{po2} \cos\beta_{o2} - \ddot{\theta} b_{o2} \sin\gamma_{o2} - \dot{\theta}^2 b_{o2} \cos\gamma_{o2}\right.$$

$$\left. - 2\dot{\theta}\dot{\beta}_{o2} L_{po2} \cos\beta_{o2}\right] + M_{pf1}\left[\ddot{\beta}_{f1} L_{pf1} \sin\beta_{f1} + \dot{\beta}_{f1}^2 L_{pf1} \cos\beta_{f1} + \ddot{\theta} b_{f1} \sin\gamma_{f1}\right.$$

$$\left. - \dot{\theta}^2 b_{f1} \cos\gamma_{f1} - 2\dot{\theta}\dot{\beta}_{f1} L_{pf1} \cos\beta_{f1}\right] + M_{pf2}\left[\ddot{\beta}_{f2} L_{pf2} \sin\beta_{f2}\right.$$

$$\left. + \dot{\beta}_{f2}^2 L_{pf2} \cos\beta_{f2} - \ddot{\theta} b_{f2} \sin\gamma_{f2} - \dot{\theta}^2 b_{f2} \cos\gamma_{f2} - 2\dot{\theta}\dot{\beta}_{f2} L_{pf2} \cos\beta_{f2}\right]$$

$$F_{zE} = F_C$$

$$F_{xR} = A_x M_T - M_o \dot{\theta}^2 \Delta X_o + M_R \ell_R \ddot{\xi} + M_{po1}\left[\ddot{\beta}_{o1} L_{po1} \cos\beta_{o1} - \dot{\beta}_{o1}^2 L_{po1} \sin\beta_{o1} + \ddot{\theta} b_{o1} \cos\gamma_{o1}\right.$$

$$\left. - \dot{\theta}^2 b_{o1} \sin\gamma_{o1} + 2\dot{\theta}\dot{\beta}_{o1} L_{po1} \sin\beta_{o1}\right] + M_{po2}\left[\ddot{\beta}_{o2} L_{po2} \cos\beta_{o2} - \dot{\beta}_{o2}^2 L_{po2} \sin\beta_{o2}\right.$$

$$\left. + \ddot{\theta} b_{o2} \cos\gamma_{o2} - \dot{\theta}^2 b_{o2} \sin\gamma_{o2} + 2\dot{\theta}\dot{\beta}_{o2} L_{po2} \sin\beta_{o2}\right] + M_{pf1}\left[\ddot{\beta}_{f1} L_{pf1} \cos\beta_{f1}\right.$$

$$\left. - \dot{\beta}_{f1}^2 L_{pf1} \sin\beta_{f1} + \ddot{\theta} b_{f1} \cos\gamma_{f1} + \dot{\theta}^2 b_{f1} \sin\gamma_{f1} + 2\dot{\theta}\dot{\beta}_{f1} L_{pf1} \sin\beta_{f1}\right]$$

$$+M_{pf2}\left[\ddot{\beta}_{f2}\, L_{pf2}\, \cos\beta_{f2} - \dot{\beta}^2_{f2}\, L_{pf2}\, \sin\beta_{f2} + \ddot{\theta}\, b_{f2}\, \cos\gamma_{f2} - \dot{\theta}^2 b_{f2}\, \sin\gamma_{f2}\right.$$

$$\left.+2\dot{\theta}\dot{\beta}_{f2}\, L_{pf2}\, \sin\beta_{f2}\right]$$

$$F_{XE} = -F_c\,(\xi + \nabla)$$

where $b_{o1} = (\ell_o^2 - 2\ell_o L_{po1}\cos\beta_{o1} + L_{po1}^2)^{1/2}$

$b_{o2} = (\ell_o^2 - 2\ell_o L_{po2}\cos\beta_{o2} + L_{po2}^2)^{1/2}$

$b_{f1} = \left[\ell_o^2 + \ell_x^2 - 2(\ell_o^2 + \ell_x^2)^{1/2} L_{pf1}\cos(\tan^{-1}\frac{\ell_x}{\ell_o} - \beta_{f1}) + L_{pf1}^2\right]^{1/2}$

$b_{f2} = \left[\ell_o^2 + \ell_x^2 - 2(\ell_o^2 + \ell_x^2)^{1/2} L_{pf2}\cos(\tan^{-1}\frac{\ell_x}{\ell_o} + \beta_{f2}) + L_{pf2}^2\right]^{1/2}$

$$\gamma_{o1} = \tan^{-1}\left(\frac{L_{po1}\sin\beta_{o1}}{\ell_o - L_{po1}\cos\beta_{o1}}\right)$$

$$\gamma_{o2} = \tan^{-1}\left(\frac{L_{po2}\sin\beta_{o2}}{\ell_o - L_{po2}\cos\beta_{o2}}\right)$$

TRANSLATIONAL DYNAMICS - CONTINUED

$$\gamma_{f1} = \tan^{-1}\left(\frac{\ell_x - L_{f1}\sin\beta_{f1}}{\ell_o - L_{f1}\cos\beta_{f1}}\right)$$

$$\gamma_{f2} = \tan^{-1}\left(\frac{\ell_x + L_{pf2}\sin\beta_{f2}}{\ell_o - L_{pf2}\cos\beta_{f2}}\right)$$

MISCELLANEOUS DYNAMICS

ENGINE $$T_L = M_R \ell_R A_z (\xi + \Delta) + M_R \ell_R (A_x - \ddot{\theta}\ell_c) - I_{R_{yy}}\ddot{\theta} + I_{R_{yy}}\ddot{\xi} - F_c\epsilon$$

SLOSH $$\ddot{\beta}_{o1} = -2\zeta_{o1}\dot{\beta}_{o1}\omega_{o1} - \left[\frac{A_z \sin\beta_{o1} + A_x \cos\beta_{o1} + \ddot{\theta}(\ell_o \cos\beta_{o1} - L_{po1})}{L_{p01}}\right]$$

$$\ddot{\beta}_{o2} = -2\zeta_{o2}\beta_{o2}\omega_{o2} - \left[\frac{A_z \sin\beta_{o2} + A_x \cos\beta_{o2} + \ddot{\theta}(\ell_o \cos\beta_{o2} - L_{po2})}{L_{po2}}\right]$$

$$\ddot{\beta}_{f1} = -2\zeta_{f1}\dot{\beta}_{f1}\omega_{f1} - \left\{\frac{A_z \sin\beta_{f1} + A_x \cos\beta_{f1} + \ddot{\theta}\left[(\ell_o^2 + \ell_x^2)^{1/2}\cos\left(\frac{\pi}{2} - \beta_{f1} - \tan^{-1}\frac{\ell_o}{\ell_x}\right) - L_{pf1}\right]}{L_{pf1}}\right\}$$

$$\ddot{\beta}_{f2} = -2\zeta_{f2}\dot{\beta}_{f2}\omega_{f2} - \left\{\frac{A_z \sin\beta_{f2} + A_x \cos\beta_{f2} + \ddot{\theta}\left[(\ell_o^2 + \ell_x^2)^{1/2}\cos\left(\frac{\pi}{2} + \beta_{f2} - \tan^{-1}\frac{\ell_o}{\ell_x}\right) - L_{pf2}\right]}{L_{pf2}}\right\}$$

$$\omega_{pn} = \left[\frac{A_z \cos\beta_{pn}}{L_{pn}}\right]^{1/2}$$

VOY-D-330
COMPUTER AND SEQUENCER

VOY-D-330
COMPUTER AND SEQUENCER

1. SCOPE

The Voyager Spacecraft performs its mission automatically to the maximum extent possible. This automatic control is supplemented by ground command to carry out trajectory corrections and to accommodate anomalies that occur during the flight.

The Computer and Sequencer (C&S) described in this section provides the automatic control. The baseline design is described along with alternatives that were considered.

2. FUNCTIONAL REQUIREMENTS

The Computer and Sequencer (C&S) is a cycled, special purpose, digital computer, which generates and distributes the onboard commands necessary for the Voyager Spacecraft to perform its mission automatically. Except for permission to separate the capsule, the C&S obviates the need for any ground command provided that (1) the flight is nominal (all systems are functioning as expected) and (2) trajectory corrections, trajectory bias, instrument calibration, and updating of time dependent or trajectory dependent sequences are not required.

2.1. TIME SEQUENCED FUNCTIONS

The entire nominal flight sequence is pad loaded into the C&S by the Launch Complex Equipment (LCE). The nominal flight sequence includes all of the events in the initial stabilization, cruise, orbit injection, capsule separation, orbit, and occultation modes. The sequencing of these events is carried out automatically by the C&S. Prior to launch, the LCE can command the C&S to read out over hardwire all or part of the information stored in memory. After launch, the command subsystem can command the C&S to read out any part of stored information via telemetry.

All elements of contingency modes which can be identified prior to launch are pad loaded into the C&S by the LCE. Contingency modes include trajectory adjust, orbit adjust, and backup modes. In the event the flight is not nominal, the Command Subsystem is used to modify the sequences stored in the C&S. In the event that contingency modes are required, the Command Subsystem is used to load the missing elements of the required sequence into the C&S. Thereafter, the sequencing of the contingency mode is carried out automatically by the C&S.

Certain events controlled by the C&S are based on functions other than time. Some examples are as follows:

2.2. PLANETARY SCIENCE SEQUENCING

Planetary Science sequencing is based on the argument of the spacecraft. The outboard gimbal of the Planetary Science Package (PSP) rotates the PSP about the normal to the orbit plane. The gimbal angle of the outboard gimbal is equivalent to the argument of the spacecraft and can be referenced to the morning terminator. A measure of this gimbal angle is provided to the C&S by the PSP. The sequencing of the Planetary Science is based on discrete values of this angle.

2.3. LIMB SENSING

Limb sensing is also based on the output of the outboard PSP gimbal. This gimbal is controlled by means of a horizon sensor which can be made to provide an indication of the planet subtended half-angle. The spacecraft is at the morning limb when the outboard gimbal angle is equal to the planet half-angle. When the complement of the outboard gimbal angle is equal to the planet half-angle, the spacecraft is at the evening limb. Indications of these limb passages are generated by the C&S and provided to the PSP.

2.4. ΔV ACCUMULATION

ΔV accumulation is accomplished in a special register. This register is set by the Command Subsystem to the complement of the desired ΔV. During engine firing, pulses from the pulse integrating accelerometer located in the G&C are used to advance this register. When the register reaches its overflow state, the signal is sent out from the C&S to turn off the engine.

2.5. MANEUVER ATTITUDE VERIFICATION

The C&S subsystem includes a 4π steradian digital Solar Aspect Sensor which is used to track maneuver turns. The output of this sensor is telemetered to the ground where it is used to confirm maneuver attitude.

2.6. EARTH OCCULTATION SENSOR

The C&S subsystem includes an earth occultation sensor. This sensor is mounted on the High Gain Antenna and has a field of view approximately the same as the main lobe of the High Gain Antenna. The C&S uses this sensor to sense the onset and termination of earth occultation. Based on the output of this sensor the C&S provides Earth occultation signals to the various using subsystems.

2.7. ANTENNA CONTROL

Certain events in the mission are highly repetitive. The control of the high gain antenna orientation is an example. Another example might be the control of one or more gimbals in the PSP. The high gain antenna gimbals are corrected in steps of 3/16 degree when the accumulated error reaches 3/32 of a degree. The program for controlling these angles is stored in the C&S. The gimbal angle time history is approximated by means of connected straight line segments. The error in the approximation is less than 3/16 of a degree. The time between 3/16 degree changes in gimbal angle, appropriate to each line segment, is stored in the C&S. The C&S increments the gimbal angle at the rate appropriate for the current line segment. This rate is changed when a new line segment is encountered.

2.8. CRITICAL EVENTS

Certain C&S controlled events are highly critical to mission success. Among these are maneuver turns, start and stop propulsion engine, and separate capsule. For these events, neither false commands (command at the wrong time) nor false dismissals (no command at the right time) can be tolerated. The C&S control of these events is organized so that the number of piece parts involved in controlling each individual event is minimized and no single piece part failure can cause either a false command or a false dismissal.

2.9. SEMI-CRITICAL EVENTS

The remaining events that are controlled by the C&S have a lesser degree of criticality. If such an event were to be falsely dismissed, there is sufficient time in the sequence to back-up the C&S with the Command Subsystem. Therefore, for the remaining events controlled by the C&S, the C&S is organized so that no single piece part failure shall cause false commands.

2.10. POWER INTERRUPTION

The implementation of the C&S is such that a temporary interruption of power will not cause a catastrophic loss of memory. Energy stored in decoupling capacitors in the C&S is used to maintain useful power for a sufficient period of time to complete a cycle in the C&S. Between cycles the states of all critical functions are maintained in non-volatile devices. Thus, the consequence of a temporary power outage is that spacecraft time is interrupted for the duration of the outage.

2.11. C&S TIME BASE

The C&S receives a 32-pps synchronization signal from the power subsystem. This signal is used by the C&S to generate all of its necessary timing functions.

2.12. C&S ENABLE

The C&S is enabled by the separation switch. C&S time starts at the enabling of this switch.

2.13. FLEXIBILITY

The C&S is designed to incorporate approximately 20% excess capacity over and above that required to carry out the currently defined mission. This excess capacity is in the form of 20% excess memory as well as 20% excess capacity in output functions.

2.14. TEST

The design of the C&S is such that the entire mission sequence can be cycled out in four hours or less. This feature is included to facilitate C&S checkout and systems cycling.

3. DESIGN CONSIDERATIONS

3.1. SUMMARY OF ALTERNATIVE C&S IMPLEMENTATIONS

Three alternative implementations were considered in the Task B Study. The salient differences between the three alternatives are listed in tabulated form below. All of the figures given in the table are based on a simplex design; that is to say, none of the designs at this phase in the study included redundancy. Redundancy was added to the recommended system after the selection was made. It must also be noted that other changes were made to the recommended system after it was selected. These changes were the result of a more detailed design that was accomplished after the selection.

Comparatively speaking, alternative No. 2 is undesirable because of its significantly lower reliability. This lower reliability stems almost entirely from the large memory size required to implement this alternative. The large memory requirement in turn stems from the fact that this alternative does not implement a straight line segment approximation for gimbal angle control. Instead, the time for each change in gimbal angle is stored as a separate word in the C&S. In view of this lower reliability expectation, alternative No. 2

Table 1. C&S Alternatives

Characteristic	Alternative No. 1	Alternative No. 2	Alternative No. 3
Memory Organization	Random	Sequential	Sequential
Special Sequence, Identification	4 flag bits on each word identify the sequence to which it belongs	Each special sequence is in a separate part of memory Jump commands are used to go from one sequence to another When returning to master sequence the C&S picks up where it left off	Same as No. 2
Time identification	Each word has a time tag indicating when it should be executed Words with the same time tag are executed one sec apart in the order in which they are scanned	Same as No. 1	Each word has a time tag indicating the number of time increments to the next word in the sequence. The zero time tag indicates that the next word should be executed during the next 1 sec interval
Time Base	Each special sequence has its own time base (1 sec or 1 min) which is used throughout the sequence Master sequence has a 1 hr time base	Same as No. 1	Any one of three time bases may be used in any sequence (1 sec, 1 min, 1 hr) Time base can be changed by a stored command, or by the command subsystem

Table 1. C&S Alternatives (Continued)

Characteristic	Alternative No. 1	Alternative No. 2	Alternative No. 3
Memory Scanning Rate	The entire memory is scanned one time during each time increment	At the start of each time increment, the C&S scans the words appropriate to this increment When it encounters a word to the subsequent increment, it dwells on that word until the proper time	The C&S dwells on the current word until the appropriate time for the execution of the next word
Gimbal Angle Control	Connected straight line segment approximation with 1/4-degree accuracy	One stored command for each 1/4-degree change in gimbal angle	Same as No. 1
Flexibility (or contingencies after launch)	All spare and used word locations in master sequence are available for contingencies	Same as No. 1 except a jump command is required to enter contingency sequence	Same as No. 2
Parts Count			
• Logic Elements	875 to 1054	669 to 814	1168 to 1402
• Memory Elements	13824	34628	9632
• Flip Flops	383 to 460	303 to 363	248 to 294
• Sense Amplifiers	1	1	19
• Memory Drivers	150	135	93
• Magnetic Logic Drivers	14	25	25
Logic Drivers	22 to 27	53 to 63	47 to 56
• Diodes	1024	3520	

Table 1. C&S Alternatives (Continued)

Characteristic	Alternative No. 1	Alternative No. 2	Alternative No. 3
Reliability (probability of 10,000 hour failure free operation - simplex design)	0.28	0.15	0.29
Power			
• Operate	27 to 30 watts	16 to 20 watts	22 to 27 watts
• Stand-By	20 to 24 watts	13 to 17 watts	20 to 24 watts

was dropped from further consideration. The tradeoffs between alternative number one and alternative number three are not definitive. However, for purposes of the Task B alternative No. 3 was selected for analysis in greater depth. The adequacy of the selected design has been confirmed during the Task C and Task D studies.

3.2. NEW REQUIREMENTS AND TECHNOLOGICAL ADVANCES

The design of the Task B C&S has been reviewed in light of updated functional requirements and technological advances. The Task B functional design has been found adequate to meet the updated functional requirements. The principal changes in requirements affecting the C&S are a change in gimbal angle accuracy from 1/4-degree to 3/16 degree and a change from two engines to a single engine. The former can be readily accommodated without modification of the C&S. The latter requires only a change in the destinations of two of the highly critical commands.

Consideration was given to incorporating optoelectronic coupling devices (Milestone Report VOY-P-TM-10) and large scale integrated circuits (Milestone Report VOY-P-TM-15). Although they are potentially useful, their use with confidence for a 1973 mission is precluded by the state of development and paucity of reliability data. On the other hand, the use of nondestructive readout memory devices (Milestone Report VOY-P-TM-19) was recommended as their development was much further along.

4. DESCRIPTION

The following is the functional description of the recommended system.

The C&S consists of five units:

a. The Master Sequencer which receives from the LCE or Command Decoder, stores and issues all quantitative commands and all semi-critical discrete commands (except Gimbal Articulation and PSP commands).

b. The Time-To-Go and ΔV Registers which receive command data from the C&S Master Sequencer, LCE, or Command Decoder; store the data; and issue commands to start and stop pitch, roll and yaw turns, start and stop engine burn, and separate the capsule.

c. The Gimbal Sequencer which receives quantitative commands from the C&S Master Sequencer or the Command Decoder and generates discrete articulation commands to High Gain Antenna gimbals and the PSP gimbals.

d. The PSP Control Logic which receives quantitative commands from the C&S Master Sequencer or the Command Decoder and generates commands and control signals to the Data Automation Subsystem.

e. The Telemetry Registers which are buffers for C&S digital telemetry data.

4.1. MASTER SEQUENCER

The Master Sequencer, shown in Figure 1, stores command data words in time sequential order of command execution. Command execution time is signalled by the overflow of a binary counter preset to the 2's complement of the time between previous command and the next command. Counter preset numbers and stepping rates are specified by the stored command data words.

The Master Sequencer has three modes of operation:

a. The Update Mode is used when new command data are being written into the magnetic core memory.

b. The Readout Mode is used when the contents of memory addresses specified by LCE or radio command are read out to the LCE or telemetry for verification.

c. The Normal Mode is used whenever a command is issued by the Master Sequencer.

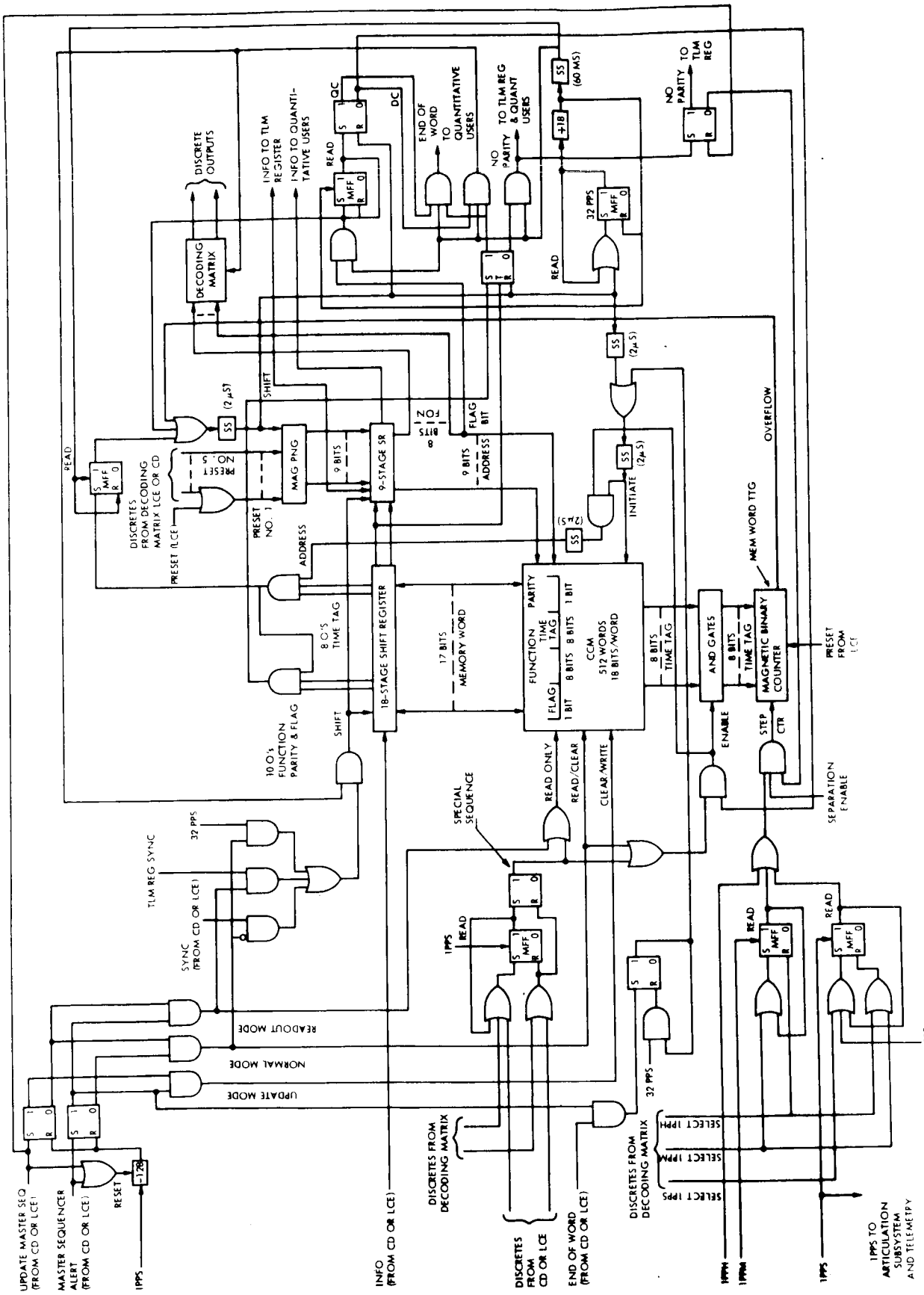

Figure 1. Block Diagram for Master Sequencer of C&S

The Master Sequencer receives command data from the Command Decoder on two lines. One line carries information bits: the other, synchronization pulses. Command data word structure is illustrated in Figure 2.

Bits 1 to 9 specify the memory location in which bits 10 to 27 are to be stored. Bit 10 is a parity bit which is one if the number of 1's in bits 11 to 27 is even, and zero if the number of 1's is odd. Bits 11 to 18 contain the 2's complement of the time to readout of the next command data word from memory.

An exception is the all 0's time tag, which indicates that the next command word is to be read out of memory immediately after execution of the current command.

Bits 19 to 26 define the destination of the current command. Bit 27 is one if the next command in the Master Sequence is a quantitative command, and zero if the next command is a discrete command.

A pulse appearing on the update Master Sequencer line followed by a pulse on the Master Sequencer Alert line places the Master Sequencer in the Update Mode. The alert pulse is followed by a 27-bit command data word which is shifted into the 18-stage and 9-stage shift registers. Upon the receipt of an end-of-word signal, a single parallel clear-and-write memory operation is initiated. The contents of the memory address specified by the word

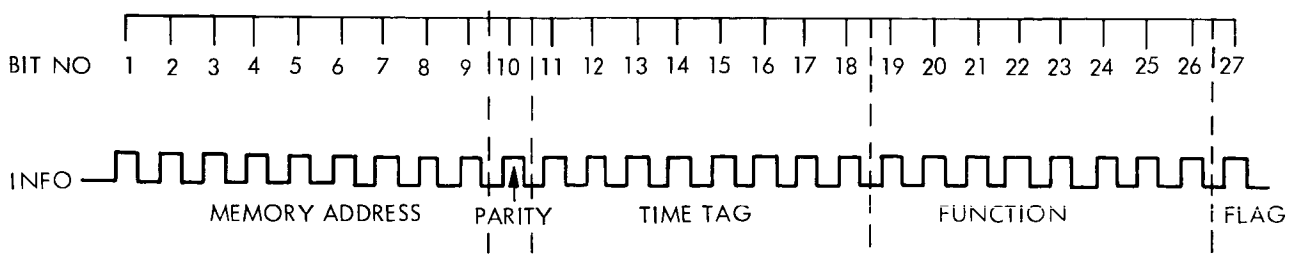

Figure 2. Command Data Word Structure

in the 9-stage register are erased and replaced by the word in the 18-stage register. This procedure is repeated each time a pulse appears on the alert line. If two successive alert pulses do not occur within a fixed period (approximately two minutes), the Normal Mode is automatically initiated by the Master Sequencer. Repetition of the pulse on the Update Master Sequencer line is not required when more than one memory word is being updated if the time between successive alert pulses does not exceed two minutes.

The Readout Mode is initiated by the occurrence of an alert pulse not immediately preceded by an update pulse when the Master Sequencer is in the Normal Mode. The alert pulse is followed by a 27-bit command data word consisting of 9 memory address bits and 18 filler bits, which are shifted into the 18-stage and 9-stage registers. An end-of-word pulse initiates a single parallel read memory operation. The contents of the memory address specified by the word in the 9-stage register are read out to the 18-stage register. The contents of the 18-stage and 9-stage registers are then shifted out of the registers to the Telemetry Registers unit. As in the Update Mode, the procedure is repeated each time an alert pulse occurs. The Normal Mode is automatically initiated if the time between successive alert pulses exceeds approximately two minutes.

The Normal Mode is essential to the issuance of any command from the Master Sequencer. Update or readout operations must not be attemped when a command execution time is imminent. However, the counting operation that leads to command execution continues in all modes. Before launch a preset signal from the LCE places the 8-stage magnetic binary counter and the 9-stage pseudo-noise generator (PNG) in known states (all 1's, for example) and selects a timing base of 1 pulse per second. At separation, incrementing of the binary counter at the 1 pps rate is enabled. Overflow of the counter initiates the following sequence of events.

a. The 9-stage magnetic PNG is shifted to its next state. At the same time the initial state of the PNG is transferred to the 9-stage shift register.

b. The entire contents of the memory address defined by the number in the 9-stage shift register are read out to the 18-stage shift register. The eight bits of time tag are also read out to the 8-stage binary counter.

c. The word in the 18-stage register is examined. If an all 0's time tag is detected, a flip-flop is set which enables initiation of the next memory readout immediately after issuance of the current command. If the entire 18 bits are 0's, indicating a vacant memory address, a parity check is forced by setting the parity flip-flop. The all 0's function is a dummy function.

d. The contents of the 18-stage and 9-stage registers are shifted at the rate of 32 shift pulses per second.

e. When 18 shift pulses have been counted and if odd parity has been detected, decoding of the eight function bits now situated in the 9-stage shift register is enabled and a discrete command is issued by the Master Sequencer. If the next command will be quantitative, the discrete command notifies the quantitative user to accept the next bits shifted out of the Master Sequencer.

f. The state of the flag bit which indicates whether the next command will be discrete or quantitative and which is now situated in the input stage of the 9-stage register is stored in a flip-flop. If an all 0's time tag has been detected or if the next command is quantitative, readout of the next word from memory is initiated at this time.

g. If an all 0's time tag has not been detected, readout of a memory word is initiated by overflow of the 8-stage binary counter. This is the next word of the Master Sequence if that word contains another discrete command. It is the next following word of the sequence if the intervening word is a quantitative. That is, the discrete command preceding a quantitative command defines the readout time of the command that follows the quantitative command. Bits to the binary counter are inhibited when a quantitative command is read out of memory.

The procedure outlined above is followed for all other discrete commands of the Master Sequence. The procedure for quantitative commands differs only in the following respects. No presetting of the binary counter occurs when a quantitative command word is read out of memory. An end-of-word signal on a common line to all quantitative command users is issued instead of a discrete command output when 18 shift pulses have been counted and if odd parity has been detected.

In the event that a discrete command word fails the parity test, issuance of the current command and all subsequent commands is inhibited until a command to proceed is received from the ground. If a quantitative command word fails the parity test, a no-parity signal instead of an end-of-word signal is sent to all quantitative command users. In either case, a no-parity signal to telemetry is maintained until reset by radio command. This procedure is discussed in Milestone Report VOY-P-TM-22.

At separation, incrementing of the 8-stage binary counter is initiated at a rate of 1 pps. However, any of three time bases (1 pps, 1 ppm, or 1 pph) can be selected thereafter by discrete command from the decoding matrix.

Quantitative command data are relayed to the Master Sequencer by the Command Decoder at a maximum rate of 1/2 bps. The Master Sequencer can be updated by the LCE at much higher rates. The memory is capable of storing data at a rate of at least 100,000 words per second. However, in order to read out specified addresses at above-normal rates, a higher-frequency pulse train must be substituted for the 32-pps train normally used to shift data out of the Master Sequencer. This is also necessary for accelerated operation of the Master Sequencer during subsystem and system testing. All lower frequencies used in the Master Sequencer are derived from the 32-pps train.

The 9-stage magnetic PNG which controls the order of Master Sequencer command execution is preset by the LCE to the memory address of the first command word of the Master Sequencer. The PNG can be placed in this state or in any of four other states by discrete commands from the decoding matrix or the command subsystem. The other four states are the initial memory addresses of four Special Sequences (Trajectory Adjustment, Orbit Adjustment, Orbit Insertion, and Capsule Separation). The discrete commands that effect PNG presetting also define the operating mode of the memory. Master Sequence command words are erased after readout whereas Special Sequence command words are preserved.

The Master Sequencer proceeds in time sequential order through the Master Sequence until it encounters a command (from memory or CD) to jump to a Special Sequence. It then proceeds through the Special Sequence until a command (the last of the sequence) to return to Master Sequence is encountered. The Master Sequencer moves rapidly through the empty addresses representing previously issued commands and takes up the Master Sequence where it left off.

Redundancy is applied to the Master Sequencer to guard against issuance of a command to the wrong destination (false command) but not against failure to issue a command (false dismissal). False dismissal of any Master Sequencer command can be tolerated because of the back-up capability of the Command Decoder. However, a false command from the Master Sequencer can, in some instances, have a catastrophic effect on the mission.

Each command output switch is such that a single part failure can produce a permanent switch opening, but two part failures are required for permanent switch closing. In the decoding matrix, each AND gate can fail in the zero state as the result of one part failure but at least two part failures are required for failure in the one state.

Within the memory, the decoding gates that provide address driver inputs have the same fail-safe characteristics as those in the decoding matrix. The parity check prevents false commands resulting from single failure of driver, drive line, core, or stage of the 18-stage shift register.

All logic circuits other than those included in the command output switches, decoding matrix, memory, and 18-stage shift register are triplicated and majority voted at the interfaces with the memory and the decoding matrix.

Non-volatility of the Master Sequencer state in the event of temporary power failure is maintained in the following ways. A magnetic PNG and a magnetic binary counter preserve the memory address and time to next memory readout. Memory drivers and control logic are

designed to provide no false outputs as a result of power outage or restoration. Magnetic flip-flops (one-stage shift registers) preserve the timing base, special sequence status, and next command type. Semiconductor flip-flops not controlled by magnetic logic are designed to assume the reset state automatically upon application of power.

4.2. TTG REGISTERS

The C&S contains eight Time-To-Go (TTG) registers, listed in Table 2.

All TTG registers, as shown in Figure 3, are triplicated and majority voted at the outputs.

A pulse appearing on its individual alert line commands a TTG Register to accept the next command data word (consisting of information and synchronization bits) appearing on lines shared with other C&S units. At this time, the register functions as a simple shift register.

Table 2. Time to Go Registers

Register	Source of Data	Command Output
TTG 1	CD or LCE	Separate capsule
TTG 2	CD or LCE	Start Engine (High Thrust)
TTG 3	CD or LCE	Stop engine (backup)
TTG 4	C&S, CD, or LCE	Stop all other turns
		Start negative positive pitch turn
TTG 5	C&S, CD, or LCE	Stop all other turns
		Start negative positive view turn
TTG 6	C&S, CD, or LCE	Stop all other turns
TTG 7	CD or LCE	Start Engine (Low Thrust)
TTG 8	C&S, CD, or LCE	Stop all other turns
		Start negative positive roll turn

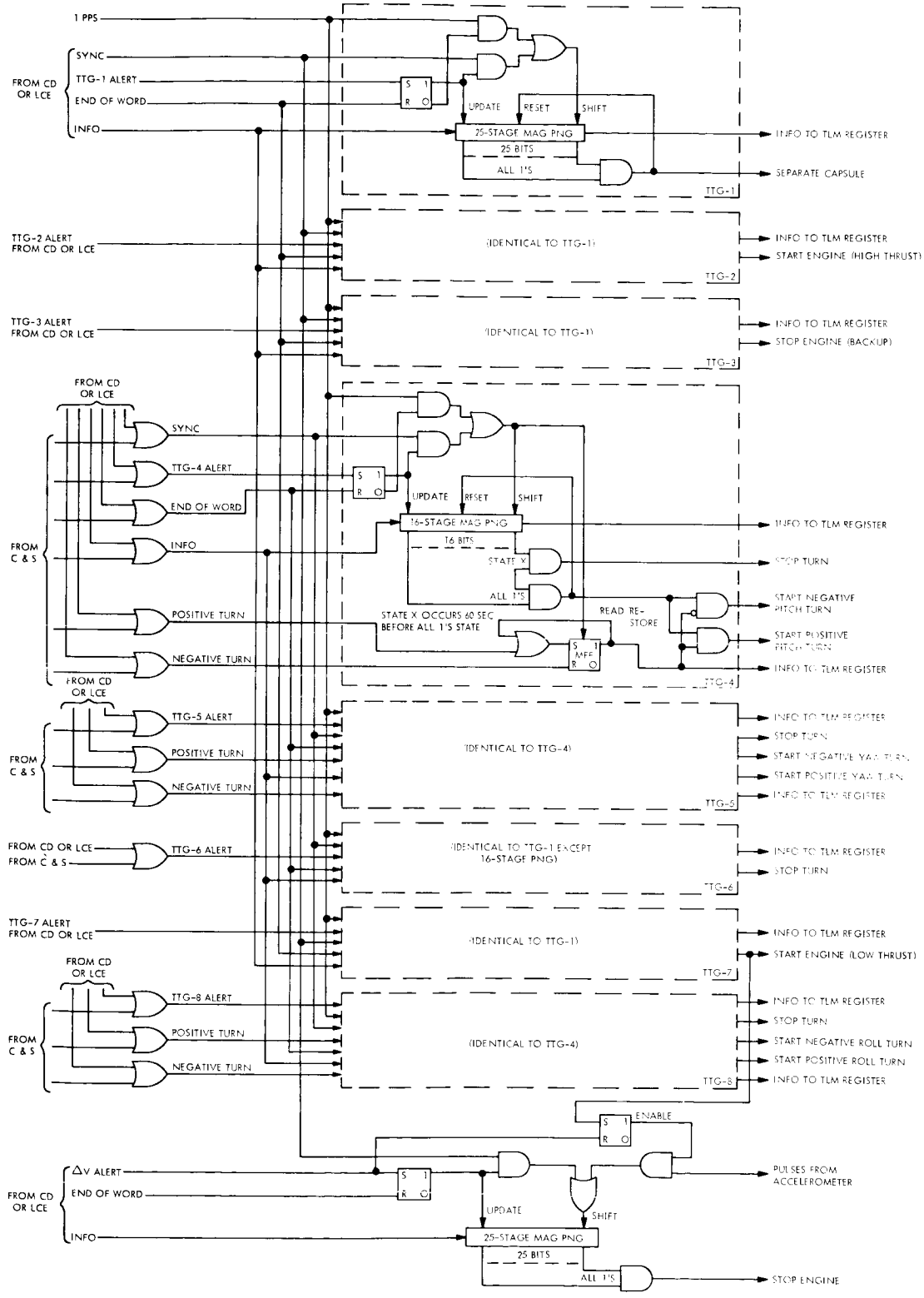

Figure 3. Block Diagram for TTG and ΔV Registers of C&S

Upon receipt of an end-of-word signal (also shared with other C&S units), the register is closed to further command data not preceded by an alert pulse and commences to function as a pseudo-noise generator (PNG). The PNG is shifted once per second until the all 1's state (or, in some instances, the state generated one minute before the all 1's state) is detected by an AND gate which then generates an output signal to the appropriate user.

If the state decoded is that occurring one minute before the all 1's state, shifting continues until the all 1's state is decoded and a second discrete output signal is generated. Upon detection of the all 1's state the PNG is reset to the all 0's state and thus inactivated.

In TTG-4, -3 or -8, the state (specified by discrete command when the register is loaded) of a magnetic flip-flop determines whether a positive or negative turn is initiated.

TTG-1 and TTG-2 are loaded by the LCE and begin their calculations of time to command readout before launch. Each of the other registers is loaded with an all 0's command word by the LCE and thereby inactivated until meaningful data are loaded by the CD or the Master Sequencer later in the mission.

Non-volatility of the states of the TTG Registers is maintained by the use of magnetic registers and magnetic turn polarity flip-flops. The flip-flops that enable PNG shifting and issuance of the capsule separation command automatically assume the reset state upon application of power.

4.3. ΔV REGISTER

The ΔV register, shown in Figure 3, is a 25-stage magnetic PNG which generates the command to stop the propulsion engine. Information from the CD is loaded into the register by shift pulses which are also generated by the CD. The register must first receive a ΔV alert from the CD in order to be loaded. An end-of-word signal from the CD closes the register

to additional information not preceded by an alert pulse. Issuance of the command to start the engine enables shifting of the PNG by pulses received from the accelerometer. When the all 1's state of the PNG is detected, a command output is generated.

The ΔV register is triplicated and majority voted at the output. Non-volatility of the state of the ΔV register is maintained by the use of a magnetic register and non-magnetic flip-flops that automatically assume the reset state upon application of power.

4.4. GIMBAL SEQUENCER

The C&S generates either a positive or a negative increment to each of four gimbals, A, B, C, and D (two gimbals of the High Gain Antenna and two gimbals of the PSP). Each gimbal uses the logic which is shown in Figure 4. The organization is such that the time to the next output pulse and the sign of the next output for each gimbal are stored in counters. Until this information is changed by a quantitative command, the outputs to any one gimbal will be generated at a constant rate. This rate is usually different for each of the four gimbals. The four counters are loaded from a common source, a 14-stage shift register.

The 14-stage shift register is loaded with a quantitative command from either the C&S or the CD. The discrete which precedes the quantitative data sets a flip-flop which permits read in of the quantitative data under control of either an external shift (if CD is used) or 32 pps (if C&S is used). When end of word occurs, further read in to the register is inhibited.

The data in the shift register consists of (1) 11 bits - time to next output in hours, (2) 2 bits - gimbal designation and (3) 1 bit - direction of gimbal movement.

The 2-flag bits select one of the four gimbal sequencers. When end of word occurs, indicating that a data word has been loaded in the shift register, the selected sequencer receives an enable which (1) resets a binary down counter, (2) selects the proper sign of the next outputs and (3) generates a delayed enable, which stores the 11 data bits into a binary up counter.

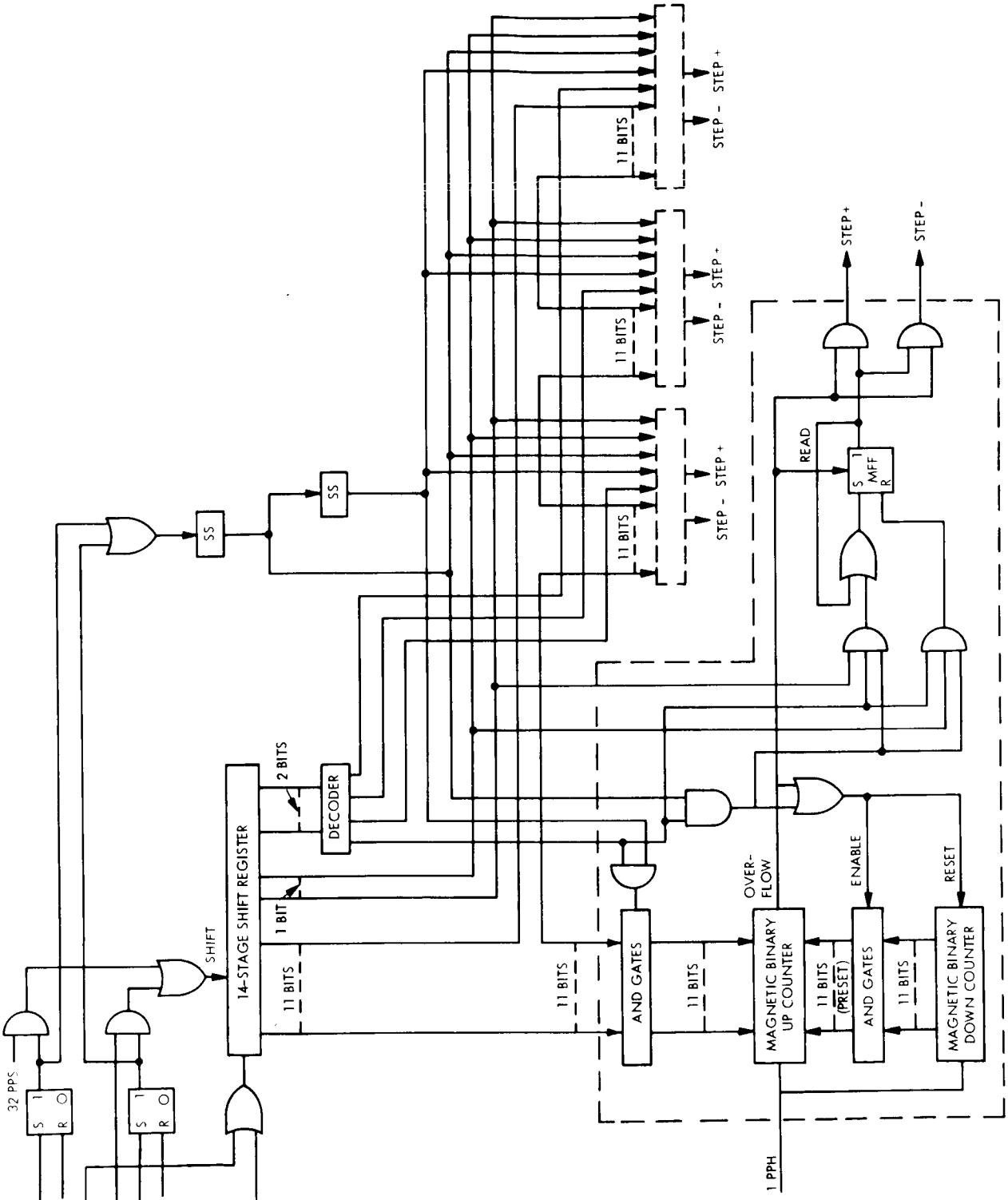

Figure 4. Block Diagram for Gimbal Sequencer of C&S

The up counter contains the 2's complement of the time to the next output and the down counter contains zero. At this time, incrementing of both counters is started, at a 1 pph rate. When the up counter overflows, it generates the gimbal output, stores the contents of the down counter in itself, and resets the down counter. The cycle then repeats, with the up counter again containing the 2's complement of the time to the next output and the down counter containing zero. This process repeats until the contents of the up counter are changed by quantitative data addressed to this gimbal sequencer.

Redundancy is utilized to protect against a runaway condition in the Gimbal Sequencer. Each of the AND gates which convey data to the up counters can fail into the zero state as the result of one part failure but each requires at least two part failures for failure into the one state. The Gimbal Sequencer is otherwise non-redundant.

Magnetic up and down counters preserve the state of the Gimbal Sequencer during power outage.

4.5. CONTROL OF SCIENCE SEQUENCE

The C&S calculates the time for initiation and termination of the science data acquisition sequence. Identical circuitry is used for each function and is shown in Figure 5.

A ten stage shift register is used to store a 10-bit turn on (off) reference angle. This register is loaded with a quantitative word from either the C&S or the CD. The word represents the 2's complement of the desired turn on angle with respect to gimbal E negative stop. The discrete command which precedes the quantitative data sets a flip-flop which selects the source of shift pulses for the incoming data. This source is either the CD or the C&S 32 pps. The end of word signal stops the shifting in of the reference word and generates a reset to a 10-stage down counter, and enables an irrelevant transfer of its contents to a 10-stage up counter. A delayed transfer of the 10-stage shift register to the 10-stage up counter then occurs. Both counters are incremented by gimbal E pulses generated as desired in Task A until the up counter overflows. This generates the science turn on, stops incrementing both

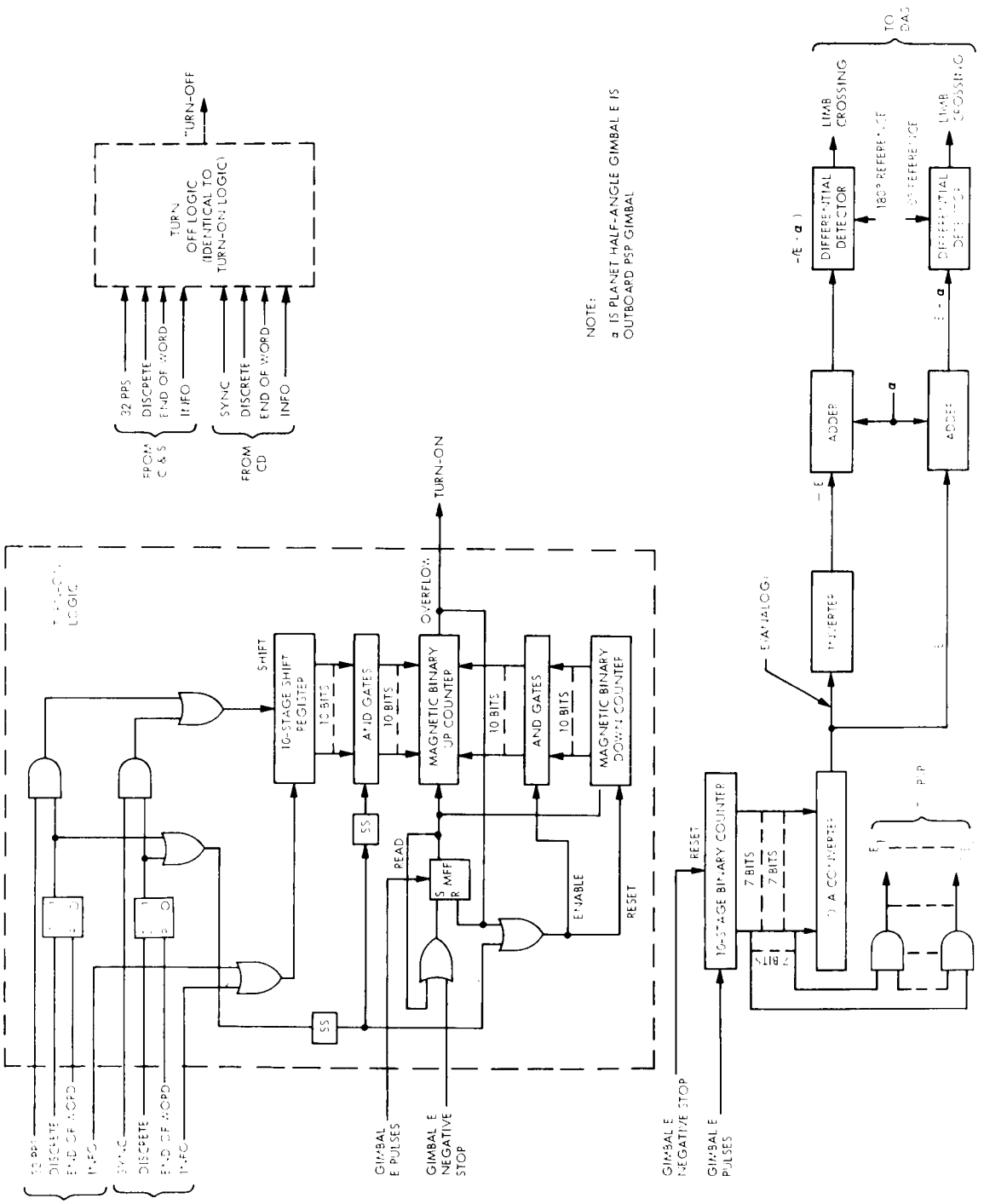

Figure 5. Block Diagram of Science Sequence Control Logic of C&S

counters even though gimbal E pulses still occur, and resets the down counter which results in its contents (specifically - the 2's complement of the desired gimbal E angle) being transferred to the up counter. When gimbal E negative stop occurs, the gimbal pulses will cause the process described to repeat.

The purpose of the magnetic counters is to provide a means of continuing the process described after a power failure without requiring an update from the ground link.

Redundancy is utilized to protect against a runaway condition. Each of the AND gates which convey data to the up counters can fail into the zero state as the result of one part failure but require at least two part failures for failure into the one state. Science Turn On/Off is otherwise non-redundant.

4.5.4. Limb Crossing Computation

A 10-stage binary counter will accumulate gimbal E pulses for the total angular excursion of the gimbal. The contents of the counter are continuously converted to a DC analog of the angular position.

This voltage is added to α, an analog signal proportionate to the planet half-angle, directly and through an inverter. The resultant angle E - α is compared to an analog equivalent of a 0-degree reference in a differential detector and, when the two are equal, the transitional output of the detector will indicate limb crossing. The equality of - (E + α) to a 180-degree reference voltage in another detector will also indicate limb crossing. Several discrete positions of the angle accumulator are decoded and returned to the PSP.

Limb-crossing-computation circuits are non-redundant. Their states are not preserved during power outage.

4.6. TELEMETRY REGISTERS

The C&S contains three 28-stage shift registers which supply information to telemetry. These are: (1) memory word and address, (2) multiplexed TTG, and (3) C&S status word. The block diagram is shown in Figure 6.

4.6.1. Memory Word and Address TLM Register

When a memory initiate signal is generated, this logic: supplies 32 pps to TLM for sync, shifts memory word and address into the shift register at a 32 pps rate, counts 28 of the 32 pps pulses, shuts off the sync, stops loading the register, and enables the serial readout of the register to TLM by external shift.

4.6.2. Multiplexed TTG TLM Register

There are 24 TTG registers in the C&S, (eight triple redundant registers). This TLM register: (1) reads the output of one TTG register in to the TLM register at a 32 pps rate. After 28 shift pulses are counted, it enables read out of the TLM register by external shift. After 28 external shift pulses are counted, it (2) switches to the next TTG register, and repeats (1) after the 24th TTG register is read out, it starts again with the 1st.

4.6.3. C&S Status Word TLM Register

When an external TLM gate is applied to the C&S, this register samples 25 C&S data bits and, under control of an external shift, reads them out to TLM. The data which is sampled and the number of register stages required for each is as shown.

	No. Bits		No. Bits
Sign Turn 1	1	C&S Time Base	2
Sign Turn 2	1	C&S Mode	2
Sign Turn 3	1		
Memory Address	9	Parity	1
Memory Word TTG	8		
		Total	25

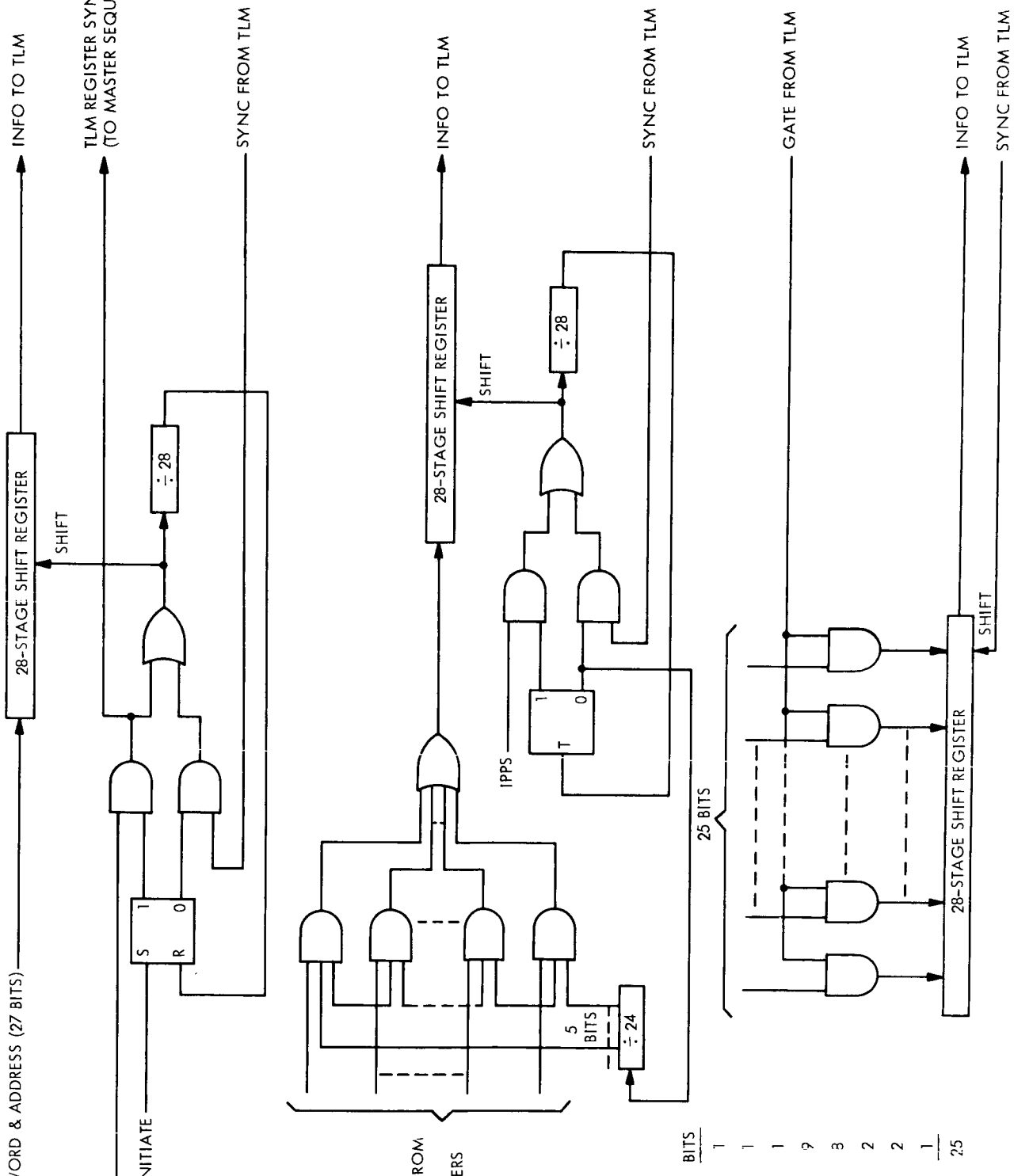

Figure 6. Block Diagram for Telemetry Registers of C&S

4.7. MASTER SEQUENCER MEMORY

The key component of the Master Sequencer is a non-destructive readout, parallel read/write, coincident-current, magnetic-core memory with a capacity of 512 eighteen-bit words. The memory has three modes of operation: clear/write, read/clear and read only (no clear). Cycle time is less than 10 microseconds for a clear/write or read/restore operation, less than 3 microseconds for a read only operation.

The memory receives the following inputs:

(a) Nine parallel bits specifying one of 512 possible memory addresses.

(b) Eighteen parallel bits of information to be stored when clear/write operation is initiated.

(c) A signal on one of three lines specifying memory operating mode.

(d) Signal on one line to initiate a memory operation.

Memory output is eighteeen parallel bits of information when read/clear or read only operation is initiated.

The decoding gates that provide input signals to the address drivers are of fail-safe design. Failure of a single part can cause gate failure into the zero state (that is, the state for driver turn-off); failure of at least two parts is required for gate failure into the one state.

Memory contents are retained intact despite power interruption. That is, no false drive currents are generated to cause destruction of data when power goes off or comes on. Energy stored in decoupling capacitors is used to maintain useful power long enough for completion of a memory cycle. This matter is further discussed in Milestone Report VOY-P-TM-27.

4.8. SOLAR ASPECT SENSOR

The C&S Subsystem contains a Solar Aspect Sensor which provides telemetered data for use in maneuver confirmation.

The sensor consists of five 2-axis heads. Each head is located such that it has an unobstructed field of view of 120 degrees x 120 degrees. The five heads combined provide a spherical, unambiguous, 2-axis indication of solar aspect relative to the spacecraft coordinate system. The output of each head consists of 14 parallel digital signals (7 in each of two axes) which represents a gray coded indication of solar aspect as seen by that head. In addition, each head provides an analog signal which is proportional to the incident solar flux. The associated electronics selects the head with the highest incidence flux. It provides three parallel digital bits indicating which head was selected, and 14 parallel digital bits indicating the solar aspect as seen by the selected head. These 17 bits are provided as inputs to the telemetry subsystem.

4.9. EARTH OCCULTATION SENSOR

C&S Subsystem contains an earth occultation sensor. The sensor is mounted on the High Gain Antenna. It has two fields of view, each of which is approximately the same size as the main lobe of the high gain antenna. The primary field of view is directed parallel to the antenna axis. The secondary field of view is directed into space. The sensor consists of an infrared radiometric balance device and associated electronics. The electronics is designed such that if any part of the Mars planetary disc enters the primary field of view of the sensor, a signal indicating occultation is provided. The sensor is designed so as to be undamaged if the sun enters any part of its field of view.

5. PHYSICAL CHARACTERISTICS

The total weight of the C&S subsystem is 35 pounds. The subsystem requires 60 watts at 2.4 kHz. The volume of the subsystem is approximately 1200 cubic inches. Figure 7 indicates the layout of the C&S in bay No. 14.

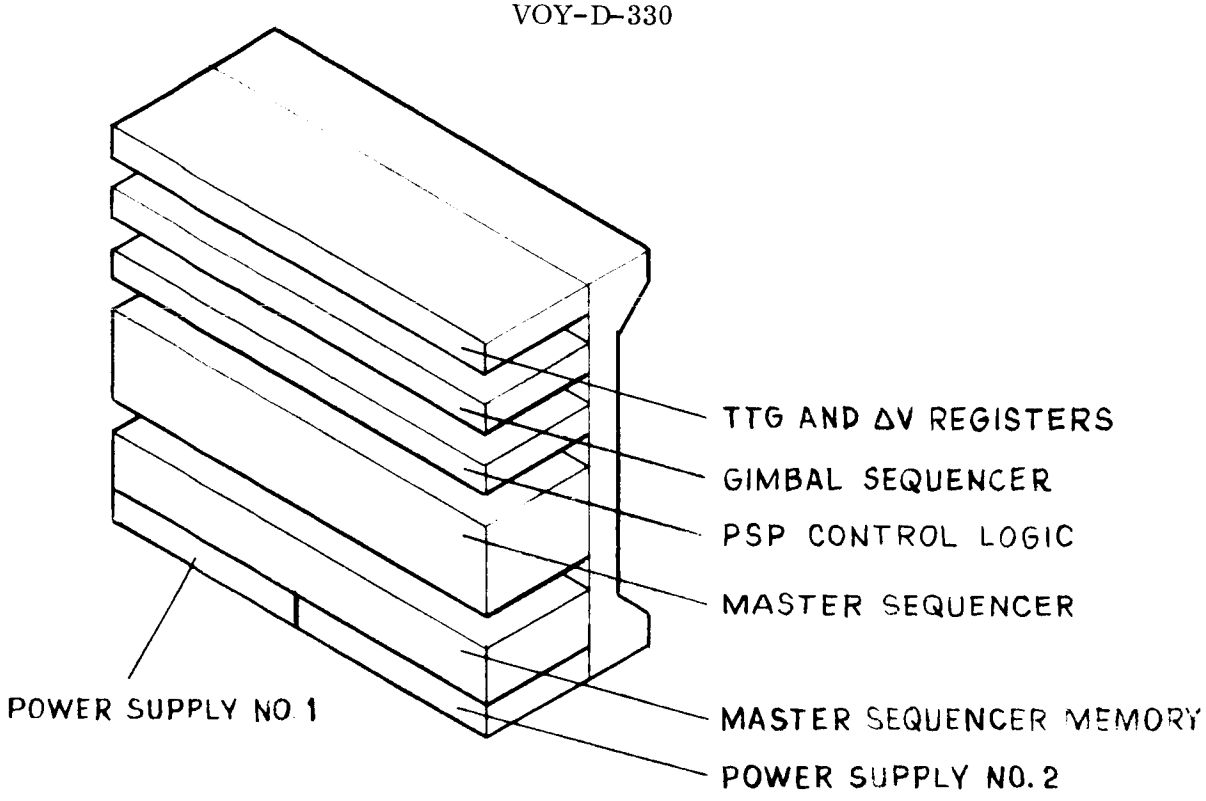

Figure 7. Bay 14 Layout

6. INTERFACES BETWEEN THE C&S AND OTHER SUBSYSTEMS

6.1. MECHANICAL INTERFACES

6.1.1. Structure

The C&S electronics is mounted to the structure in Electronic Assembly No. 14. The solar aspect of the C&S subsystem is mounted on the periphery of the solar array. Five sensor elements are used. Each sensor is mounted such that it has an unobstructed field of view of 120 degrees by 120 degrees. The combined fields of view of the five sensors covers 4π steradians. The earth occultation sensor of the C&S subsystem is mounted on the high-gain antennas. This sensor has two fields of view. One is parallel to the main lobe of the antenna, the other is directed into space. Each field of view is approximately the same in size as the main lobe of the antenna. Alignment and mounting surfaces are provided by the Structural and Mechanical subsystem.

6.1.2. Thermal

The C&S electronics dissipates 60 watts in Electronic Assembly No. 14.

6.2. ELECTRICAL INTERFACES

6.2.1. Power

The C&S receives 2.4 kHz power from the power subsystem. The power is provided on two separate pairs of lines. The combined C&S load on these lines is 60 watts. In addition, the power subsystem provides a 32-pps synchronizing signal to the C&S.

6.2.2. Telemetry

The C&S provides the following outputs to telemetry:

a. A 28-bit digital word which consists of the sampled state of 24 time to go registers. Subcommutation between the 24 TTG registers is carried out within the C&S.

b. A 28-bit digital word which consists of the word last executed by the C&S, the address of that word, and the number of time increments to go to the next word.

c. A 25-bit digital word which consists of one bit indicating parity error, two bits indicating C&S operating mode, two bits indicating C&S time base, three bits indicating signs stored in the turn registers, nine bits indicating the address of the word last executed, and eight bits indicating the number of time increments to the next word.

d. A 21 bit digital word indicating the output of the solar aspect sensor. The above outputs to telemetry are stored in buffer registers by the C&S and scanned out serially by the telemetry subsystem. The telemetry subsystem provides a gating signal indicating that a word is being scanned out, as well as the pulses necessary to scan out the word.

In addition to the above outputs to telemetry, the C&S also provides indications of four power supply voltages. These outputs are conditioned to fit within the zero to 3-1/2-volt telemetry format.

6.2.3. Output to Users

The C&S provides discrete outputs to various other subsystems.

The C&S provides the DAS with discrete outputs indicating limb crossings, terminator crossings, turn on/off commands, and other discrete events based on the argument of the spacecraft (as derived from the outboard gimbal of the PSP). Discrete outputs from the C&S are mechanized as normally open, DC isolated, semi-conductor switches. The output event is indicated by a 60 (±10) ms closure of the switch.

The C&S provides quantitative commands to the capsule and to the Science subsystems. These quantitative commands consist of 16-bit binary coded words. The output is in the form of a DC isolated normally open semiconductor switch. Logical 1's are indicated by a 30-ms switch closure, logical zero's are indicated by the open state of the switch. The output of this semi conductor switch is provided in common to all quantitative command users. Another output line is also provided to quantitative command users. This line provides continuous synchronizing pulses. The pulse repetition frequency is 32 cps. The logical 1's of the quantitative output are coincident with the synchronizing pulses. The synchronization output is through an isolation transformer.

Each user of quantitative commands is also provided a discrete command line. The first command on this line is the alert which is used to signify that the subsequent quantitative word is intended for that user. After 16 bits of quantitative data have been sent out, an end of word pulse is provided in common to all quantitative command users.

The C&S provides 1 pps synchronization pulses to the articulation and telemetry subsystem. These pulses are used to synchronize the slewing of gimbals.

6.2.4. Separation Switch

The separation switch provides the C&S with an enable signal. Prior to separation, the switch is in a closed state. After separation, the switch is in an open state. The open state of the switch permits the C&S to carry out the sequence of events.

6.2.5. Guidance and Control

The guidance and control subsystem provides the C&S with inputs from a pulse integrating accelerometer. Each pulse from the accelerometer signifies an increment of ΔV. The C&S accumulates these inputs in a register. When the register overflows the C&S provides an output signal to the G&C and the propulsion subsystem to turn off the propulsion engine.

6.2.6. Planetary Science Package

The outboard gimbal of the science package rotates the package about the normal to the orbit plane. A gimbal pick-off is provided. This pick-off generates a pair of pulses for every 3/16-degree change in gimbal angle. The order of the pulse pair signifies the direction of rotation. These pulses are provided to the C&S by the PSP subsystem. When the gimbal reaches negative gimbal stop, a gimbal stop sensor produces a pulse. This pulse is also provided to the C&S by the PSP subsystem. The gimbal is controlled closed loop within the PSP subsystem. One of the components of that closed loop control is a horizon sensor which can be made to provide an indication of the planet half-angle. An analog signal proportional to planet half-angle is provided to the C&S. The C&S uses the outputs from the PSP subsystem to generate various control signals indicating the following events: limb crossings, terminator crossings, and other events based on the argument of the spacecraft.

6.2.7. Command Subsystem and Launch Complex Equipment

The C&S receives discrete and quantitative commands from the Command Subsystem and the launch complex equipment. Discrete commands are signified by the closure of a DC isolated semi-conductor switch. The discrete command for each unique function is received on a

separate line. Quantitative commands consist of a discrete command alert, a binary coded quantity, synchronization pulses and end-of-word pulses. The end-of-word pulse is similar in format to the discrete commands except that it is received on a common line. The quantity consists of a binary coded sequence of 1's and 0's on another common line. 1's are signified by the closure of a normally open, DC isolated semi-conductor switch. 0's are signified by the open state of the switch. These 1's and 0's are synchronous with the synchronization pulses which are received on another common line from a DC isolated source. The following quantitative commands are received from either the CD or the LCE:

Function	Bits	Function	Bits
Gimbal angle A slope	14	TTG 4 update	16
Gimbal angle B slope	14	TTG 5 update	16
Gimbal angle C slope	14	TTG 6 update	16
Gimbal angle D slope	14	TTG 7 update	25
Modify or scan word in memory sequence	27	TTG 8 update	16
TTG 1 update	25	ΔV register update	25
TTG 2 update	25	SCIENCE Turn on Threshold	10
TTG 3 update	25	SCIENCE Turn off Threshold	10

7. COMPUTER AND SEQUENCER EQUIPMENT AND PERSONNEL SAFETY HAZARD

The function of the C&S is to generate the necessary onboard commands to make the Voyager spacecraft automatic. Therefore, many of the C&S commands would constitute a safety hazard if they were generated at an inappropriate time. Some examples are as follows:

a. Enable the Guidance and Control Subsystem. If this command were issued prior to separation, the Guidance and Control would dissipate its supply of cold gas in a futile attempt to control the attitude of the flight vehicle.

b. Trajectory Adjust Sequence. If this sequence were issued while the system is still on the pad, it would constitute a serious hazard to personnel and equipment. If the sequence were issued after separation but at an inappropriate time, it would result in a serious hazard to the mission.

c. Orbit Injection Sequence. If this command were issued while the system is on the pad, it would constitute a serious hazard to equipment and personnel. If this sequence were issued after separation, but at an inappropriate time, it would probably result in abort of the mission.

d. Capsule Separation Sequence. If this sequence were issued while the system is on the pad, it would result in a serious hazard to equipment and personnel. If the sequence were issued at an inappropriate time after separation, it would result in the aborting of the planetary lander portion of the mission.

e. Deployment of the High Gain Antenna. If this sequence were issued prior to jettisoning of the shroud, it would constitute a hazard to equipment.

f. Deployment of the PSP. If this sequence were generated prior to orbit injection, it would result in a serious hazard to the equipment.

Necessary precautions taken to reduce the probability of such untimely commands to an acceptable minimum are as follows:

a. During prelaunch, up to the time that pyrotechnics are armed, the hazard is essentially nil.

b. While the flight vehicle is mated to the launch vehicle, the C&S is effectively disabled by the separation switch. During this time, the pyrotechnics may be safely armed. Thus, up to actual separation of the flight vehicle, hazards attributable to the C&S are minimized.

c. After separation, the C&S is enabled. In the enabled mode, the hazard is minimized by the following design features of the C&S:

   1. The C&S will issue no false commands due to the failure of any single piece part. A false command is one which is issued at an inappropriate time.

   2. The number of piece parts involved in generating critical commands such as those listed above has been reduced to a minimum. Thus, the probability of two piece part failures causing a false command has been minimized.

VOY-D-340
POWER SUBSYSTEM

VOY-D-340
POWER SUBSYSTEM

1. INTRODUCTION

Included in this section is a description of the baseline Voyager Power Subsystem, with a discussion of the alternative subsystem configurations considered, the trade-offs made in selecting the baseline subsystem, and the analysis of the component performance requirements.

Applicable documents:

a. From the Voyager Task A Study:

1. VB236FD101, Functional Description of the Preferred Configuration of the Power Subsystem.

2. VB236AA101, Alternate Approaches Considered.

b. From the VOYAGER Task B Study:

VC236FD101, Power Subsystem Functional Description.

c. Elsewhere in the VOYAGER Task D System Update:

1. VOY-D-100 Guidelines and Study Approach
2. VOY-D-220 Spacecraft Configuration
3. VOY-D-230 Flight Sequence
4. VOY-D-260 Trajectory and Guidance Analysis
5. VOY-D-361 Structure
6. VOY-D-362 Temperature Control

2. FUNCTIONAL REQUIREMENTS

The power Subsystem supplies electrical power to the spacecraft from launch through all mission phases. It also supplies raw power to the flight capsule during periods of solar

array illumination up to the time of capsule separation, and to spacecraft-mounted capsule support equipment until shortly after termination of capsule data transmission.

The Power Subsystem must provide electrical power in the following forms:

a. 2400-Hz single-phase, square-wave ac at 50 VRMS ± 2% regulation.

b. 400-Hz three-phase, stepped square-wave ac at 26 VRMS ± 5%.

c. 400-Hz single-phase, square-wave ac at 28 VRMS ± 5%.

d. Unregulated dc from the batteries at 37 to 52 V.

e. Unregulated dc from the array or battery at 37 to 65 V.

The load requirements for the major mission phases are summarized in Table 1. The loads are averaged over each mission phase, and are enclosed in the blocked areas.

The Power Subsystem also generates and distributes timing and synchronizing signals:

a. 1.296 MHz - Telemetry Subsystem

b. 160 Hz - High Gain Antenna Articulation

c. 32 pps - Computer & Sequencer Subsystem

3. SUBSYSTEM ALTERNATIVES AND TRADE-OFF STUDIES

3.1 AC VS DC POWER DISTRIBUTION

A study was performed to compare the merits of candidate ac and dc power distribution systems and to determine the optimum electrical distribution design for Voyager. The results of the study favored the selection of ac distribution.

Table 1. Energy Balance Table

VOYAGER TASK D SYSTEM UPDATE, SEPTEMBER, 1967

MISSION PHASE

1 LAUNCH TO ACQUISITION
2 CRUISE
3 MIDCOURSE MANEUVER
4 MARS ORBIT INSERTION
5 ORBIT WITH CAPSULE (UP TO ENCOUNTER + 30 DAYS) - FULL SCIENCE (41 MIN)
6 - OTHER TIMES
7 ORBIT TRIM WITH CAPSULE
8 CAPSULE ENTRY AND LANDING
9 ORBIT W/O CAPSULE - SPACECRAFT DAY - FULL SCIENCE (41 MIN)
10 - OTHER TIMES (5 HR 01 MIN)
11 - ECLIPSE (84 MIN.)
12 ORBIT TRIM W/O CAPSULE

MISSION PHASE	1	2	3	4	5	6	7	8	9	10	11	12
2400 CPS INVERTER LOADS												
RADIO	30.0	30.0	30.0	30.0	30.0	30.0	30.0	30.0	30.0	30.0	30.0	30.0
TELEMETRY	15.0	15.0	15.0	15.0	15.0	15.0	15.0	15.0	15.0	15.0	15.0	15.0
COMMAND	20.2	20.2	20.2	20.2	20.2	20.2	20.2	20.2	20.2	20.2	20.2	20.2
DATA STORAGE			11.0	11.0	37.0	12.0	11.0	11.0	37.0	12.0	11.0	11.0
GUIDANCE + CONTROL	37.3	26.9	39.5	45.7	26.9	26.9	39.5	26.9	32.1	32.1	32.1	39.5
ARTICULATION		5.3	5.3	5.3	5.3	5.3	5.3	5.3	5.3	5.3	5.3	5.3
PYRO CONTROL	1.5	1.5	1.5	1.5	1.5	1.5	1.5	1.5	1.5	1.5	1.5	1.5
COMP. + SEQUENCER	60.0	60.0	60.0	60.0	60.0	60.0	60.0	60.0	60.0	60.0	60.0	60.0
SCIENCE					121.0	4.0			121.0	4.0		
DATA ACQUISITION					50.0	20.0			50.0	20.0	20.0	
PSP HORIZON SENSOR					9.0	9.0			9.0	9.0	9.0	
CLOCK AND SYNCH	8.8	8.8	8.8	8.8	8.8	8.8	8.8	8.8	8.8	8.8	8.8	8.8
ENVIRON. CONTROL											9.0	
RADIO RELAY								50.0				
LOAD SUBTOTAL	172.8	167.7	191.3	197.5	384.7	217.7	191.3	228.7	389.9	217.9	221.9	191.3
HARNESS LOSS	1.7	1.7	1.9	2.0	3.9	2.1	1.9	2.3	3.9	2.2	2.2	1.9
TOTAL INVERTER OUTPUT	174.5	169.4	193.2	199.5	388.6	214.8	193.2	231.0	393.8	220.1	224.1	193.2
EFFICIENCY	0.847	0.844	0.856	0.858	0.899	0.864	0.856	0.869	0.900	0.866	0.867	0.856
THERMAL LOSS	31.6	31.3	32.6	33.0	43.5	33.8	32.6	34.7	43.8	34.1	34.3	32.6
TOTAL 2400 CPS INVERTER INPUT	206.1	200.7	225.8	232.5	432.1	248.7	225.8	265.7	437.6	254.2	258.5	225.8
400 CPS 3 PH INVERTER LOADS												
GYROS	21.0		10.5	21.0			10.5		10.5	10.5	10.5	10.5
LOAD SUBTOTAL	21.0		10.5	21.0			10.5		10.5	10.5	10.5	10.5
HARNESS LOSS	0.2		0.1	0.2			0.1		0.1	0.1	0.1	0.1
TOTAL INVERTER OUTPUT	21.2		10.6	21.2			10.6		10.6	10.6	10.6	10.6
EFFICIENCY	0.583		0.583	0.583			0.583		0.583	0.583	0.583	0.583
THERMAL LOSS	15.2		7.6	15.2			7.6		7.6	7.6	7.6	7.6
TOTAL 400 CPS 3 PH INVERTER INPUT	36.4		18.2	36.4			18.2		18.2	18.2	18.2	18.2
400 CPS 1 PH INVERTER LOADS												
SCIENCE INSTR.					10.0				10.0			
PSP GYMBALS					6.0				6.0	6.0	6.0	
LOAD SUBTOTAL					16.0				16.0	6.0	6.0	
HARNESS LOSS					0.2				0.2	0.1	0.1	
TOTAL INVERTER OUTPUT					16.2				16.2	6.1	6.1	
EFFICIENCY					0.800				0.800	0.686	0.686	
THERMAL LOSS					4.0				4.0	2.8	2.8	
TOTAL 400 CPS 1 PH INVERTER INPUT					20.2				20.2	8.8	8.8	
INVERTER INPUT DIODE LOSS	0.6		0.3	0.6	0.3		0.3		0.6	0.4	0.4	0.3
MAIN REGULATOR OUTPUT	243.0	200.7	244.3	269.4	452.6	248.7	244.3	265.7	476.6	281.6	285.9	244.3
EFFICIENCY	0.859	0.842	0.859	0.867	0.898	0.861	0.859	0.866	0.900	0.870	0.871	0.859
THERMAL LOSS	40.0	37.6	40.0	41.4	51.6	40.3	40.0	41.2	53.0	42.1	42.4	40.0
MAIN REGULATOR INPUT	283.0	238.3	284.4	310.8	504.2	289.0	284.4	307.0	529.5	324.8	328.3	284.4
UNREGULATED DC LOADS												
CAPSULE	200.0	200.0	200.0	200.0	200.0	200.0						
RADIO	75.0	147.0	147.0	147.0	147.0	147.0	147.0	147.0	147.0	147.0	147.0	147.0
GYRO HEATERS	42.0		21.0	42.0			21.0		21.0	21.0	21.0	21.0
PSP HEATERS		5.0	5.0	5.0			5.0	5.0				5.0
UNREGULATED DC LOAD SUBTOTAL	317.0	352.0	373.0	394.0	347.0	347.0	173.0	152.0	168.0	168.0	168.0	173.0
HARNESS LOSS	3.2	3.6	3.8	4.0	3.5	3.5	1.7	1.5	1.7	1.7	1.7	1.7
TOTAL UNREGULATED DC LOAD	320.2	355.6	376.8	398.0	350.5	350.5	174.7	153.5	169.7	169.7	169.7	174.7
UNREGULATED BUS POWER	603.2	593.9	661.1	708.8	854.7	639.5	459.1	460.5	699.2	493.5	498.0	459.1
DIRECT BATTERY LOADS												
FAILURE DETECTORS	8.8	8.8	8.8	8.8	8.8	8.8	8.8	8.8	8.8	8.8	8.8	8.8
THRUST VECT CONTR (PEAK)			(701)	(701)			(701)					(701)
SOLENOID VALVES (PEAK)			(448)	(448)			(448)					(448)
ARTICULATION (PEAK)			(112)	(112)			(112)					(112)
DIRECT BATTERY LOAD SUBTOTAL	8.8	8.8	8.8	8.8	8.8	8.8	8.8	8.8	8.8	8.8	8.8	8.8
HARNESS LOSS	0.1	0.1	0.1	0.1	0.1	0.1	0.1	0.1	0.1	0.1	0.1	0.1
TOTAL DIRECT BATTERY LOAD	8.9	8.9	8.9	8.9	8.9	8.9	8.9	8.9	8.9	8.9	8.9	8.9
BATTERY BUS POWER	615.1	8.9	673.0	720.7	8.9	8.9	471.0	8.9	8.9	8.9	509.9	471.0
BATTERY DIODE LOSS	6.2	0.1	6.8	7.3	2.7	0.1	4.9	0.1	0.1	0.1	5.2	4.8
BATTERY POWER OUTPUT	621.3		679.8	728.0	265.2		475.7				515.0	475.7
BATTERY ENERGY OUTPUT (W-HR)				1541.0	181.0						721.0	
BATTERY THERMAL LOSS	127.9	49.6	140.0	149.9	54.6	117.0	97.9		43.7	233.0	106.0	97.9
BATTERY ENERGY INPUT (W-HR)						770.0				1169.0		
BATTERY POWER INPUT		49.6				117.0		49.6	43.7	233.0		
CHARGER OUTPUT		58.6			9.0	126.0		58.6	52.7	247.0		
EFFICIENCY		0.879			0.704	0.900		0.879	0.874	0.910		
BATTERY CHARGER THERMAL LOSS	3.0	8.1	3.0	3.0	3.8	14.0	3.0	8.1	7.6	24.0	3.0	3.0
CHARGER INPUT	3.0	66.7	3.0	3.0	12.8	139.9	3.0	66.7	60.3	264.0	3.0	3.0
ARRAY BUS POWER		660.5			612.3	779.4		527.2	759.5	759.5		

The portion of the power subsystem investigated is indicated in Figure 1. The tradeoff analysis was performed on the Task B power subsystem configuration. However, the slight change in voltage ranges does not invalidate the results of the study.

Configurations equivalent with respect to redundancy were analyzed for each of the three candidate systems. These candidate systems are briefly described in Table 2.

Performance parameters selected for study were: weight, reliability-figure-of-merit, efficiency (because of its effect on power source weight), and certain factors which are less tangible but no less important to program success, flexibility to accommodate user voltage and power changes, noise, testability, magnetic dipole, and inherent isolation.

All three systems were approximately equal in reliability-figure-of-merit. The ac and central dc systems were approximately competitive in efficiency and weight, while the decentralized dc system was predicted to be 70 to 80 pounds heavier. These values are illustrated in Table 3.

Probably the most important of the less tangible factors is flexibility. Both the ac and decentralized dc most easily accommodate changes in user voltage and power requirements, giving the fewest problems in integrating the spacecraft system design.

The noise level in the ac system is high, but identifiable early, while the noise - EMI problem is more subtle for the two dc systems, usually requiring fixes during system test. The ac and decentralized dc systems are the most easily testable, requiring a single pair of power leads to test any user component, since the user components would contain their own "power supplies". The central dc system would require many special power supplies or special dummy loads to test the user components.

The magnetic dipole is least for the ac system.

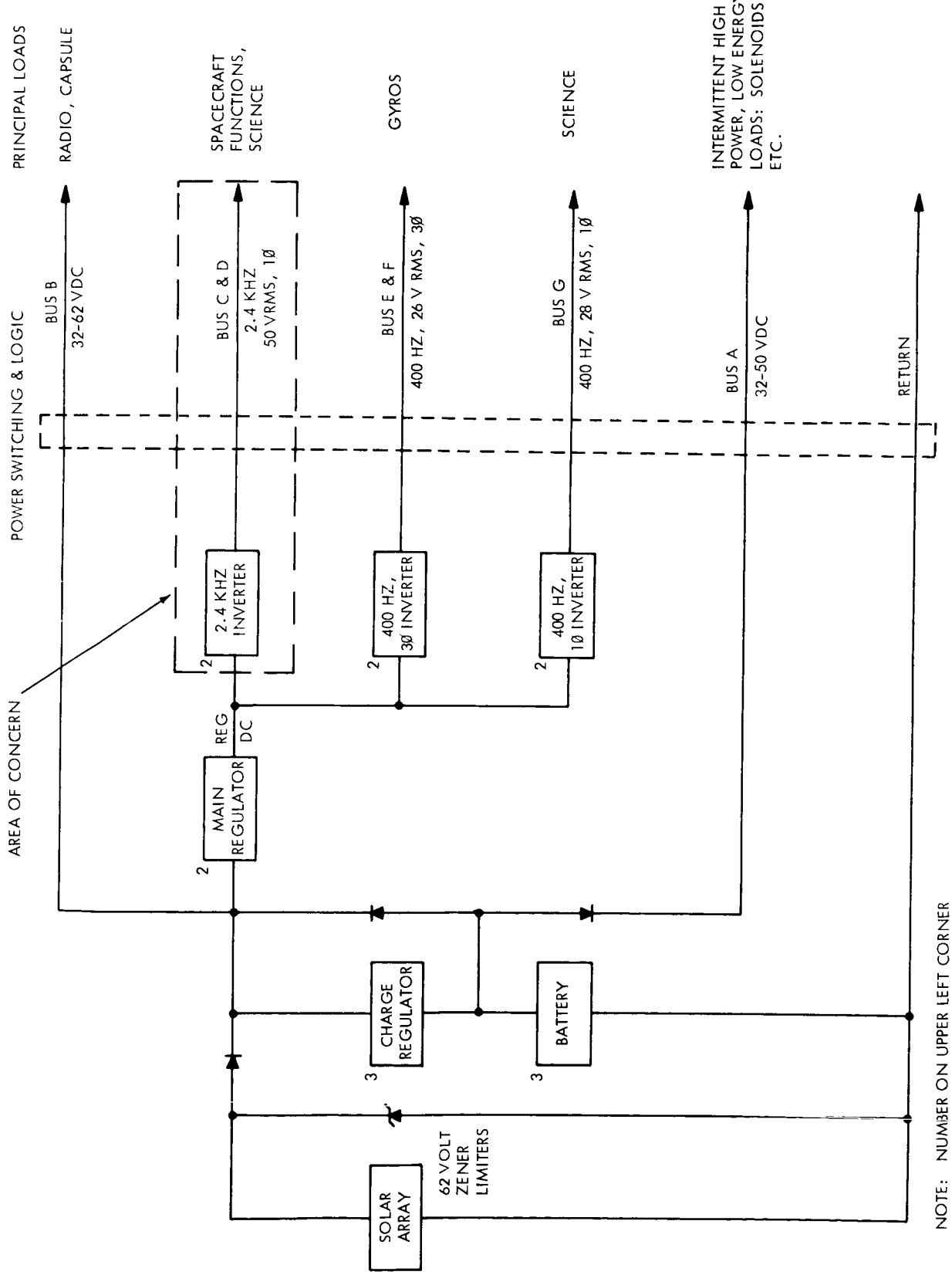

Figure 1. Task B Power Subsystem Schematic

Table 2. Configurations Studied

Candidate	A	B	C
#1 - AC	Single String: 1 DC/AC Inverter 38 T/R's 1 Harness	Redundant: 2 DC/AC Inverters 2 Fault Sensors 55 T/R's 2 Harnesses	Redundant: 2 DC/AC Inverters 2 Fault Sensors 55 T/R's with redundant input fuses 2 Harnesses
#2 - Centralized DC	Single String: 2 DC/DC Converters each spaced 180° apart 1 Harness/Converter	Redundant: 4 DC/DC Converters - pair spaced 180° apart 4 Fault Sensors 1 Harness/Converter	Redundant: 4 DC/DC Converters - pair spaced 180° apart 4 Fault Sensors 1 Harness/Converter Redundant fuses - all DC loads
#3 - Decentralized DC	Single String: 13 DC/DC Converters 1 Harness/Converter	Redundant: 26 DC/DC Converters 26 Fault Sensors 1 Harness/Converter	Redundant: 26 DC/DC Converters 26 Fault Sensors 1 Harness/Converter Redundant fuses - all DC loads

Table 3. Results of Trade Study

Candidate	Performance Parameter	A - Single String	B - Redundant	C - Redundant & Load Fault Protection
	Reliability Figure of Merit	0.9580	0.9891	0.9999
#1 - AC	Wt. (Lbs.)	45.8	74.6	74.6
	Relative Efficiency	0.988	0.992	0.992
#2 - Centralized DC	Reliability Figure of Merit	0.9774	0.9994	0.9993
	Wt.	47.3	87.5	87.5
	Relative Efficiency	1.000	1.000	1.000
#3 - Decentralized DC	Reliability Figure of Merit	0.9343	0.9985	0.9984
	Wt.	63.4	161.8	161.8
	Relative Efficiency	0.926	0.857	0.857

The T/R or power supply used with each user load contains a filter which provides a reasonable degree of isolation with the ac or decentralized dc systems. The central dc system has the lowest degree of isolation.

3.2 BATTERY SELECTION

Ni-Cd batteries were selected to be the principal batteries on the Voyager Spacecraft, based on the following summarized decision factors:

a. Disappointing tests results on silver-cadmium (Ag-Cd) batteries.

b. The non-magnetic requirement had not been imposed on the system.

c. Superior cycle life and generally more reliable performance of nickel-cadmium (Ni-Cd) batteries.

The Ni-Cd battery will be supplemented by a secondary silver-zinc battery to supply energy for long maneuver periods.

The MSD Battery Performance Test Program was initiated to fill a need for quality information on the performance of secondary silver-cadmium and silver-zinc batteries as related to the requirements of the Voyager mission. Tests were performed on 20-ampere-hour sealed AG-Cd cells and 50-ampere-hour vented Ag-Zn cells to determine charge and discharge characteristics and cycle life at various depths of discharge in 7- and 24-hour duty cycles.

The results of the tests carried out on the Ag-Cd cells were disappointing. The sealed cells were considerably heavier than anticipated, having a specific energy density of only 14 watt-hours per pound (compared to an initial estimate of 20 to 25 w-hr/lb). The cycle life was considerably shorter than anticipated. The table below summarizes the results obtained. The discharge time in all cases is one hour.

Cycle Time	Depth of Discharge	Cycles Completed
7 hours	20%	633 (continues)
7 hours	40%	Failed at 285
24 hours	40%	Failed at 135
24 hours	60%	Failed at 126

To contrast with this, 5-year-old Ni-Cd cells have completed over one year on a 24-hour cycle at 60 percent DOD and are continuing satisfatorily after first having been overcharged at the 7-hour rate for 500 days and then been placed on a shelf for 3 years.

One pack of the Ag-Cd cells was placed on float charge (at 1.42 v/cell, slightly higher than the open-circuit voltage of the cell) for a period of 6 months after first having been formed, floated for a month, and discharge characteristics having been measured. The battery capacity decreased by 30 percent during the 6-month float, and the pack could not be charged successfully from a 40 percent discharge in a 7-hour cycle. Thus, the Ag-Cd cells could not meet the performance and life requirements for the Voyager mission.

In the test program, the float charge test was made also on an Ag-Zn battery pack. The decrease in capacity was about 15 percent after 6 months, and though the cycle life was decreased to about half that of a new Ag-Zn battery, the pack lasted 170 cycles at 20 percent DOD before it failed.

Because there is a one-time large energy requirement during the Mars orbit insertion maneuver of almost twice that experienced during a normal orbit solar eclipse, it was decided to supplement the Ni-Cd battery with an Ag-Zn battery. It is expected that the Ag-Zn battery will experience about 10 discharges over its approximately 9-month life, and it is felt that the test program results substantiate the choice of an Ag-Zn battery for this service. Since the energy density of the secondary Ag-Zn cell (approximately 47 watt-hours per pound) is about 4 times greater than that of a Ni-Cd cell, the use of an Ag-Zn battery for this few-cycle service will result in an appreciable weight savings of approximately 135 pounds.

3.3. APPLICATION OF REDUNDANCY

The power subsystem is critical to the operation of the spacecraft. Failure of power subsystem elements will result in partial or complete loss of the mission. It is essential, therefore, to provide redundancy for the major elements of the power subsystem.

Weight, power and thermal control considerations require the selection of duplex standby redundancy for the power conditioning equipment. Other portions of the power subsystem are made redundant using majority logic, or by providing excess capacity.

Redundancy may be implemented by connecting components in simple parallel, series, or quadruple arrangements. This may be done without additional circuitry for simple elements such as diodes, resistors, relay contacts, etc. Operational amplifiers or other low-impedance output devices cannot be made redundant in this manner since the failed unit will usually overload the output of the redundant unit. When a passive connection between redundant elements is not feasible, a method must be found to remove the failed element from the system. The system must then contain active devices which detect failures and substitute working units for the failed units. This implies additional weight, power consumption, and system disturbance problems to be evaluated. The additional equipment added also introduces new failure modes into the system.

There are three approaches to implementing active redundancy:

a. Majority logic redundancy. This system (Figure 2) requires three similar operating units, load-sharing controls, comparator circuits (failure detection) and three sets of input/output switching circuits.

   If the load may be evenly divided or if the magnitude of the load is not pertinent to the failure criteria load-sharing controls may be eliminated, i.e., the load for each redundant component is isolated from the others. Failure would then require redistributing the load to the operation components with a resulting disturbance.

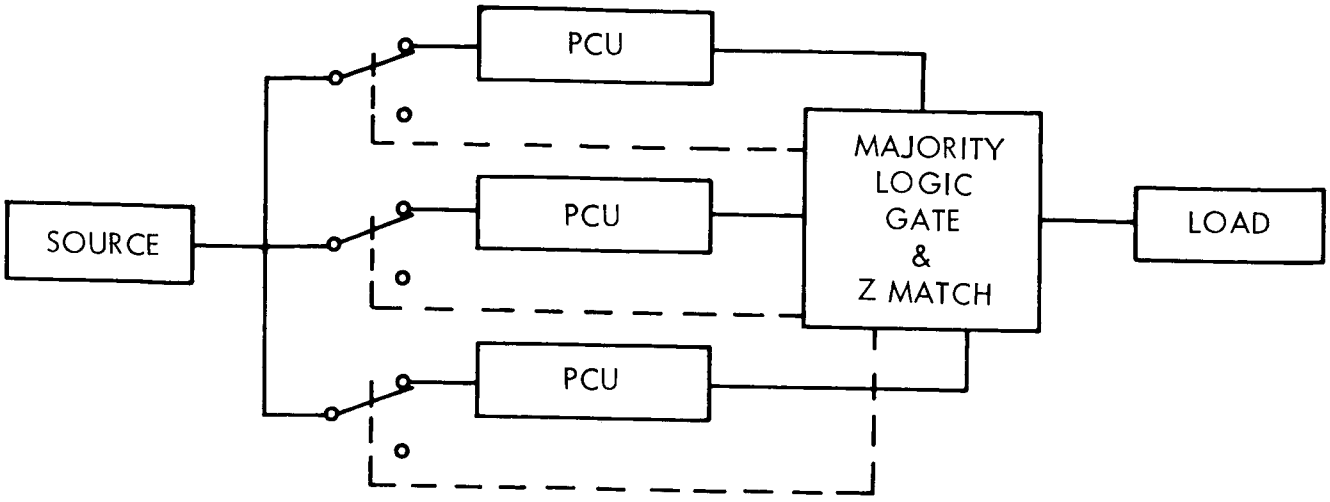

Figure 2. Majority Logic Redundancy

b. Duplex Load-sharing Redundancy. If it is possible to determine proper operation of a component independently, two-element redundancy (Figure 3) with load sharing may be used. Again, either load-sharing controls may be used or the load may be split. In the latter case the load of the failed component is shifted to the operational component. System disturbance is minimized with load-sharing controls, but is greater in general than the disturbance to the majority logic approach, since the load change on the operational systems is greater by a factor of at least three. This system uses two active components, two failure detectors and two sets of input/output switches.

c. Duplex Standby Redundancy. An alternative to "b" is to supply the load from one prime unit. Redundancy is accomplished by detecting a failure in the prime unit and substituting a redundant unit (Figure 4). The load increment and system disturbance is maximum. This method requires two components with only one activated, one failure detector and one set of input/output switches. Savings are achieved in weight, power, and consequently, thermal dissipation.

Table 4 summarizes these results. Duplex standby redundancy is the method applied to the power conditioning equipment for the Voyager Power Subsystem.

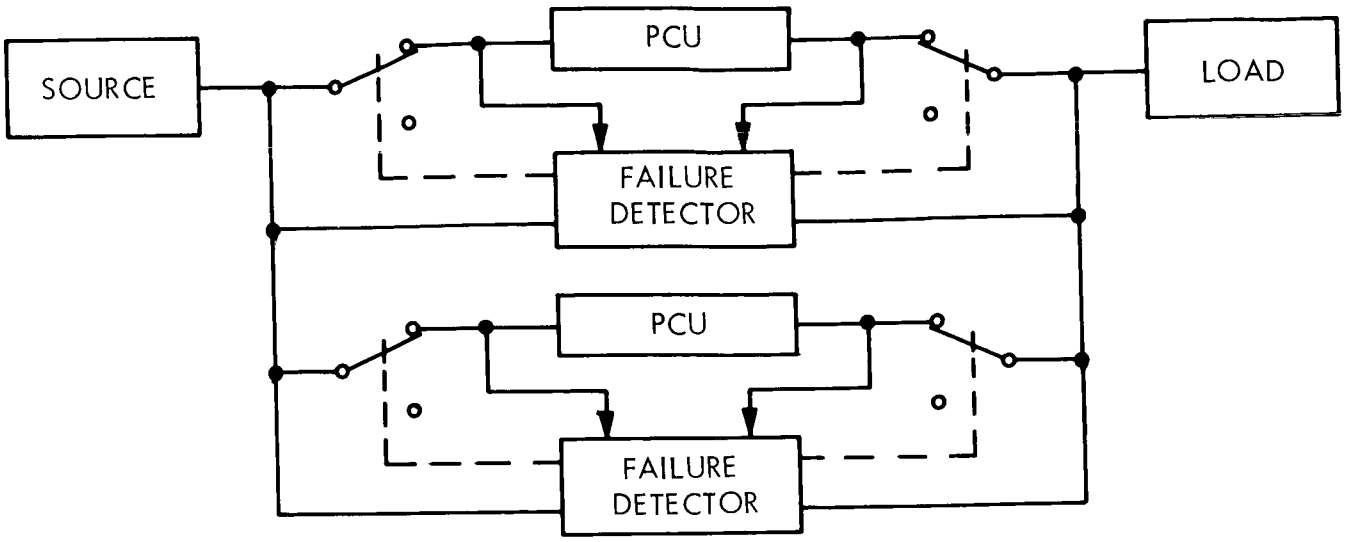

Figure 3. Duplex Sharing Redundancy

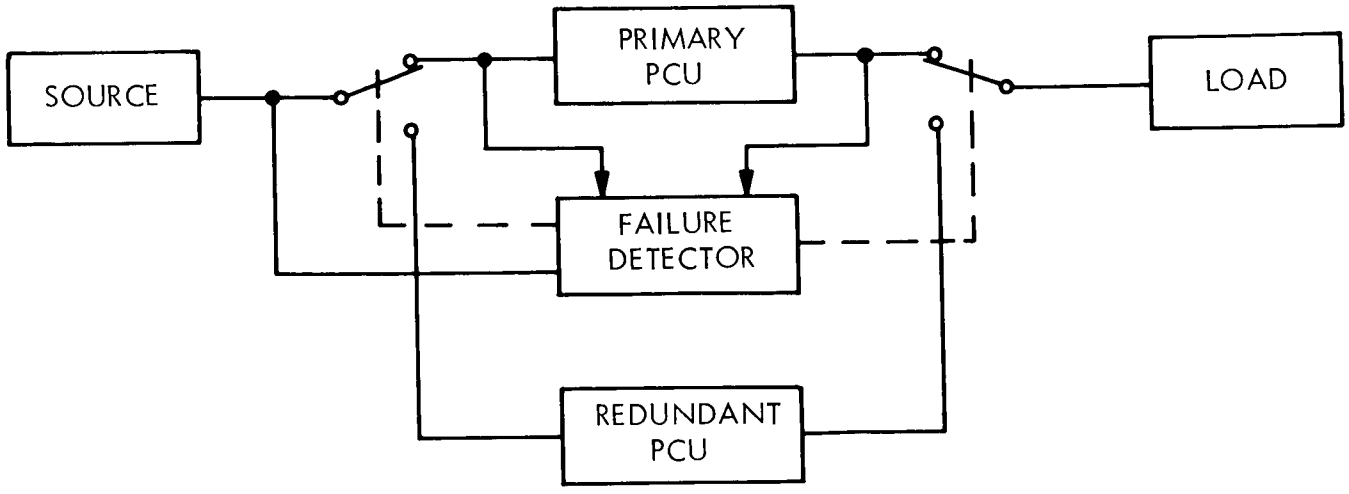

Figure 4. Duplex Standby Redundancy

Table 4. Comparison of Redundancy Methods

System	Components	Failure Detectors & Power Switching	Load Disturbance	Power Loss	Weight
Majority Logic	3	3	16%	Greatest	Greatest
Duplex Load Sharing	2	2	50%	-------	-------
Duplex Standby	2	1	100%	Least	Least

In the case of the 400-Hz, 3Ø inverter, each inverter powers a single set of gyros, separately. Thus, when both sets of gyros (one of which is redundant) are operating during critical maneuvers, both inverters are also operating, which is an approximation to the duplex sharing redundancy.

Redundancy is provided in the clock and synchronizer in dual forms.

The most probable failure mode in the master oscillator is complete loss of output signal. Such a failure would result in replacement by a complete operating standby clock and oven. Frequency drift failure will be detected through telemetry and the redundant clock switching will be by ground command. Ground monitoring of the clock frequency should be possible since doppler shift will be accurately determined for spacecraft tracking. It appears that, even though error can be detected and the last possible correction to the C&S can be made only about 30 minutes before Mars Orbit Insertion, the ± 1% accuracy of the 2.4 kHz backup oscillator is adequate beyond this point in time to insure capture in a reasonable orbit about Mars.

Alternative methods utilizing on-board frequency drift detectors and majority voting logic for the clocks were considered. Majority voting logic is not feasible for the clocks without slaving the oscillators. The frequency stability would then be completely dependent on the

master clock and the redundant intent would not be realized. On-board frequency drift detectors are feasible but the complexity of the required system would not enhance the reliability of the system. This method remains a viable alternative if time and telemetry functions required for ground based frequency measurements become inconsistent with program objectives.

The various timing signals for the power subsystem and other subsystems are derived from the master oscillator by means of digital dividers in a majority-logic voting redundancy configuration. The three-phase and single-phase timing signals are generated by factor-of-six dividers with appropriate logic operating from the 2400 Hz level. All frequencies below 2400 Hz are derived from the 2400-Hz output. There is an additional 2400-Hz oscillator provided as back-up to the clock, should the redundant clock fail completely. It will have a frequency accuracy of ± 1 percent, which should be adequate for the accuracy requirements of the gyros in the G&C subsystem.

Redundancy is provided in the batteries through excess capacity or load management. The most critical event for the batteries is the Mars orbit insertion maneuver, where 50 percent of the battery total rated capacity will be discharged. If the Ag-Zn battery, which has 53 percent of the rated capacity, should fail, the maneuver can still be performed by careful load management. The capsule is the first candidate to be turned off, and transmitter operation can be curtailed to the most critical time periods to reduce the energy demand to about 1000 watt-hours. This would discharge the surviving Ni-Cd batteries to about 65 percent of capacity.

During the occulted-orbit phase, it is not planned to rely on the Az-Zn battery. The Ni-Cd batteries were sized on the basis that non-vital loads (such as the transmitter, tape recorders, PSP gimbals, the DAS, and PSP horizon sensor) could be switched off, and the surviving single Ni-Cd battery would be discharged to a depth of 60 percent.

3.4 SELECTION OF SOLAR CELL BASE RESISTIVITY

Sources of recent radiation damage data indicate that, at the ionizing radiation dose level expected for the Voyager mission, silicon N/P cells with a base resistivity of 1 ohm-cm degrade no more than 10 ohm-cm cells. Measurements made at GE-MSD and discussions with solar cell vendors indicate that the 1 ohm-cm cells are available with an initial higher efficiency than the 10 ohm-cm cells. Therefore, the 1 ohm-cm cells were selected for use in the Voyager solar array.

The most recent data on radiation damage was found published in:

a. R. Rasmussen, (RCA), "Calculation of 1-Mev Electron Flux and Radiation Degradation of Solar Cell I-V Curves by Computer", conference record of the Sixth Photovoltaic Specialists Conference, Volume III.

b. J. A. Palmer, "Solar Space Manual", (Rough Draft), Hoffman Electronics Corporation, April, 1967.

The radiations damage estimates were made using established techniques, which are discussed in Appendix A, and were based on the environment given in "Voyager Environmental Predictions Document", JPL, October 26, 1966. Based on these damage estimates and weight-area trade-offs, 10-mil covers were selected for use on Voyager. For this fused silica shield thickness, the residual equivalent 1-Mev electron dose reaching the solar cells is approximately 10^{14} e/cm^2. Both the above radiation damage data sources indicate that at this dose level, the 10-ohm-cm cells degrade slightly more than the 1 ohm-cm cells. This is primarily due to the faster rounding of the knee of the solar cell V-I curve for the 10-ohm-cm cells.

The short-circuit current will degrade less for the 10 ohm-cm cells, and the open-circuit voltage will degrade about the same for both types of cells; however, the data published for

the power point degradation, which is the important degradation parameter, indicates that the 10-ohm-cm cells degrade more by 1 or 2 percent. It can be inferred from this data that this indicates a faster rounding of the knee of the V-I curve.

GE-MSD has measured the initial efficiencies of a group of TI N/P cells to obtain performance data. Two groups of 24 1-ohm-cm and 10-ohm-cm cells (96 cells in all) were obtained at times about 6 months apart, selected at random from the production line. The efficiencies measured are noted:

	TI N/P CELLS	
	1 Ohm-cm	10 Ohm-cm
a. 1st Group of 24 Cells	11.80%	10.92%
b. 2nd Group of 24 Cells	11.82%	10.81%

It appears from these measurements that the 1-ohm-cm cells have an initial efficiency approximately 8 percent greater than the 10-ohm-cm cells. Information from other vendors indicates a difference in the same direction, although of varying amounts from vendor to vendor.

3.5 ARRAY/BATTERY LOAD SHARING

It is planned to prevent unnecessary array/battery load sharing by proper programming of the spacecraft loads.

In several mission phases the solar array power capability is marginal, particularly during the early part of the orbiting phase when the Science subsystem is operated and the capsule is still on board and using power. During these phases, whenever the total spacecraft power requirements exceed the maximum power output of the solar array, the array/battery bus voltage will be drawn down to the battery discharge voltage. When the load falls back to an in-

termediate level, the array/battery operating point may remain down at the battery discharge voltage, even though the solar array would be fully able to supply the required power without discharging the battery. This is the array/battery load-sharing lock-in problem. The problem exists because of the multiple operating points possible with a switching-type voltage regulator, as shown in Figure 5.

If the power subsystem were to be permitted to remain in this state, the battery would eventually completely discharge, and the main voltage regulator would not be able to maintain regulation on the regulated bus.

The array/battery may be forced out of the load-sharing state by reducing the spacecraft power demand to a point below P_1. This will cause the operating point to rise up onto the array V-I curve and the battery discharge will cease. The normal spacecraft demands may then be re-imposed on the power subsystem. The interruption in load required for this operating point correction need only be momentary, and can be programmed by the C&S to last a few seconds.

The most likely candidate for power interruption is the capsule. The electrical power required for the capsule is used only for heating nearly all the time, the capsule electronic equipment seldom being operated except for checkout. Thus, it should be possible to program a momentary interruption of the capsule power to follow each maneuver or other condition where array/battery load-sharing can occur. This would also include an interruption after each Science operating period (periapsis passage) until the capsule is separated.

After capsule separation, the spacecraft power requirements are reduced by 200 watts, but at some point, solar eclipses begin, requiring power to recharge the batteries. However, this battery-charging power will not result in a load-sharing state on emergence from eclipse, since at the battery discharge voltage, the battery charge regulators will not accept charging power. Thus, until the array/battery bus voltage rises up onto the array V-I characteristic

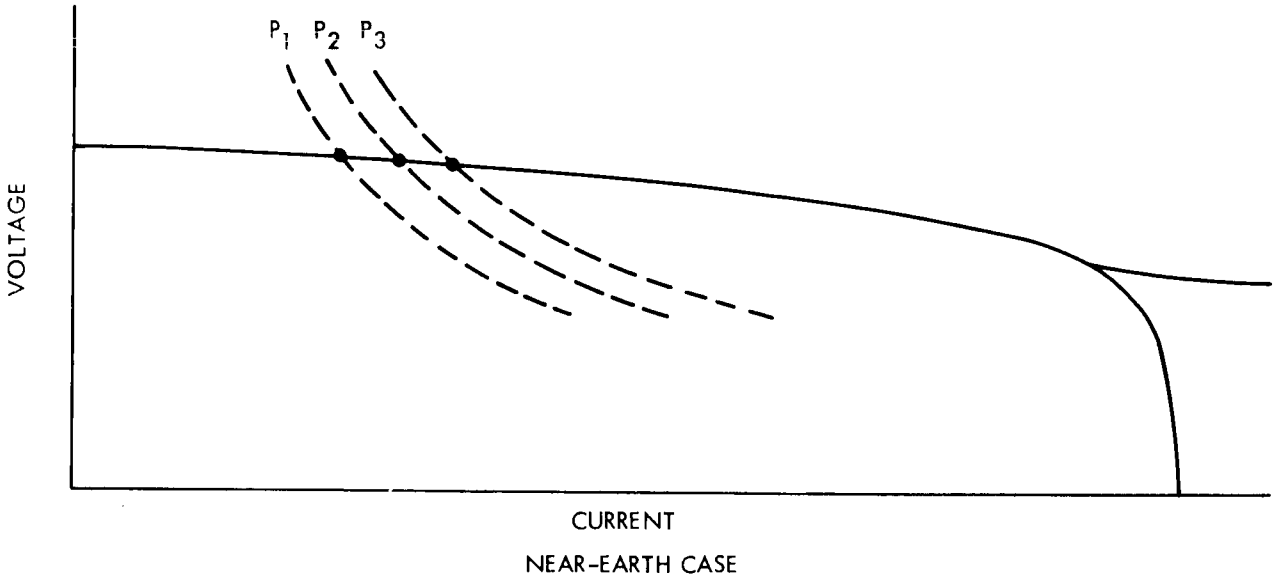

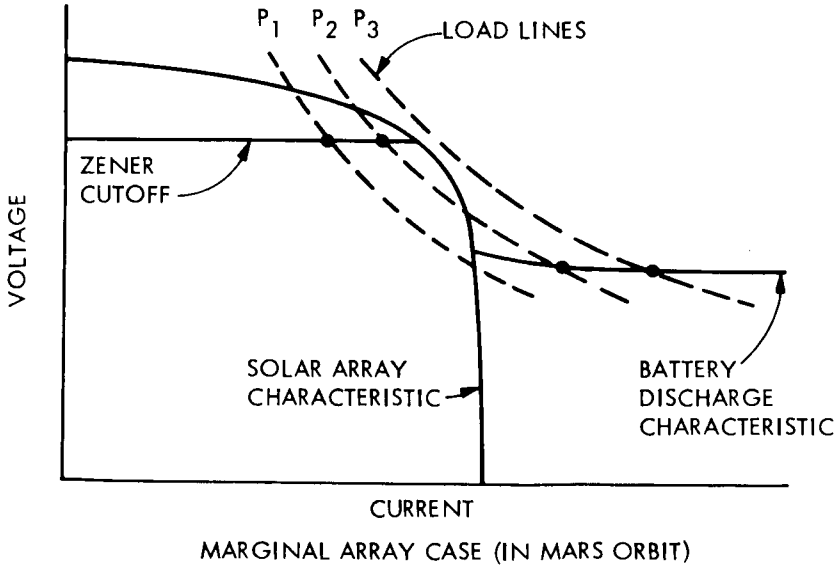

Figure 5. Array/Battery Load-Sharing Characteristics

curve, the spacecraft electrical loads will be less than the critical power level. In any case, if necessary, the battery chargers may be turned off momentarily to assist in establishing the correct operating point.

4. BASELINE POWER SUBSYSTEM DESCRIPTION (Figure 5A)

4.1 POWER FLOW

Primary power is obtained from the solar array, and is used to power the spacecraft and recharge the secondary batteries. Power from the array or battery is supplied to some users directly, and the remainder is conditioned to ac and distributed to the majority of the spacecraft subsystems.

The solar array consists of 93 diode-isolated strings, each with its own zener regulator to limit the voltage to 65 volts. Array output is fed to the array/battery bus and the three battery charge regulators through the array/battery enabling switch, SW-1, which is closed by the launch complex equipment prior to launch. Independent contacts on this switch also connect the three batteries into the power system.

Power is distributed to the loads through six busses:

a. Bus A Supplies raw battery power at 37 to 52 VDC corresponding to the extremes of battery discharge and charge for momentary peak loads. Dc power, rather than ac power, is distributed to these loads since their associated peak power levels would require unnecessarily high ratings for the ac inverters. The momentary power requirements of the solenoid valves, stepper motors, and thrust vector control are of short enough duration to minimize the power loss caused by the inefficiency of passing this power through the battery chargers and the batteries.

b. Bus B Supplies raw array or battery power at 37 to 65 VDC, corresponding to the extremes of battery discharge and the upper array voltage limit established by the zener regulators. Users of this power are the radio subsystem, the capsule, and heaters for the Planet Scan Platform; and this is the input power for the main regulators.

ENABLE BATTERIES &

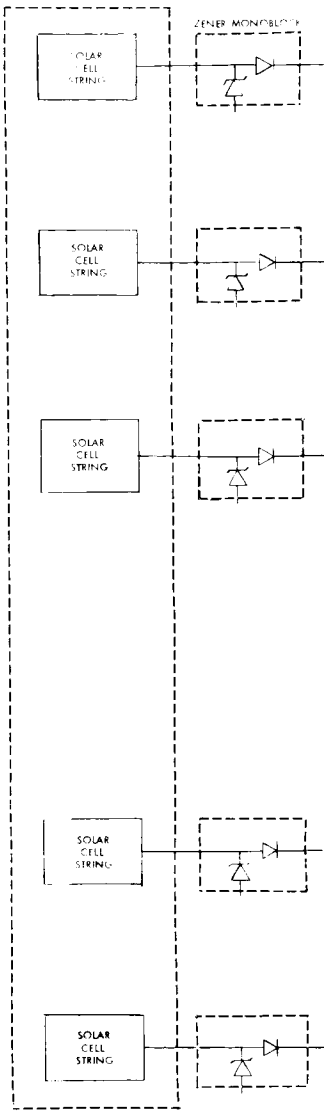

NOMENCLATURE
- ○ TELEMETRY MEASUREMENT
  - V = VOLTAGE
  - I = CURRENT
  - D = DISCHARGE, AMPERE-HOURS
  - S = SWITCH STATE
- ⊡ = COMMAND INPUT

FOLDOUT FRAME

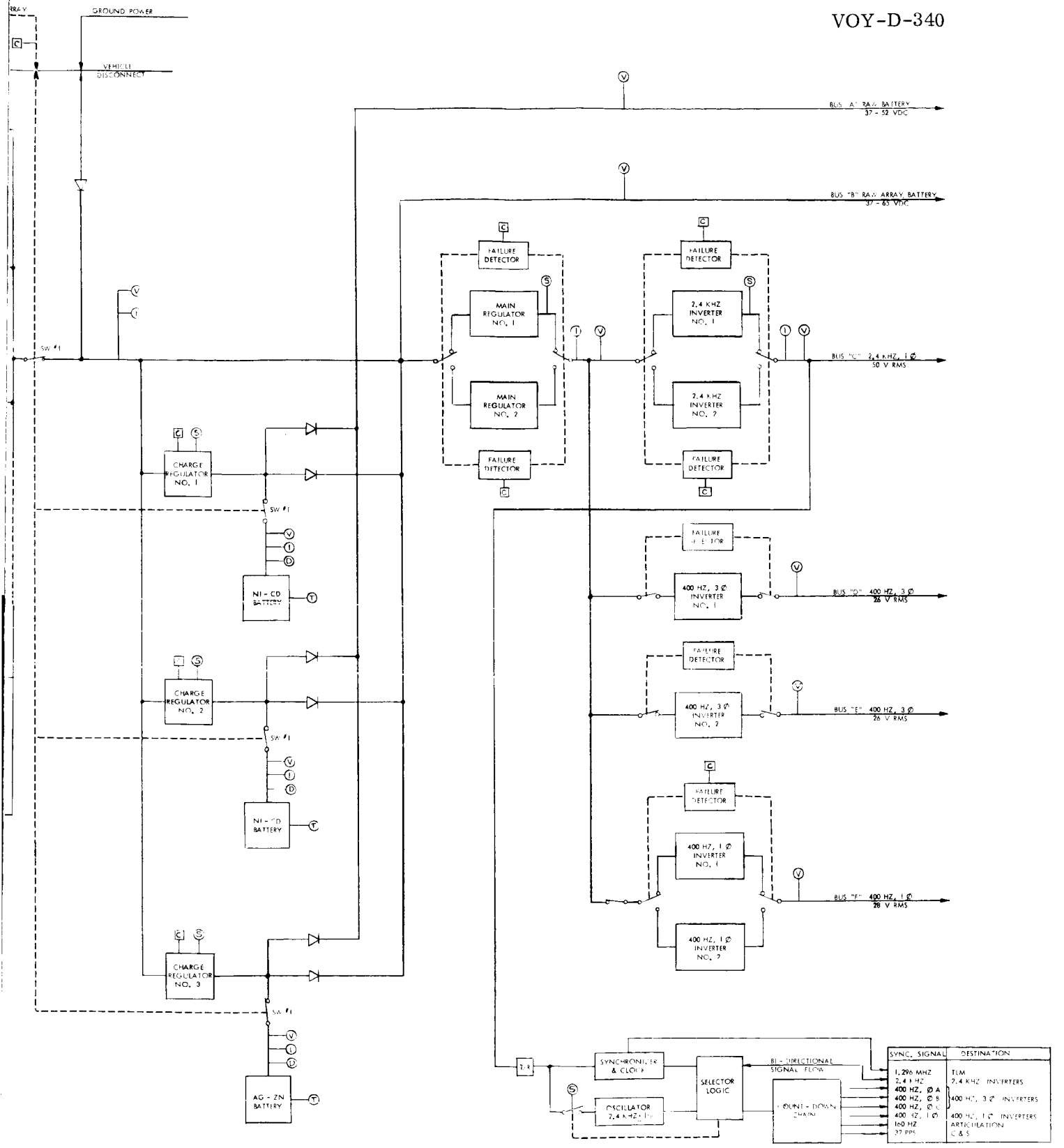

Figure 5A. Power Subsystem Functional Block Diagram

c. Bus C Supplies 2.4-kHz, single-phase, square-wave power at 50 V rms ± 2 per cent from either of two inverters for the majority of the spacecraft subsystems. The inverters receive input power of 35 VDC ± 1 percent from the main regulator operating off Bus B. A failure detector is identified for each main regulator and each inverter. Failure of either an inverter or a regulator will cause the failure detector to transfer the load to the redundant unit.

d. Busses D & E Supply 400-Hz, three-phase, stepped square-wave power at 26 V rms ± 5 percent to each of two sets of gyros. The two inverters receive input power from the output of the main regulator and are turned on by external control signals from the Command, Computer and Sequencer or the Guidance and Control Subsystems.

e. Bus F Supplies 400-Hz, single-phase, square-wave power at 28 V rms ± 5 percent to the Science Subsystem and the Planet Scan Platform. Two inverters are used with the redundant unit on standby, controlled by a failure detector. Bus F is energized by external control signals from the Command or the Computer and Sequencer Subsystems.

4.2 OPERATIONAL MODES

4.2.1 Prelaunch

The sequence of events from hangar checkout to on-pad operations are:

a. The Overall Flight Spacecraft is transferred to the launch pad. The power subsystem is inoperative, with all contacts of switch SW-1 open.

b. Subsequent to on-pad mating, ground power is gradually applied through the umbilical disconnect and raised to a level of 37 to 65 V dc. The battery charge regulators are turned off.

c. Switch SW-1 is closed through umbilical signal leads only after proper ground power voltages have been established. This sequence prevents arcing across the switch contacts by eliminating the possibility of large battery currents during switch closure.

d. Battery charging is initiated, to the degree required, by selection, through the command link, of proper charge regulator settings. Normal on-pad check-out of the power system may now proceed.

e. Subsequent to removal of the umbilical, just prior to launch, the batteries supply all power at a discharge voltage in the range of 37 to 46 V dc.

4.2.2 Launch Phase

The batteries continue to supply power. Loads are supplied through load control-switches receiving signal input external to the power system. The load sharing control circuitry is disabled by C&S until after Mars orbit insertion.

4.2.3 Acquisition

With solar acquisition, the solar array output is obtained and battery charging commences through the charge regulators. The main regulator receives input power at the array output voltage and converts it to 35V ±1% for further processing by the inverters. Raw battery power may be periodically demanded by heater elements or solenoid valves. The charge regulators will supply this power up to the limit of 5 amperes. The array power capability is sufficiently in excess of the power requirements that load-sharing will not occur.

4.2.4 Cruise

Cruise operation is identical to that described above. The batteries will have achieved full charge. During long periods without battery use the charge regulator limits will be reduced to their lowest settings to minimize the stress on the batteries. Some period prior to planned maneuvers the highest settings may be used to assure maximum battery capability.

4.2.5 Mid-Course Maneuvers

During the maneuvers, the batteries supply part or all of the power required depending on the spacecraft solar attitude. Array/battery load-sharing condition may be terminated at the conclusion of the maneuver by a programmed temporary interruption of power to the capsule by a control signal from the computer and sequencer. Periods between maneuvers are sufficiently long to permit fully recharging the batteries.

4.2.6 Mars Orbit Insertion

Similar to Mid-Course Maneuvers.

4.2.7 Orbit with Capsule (Up to Encounter + 30 Days)

During this period spacecraft power consumption will be at its highest level. When the Science Subsystem is operated at the same time power is provided to the capsule, array/battery load-sharing will occur. At the completion of the science operating period, power to the capsule will be interrupted momentarily by the C&S to end the load-sharing condition. There is sufficient excess array power available to fully recharge the batteries during the period remaining when the Science is not operating.

4.2.8 Orbit without Capsule

During this phase, solar eclipses of up to 84 minutes will occur, and large amounts of power are used to fully recharge the batteries at times when the science is not operating. During science operation, no useful battery charging will take place, but sufficient solar array power is available so that load-sharing will not occur. The inherent characteristics of the battery chargers will prevent load-sharing lock-in on emergence from eclipse.

4.3 BATTERY CHARGING

The nickel-cadmium batteries are charged at a constant current at approximately the C/8 rate until fully charged, and then the third-electrode signal causes the charge rate to be reduced to a maintenance level of C/40. The silver-zinc battery is charged at a current-limited constant voltage until fully charged, and when the charge current tapers naturally to a low level, the charge voltage is reduced to a safe "float" level just above the open circuit voltage.

The nickel-cadmium battery charger is a constant-current PWM regulator, with the current limit set to the maximum level required to recharge the batteries during the heaviest duty

cycle in the occulted portions of the Mars orbiting phase, 2.5 amperes for each battery. The charging voltage is limited to 49.6 volts (1.55 volts per cell for the 32-cell battery) to prevent excessive overcharge of the batteries at low temperatures. The charge rate, approximately C/8, is low enough so that the batteries could be charged and overcharged at this rate continuously, array power availability permitting. However, limitations imposed by the Thermal Control Subsystem require that the charge rate be reduced when the battery is fully charged to prevent the high heat dissipation in overcharge from overheating the batteries. The charge rate in overcharge will be reduced to a level sufficient to maintain the capacity of the battery -- C/40 (0.5 amp per battery). The charge rate reduction will be initiated by a signal from the third electrode in the Ni-Cd battery. Backup sources of this control signal will be C&S and Command.

The results of tests made during MSD's Battery Performance Test Program have shown that the gas evolution in Ag-Zn cells is reduced to negligible levels by lowering the charge voltage to the "float" voltage after the battery is fully charged. The voltage combination found to be most advantageous for securing full charge with minimum gassing in Ag-Zn cells are:

Charge voltage per cell: 1.94

Float voltage per cell: 1.87

A two-step charger to perform this function was developed, built, and utilized in the test program, and is essentially similar to the charge regulator proposed here. Using this charger, the battery voltage early in charge is low while the current is being limited. Later in the charging period, the battery voltage approaches the voltage limit, and the charge current will taper off as a consequence. The two-step charger senses this current tapering, and when the current has fallen to about half its limit value, the charger will automatically switch to the lower float voltage limit. At this lower voltage, the charge current will drop to a few milliamperes. A subsequent discharge will reset the recharger for the next charge cycle through the action of the charge current interruption.

The voltage limits imposed by the charger are indicated below. A and B are the charge voltage limits, and A' and B' the float voltage limits. A and A' are for the full complement of cells, and B and B' are provisions to allow for the short-circuit failure of a single cell in the battery.

Charge Voltage Limits

A = 52.4 v (charge, 27 cells)

A' = 50.5 v (float, 27 cells)

B = 50.4 v (charge, 26 cells)

B' = 48.6 v (float, 26 cells)

The charge current limit is set at 0.5 ampere, which is sufficient to recharge the battery within 48 hours after a 50 percent discharge (the maximum likely to occur during the Mars orbit insertion maneuver).

The B and B' voltage limits are set in by ground command, and are provided since an internal short circuit is the commom mode of failure of a silver-zinc cell. The failure of a cell in the Ag-Zn battery may be deduced from the following:

a. Uneven sharing of load with the Ni-Cd battery during battery discharge cycles. If the Ag-Zn battery has a partially or fully shorted cell, it will provide a smaller share of the load current.

b. Excessive battery temperature or charge current during long periods of float charge. Under normal conditions the regulator provides the means to limit the total number of ampere-hours recharged into the battery. If a cell is shorted, the regulator voltage limit cannot perform this function, and the battery will become excessively charged. Since a short-circuit failure is gradual, the Ag-Zn battery charge current may be monitored on the ground to determine when this type of failure occurs.

Since it is possible to continue to use the Ag-Zn battery after this type of failure, though in a limited manner, the secondary set of voltage limits, B and B', were included.

After the final orbit trim maneuver, the Ag-Zn battery charger will be turned off to save charging power. The Ag-Zn battery will discharge during the next few orbits, and then will be "stored" in the discharged state. This is a relatively low-stress condition for Ag-Zn cells, and they may be recharged at a later time if additional high usage maneuvers are subsequently required.

4.4. POWER SYSTEM FAILURE DETECTION

Automatic onboard failure detection is required in order to apply redundancy to the Power Subsystem power conditioning equipment. The failed unit cannot be replaced by command, since the command subsystem operation is dependent on correct operation of the Power Subsystem.

The functions performed by the Power Subsystem failure detectors are:

a. Detect failures

b. Remove the failed unit

c. Replace the failed unit with a redundant unit

The failure detectors also discriminate against failures in the power source or the load.

4.5. SYNCHRONIZATION

The frequencies generated in the Voyager Power Subsystem are used in various parts of the Power Subsystem as timing and synchronization signals. The same clock is used to supply additional frequencies to other subsystems. The present design supplies synchronizing frequencies to the indicated user subsystems:

Frequency	Subsystem
1.296 MHz	Telemetry
2400 Hz	ALL
400 Hz (3 Phase)	Attitude Control (high accuracy required for Gyros)
160 Hz	High Gain Antenna Articulation
32 Hz	Computer & Sequencer

Frequency drift will be less than 1 PPM in six months in order to enable orbit insertion timing commands to be set into the C&S prior to launch and maintain the completely automatic vehicle concept.

An additional backup oscillator provides a redundant 2.4 kHz signal with a frequency accuracy of ±1 percent, and all frequencies below this point may be derived from this signal.

In addition to the frequencies supplied there are some intermediate frequencies which may be made available to the various subsystems with minor changes. It is possible, with additional circuits, to obtain any frequency required which is related to the clock frequency by an integer. It is expected that frequencies required by the Science Subsystem other than those readily available will be generated within that subsystem to maintain synchronizer interchangeability for different missions.

Although the clock required power from the 2.4 kHz inverter to operate, and the inverter derives its synchronization signal from the clock, the free-running capability of the 2.4 kHz inverter will permit the system to start up.

5. EQUIPMENT FUNCTIONAL DESCRIPTION

5.1. SOLAR ARRAY

The solar array consists of 16 fixed trapezoidol panels arranged in an annular ring about the spacecraft, canted at a solar incidence angle of 33.9 degrees. Nine additional, smaller, panels are deployed normal to the sun in the annular space around the fixed panels.

Shadows cast by the Canopus tracker, and support brackets for the high gain antenna (HGA) and planet scan platform (PSP) reduce the area available on four of the fixed panels.

The string cell arrangements are summarized as follows:

Panel Type	No. of Panels	Strings	Series Cells	Parallel Cells
Full Panels	12	4	125	5
		1	125	6
Canopus Sensor Bay	2	4	126	6
High Gain Antenna Bay	1	3	124	5
Planet Scan Platform Bay	1	4	124	3
Deployed Panels	9	2	126	6-1/2

The total array contains 63,130 equivalent 2x2 cm cells.

The solar cell characteristics are as follows:

Type:	N/P, silicon
Dimension:	2 x 2 centimeters, 13 mils thickness, and a few 1 x 2 centimeters.
Effective cell area:	95 percent
Contacts:	Sintered titanium - silver, standard top and bottom contact configuration.
Bare cell efficiency:	11.0% at zero air-mass at mean earth-sun distance, cell temperature 28°C.
Base resistivity:	1 ohm-centimeter

Protective solar cell cover windows are bonded to each solar cell.

Characteristics are:

Material:	Fused silica, Corning No. 7940
Filter:	Blue, 0.41 micron cut-on frequency, deposited on solar cell side of window, antireflection coating on opposite face.
Thickness:	10 mils

The window-to-cell bond is GE clear silicone rubber RTV-602. The solar cells are bonded to the panel substrate using GE silicone rubber RTV-560.

The panel substrates consist of honeycomb with fiberglass face sheets.

The solar cells are interconnected by means of 3 mil expandable strips of silver plated molybdenum. Molybdenum was selected for its expansion characteristics relative to the silicon cells, and its high electrical conductivity.

Zener Regulators. Zener regulators are used to limit the voltage output of the solar array to a value in the range of 54 to 65 volts. A separate zener regulator is used for each string in the array. Therefore, 93 regulators are required. Each regulator is potted into a block of aluminum using a resilient thermal conductor and the monoblock contains two parallel strings of eight zener diodes and the two redundant array isolation diodes, as shown in Figure 6. Each diode is rated at 7.5 volts and three watts. Taking into account the dependence of zener voltage with temperature, the zener regulator will limit the array voltage to 54 to 65 volts. The maximum power dissipating requirements per regulator is limited to the power output of a single solar cell string, estimated to be a maximum of 40 watts near the earth. The monoblocks will be mounted on the webs of the trusses supporting the solar array to provide the necessary heat dissipation capability.

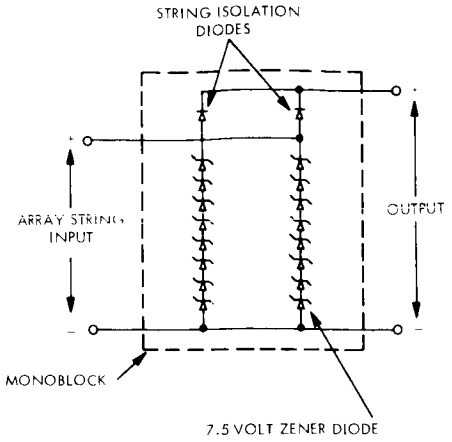

Figure 6. Zener Regulator Schematic

5.2. BATTERIES

Three batteries are used. They are discharged in parallel and charged separately: The three batteries are:

a. Two nickel-cadmium batteries, each with 32 cells of 20 ampere-hour capacity.

b. One silver-zinc battery with 27 cells of 45 ampere-hour capacity.

Nickel-cadmium (Ni-Cd) batteries were selected to replace the silver-cadmium (Ag-Cd) batteries proposed previously in Task A and Task B because of the disappointing cycle-life and long-term float charge performance measured for Ag-Cd cells. Silver-zinc cells demonstrated better long-term float charge life, and in view of the limited cycling required from the Ag-Zn battery during maneuvers, appear to be able to meet the Voyager requirements.

The nickel-cadmium batteries each weigh about 80 pounds and occupy 0.7 cu ft of volume. The 32 cells are hermetically sealed in stainless-steel cases, each can containing two ceramic bushings which serve as the positive and negative terminals. A terminal is attached directly to the can for the third electrode signal. The cells are mounted in an unsealed

magnesium box with two connectors -- one for power and telemetry, and the other a special access connector for pre-installation checkout of each cell.

Each Ni-Cd cell will contain a third electrode, but only three units in the battery will be used to control battery charging. The third-electrode voltage is sensitive to oxygen pressure evolved during overcharging, and with the proper voltage bias, the signal can be used to switch the battery to the trickle charge rate when the proper degree of overcharge has occurred. The third-electrode signals will be gated to select the first of the three to indicate the desired level of overcharge.

The silver-zinc battery weighs about 45 pounds and is 0.40 cu ft in volume. The 27 cells are in plastic cases, equipped with 10 psi vents. The battery box is magnesium, sealed, with a 20 psi safety vent, and also has two connectors, as for the Ni-Cd battery.

The special access connector, used with both battery types, permits discharge of each cell individually to a uniform voltage prior to installation of the battery in the spacecraft. This permits balanced initial charging of all cells in the battery.

The relative numbers of cells in the two types of batteries were selected so that the Ag-Zn battery is preferentially discharged during the maneuvers, and so that, in the event of a short-circuit failure of one cell in the Ag-Zn battery, the Ag-Zn battery will still support a substantial portion of the load.

5.3. MAIN VOLTAGE REGULATOR

The main voltage regulator is designed to provide sufficient regulation so that, after the power is conditioned by the 2400 Hz inverter, the ac is well-regulated enough to meet the requirements of the majority of the user subsystems. Operating from the solar array/ battery bus this power conditioning unit provides a regulated 35 volts ± 1 percent over expected input voltage and load variations. The design maximum average output power is

500 watts, with a peak capacity of 750 watts. Efficiency is 90 percent at design load with lower efficiency at low power due to fixed losses. A functional circuit diagram is shown in Figure 7.

The high efficiency is achieved by using a transistor switch to provide low loss pulse width modulation with appropriate input and output filters to obtain current transformation. Basically this circuit is a form of dc transformer. Under theoretically ideal conditions, input and output parameters are related by a constant K which represents the portion of time the transistor switch is closed (i.e., $I_i = KI_o$ $KE_i = E_o$ $O \leq K \leq 1$). The variable losses consist primarily of the power dissipated in the resistances of the input and output inductors, the saturated switching transistor, the forward resistance of the power diode and the switching loss in the transistor during turnoff. The fixed losses are primarily associated

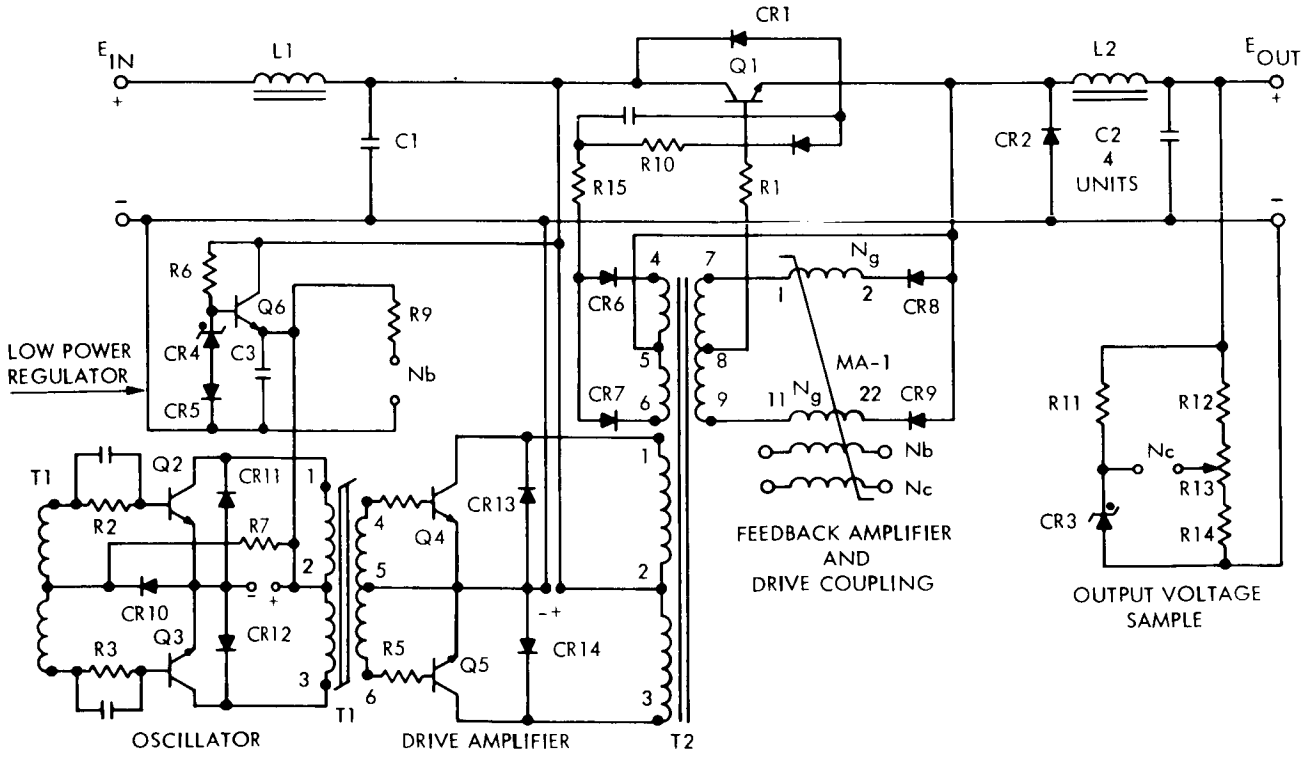

Figure 7. Main Regulator

with the driving circuit. Experience with the laboratory models have shown that higher efficiency over a broader range is possible but requires a more critical design with accompanying loss of reliability. The critical design area for this type of regulator is concerned with the turnoff switching time and the associated stress on the switching element. The size, weight and power loss of the total component are closely related to this parameter. Laboratory tests on this regulator indicate sufficient design margin is available to justify the use of a 750-watt regulator in a long-life vehicle.

The remaining circuits in the regulator consist of a power oscillator to generate the ac driving power and a magnetic amplifier to provide the pulse-width modulation control. The magnetic amplifier design was selected for ruggedness, wide range of control and power handling capability. The control signal is derived from the output voltage with a zener diode standard and applied to the control windings of the magnetic amplifier.

5.4. BATTERY CHARGE REGULATORS (BCR)

The battery charge regulators for both the nickel-cadmium and silver-zinc batteries are basically current-limiters which transform into voltage-limiters at selected high voltage limits. In addition, the Ag-Zn BCR reduces the charge voltage limit to the "float" level when the charge current has tapered to a preset low level. Both types of BCR may be switched to lower-stress limits by ground command.

5.4.1. Nickel-Cadmium Battery Charger

The BCR for the Ni-Cd battery is a pulse-width-modulated current- and voltage-limiter with three states (OFF, Setting A, and Setting B). Setting A is the normal high-current setting for recharging the battery rapidly during the occulted-orbiting phase of the mission. When there are no solar eclipses, or when the battery is fully recharged after a maneuver, the current limit is reduced to the B setting, which is a maintenance level of C/40. This is done using a third-electrode signal, and is backed up using a signal from the C&S or by command. The high-voltage limit is set to prevent excessive over-charge from occurring at the lower range of battery temperatures.

The power circuitry required for regulation is similar to that required for the main voltage regulator (Paragraph 5.3). A modification of the error control signal is required to incorporate the dual voltage-current regulation modes. The error circuit is shown in Figure 8. The output of the current transformer controls the conduction of Q_1 and hence the bias current in the zener diode standard. Selection of R_4 and R_5 so that the bias current in the zener approaches zero as the charge current approaches the design limit will result in a change of control mode from voltage regulation to current regulation. Since the voltage control loop undergoes a reduction in gain as the transition is approached critical instability points are avoided.

5.4.2. Silver-Zinc Battery Charger

This is a series-dissipative current- and voltage-limiter, which also has three states. The A setting is a pair of voltage limits for the full complement of cells (27). The battery will charge at the current limit until the upper voltage limit is reached. The upper voltage limit will then act until the charge current has tapered to about C/200, at which point the voltage limit will drop to the "float" voltage. When the battery is fully charged, the current will fall to very small values (a few mamp.) at the float voltage.

The B setting is a pair of limits set for a 26-cell battery, which allows for the short circuit failure of a single series cell and extends the useful life of the Ag-Zn battery. This regulator requires an error circuit similar to that required for the Ni-Cd battery charger but with an added multilevel voltage regulation feature. The circuit is shown in Figure 9. Transistor Q_1, Resistors R_4 and R_5, function as before to provide the current regulation, voltage regulation mode transition. The additional decreased voltage regulation mode is provided by Q_2, R_6 and R_7. When the charge current falls below the voltage at which the base of Q_2 is biased by R_8 and R_9, current flows through R_7 lowering the effective standard voltage. The resulting decrease in regulated voltage decreases the charge current further increasing the conduction of Q_2. The effect of this positive feedback is to produce a rapid change of operating point until Q_2 is saturated. The circuit will remain in this state until

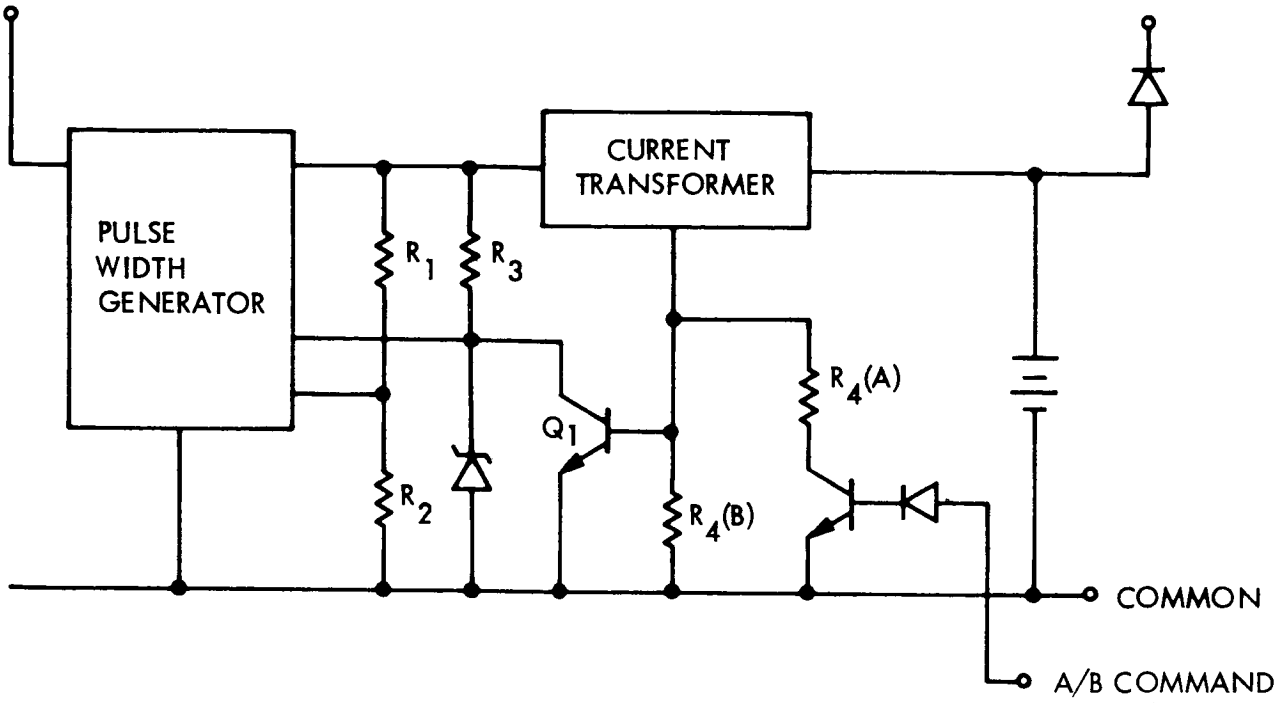

Figure 8. Nickel Cadmium Battery Charge Regulator

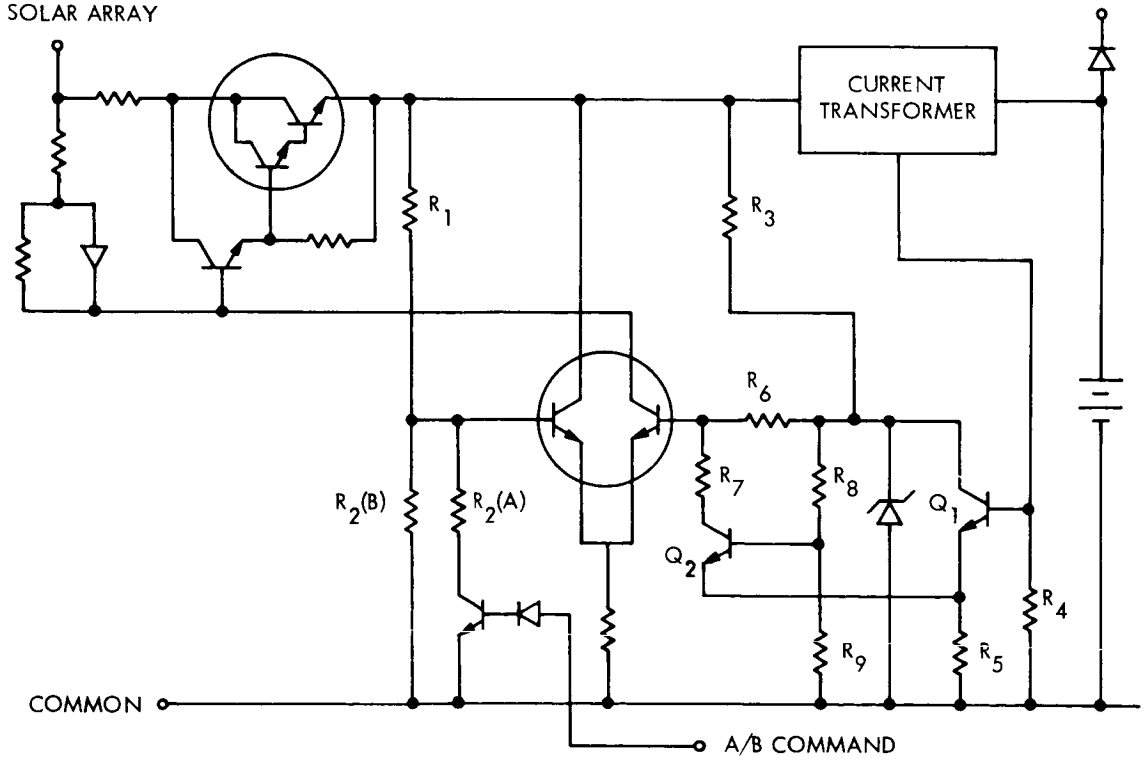

Figure 9. Silver Zinc Battery Charge Regulator

the charge current rises sufficiently to decrease conduction in Q_2 and the reverse of the previous snap action occurs. (See Ni-Cd and Ag-Zn Battery Charger Logic circuits, Figures 10 and 11.)

5.5. 2400 Hz INVERTER

The 2400 Hz inverter supplies an alternating 50 volt square wave to the ac distribution system from the regulated 35 volt dc bus. This output is the main distribution for all power users. The output regulation estimate is 2.5 percent for input voltage variations and load variations from full to half load. The circuit diagram is shown in Figure 12. The inverter has the capability of free-running operation to ensure initiation of system functions. The same synchronization signal is applied to both inverters. In the event of failure of both the synchronizer and the 2.4 kHz backup oscillator, the inverter will establish the total distribution frequency to ensure compatibility between components using the power distribution bus as a source of timing signals.

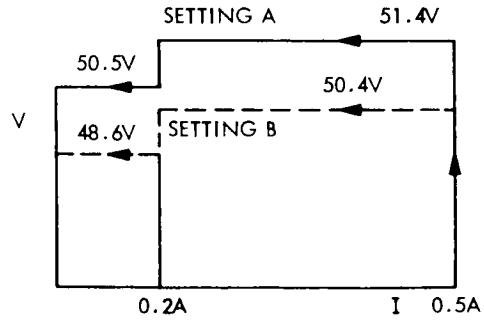

Figure 10. Ni-Cd Battery Charger Logic

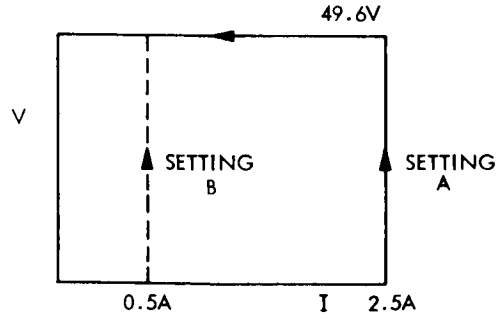

Figure 11. Ag-Zn Battery Charger Logic

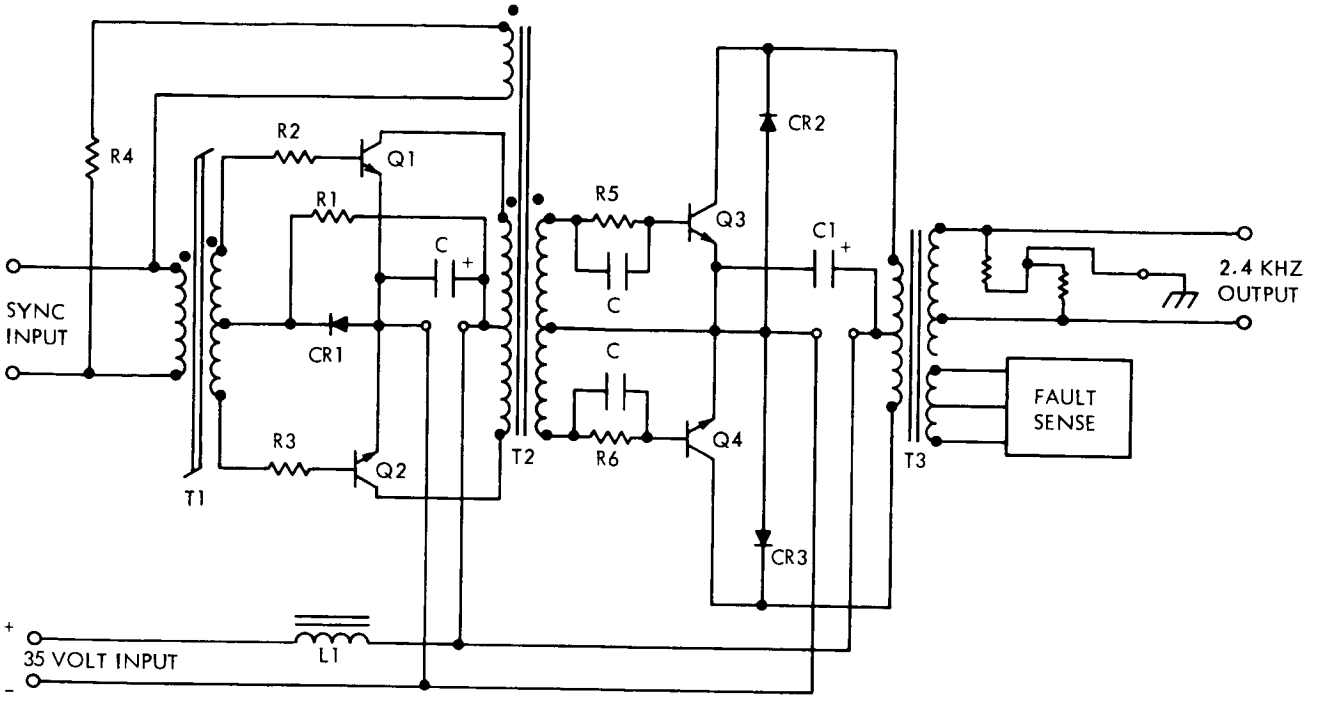

Figure 12. 2.4 kHz Inverter

The selection of 2400 Hz as the power distribution frequency is based on consideration of power, weight, reliability and harmonic relationship with 400 Hz. Size and weight of filter elements and transformers decrease with increasing frequency. Switching losses and copper loss and hysteresis loss increase with frequency. Increasing the frequency significantly beyond 2400 Hz would require the use of lower loss magnetic materials. The lower saturation flux density and increased switching losses would necessitate a frequency increase to approximately 10 kHz to realize significant improvement in power, weight and size. This frequency would raise the ambient noise level and reduce the life and reliability of the switching transistors.

5.6. 400 Hz SINGLE-PHASE INVERTER

The 400 Hz power required by Science and PSP will be supplied by an inverter similar in configuration to the 2400 Hz inverter. Synchronization will be provided from the clock and synchronizer and free run capability is also provided. Output regulation with input line and load variation will be 5 percent.

5.7. 400 Hz THREE-PHASE INVERTER

This component consists of three driven transistor-core inverters (Figure 13) with the same configuration as the 400 Hz and 2400 Hz inverters. The self-start capability is present but phase control is provided by the output of the 400 Hz function generator. It is considered that the redundancy present in the function generator as well as the highly redundant 2400 Hz output is sufficient protection against failure. The positive feedback inherent in the self-start function is utilized here to reduce the driving power required.

The synchronizing input from the function generator provides frequency as well as phase control with an accuracy determined by the master oscillator (i.e., 1 PPM in six months). This high accuracy obtained by this configuration is in excess of the precision required by the three-phase gyro load and provides additional design margin. The actual three-phase output is obtained as a sum of portions of the output of each of the three inverters. Figure 14 illustrates the results of combining windings from the three inverters (ϕ_1, ϕ_2, ϕ_3) to provide a stepped output voltage (ϕ_a). The output waveform developed by this method is more effective as a drive for the gyro motors due to the lower harmonic content.

Filters may be used to improve the low power factor of the gyro motor load and reduce the volt-ampere rating of the inverter. This is not considered justifiable at present since the magnitude of the losses involved are small, the accuracy and stability of phase control would be reduced and the capacitors required for this compensation would reduce the reliability of the system.

Two three-phase inverters are used to power two sets of gyros in a standby redundant configuration. During critical periods both systems are energized providing a passive redundant configuration.

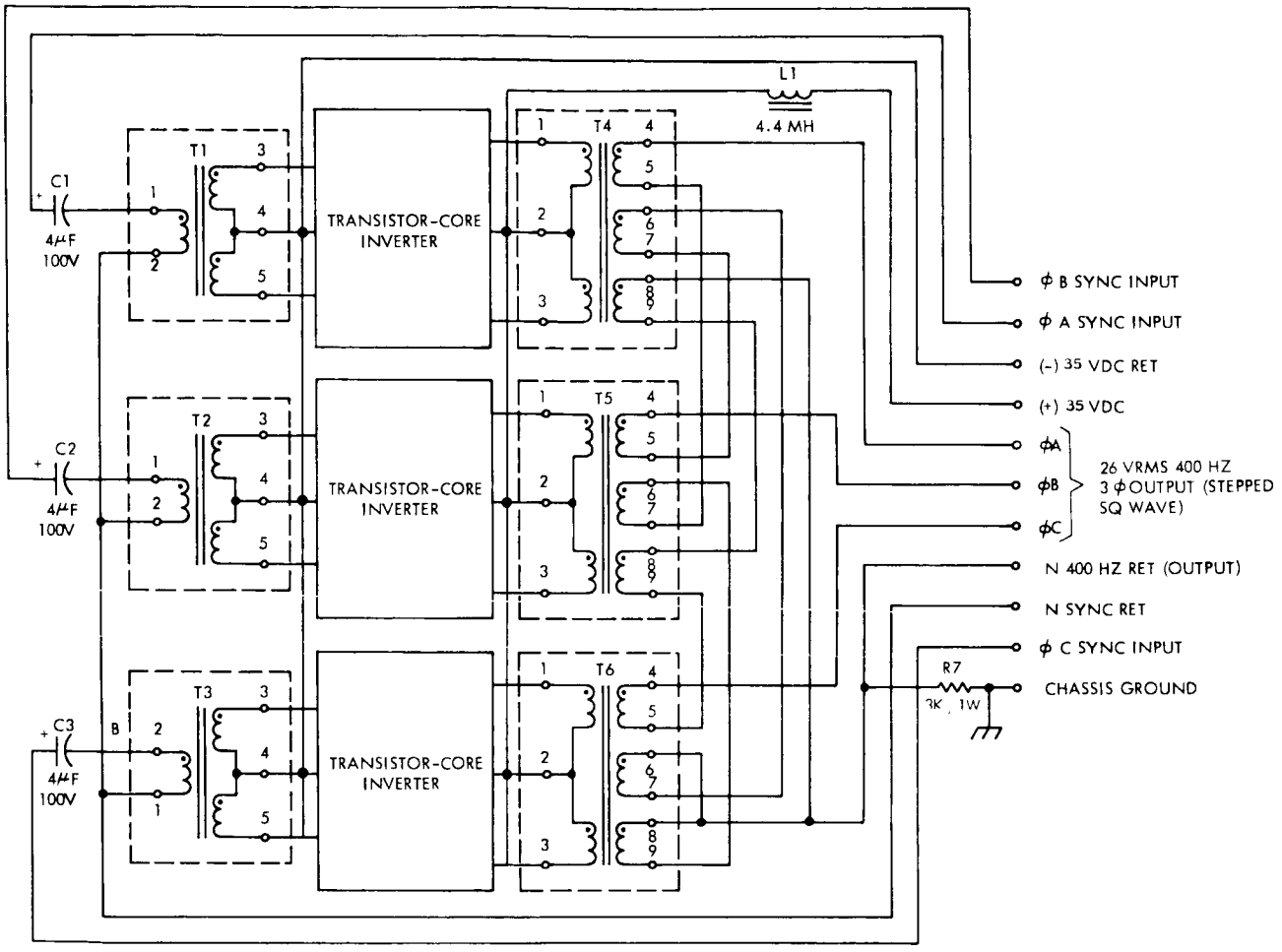

Figure 13. 400 Hz 3-Phase Inverter

ϕ_1	ϕ_2	ϕ_3	$\phi_A = \phi_1 + \phi_2' + \phi_3'$
+1	-1	+1	1
+1	-1	-1	3
+1	+1	-1	1
-1	+1	-1	-1
-1	+1	+1	-3
-1	-1	+1	-1

VOLTAGE COMBINATION TO PRODUCE STEPPED 3φ OUTPUT

Figure 14. Voltage Combination to Produce Stepped 3ϕ Output

5.8. CLOCK AND SYNCHRONIZER

The configuration of the clock and synchronizer is illustrated in Figure 15. The frequency standard configuration requirements and selection is summarized below:

Stability Requirement	1 PPM/6 Months
Preferred Range	1 to 5 MC
Selected Configuration	
Crystal	1.296 MC at Cut Glass Envelope
Temp. Control	Proportional Control $\pm$ 0.1°C
Oven Alternatives	Single or Dual Dewar Flask ECCO Foam or Equivalent

The stability indicated is required to provide the capability of injecting valid orbit insertion timing commands at launch. Factors of frequency stability and structural strength are traded off in the selection of the primary crystal frequency standard. The clock frequency was selected from the optimum frequency range so as to provide integer ratios with the timing signals required for telemetry and the frequencies required for power distribution. The selection of the oven is influenced by tradeoffs between structural strength, weight, and power. The foam oven offers advantages of weight and reliability at the cost of power.

The redundant clock configuration is shown in Figure 16. Provision is made for operating from either master oscillator by command. The internal logic consists of signal amplitude detectors, digital logic and gates to implement switching in the event of catastrophic failure.

The first counter divides the clock frequency by a factor of three (Figure 17), and is typical of the other counters in the system. Logic is provided to drive the two flip-flops to the reset state from the first stage to reduce propagation time problems. The increased design margin provides a conservative design without significant circuit modification. The single shot circuits provide the reset signal from the output of any majority gate to one pair of flip-flops to establish the factor of three count and maintain synchronization. Since the reset signal

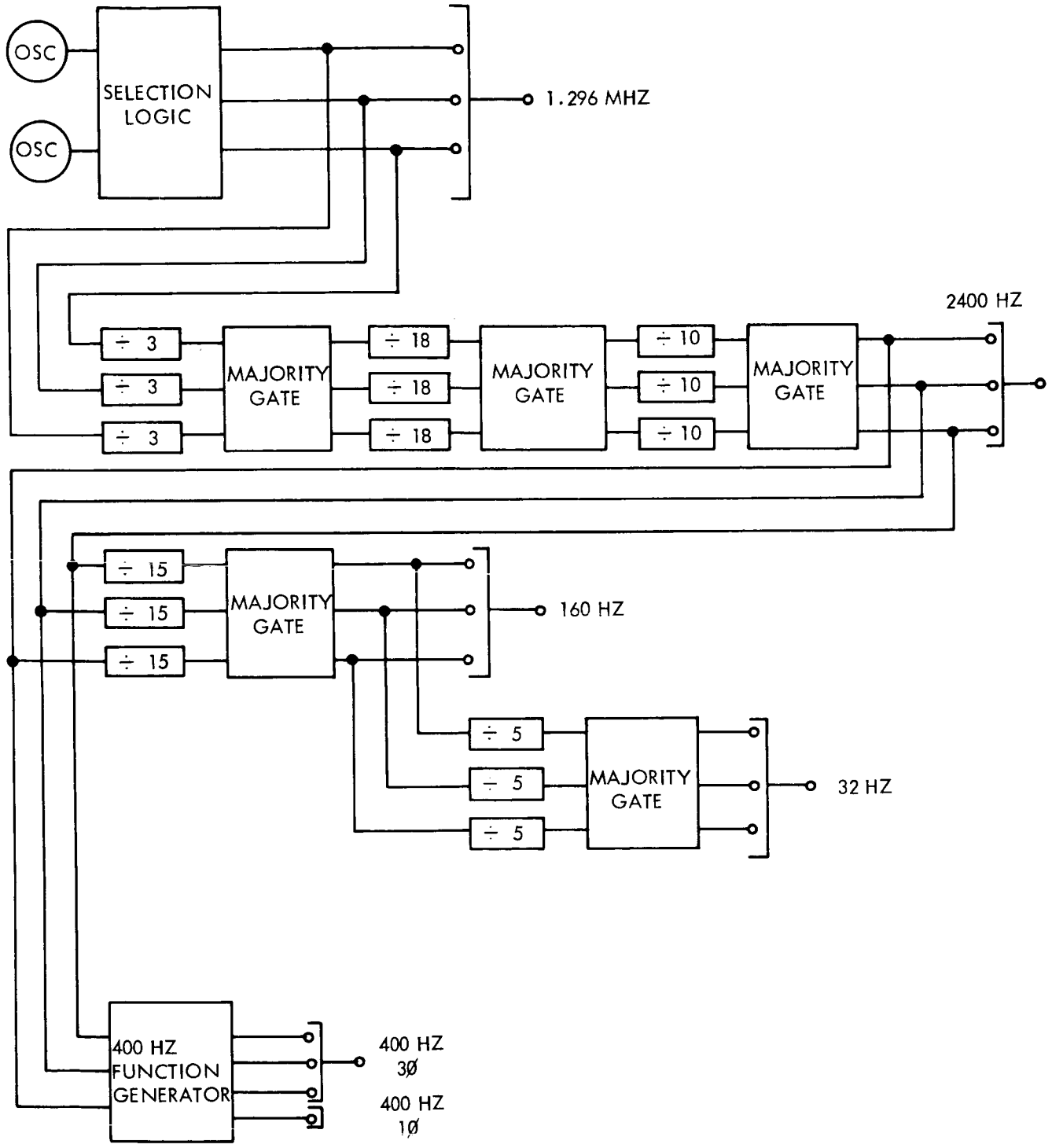

Figure 15. Clock and Synchronizer Configuration

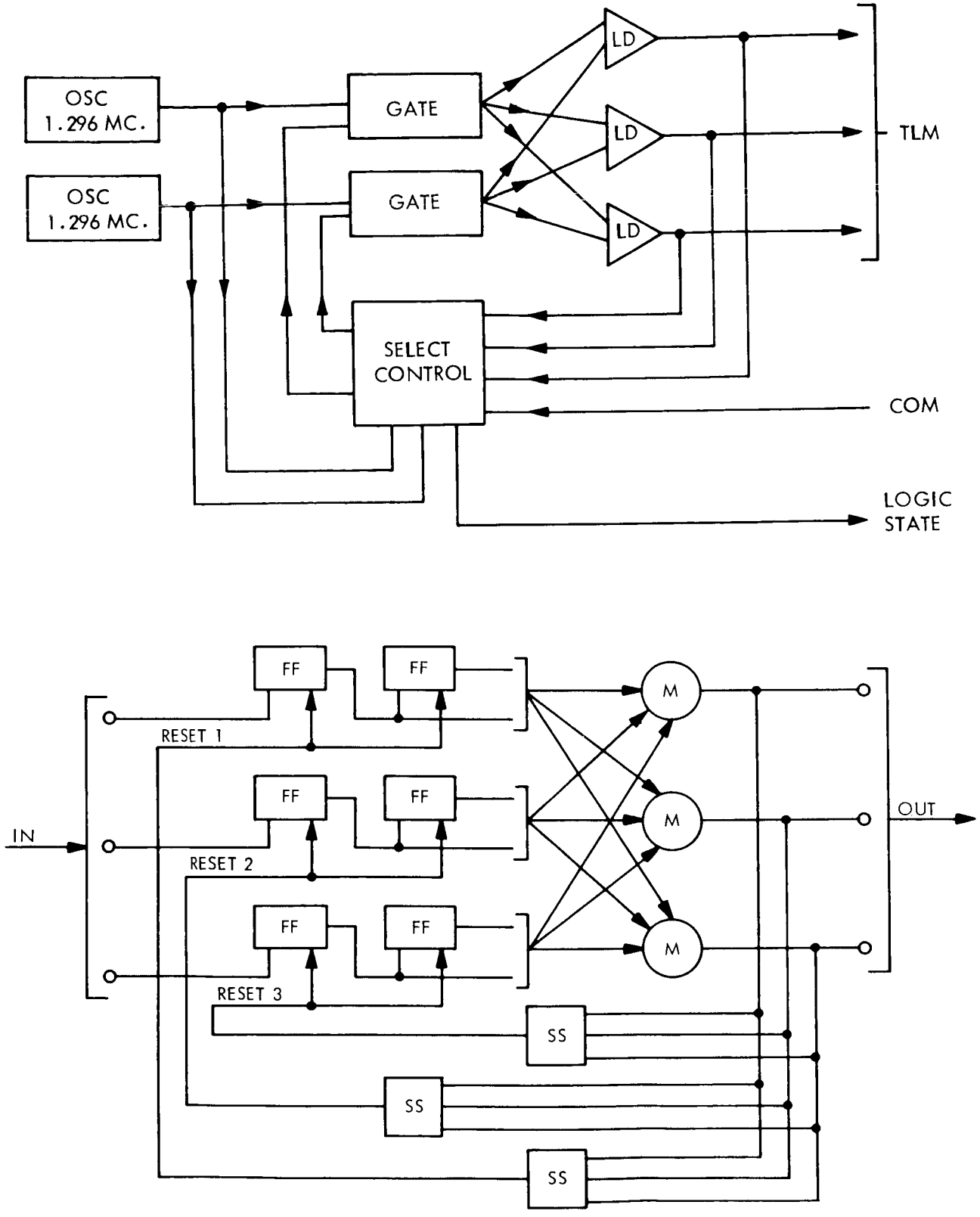

Figure 17. Divide-By-Three Counter

can be derived from any one of the majority gates, the possibility of one faulty gate providing spurious reset signals will be considered in the final microcircuit selection.

The function generator which supplies the 400 Hz 3-phase control signals (Figure 18) is a factor-of-six divider with the logic indicated by Table 5 providing the three phase output. The inverted outputs are used for phases one and three to maintain similarity in logic circuits.

The methods and means of obtaining the clock and synchronizer function are selections based on present requirements. The application of microcircuits makes the use of redundancy feasible. These circuits constrain the configuration to those which utilize available flight worthy elements. The final configuration will be based on the evaluation of the reliability of these parts.

Table 5. Truth Table for 400-Hz Three-Phase Function Generator

÷ 6 Count	FF State	ϕ_1	ϕ_2	ϕ_3
0 0 0	a' b' c'	1	0	1
0 0 1	a' b' c	1	0	0
0 1 0	a' b c'	1	1	0
0 1 1	a' b c	0	1	0
1 0 0	a b' c'	0	1	1
1 0 1	a b' c	0	0	1
		$\phi_1 = a'(b' + c')$ $\phi'_1 = a + b\,c$	$\phi_2 = b + a\,c'$ $\phi'_2 = b'(a' + c)$	$\phi_3 = b'(a + c')$ $\phi'_3 = b + a'\,c$

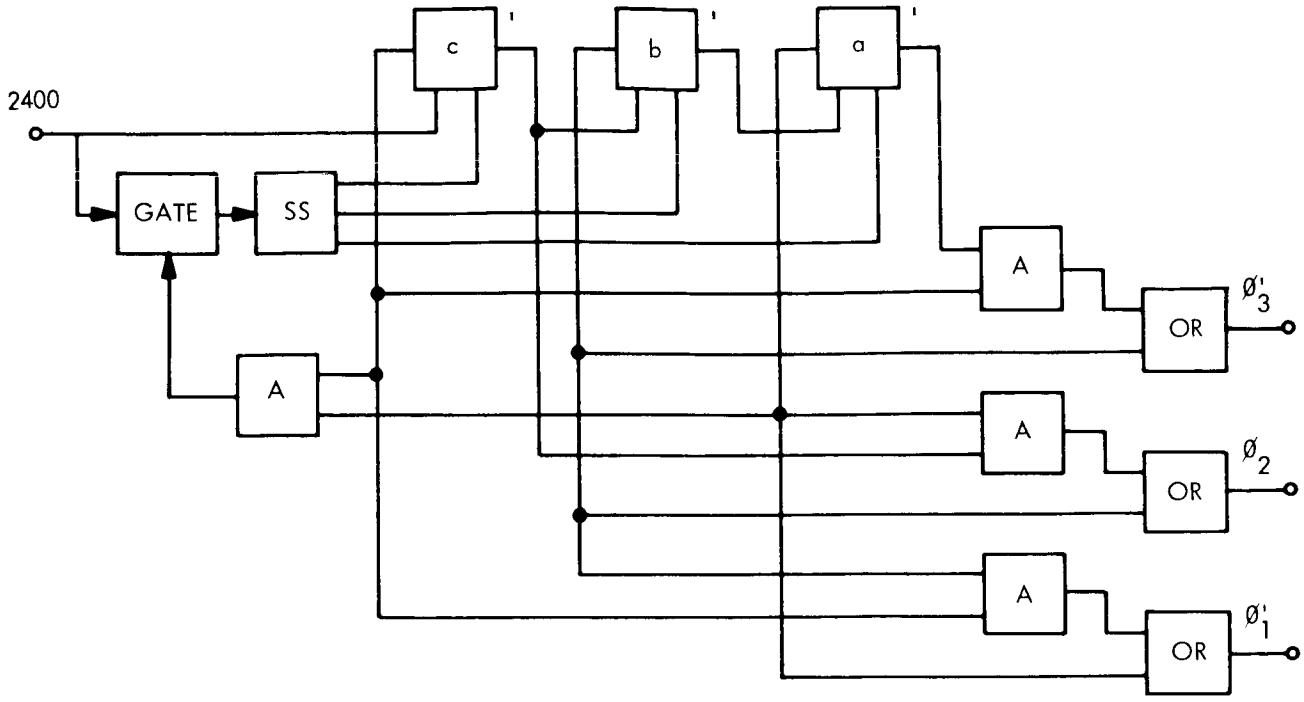

Figure 18. 400-Hz Function Generator

5.9. FAILURE DETECTORS

The failure detectors consist of voltage, current and power comparators, logic networks, and relay trip circuits. The failure detector internal logic is designed to:

a. Detect failures in the power conditioning unit (PCU) being monitored.

b. Discriminate against failures external to the PCU (power source or load failures).

c. Remove the failed unit.

d. Insert a redundant unit into the subsystem.

The failure detector measures performance parameters external to the PCU (input and output current and voltage) and from these deduces the operating condition of the PCU. A typical set of failure detector logic is given in Figure 19.

In order to reduce cost, test time, and integration problems, it is desirable to maintain as much similarity as possible between the failure detectors for the different types of PCU's. A "universal" set of logic may be developed using output/input voltage and current ratios. The failure threshold criteria, using applicable ratios, will be:

(1) $V_o(\text{Min}) < V_o < V_o(\text{Max})$

(2) $V_i(\text{Min}) < V_i < V_i(\text{Max})$

(3) $I_o(\text{Min}) < I_o < I_o(\text{Max})$

(4) $I_i(\text{Min}) < I_i < I_i(\text{Max})$

(5) $K(\text{Max}) > \frac{V_o}{V_i} > K(\text{Min})$

(6) $L(\text{Max}) > \frac{I_o}{I_i} > L(\text{Min})$

(7) $\frac{P_o}{P_i} > N$

All the failure and inhibit criteria necessary for the Voyager PCUs may be determined by these inequalities.

The basic comparator circuit function is given in Figure 20, where voltage sensing is shown for illustration. Figure 20(a) shows absolute magnitude limit sensing, as for Inequalities (1) through (4). Figure 20(b) illustrates ratio limit sensing, required for Inequalities (5), (6), and (7). The actual signals monitored are KV_A and V_B, but if $V_B > KV_A$, then $\frac{V_B}{V_A} > K$.

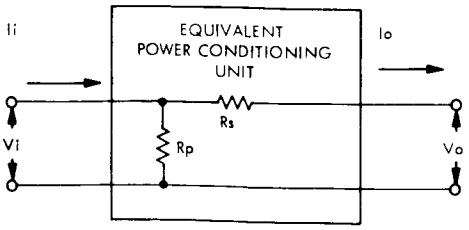

	Vo	Io	Vi	Ii	TRANSFER
THROUGH SHORT	INC.	INC.	DEC.	INC.	YES
OPEN	DEC.	DEC.	INC.	DEC.	YES
OVERLOAD	DEC.	INC.	DEC.	INC.	NO
EFFICIENCY DEC.	NO CHGE.	NO CHGE.	DEC.	INC.	YES
SOURCE VOLTAGE DEC.	DEC.	DEC.	DEC.	DEC.	NO

Figure 19. Failure Detection Logic

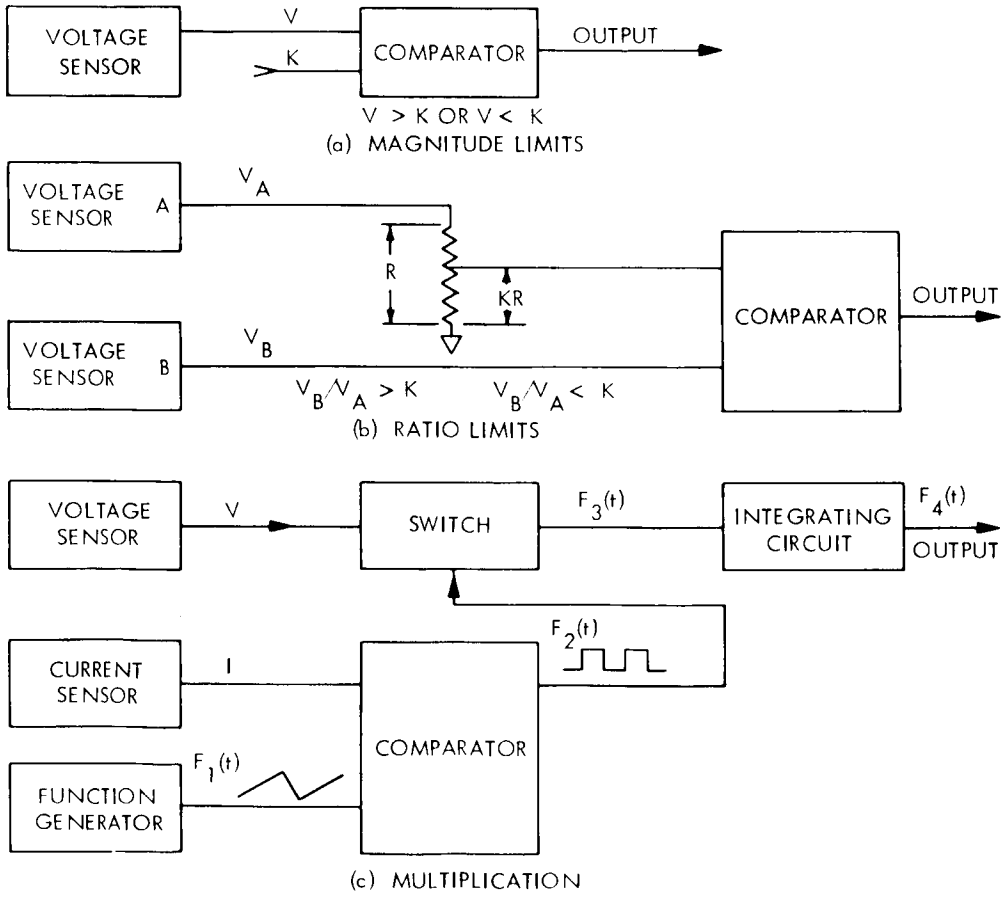

Figure 20. Basic Circuit Functions

Components such as inverters, converters, and transformers, which receive a regulated input voltage, have output/input voltage ratios which remain relatively constant over a wide range of operation. Therefore, an efficiency-loss type of failure may be sensed using the output/input current ratio. Figure 21 shows the failure detector configuration for the inverters. Included are the inhibit function applied at high loads to discriminate against the efficiency loss associated with overloads caused by load faults, and the low-load inhibit which takes into account the lower inverter efficiency inherent at low output levels.

In the case of the main voltage regulator, the ratios of the input and output parameters vary over a wide range (the input and output voltage from 37 to 65 volts, and the output current from 0 to 25 amperes). A relatively high efficiency is maintained in the regulator over the range of input voltages, and it is possible to detect efficiency-loss failures by placing a lower limit on efficiency with inhibit functions similar to those for the inverters. In order to obtain a measurable signal proportional to power, it is necessary to multiply the voltage and current signals. Figure 20(c) illustrates a method for performing the required multiplication. The functions illustrated are F_1 (a linear sawtooth function), F_2 (a pulse-width-modulated signal for which the modulation is a function of current) (this signal controls the switching element), F_3 (a signal for which the pulse width is a function of current and amplitude is a function of voltage), and F_4 (which is F_3 smoothed out into an analog signal forming a linear function of the product of V(t) and I(t)).

A block diagram of the failure detector for the main regulator is shown in Figure 22. Laboratory measurements with this configuration connected to the 500-watt main regulator performed as predicted and maintained fault criteria limits within 2.2 percent over the Voyager temperature range. Significant parameters of this design are given in Table 6.

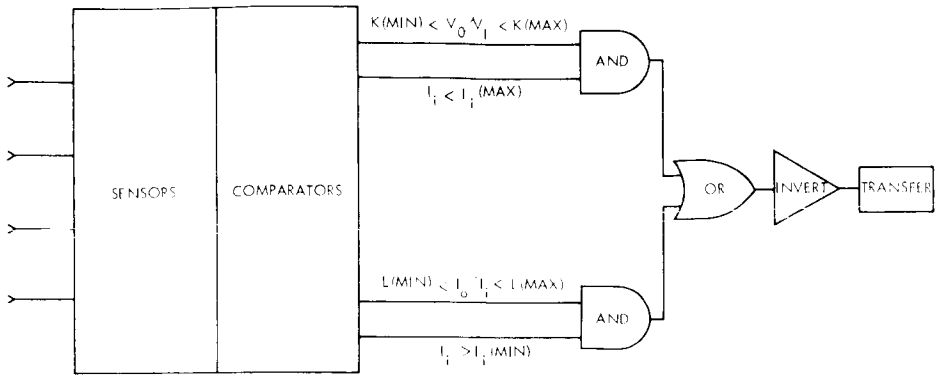

Figure 21. Fault Sensing for Converters and Inverters

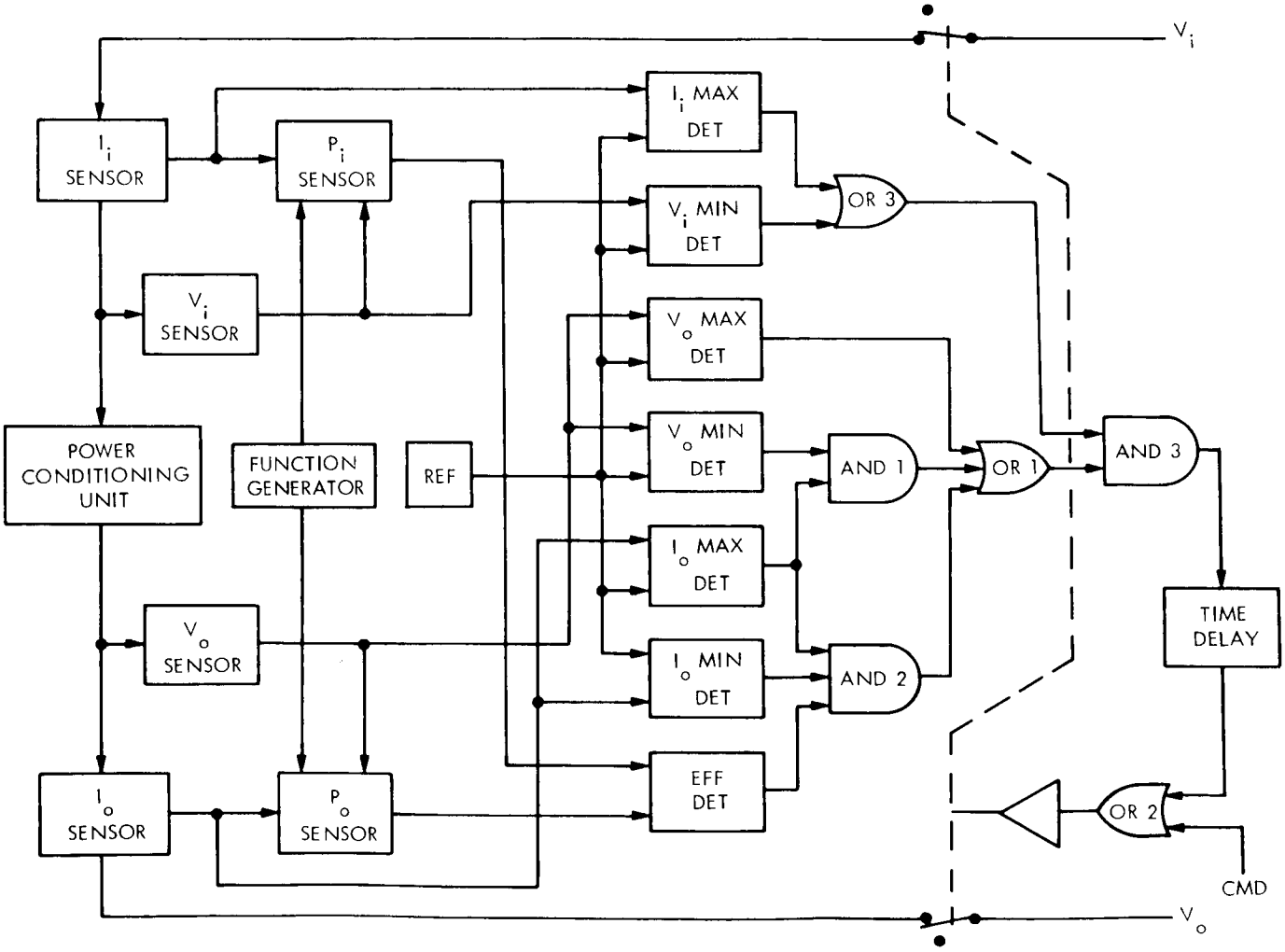

Figure 22. Failure Detection Functional Diagram

Table 6. Failure Detector Performance

Failure Detector		Power Conditioning Unit - Regulator		Figure of Merit	
Power	1.24 Watts	V_i	37 - 65 Volts	500 Watt Regulator Alone	0.98827
Volume	24 in^3	V_o	35 Volts	Failure Detector Alone	0.99171
Weight	0.75 lbs.	I_o (Max)	20 Amperes	FD/REG System	0.99984
		Efficiency	> 90%		

5.10. MISCELLANEOUS CIRCUIT ELEMENTS

Some telemetry circuits require ac drive voltage and special signal conditioning. An ac square wave drive voltage is required for the low power consumption dc current measurements. The oscillator circuit performing this function is similar to the oscillator used in the main regulator. The dc current measuring circuit is shown in Figure 23. The ac current measuring circuit consists of a current transformer and rectifier designed to reflect a minimum impedance to the power bus.

The ac voltage sensor requires rectification and minimum filtering for telemetry monitoring or fault sensing. The three-phase voltage telemetry monitor couples the voltage of each phase into a single resistor such that with the absence of any one phase, the output telemetry voltage has a discrete change signifying that corrective action is required on that three-phase inverter.

During critical maneuvers energy is supplied principally by the batteries and it is desirable to know the number of ampere-hours extracted. In addition, ampere-hour data will provide useful information in securing proper recharging of the Ni-Cd batteries without excessive overcharging. Since the telemetry sampling rate is low, discrete current measurements would provide limited information. A means for implementing an ampere-second meter for

this purpose is shown in Figure 24. Capacitor C has a given charge rate (determined by RC) if Q1 is fully ON. Since Q1 ON time is determined by the battery current (I), the charge voltage on C is a function of I. The voltage is sampled at intervals of 149.2 seconds during maneuvers and 22.4 seconds during orbit (telemetry sampling rate). The capacitor is discharged after each sampling interval and the cycle is repeated. These measurements and the telemetered battery voltage measurements provide a measure of the total energy removed from the battery.

The 2.4 kHz oscillator used as back-up to the clock and synchronizer is shown in Figure 25.

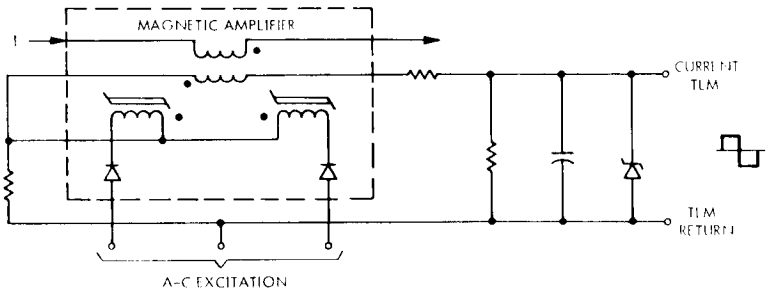

Figure 23. DC Current TLM Sensor

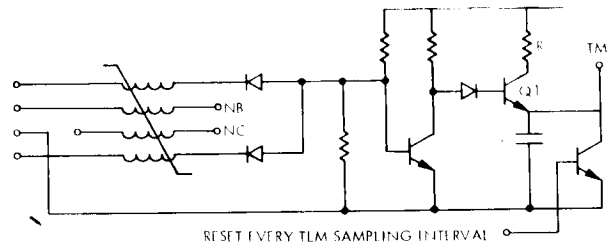

Figure 24. Ampere-Second Meter

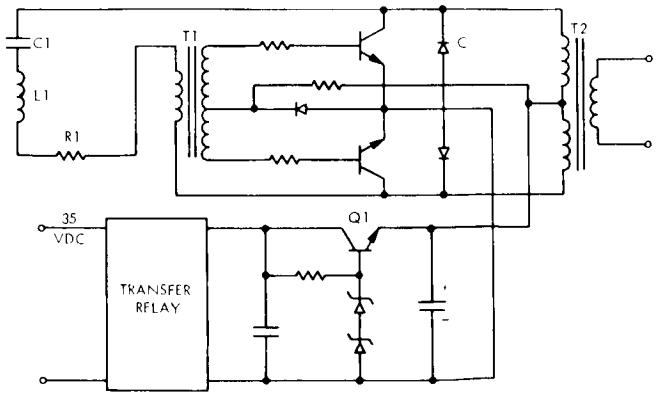

Figure 25. 2.4 kHz Backup Oscillator

6. PHYSICAL AND PERFORMANCE CHARACTERISTICS

6.1. SOLAR ARRAY

The physical characteristics of the solar array are described below:

a. Form: Fixed panels: 16 trapezoidal panels canted at a 33.9 degree angle to the sun, arranged in an annular ring about the spacecraft.

Deployed Panels: 9 rectangular panels, deployed normal to the sun in an annular space outside the fixed panels.

b. Panel configuration and layout: Figure 26.

c. Array area: Total surface area: 310.5 ft^2

Projected panel area: 270.3 ft^2

d. Effective solar cell area: Total 258.2 ft^2

Projected 224.5 ft^2

e. Average packing factor: 0.831

f. Weight:

Solar panels and support structure:	475.8 lb
Harness	25 lb
Zener regulators	8 lb

g. Attachment: Bolts

h. Electrical mating: Connectors for special access and operation.

i. Zener regulators: Monoblocks 1/2 x 1 x 2 in. mounted on the solar panel support ribs. One monoblock is required for each string:
Full panels: 5 monoblocks
Canopus sensor bay: 4 monoblocks
HGA bay: 3 monoblocks
PSP bay: 4 monoblocks
Deployed panels: 2 monoblocks

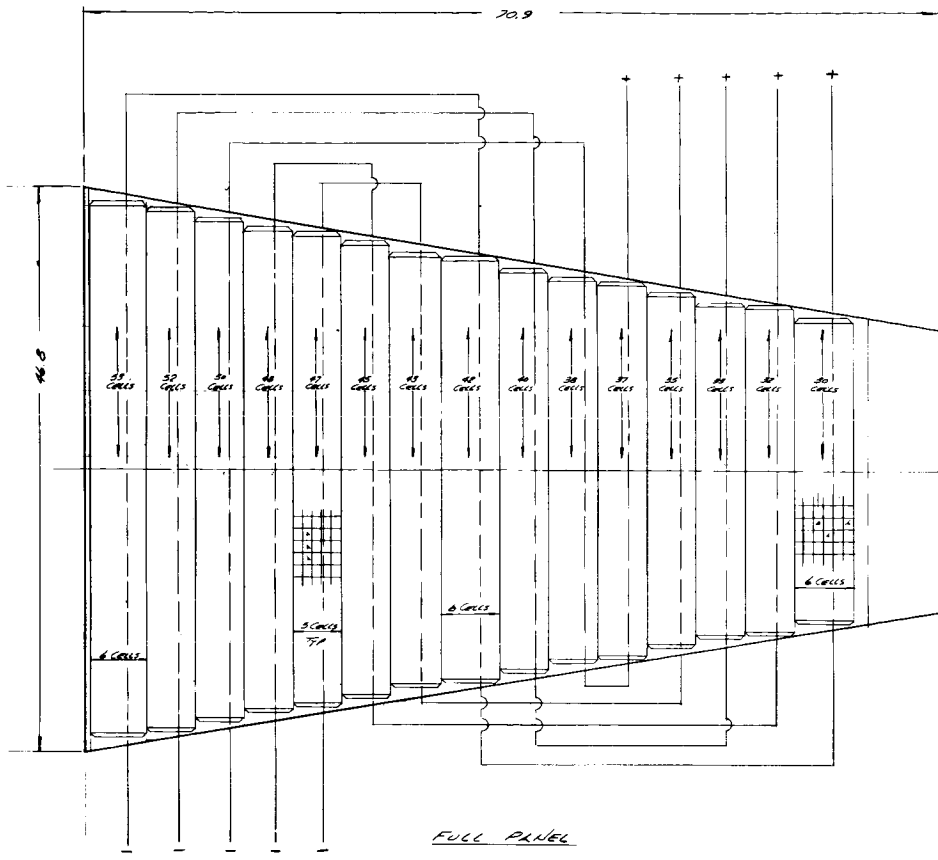

FULL PANEL

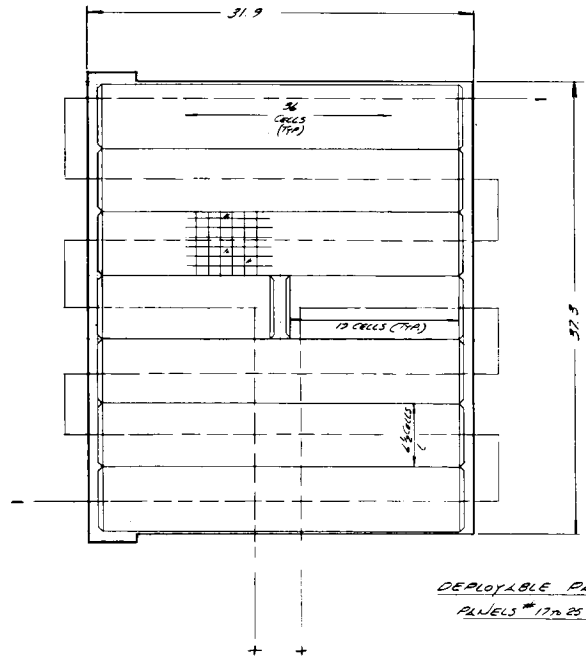

DEPLOYABLE PANELS
PANELS #17 & 25

FOLDOUT FRAME

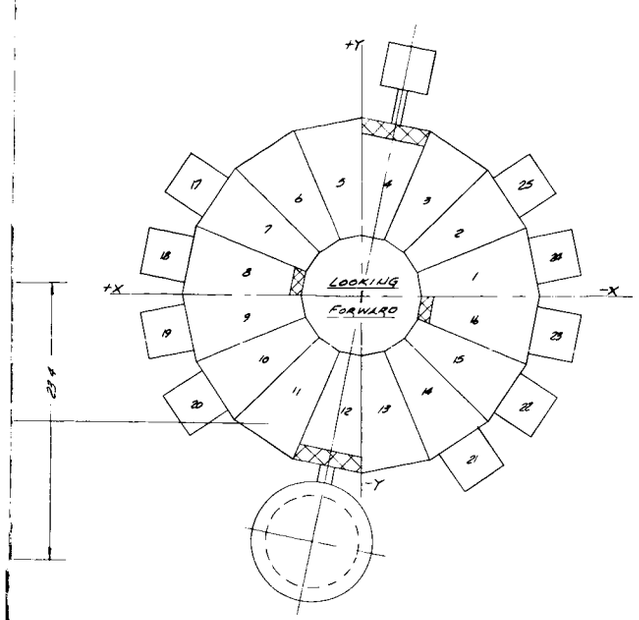

KEY FOR TABULATION

PANEL CONFIGURATION	CELL ARRANGEMENT	# NUMBER OF CELLS	CELL WEIGHT (POUNDS)/PANEL	NUMBER OF PANELS	TOTAL NUMBER OF CELLS
FULL	ONE STRING 125 SERIES X 6 PARALLEL FOUR STRINGS 125 SERIES X 5 PARALLEL	750 2,500	5.10	12	39,000
HI-GAIN ANTENNA	THREE STRINGS 124 SERIES X 3 PARALLEL	1,488	2.34	1	1,488
PLANET SCAN PLATFORM	FOUR STRINGS 120 SERIES X 3 PARALLEL	1,860	2.92	1	1,860
CANOPUS SENSOR	TWO STRINGS 126 SERIES X 6½ PARALLEL	1,638	2.57	9	14,742
CANOPUS SENSOR	FOUR STRINGS 126 SERIES X 6 PARALLEL	3,024	4.74	2	6,048
		TOTALS	99.07	25	63,138

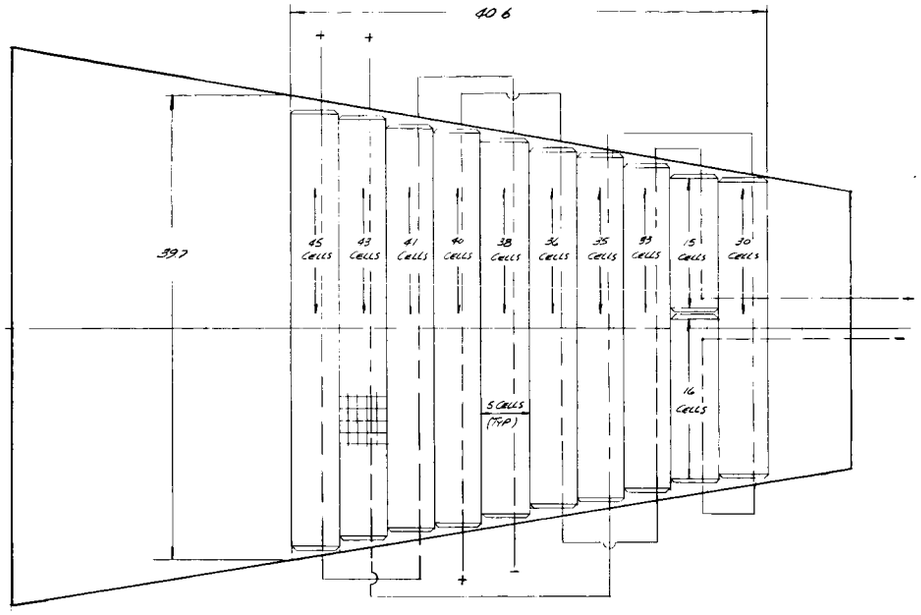

HI-GAIN ANTENNA PANEL # 12

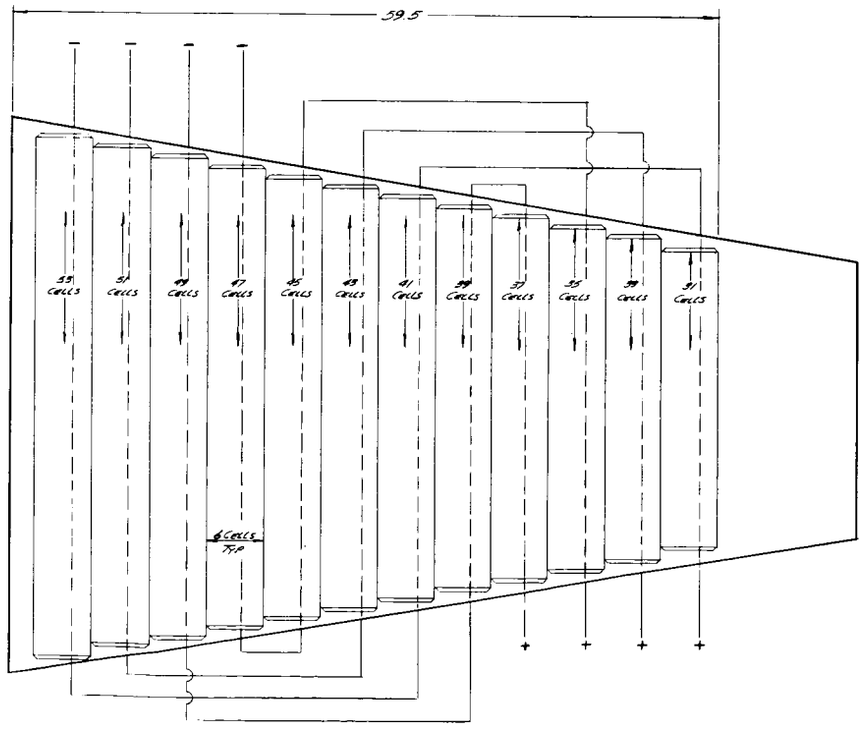

CANOPUS SENSOR PANEL
PANELS # 8 & 16

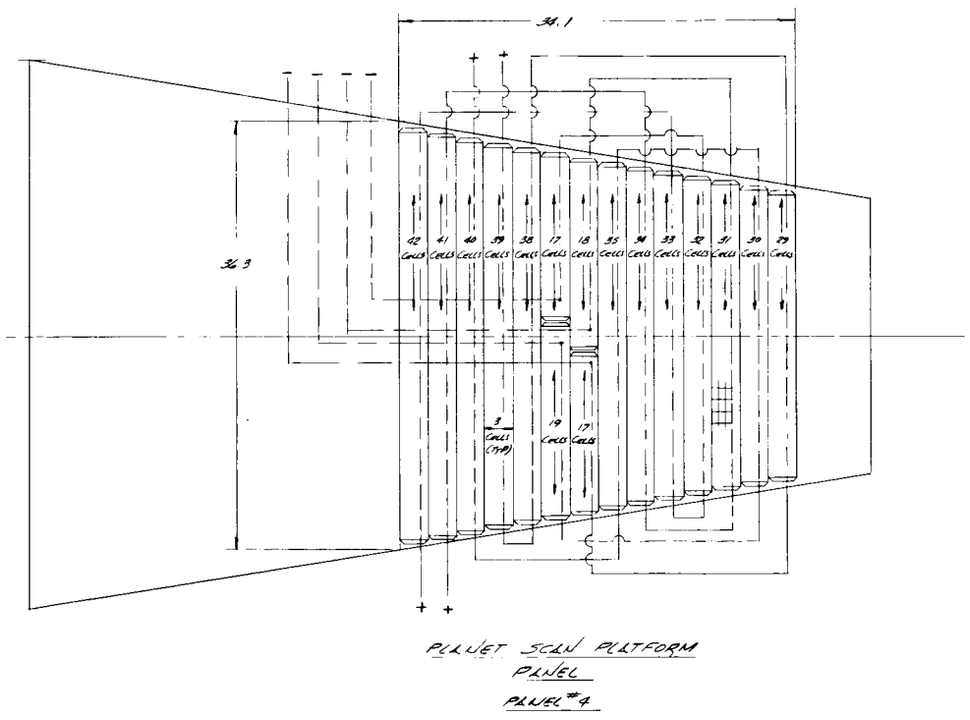

PLANET SCAN PLATFORM PANEL
PANEL # 4

Figure 26. Panel Layout

The performance of the solar array is summarized in Figure 27, which presents array power output at the nominal design voltage (54 volts) as a function of time. This power-time profile is based on the trajectory having an arrival date of 19 March 1974, the latest arrival date, resulting in the most marginal array performance during the time the capsule is on board. For comparison, a condensed power demand profile is also shown. Note that array/battery load sharing will be a problem following the late maneuvers, during the first 30 days in orbit while the capsule is on board, and potentially during the final part of the orbiting phase when eclipses occur.

6.2. ELECTRONICS MODULE EQUIPMENT

Power Subsystem equipment aside from the solar array is mounted in Bays 1, 2 and 15. The performance and physical characteristics of this equipment is summarized in Table 7.

The location and physical arrangement of the elements of the Power Subsystem are shown in Figure 28.

6.3. ADAPTABILITY OF THE POWER SUBSYSTEM TO FUTURE MARS MISSIONS

Depending on the growth of the spacecraft electrical loads, the Power Subsystem will be adequate for other Mars opportunities in 1975-1979. The Power Subsystem element affected by the change in mission year will be the solar array, since its power output in Mars orbit depends on the Mars heliocentric distance.

The performance of the solar array during the Mars orbiting phase is shown for four opportunities in Figure 29. For no other mission is the solar array minimum power output less than for the 1973 mission. For the 1975 mission, the output during the first 30 days while the capsule is on board will be less than for the equivalent period in the 1973 mission, but this will mean only a reduction in margin in this period. It is reasonable to expect that the

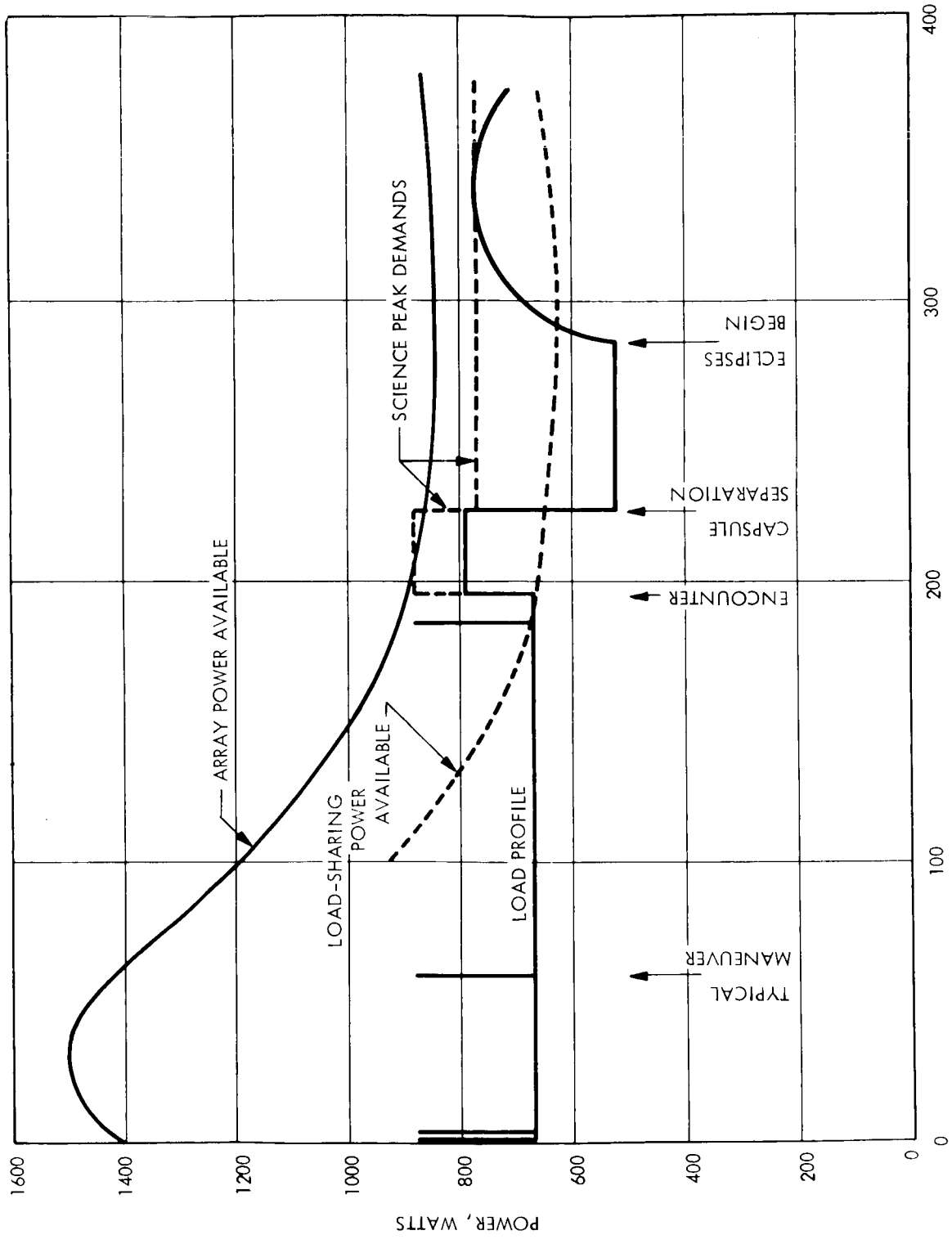

Figure 27. Solar Array Performance Summary

Table 7. Physical and Performance Characteristics of Electronics Module Equipment

UNIT	NUMBER	WEIGHT (lb)	VOLUME (cu ft)	CAPACITY (Amp Hr)	VOLTAGE (Output)	FREQUENCY	REGULATION		POWER OUTPUT (watts)		SERVES BUS
							Steady-State	Transient	Maximum Peak	Maximum Average	
Ni-Cd Battery	2	80		20	37-49		---	---	3000	10 (515 in Eclipse)	A (& B in Eclipse)
Ag-Zn Battery	1	45		45	37-52						
Main Regulator	2	20	.33		35		± 1	± 3	750	500	Inverters
2.4 kHz Inverter	2	8	.13		50 rms	2.4 kHz stepped sq wave	± 2.5	± 5	600	400	C
400 Hz, Three-Phase Inverter	2	4.	.07		26 rms	400 Hz 3ø stepped sq wave	± 5	± 10	30	20	D&E
400 Hz, Single-Phase Inverter	2	1.5	.03		28 rms	400 Hz 1ø sq wave	± 5	± 10	30	20	F
Failure Detectors	7	.75	.02							Consume 1.24 w each	

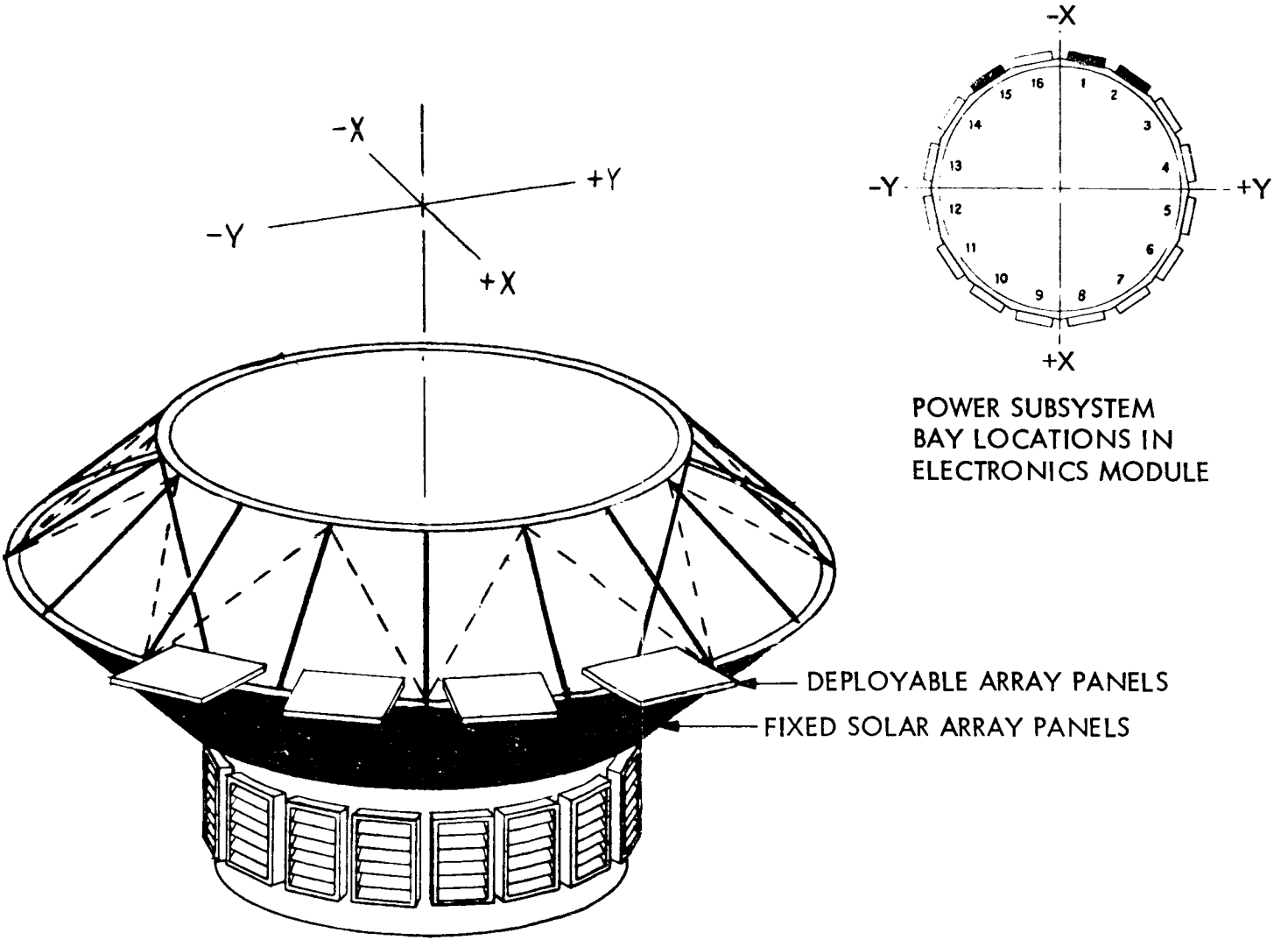

Figure 28. Power Subsystem Equipment Location and Arrangement

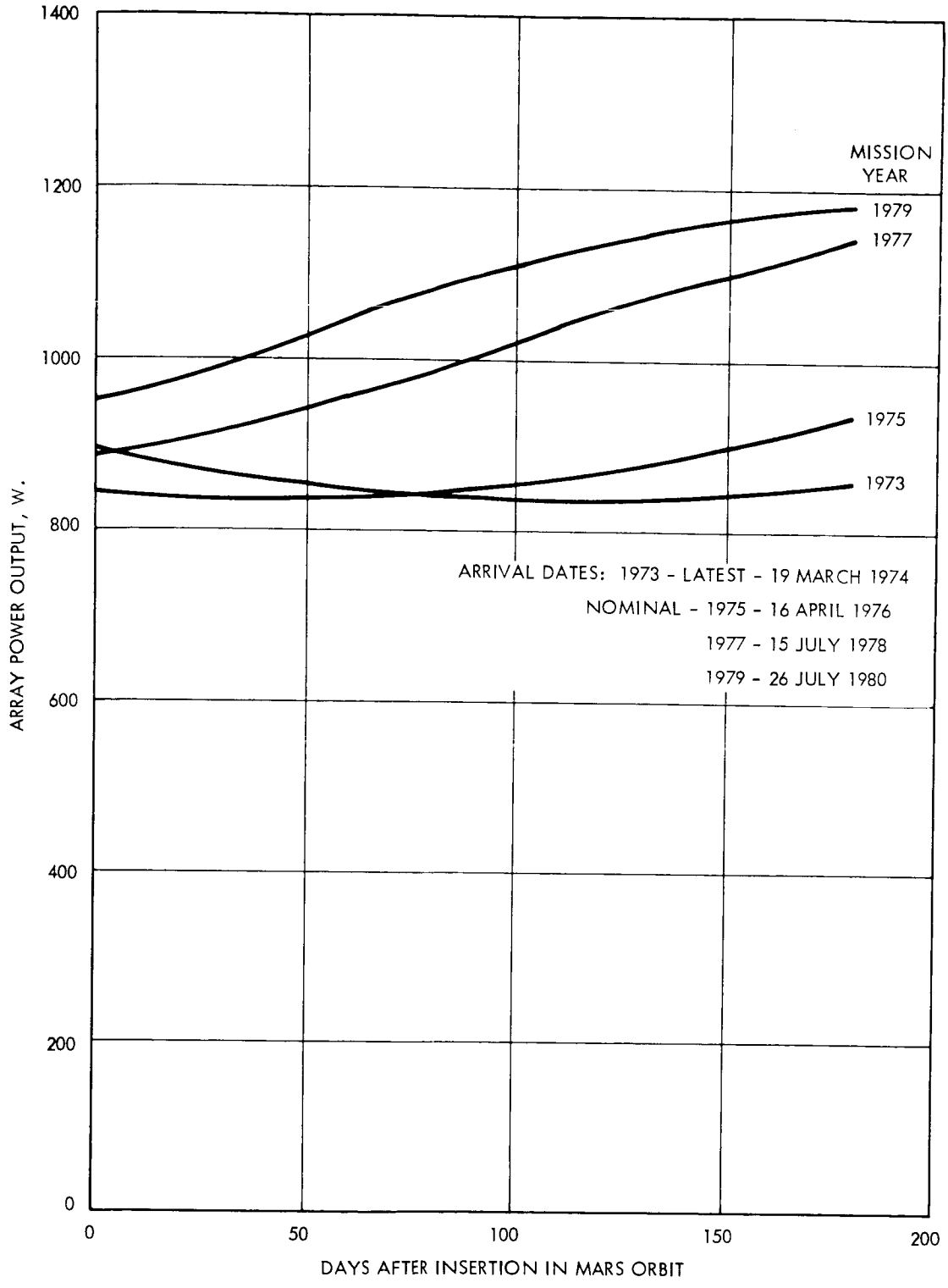

Figure 29. Solar Array Performance for Other Mars Missions

1975 capsule will utilize an RTG power supply, eliminating the requirement for the 200 watts of capsule heating. However, if this is not done, and the spacecraft power requirements increase in addition, then the array may still be adequate if careful management of the science and capsule loads is practiced.

7. INTERFACE DEFINITION

Tables 8 through 11 define major interfaces of the power subsystem.

7.1. SPECIAL ACCESS REQUIREMENTS

Special battery access to each intercell connection will be available for uniformly discharging each cell prior to final installation in the spacecraft. These access points will be located directly on a connector at the battery case.

7.2. THERMAL INTERFACE REQUIREMENTS

Battery operating temperatures must be limited to 30 to 80 °F.

Table 8. Power System Telemetry Requirements

Measurement	Sensor Output	% Error, Full Scale	Engineering Units
Full-Time			
Array/Battery Voltage	0-3.2 V	5	35 to 70 V
Battery Ampere-Hour Discharge	0-3.2 V	5	0 to 2000 A-Hr
2.4-kHz Inverter Voltage	0-3.2 V	5	45 to 55 VAC
2.4-kHz Inverter Current	0-3.2 V	5	0 to 12A
Main Regulator Voltage	0-3.2 V	5	33 to 37 V
Main Regulator Current	0-3.2 V	5	0 to 20 A
Array/Battery Bus Current	0-3.2 V	5	0 to 60 A
Power Subsystem Redundancy Control Status	Digital		7 Bits
Battery Raw Bus Voltage	0-3.2 V	5	35 to 54 V
400-Hz 3-Phase Inverter No. 1 Voltage	0-3.2 V	5	22 to 30 VAC
400-Hz 3-Phase Inverter No. 2 Voltage	0-3.2 V	5	22 to 30 VAC
400-Hz 1-Phase Inverter Voltage	0-3.2 V	5	25 to 33 VAC
Total 400-Hz Inverter Input Current	0-3.2 V	5	0 to 3 A
Battery No. 1 Temp.	0-100 mv	5	0 to 130°F
Battery No. 2 Temp.	0-100 mv	5	0 to 130°F
Battery No. 3 Temp.	0-100 mv	5	0 to 130°F
Battery No. 1 Voltage, Coarse	0-3.2 V	5	35 to 54 V
Battery No. 2 Voltage, Coarse	0-3.2 V	5	35 to 54 V
Battery No. 3 Voltage, Coarse	0-3.2 V	5	35 to 54 V
Battery No. 1 Current	0-3.2 V	5	-5 to 40 A
Battery No. 2 Current	0-3.2 V	5	-5 to 40 A
Battery No. 3 Current	0-3.2 V	5	-5 to 40 A
Sun-Oriented			
Solar Array Temp. No. 1	0-100 mv	5	-50 to +200°F
Solar Array Temp. No. 2	0-100 mv	5	-50 to +200°F
Solar Array Temp. No. 3	0-100 mv	5	-50 to +200°F
Solar Array Temp. No. 4	0-100 mv	5	-350 to +50°F
Solar Array Temp. No. 5	0-100 mv	5	-350 to +50°F
Solar Array Temp. No. 6	0-100 mv	5	-350 to +50°F
Array Current	0-3.2 V	5	0 to 60 A
Battery No. 1 Voltage, Fine	0-3.2 V	5	45 to 50 V
Battery No. 2 Voltage, Fine	0-3.2 V	5	45 to 50 V
Battery No. 3 Voltage, Fine	0-3.2 V	5	48 to 53 V
Charge Regulator No. 1 State	Digital		
Charge Regulator No. 2 State	Digital		
Charge Regulator No. 3 State	Digital		
Battery No. 1 Temp.	0-100 mv	5	0 to 130°F
Battery No. 2 Temp.	0-100 mv	5	0 to 130°F
Battery No. 3 Temp.	0-100 mv	5	0 to 130°F

Table 9. Command Requirements

Item No.	Function	Signal Source
1	Charge Regulator No. 1 - Turn OFF	CD
2	- Setting A	CD
3	- Setting B	CD, C&S, BCR
4	Charge Regulator No. 2 - OFF	CD
5	- Setting A	CD
6	- Setting B	CD, C&S, BCR
7	Charge Regulator No. 3 - OFF	CD
8	- Setting A	CD
9	- Setting B	CD
10	Main Regulator - Switch to No. 1	CD
11	- Switch to No. 2	CD
12	2.4-kHz Inverter - Switch to No. 1	CD
13	- Switch to No. 2	CD
14	400-Hz Inverter - Switch to No. 1	CD
15	- Switch to No. 2	CD
16	Master Clock - Switch to Oscillator No. 1	CD
17	- Switch to Oscillator No. 2	CD
18	Enable Array and Batteries, SW 1	LCE
19	Disable Array and Batteries, SW 1	LCE

Table 10. Umbilical Disconnect Requirements

Item No.	Function
1	Array/Battery Bus Voltage
2	Battery No. 1 Voltage
3	Battery No. 2 Voltage
4	Battery No. 3 Voltage
5	Battery No. 1 Temperature
6	Battery No. 2 Temperature
7	Battery No. 3 Temperature
8	Battery Temperature Sensor Return
9	External Power, 37 to 65 VDC, 20 Amps
10	External Power Return
11	Array/Battery Enable Switch, SW-1, Monitor
12	Turn ON Enable Switch, SW-1
13	Turn OFF Enable Switch, SW-1
14	Enable Switch, SW-1, Drive Return

Table 11. Direct Access Requirements

Item Number	Function
1	Battery Ampere-Hour Discharge
2	2.4-kHz Inverter Voltage
3	2.4-kHz Inverter Current
4	2.4-kHz Inverter Transfer Switch State
5	Main Regulator Voltage
6	Main Regulator Current
7	Main Regulator Transfer Switch State
8	Array/Battery Bus Current
9	Battery Raw Bus Voltage
10	400-Hz 3-Phase Inverter No. 1 - Phase A
11	400-Hz 3-Phase Inverter No. 1 - Phase B
12	400-Hz 3-Phase Inverter No. 1 - Phase C
13	400-Hz 3-Phase Inverter No. 2 - Phase A
14	400-Hz 3-Phase Inverter No. 2 - Phase B
15	400-Hz 3-Phase Inverter No. 2 - Phase C
16	400-Hz 1-Phase Inverter Voltage
17	Total 400-Hz Inverter Current
18	Battery No. 1 Current
19	Battery No. 2 Current
20	Battery No. 3 Current
21-40	Battery Cell Voltage Monitor (2 Ni-Cd Batteries) Cells 3, 6, 9, 12, 15, 18, 21, 24, 27, 30
41-48	Battery Cell Voltage Monitor (1 Ag-Zn Battery) Cells 3, 6, 9, 12, 15, 18, 21, 24
49	1.296-kHz Clock Signal
50	Stimulate Failure Detector - Main Regulator No. 1
51	Stimulate Failure Detector - Main Regulator No. 2
52	Stimulate Failure Detector - 2.4-kHz Inverter No. 1
53	Stimulate Failure Detector - 2.4-kHz Inverter No. 2
54	Stimulate Failure Detector - 400-Hz 3-Phase Inverter No. 1
55	Stimulate Failure Detector - 400-Hz 3-Phase Inverter No. 2
56	Stimulate Failure Detector - 400-Hz 1-Phase Inverter
57	Stimulate Back-Up Oscillator
58-73	Switch State Monitors for K1 - K16

APPENDIX A SOLAR ARRAY ANALYSIS

A.1. SOLAR ARRAY PERFORMANCE

A.1.1. PERFORMANCE FACTORS AND CONTINGENCIES

In calculating the solar array output, the following performance factors and contingencies were used:

Basic cell efficiency, air-mass zero, at 85°F		11%
Filter transmission loss		8%
Radiation degradation:		
Residual I_{sc} factor		0.935
Residual V_{oc} factor		0.96
Residual power factor		0.90
General loss and contingency factor, which includes allowances for:		0.90
Manufacturing losses	2% rms	
Measurement uncertainties	4% rms	
Micrometeroid erosion	4.5% rms	
Ultraviolet effect on filter	5.5% rms	
Random cell failures	5% rms	

The thermal analysis of the solar panels is discussed and a temperature profile of the panels is given in Section VOY-D-362. The solar panels are not at a uniform temperature, and it is necessary to balance the number cells in each series string and select their locations on the panel so that a reasonably uniform voltage characteristic is obtained for all series strings.

Since the principal effect of temperature is to increase or decrease the cell voltage characteristics in a nearly linear manner, it is sufficient to select a cell layout which provides a uniform string average temperature, weighted by the number of cells at each temperature node. The average string temperatures determined at 1 AU to the nearest degree Fahrenheit, are:

Full panels	142°F
Canopus Sensor panels	142°F
HGA and PSP panels	149°F
Deployed panels	128°F

It was found that the effect of radiative heat input from the vehicle was small, and the solar panel temperature variation as a function of sun distance could be approximated to the nearest degree R using:

$$T = T_1 \left(\frac{1}{AU} \right)^{1/2} {}^{o}R$$

A.1.2. METHOD OF ESTIMATING SOLAR ARRAY OUTPUT

As the solar intensity decreases, the power output of the array decreases, but there is an accompanying decrease in temperature which increases the voltage at which the power is available. Thus, the non-linear relationship between solar intensity and array power output characteristics must be considered in determining the proper voltage match between the array, the battery, and the power conditioning equipment.

The solar array power output is determined using a computer program which directly calculates the voltage-current characteristics of the whole array. The computer program takes into account the following performance parameters:

- Solar intensity
- Temperature
- Solar incidence angle
- Series cells in a string
- Parallel cells in a string
- Number of strings
- Basic cell characteristics (temperature-dependent V-1 characteristics based on measured cell data)
- Losses and uncertainties

The output of the program is a listing, for each different operating condition, of:

Voltage vs: Total current and Power

The program calculates the array output based on the V-1 characteristics of a single cell, adjusting the voltage and current scale factors to account for the numbers of cells in series and parallel. The single-cell V-I curve is obtained from:

$$I = I_{sc} - \frac{V}{R_p} - I_o \left[e^{K(V+R_s I)} - 1 \right]$$

where the variables are: I = Cell current output

V = Voltage on cell

and the coefficients are:

I_{sc} = Illumination current (virtually equal to the short circuit current)

R_p = Shunt resistance of the cell

I_o = Reverse saturation current of the ideal diode characteristic

K = Coefficient of the exponential

R_s = Series resistance of the cell

The coefficients are treated as functions of temperature, using sixth-degree polynomial approximations, to more accurately reflect changes in cell characteristics with temperature.

The correction for angle of incidence include the cosine and an allowance for increased reflection from the cell and filter at large incidence angles, and is applied to I_{sc} as a multiplier. Other loss factors are also applied to I_{sc}, and the voltage component of radiation damage is applied as a downward voltage shift to the basic V-I curve.

The computer program also takes into account the forward voltage drop in the array isolation diode as a function of diode temperature.

A.1.3. SOLAR ARRAY POWER OUTPUT

The calculated voltage-current characteristics of the solar array are given in Figure A-1 and the voltage-power characteristics in Figure A-2. The curves show that adequate array power is available at 54 volts for the entire range of sun-spacecraft distances to be encountered during the 1973 flight. Even though the maximum power voltage at 1.666 AU is approximately 58 volts, power can be extracted at 54 volts with less than a 2 percent penalty. Thus, the array may be treated as having nearly a constant range of source-voltage characteristics.

A design voltage of 54 volts was selected to allow adequate margin for uncertainties in solar cell voltage and temperature characteristics so that the power available at 1.0 AU would not fall below that at 1.666 AU.

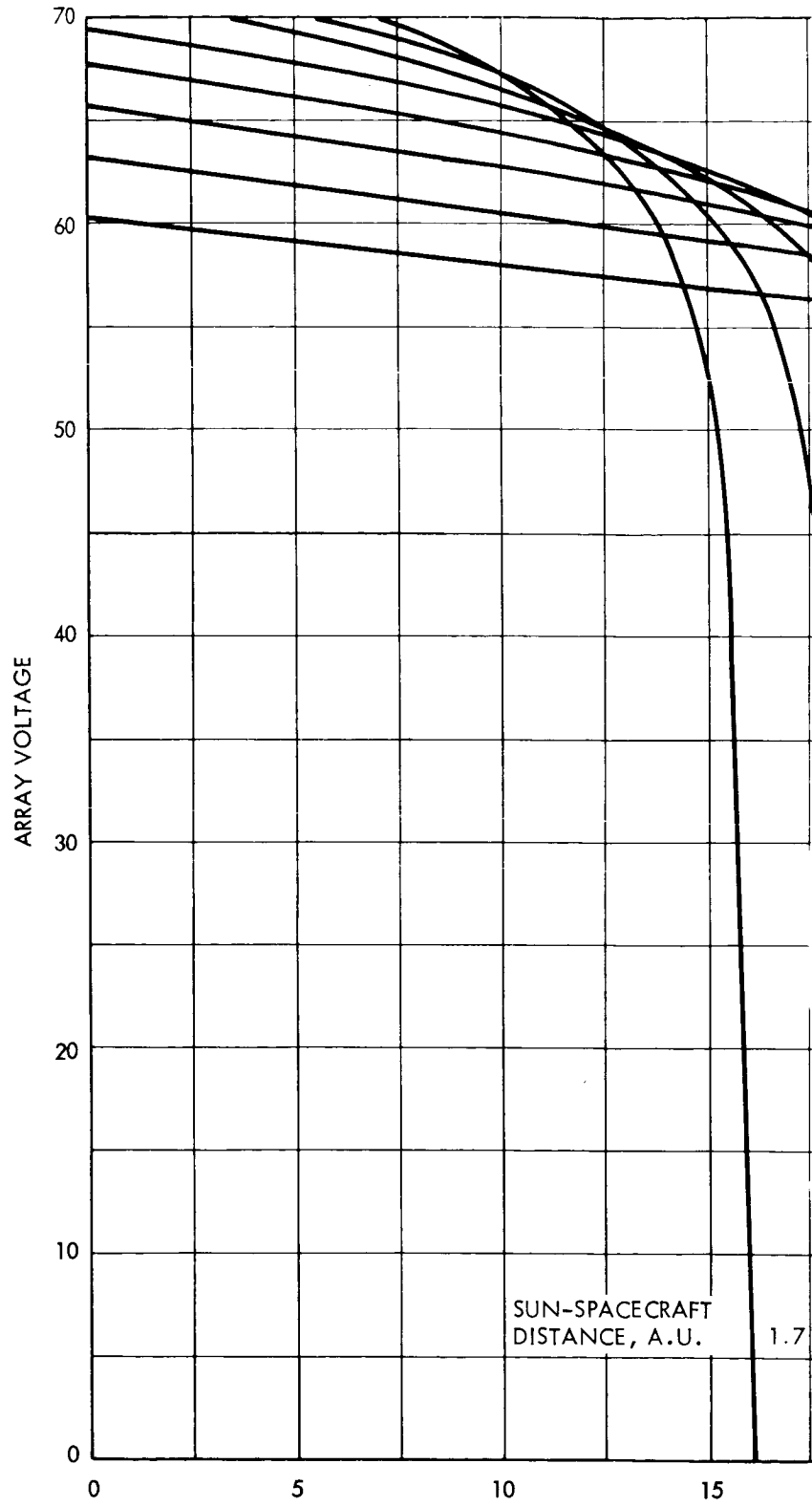
70
60
50
40
30
20
10
0
ARRAY VOLTAGE
0
5
10
15
SUN-SPACECRAFT
DISTANCE, A.U.
1.7

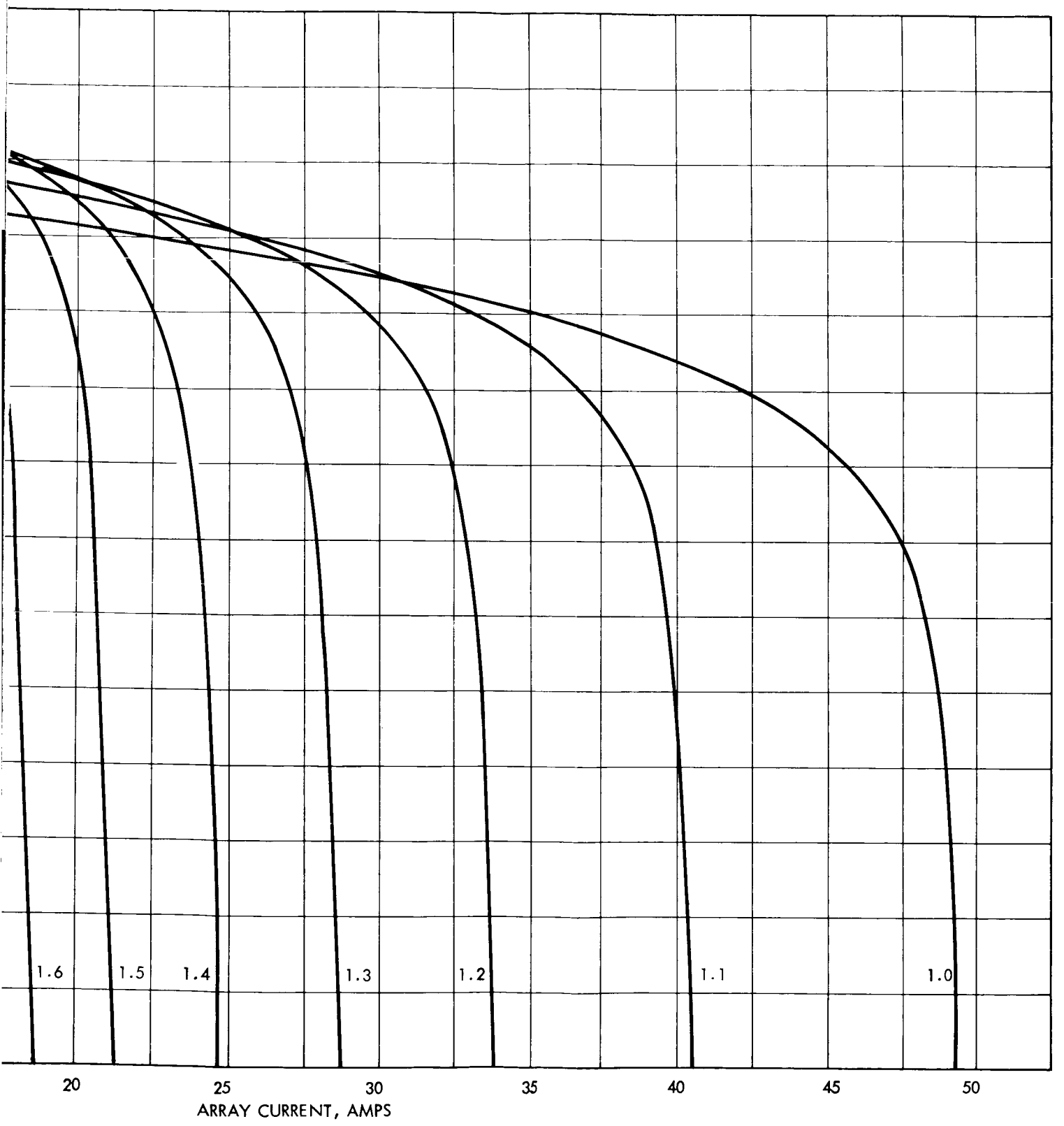

Figure A-1. Solar Array Voltage-Current Characteristics

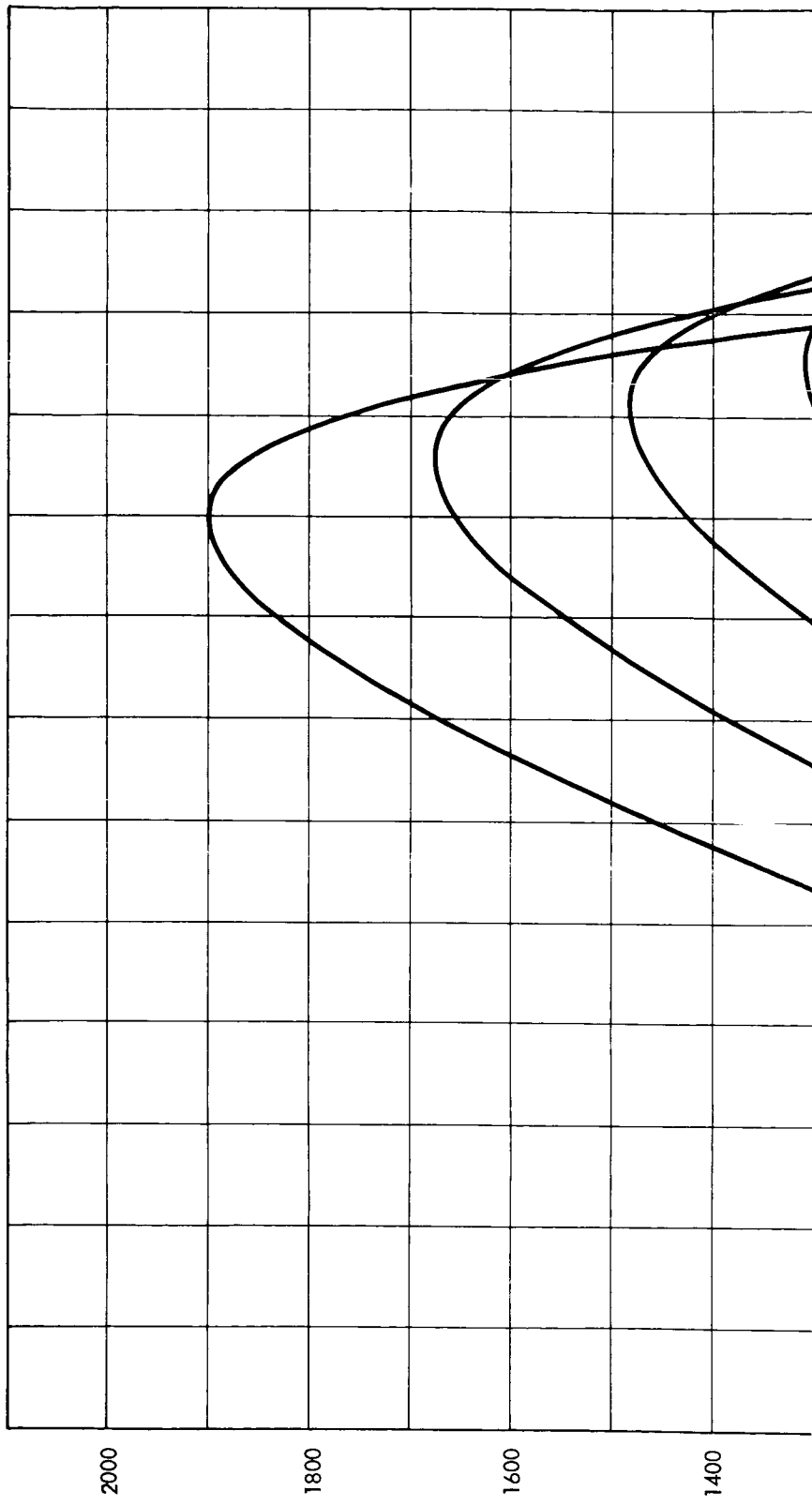
2000
1800
1600
1400

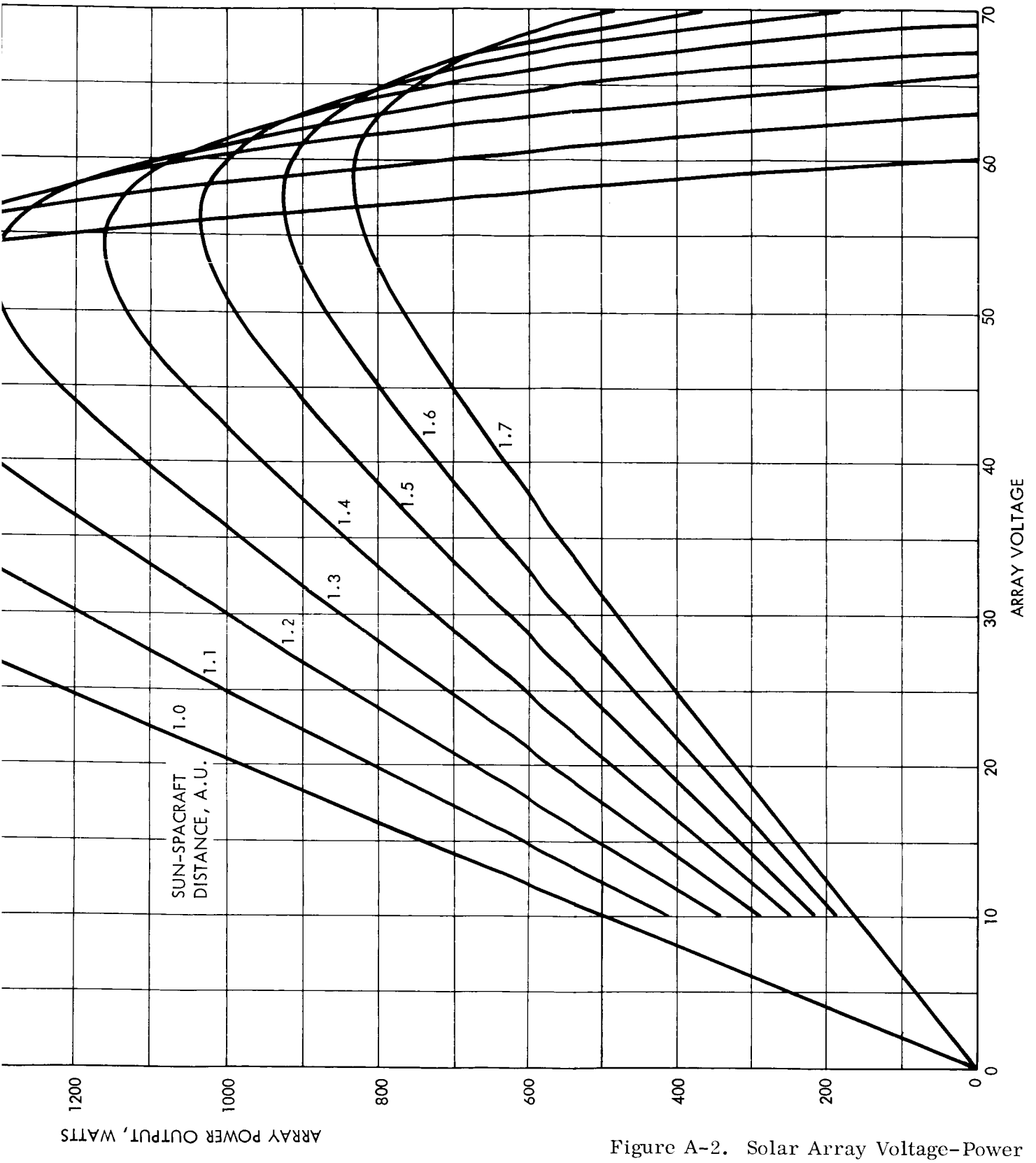

Figure A-2. Solar Array Voltage-Power Characteristics

FOLDOUT FRAME

Figure A-3 shows the array power output characteristics as a function of sun distance. The curve marked "Power Available at 54 Volts" is the power which can be extracted from the solar array at 54 volts. To the left of the point of tangency (approximately 1.4 AU), the maximum power can be extracted from the array only at voltages of less than 54 volts.

The array/battery load-sharing problem is discussed in Section 3.5. The "load-sharing" power is defined as the array power output available when the array/battery bus (Bus B) is drawn down to 38 volts. When the array and the battery are sharing the load, this is the maximum power which the array can supply, and the battery must supply the remainder. Note that the array power is decreased 26 percent from its 54-volt potential power when sharing occurs at Mars aphelion (1.666 AU).

The solar array performance presented earlier in Figure 27 was derived using the trajectory data shown in Figure A-4. The transfer trajectory with the latest calendar arrival date was selected for the design worst case since this results in the least array power availability during the first 30 days in orbit when the power demands are greatest.

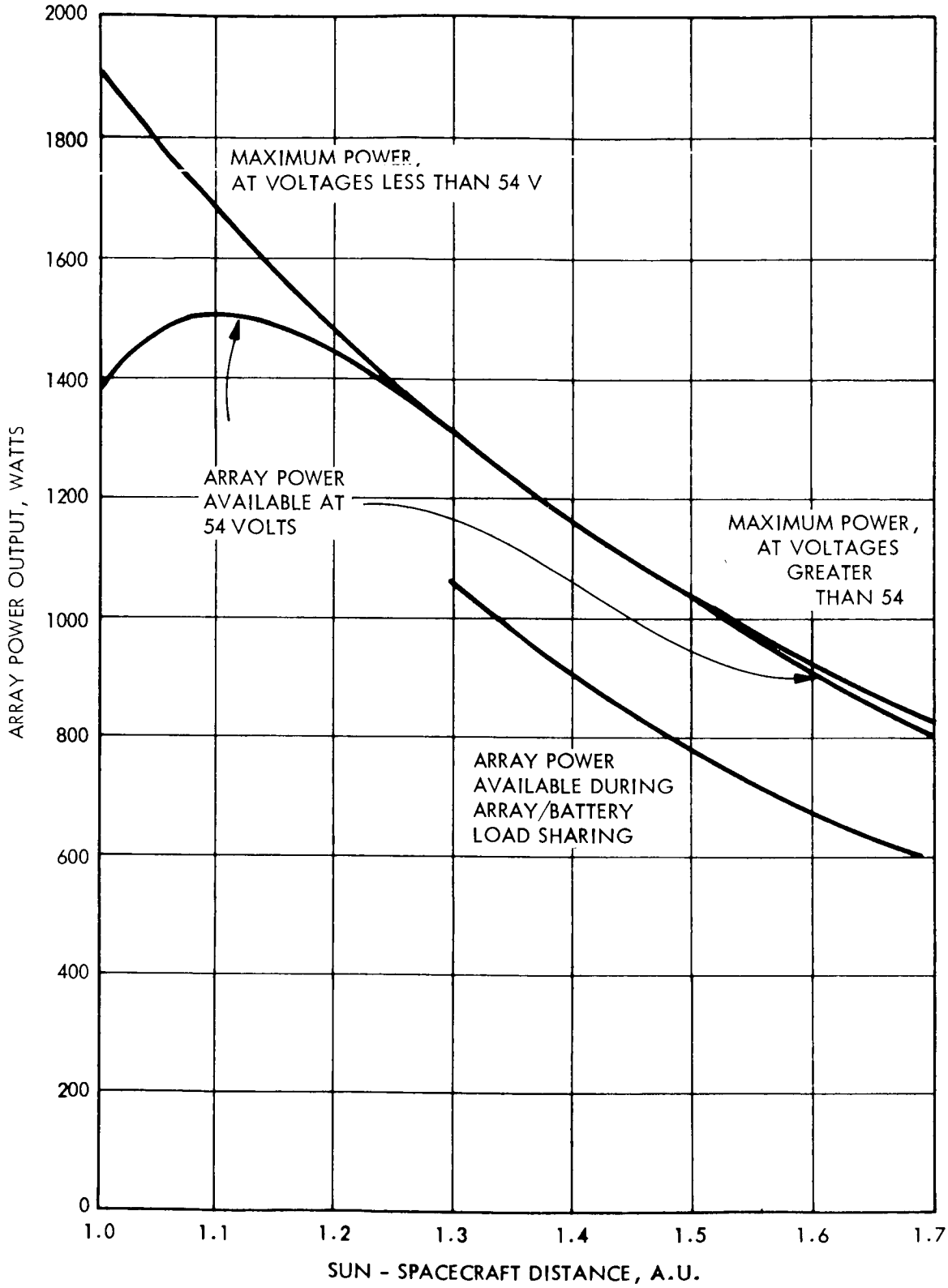

Figure A-3. Sun-Distance Dependence of Solar Array Power Output

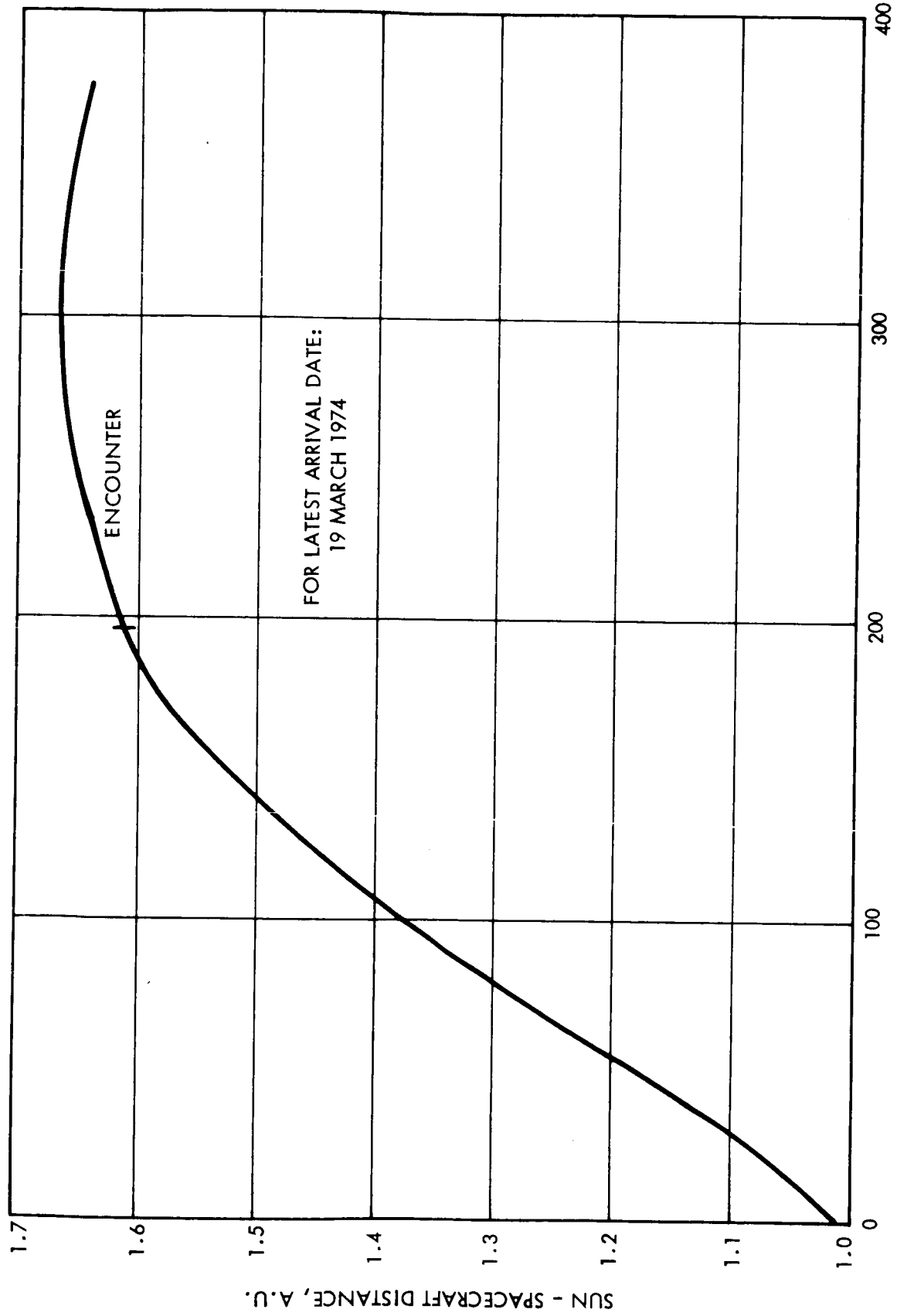

Figure A-4. Typical Mission Trajectory

A.2. RADIATION DEGRADATION OF THE SOLAR ARRAY

A.2.1. CHARGED PARTICLE RADIATION ENVIRONMENT

The charged particle radiation environment consists of three major components: 1) solar cosmic rays, 2) geomagnetically trapped radiation (Earth), and 3) primary galactic cosmic rays. The component of the environment making the principal contribution to solar array degradation is the solar flare protons.

The environment estimates presented here are based upon the Voyager Environmental Predictions document, JPL, October 26, 1966.

Solar Cosmic Radiation. The solar cosmic radiation consists principally of high energy protons (solar flares) which are sporadically emitted by the Sun during active solar periods and of very low energy protons and electrons (solar wind) that are continually emitted by the Sun at a somewhat constant rate.

Solar Flares. Solar flares are grant eruptions on the solar surface which inject large quantities of high energy protons into the solar system. The duration of these flares are on the order of hours to days. Their occurrence appears to follow in a somewhat general way the eleven-year solar sunspot cycle. Thus, a higher occurrence of these flares is expected during years of maximum solar activity. An estimate of the time-integrated proton flux per year for a year of maximum solar activity is given in Figure A-5. The peak proton flux during a given flare is taken to be 3×10^4 protons/cm^2/sec, with energies greater than 30 Mev.

Solar Wind. The solar wind consists of very low energy protons and electrons that are continually emitted by the Sun. The mean velocity of the solar wind at a distance from the Earth of 0.5 to 1.75 AU is 450-500 KM/sec. The mean flux is given in Table A-1. During periods of disturbed solar conditions this flux may increase by a factor of 10 to 100 with energies up to 100 Kev at 1.0 AU. The electron flux is on the order of 10^8 to 10^{10} electrons/cm^2/sec with energies of a few electron volts at 1.0 AU.

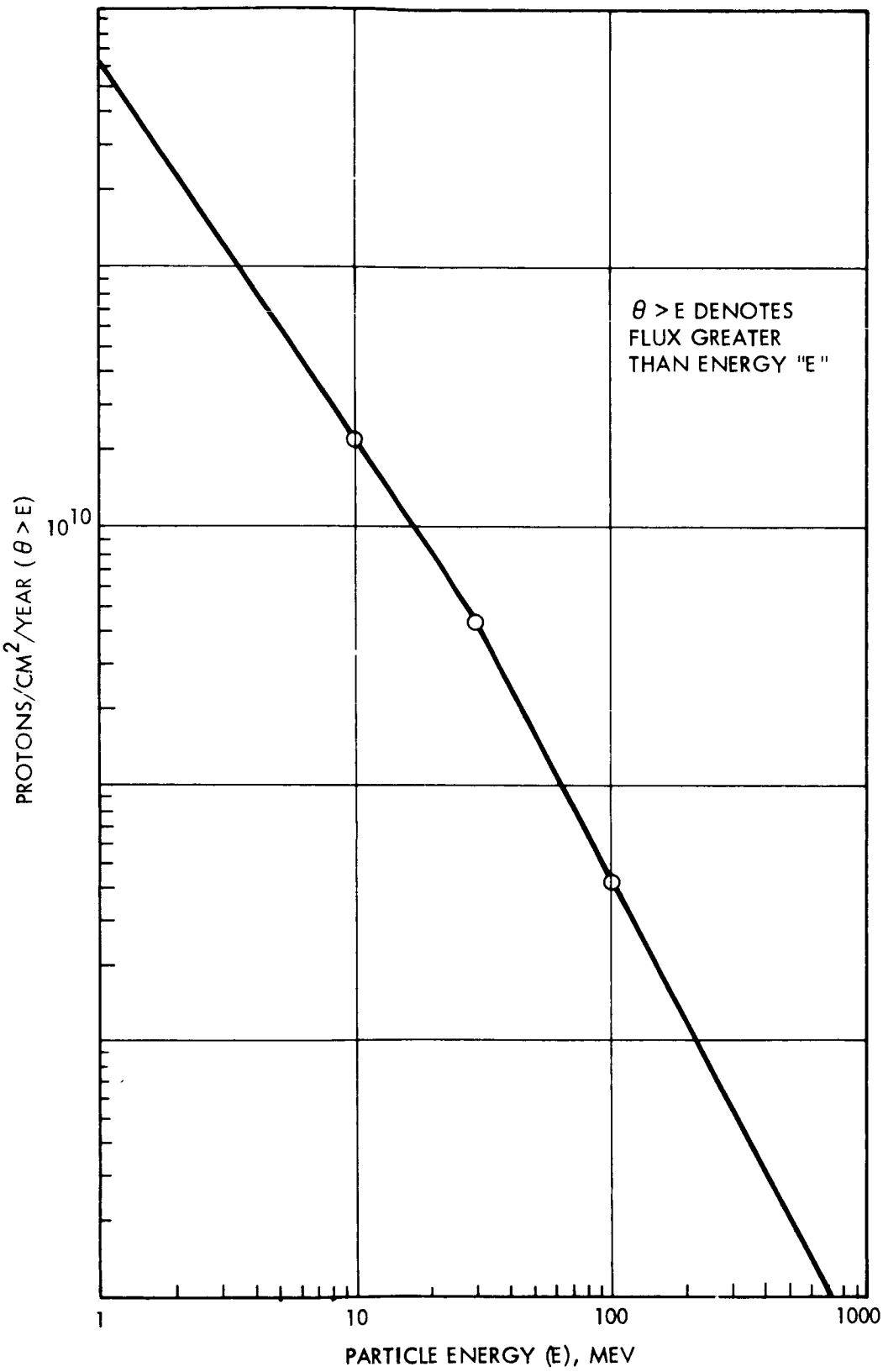

Figure A-5. Solar Flare Protons, Integral Isotropic Flux - Yearly Dose

Geomagnetically Trapped Radiation. The geomagnetically trapped radiation near the Earth consists of high energy electrons and protons. The peak fluxes and the total integrated fluxes to be encountered during passage through the belts are given in Table A-2. The proton flux is variable within a factor of 2 to 10. The electron flux is variable within a factor of 2 to 10 for magnetic shells less than 3 ($L < 3$), and for magnetic shells greater than 3 ($L > 3$), it is variable within a factor of 10 to 100.

Primary Galactic Cosmic Radiation. The primary galactic cosmic radiation consists principally of very high energy protons and, to a lesser extent, heavier nuclei. The omni-directional flux is given in Table A-3, where the elemental composition is given in Table A-4. The average yearly flux is 7.8×10^7 particles/cm^2, while the estimated maximum peak yearly flux during a year of solar minimum is taken to be 1.2×10^8 particles/cm^2.

Table A-1. Mean Values of the Solar Wind Near Earth

Distance from Earth (AU)	Mean Density Hydrogen atoms/cc	Hydrogen atoms/cm^2-sec
0.5	20	8×10^8
1.0	5	2×10^8
1.75	2	10^8

Table A-2. The Omnidirectional Flux of the Magnetically Trapped Radiation Near Earth

Particle Type	Energy	Peak Flux Particles/cm^2-sec	Integrated Flux Particles/cm^2
Proton	E > 4 mev	2.0×10^6	1.0×10^9
	E > 15 mev	1.4×10^5	6.0×10^7
	E > 34 mev	2.4×10^4	1.2×10^7
Electron	E > 40 kev	4.5×10^8	
	E > 0.5 mev	4.0×10^8	
	E > 2 mev	1.5×10^8	
	E > 0.5 mev		1.9×10^{11}
	E > 1.0 mev		1.8×10^{11}
	E > 2.0 mev		6.4×10^{10}
	E > 5.0 mev		2.1×10^9

Table A-3. The Omnidirectional Flux of Primary Galactic Cosmic Radiation

Type	Energy	Peak Flux Particles/cm^2 - sec
Protons	E > 500 mev	3.8
	E > 2 Bev	2.1
	E > 10 Bev	0.45
Electrons	E > 100 mev	10^{-2} to 10^{-1}
Gamma	E ~ 100 to 200 kev	10 to 40
Total Flux		7 to 4 (in Earth's Atmosphere to free space)

Table A-4. Elemental Composition of Primary Galactic Cosmic Rays

Element	Atomic No.	Percent of Total
Hydrogen	1	80 to 85
Helium	2	11 to 16
Light nuclei (L)	$3 \leq Z \leq 5$	2
Medium nuclei (M)	$6 \leq Z \leq 9$	1
Heavy nuclei (H)	$Z \geq 10$	3

A.2.2. METHOD OF CALCULATING RADIATION DAMAGE TO SOLAR CELLS

The effects of charged particle radiation damage in silicon solar cells are described in detail in References 1 and 2*. The principal effect is to degrade the minority carrier diffusion length (L) in the base region of the solar cell. This reduction in L in turn reduces the solar cell current, voltage and power producing capabilities. The variation of the solar cell open circuit voltage (V_{OC}), short circuit current (I_{SC}) and maximum power (P_{max}) as a function of the 1-Mev electron dose is given in Figure A-6 for solar cells with 1 ohm-centimeter base resistivity. The reduction in L with radiation dose is given by Equation A-1, where K is the radiation damage constant, L_o is the initial value of L and ϕ is the radiation dose incident on the solar cell. The radiation damage constant is a function of the type of radiation particle as well as the particle energy. The damage constant for protons as a function of proton energy is given in Figure A-7.

$$\frac{1}{L^2} = \frac{1}{L_o^2} + K\phi \qquad \text{(A-1)}$$

The damage constant function when integrated over the proton energy spectrum incident upon the solar cell will then determine the total reduction in L. For convenience, this reduction in L is then utilized to determine a dose of 1-Mev electrons which would cause the same amount of degradation in L as the incident proton dose. This "equivalent 1-Mev electron dose" can be determined directly by utilizing Equation A-2 where Kp(E) is given by Figure A-7 and $\phi p(E)$ is the differential proton flux as a function energy which is incident upon the

*REFERENCES

1. From the Voyager Task A Study Report: VB 236 FD101, Appendix I-5, Solar Array Performance.

2. Conference Record of the Sixth Photovoltaic Specialists Conference, Volumes II & III, IEEE, March 28, 29, 30, 1967, Cocoa Beach, Florida.

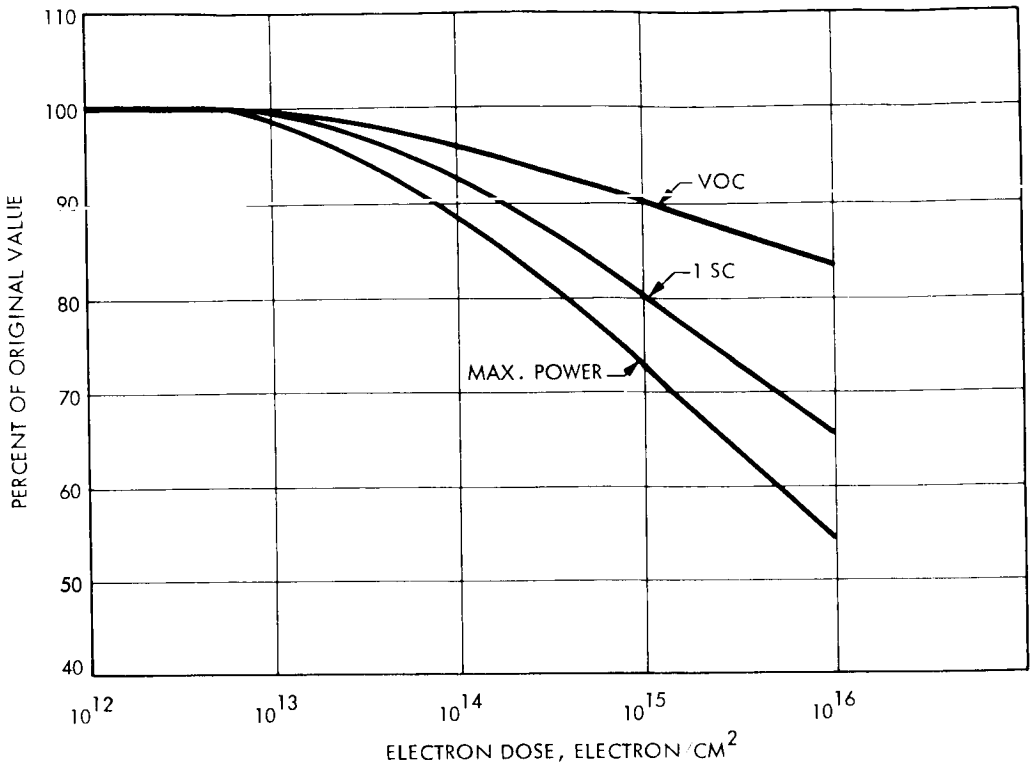

Figure A-6. N/P Solar Cell Characteristics Under 1.0 Mev Electrons (1 Ω -cm)

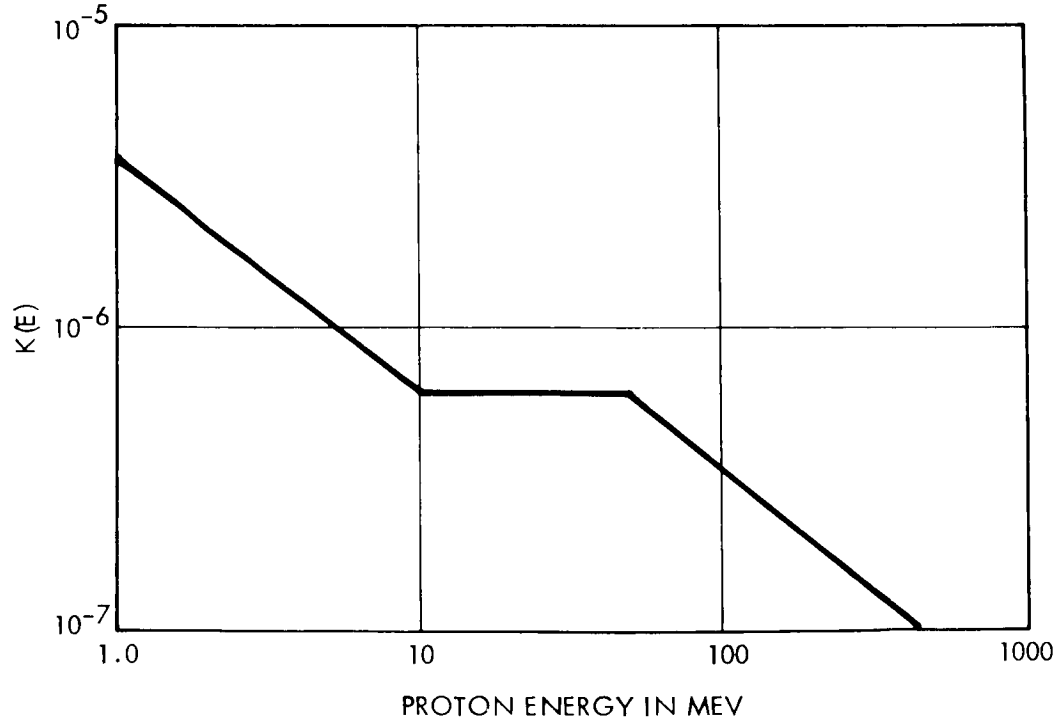

Figure A-7. Degradation Constants for Protons

cell. The "equivalent 1-Mev electron dose" so determined is then utilized in conjunction with Figure A-6 to determine the current, voltage and maximum power degradation of the solar cell.

$$\phi\,(1\text{-Mev, eq.}) = \frac{10^{10}}{1.7} \int \mathrm{Kp(E)}\phi\,\mathrm{p(E)dE} \qquad \text{(A-2)}$$

When a shield material is placed upon the solar cell, the amount of the incident radiation absorbed by the shield material must be properly taken into account in order to determine the characteristics of the radiation that is actually incident on the surface of the cell. This is accomplished by carrying out calculational procedures which utilize standard range-energy shielding techniques, including considerations of the omnidirectional nature of the incident radiation flux. These techniques are described in detail in Reference 1. Once the radiation dose behind the shielding is determined, the above procedure is utilized to estimate the solar cell damage. For an omnidirectional radiation environment, the incident dose received on one side of a flat surface is taken as one-fourth of the omnidirectional flux.

A.2.3. SOLAR ARRAY RADIATION DAMAGE ESTIMATE

The radiation degradation of the solar array represents a significant design constraint, amounting to an estimated 10 percent decrease in array power output over the life of the mission.

The essential results of the radiation damage calculations are given in Figure A-8, which shows the fraction of original solar cell short circuit current and open circuit voltage together with maximum power that remains after a 14-month mission. The results are shown for various thicknesses of fused silica cover glass assuming a back side shielding of 0.2 grams/cm^2 (equivalent aluminum). Due to the moderately low total integrated doses expected during the mission, no significant difference between the degradation of 1 and 10 Ω-cm cells is anticipated. Hence, the curves shown in Figure A-8 would be applicable for solar cells with either base resistivity. It is interesting to note that, due to the relatively

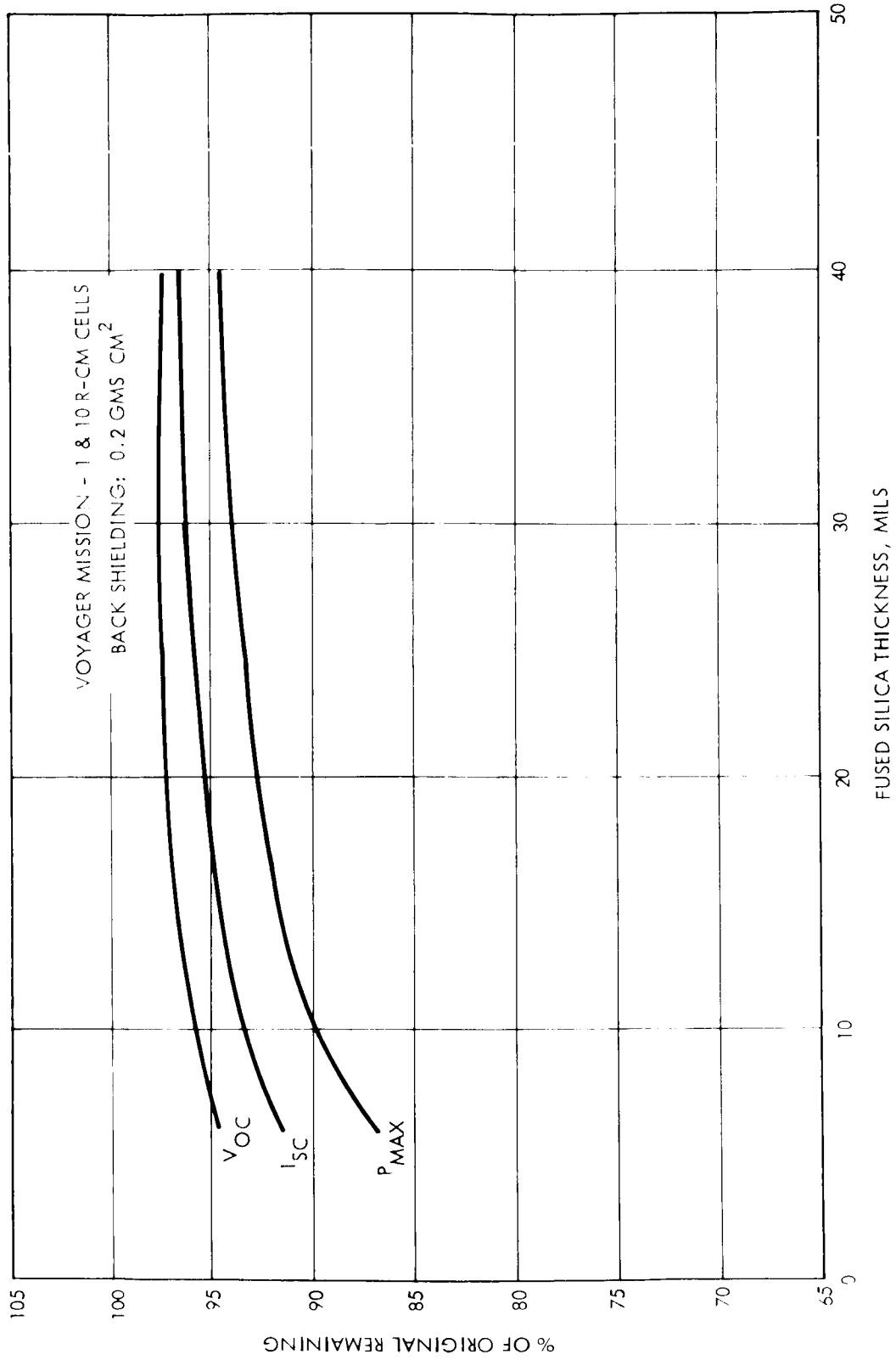

Figure A-8. Silicon Solar Cell Radiation Degradation vs. Cover Glass Thickness

low radiation doses accumulated during the transit phase through the Van Allen belts, the solar flare protons represent the most hazardous component of the environment. The solar flare environment utilized in the present study is indicative of the anticipated environment during a year of maximum solar activity. Hence, the current estimate of solar cell degradation should represent a somewhat conservative design figure for missions carried out during periods of minimum solar activity.

A solar array weight/area tradeoff indicates the optimum cover glass thickness to be between 6 and 10 mils. A thickness of 10 mils was selected, since it results in less breakage, lower cost.

VOY-D-340

APPENDIX B
POWER SUBSYSTEM ELEMENT SIZE DETERMINATION

The solar array and battery size requirements are determined with the aid of the Energy Balance Table, Table 1, where the electrical loads are summarized. The accounting of the loads includes the various power subsystem losses and is extended to determine the loads directly at the solar array and the battery.

The following loss and efficiency factors were used in the load analysis:

a. Harness Loss. The power loss in the power distribution harness was assumed to be 1 percent for all loads, both ac and dc.

b. 2400-cps Inverter Efficiency. The main inverter was taken to be 90 percent efficient at full load, and the no-load loss to be one-half the full-load loss. The inverter thermal loss at intermediate power levels was assumed to vary linearly between the two defined end points.

c. 400 cps Inverters. Both types of 400 cps inverters were taken to be 80 percent efficient at full volt-ampere load, with part load efficiency varying in a manner similar to that of the 2,400 cps inverter.

d. Main Regulator Efficiency. The full load efficiency was taken to be 90 percent, with part load efficiency varying as for the 2,400 cps inverter.

e. Battery Diodes. The battery discharge diode drop was taken to be 0.35 volt, for an efficiency of 99 percent.

f. Battery Charger. There are two battery charge regulators: a PWM type for the Ni-Cd battery and a series-dissipative type for the Ag-Zn battery. Since all the battery charging power in the occulted-orbiting phase, the critical design phase, goes to the Ni-Cd battery, the charger efficiency is based on the model for the PWM BCR. The loss in the PWM BCR is taken to be 1 watt each plus 8 percent of the input power.

The Nickel-Cadmium battery charging power was determined based on the following data and assumptions:

a. Minimum Mars orbit period (worst case) is 7 hours, 6 minutes.

b. Maximum Mars orbit eclipse will be 84 minutes.

c. Minimum time available for recharge will be 5 hours, 1 minute during Mars orbit, the remaining daylight time being allocated to full science operation, when sufficient power is not available to also charge the batteries.

d. The Ni-Cd batteries will have an effective watt-hour-charging efficiency of 62 percent, based on the charge rate as determined with the above restraints.

From the Energy Balance Table, the energy drawn from the batteries during an 84 minute eclipse, following capsule release, is 721 watt-hours. Based on a 62 percent efficient charge, this means that 1165 watt-hours of power must be returned to the Nickel-Cadmium batteries through the 5 hour charge period.

The Ni-Cd batteries were sized based on the assumption that one of the two batteries could fail and the remaining battery could supply reduced spacecraft loads while discharging to no greater than a 60 percent depth of discharge. The normal loads are 515 watts during eclipse periods and nonessential loads amount to 207 watts, leaving 308 watts of essential loads required to keep the spacecraft alive. Using the guidelines, two 32-cell 20 ampere-hour Ni-Cd batteries are required and would be charged at a rate of 2.5 amps each (233 watts, total) and trickle-charged at 0.5 amps each (49 watts, total).

The silver-zinc battery was sized based on the assumption that this battery would provide all power required during maneuvers in excess of the capacity of the Ni-Cd batteries, and permit no greater than a 50 percent depth of discharge of all batteries. The worst case condition occurs during the orbit insertion maneuver when 728 watts may be required for as long as two hours. The maximum energy requirement is then 1541 watt-hours, and the total battery capacity requirement is 3082 watt-hours. When the Ni-Cd battery capacity is

subtracted from this value the required silver zinc capacity is a 45 ampere-hour 27-cell battery. Since the Ag-Zn battery is only required during maneuvers, a 48-hour charge period is allowable. The charge current at this rate is 0.5 amps, and the maximum charging power for the silver zinc battery is 26 watts.

The Mars orbit insertion maneuver will last approximately two hours, so the energy required to heat the capsule will be 408 watt-hours. At an energy density of 37.5 watt-hours per pound and an allowable depth of discharge of 50 percent, the penalty in Ag-Zn battery weight to power the capsule through maneuvers is 22 pounds.

VOY-D-350
ELECTRICAL SYSTEM

VOY-D-350
ELECTRICAL SYSTEM

1. INTRODUCTION

This section describes the electrical system of the Voyager spacecraft. The system provides the electrical interfaces and connections between the power supply and the spacecraft subsystems. The principal segments of the electrical system are:

a. Power switching and logic unit - distributes power to the user subsystems when the user does not provide its own control signals, i.e., capsule power on/off.

b. Pyrotechnic controller - transforms the planetary vehicle ac power to dc power, stores the energy, and provides switches for firing the electroexplosive devices as required during the mission.

c. Electrical harnessing - provides reliable transportation of electrical energy between related spacecraft subsystems throughout ground test, launch, and flight operations.

2. POWER SWITCHING AND LOGIC UNIT

The power switching and logic unit (PS&L) incorporates the power distribution (switching) components for all subsystems which require external power-switch signals. For example, the autopilot is turned on by a command from the computer and sequencer, and the "autopilot on" switch is located in the PS&L.

The PS&L consists of power switches, the enable switch, the capsule switches, load fault protection devices, and special telemetry circuits. When major blocks of power are to be switched by control signals originating external to the user subsystem, the function is handled in the PS&L. The switching elements assigned to the PS&L are indicated in Table 1 and the associated commands are shown in Table 2. All relays are oriented for minimum magnetic field.

Table 1. Power Switching and Logic Unit Switching Elements (Sheet 1 of 2)

Power Supply	Subsystem	Element	Power, Watts	PS&L Switch Req't. & Signal Source	Fault Protection & Location
DC	G&C	Gyro & Accel. Heaters	21	K14	Input to each Heater
	Articulation	Antenna Drive	112 max.	—	None
	Propulsion	Thrust Vector Control	701	K16 C&S, CD	None
		Solenoid Valves	448	—	None
	Science	PSP Heaters	5	K15	Input to each Heater
	Radio	Power Amp. #1	75	—	Input to each Amplifier
		Power Amp. #2	147	—	↓ ↓ ↓
		Power Amp. #3	147	—	
	Capsule	——	200	K1 C&S, CD K2	Overcurrent Sensor to Open K1
2.4 KHZ	Radio	Receiver #1	7.14	—	Input to each Receiver & Exciter
		Exciter #1	8.32	—	
		Receiver #2	7.14	—	↓
		Exciter #2	8.32	—	
		Receiver #3	7.14	—	
		Exciter #3	8.32	—	
	Temperature Control	Misc. Gas & Flex. Lines	9	—	Input to each Heater
	Science	DAE & Electronics	171	K3 C&S, CD	Input to each Science Load
		PSP Horizon Sensor	9	K8	↓

Table 1. Power Switching and Logic Unit Switching Elements (Sheet 2 of 2)

Power Supply	Subsystem	Element	Power, Watts	PS&L Switch Req't. & Signal Source	Fault Protection & Location
2.4 KHZ	C&S	——	60	—	None
	G&C	Gyro & Accel. Pkg.	5.2	—	None
		Control Electronics	25.1	—	None
		Canopus Tracker	1.8	K5&6 C&S, CD, G&C	None
		Autopilot	8.4	K4 C&S, CD	None
		Electronics	8		
	Telemetry	——		—	None
	Articulation	——	5.3	K7 C&S, CD	Input to each Load
	Capsule	Relay Radio	50	K9 C&S, CD	Input to each Load
	Command	Power Supply Input	20.2	—	None
	Data Storage	Power Supply Input	37	—	Input to each Recorder
400 HZ	G&C	Gyro Set #1	10.5	K10 C&S, CD, G&C	None
	G&C	Gyro Set #2	10.5	K11 C&S, CD, G&C	None
	Science	Instruments	10	K12 C&S, CD	Input to each Load
		PSP Gimbals	6	K13	

Table 2. PS&L Command Relays

Relay	Power Command	Signal Source
K1 - ON	Power to Capsule	CD, C&S
K1 - OFF	Power to Capsule	CD, C&S
K2 - ON	Power to Capsule (Back-up relay)	CD, C&S
K2 - OFF	Power to Capsule	CD, C&S
K3 - ON	Power to Data Automatic Equipment	CD, C&S
K3 - OFF	Power to Data Automatic Equipment	CD, C&S
K4 - ON	Power to Autopilot Electronics	CD, C&S, G&C
K4 - OFF	Power to Autopilot Electronics	CD, C&S, G&C
K5 - ON	Power to Canopus Tracker No. 1	CD, C&S, G&C
K5 - OFF	Power to Canopus Tracker No. 1	CD, C&S, G&C
K6 - ON	Power to Canopus Tracker No. 2	CD, C&S, G&C
K6 - OFF	Power to Canopus Tracker No. 2	CD, C&S, G&C
K7 - ON	Power to Articulation	CD, C&S
K7 - OFF	Power to Articulation	CD, C&S
K8 - ON	Power to PSP Horizon Sensor	CD, C&S, G&C
K8 - OFF	Power to PSP Horizon Sensor	CD, C&S, G&C
K9 - ON	Power to Capsule Radio Relay	CD, C&S
K9 - OFF	Power to Capsule Radio Relay	CD, C&S
K10 - ON	Power to Gyro Set No. 1	CD, C&S, G&C
K10 - OFF	Power to Gyro Set No. 1	CD, C&S, G&C
K11 - ON	Power to Gyro Set No. 2	CD, C&S, G&C
K11 - OFF	Power to Gyro Set No. 2	CD, C&S, G&C
K12 - ON	Power to Science	CD, C&S, DAE
K12 - OFF	Power to Science	CD, C&S, DAE
K13 - ON	Power to PSP Gymbals	CD, C&S
K13 - OFF	Power to PSP Gymbals	CD, C&S
K14 - ON	Power to Gyro Heaters	CD, C&S, G&C
K14 - OFF	Power to Gyro Heaters	CD, C&S, G&C
K15 - ON	Power to PSP Heaters	CD, C&S, DAE
K15 - OFF	Power to PSP Heaters	CD, C&S, DAE
K16 - ON	Power to Thrust Vector Control	CD, C&S
K16 - OFF	Power to Thrust Vector Control	CD, C&S

A motor driven enable switch contains "make before break" contacts to transfer from ground power to spacecraft power about 10 minutes prior to lift-off. Either the primary or backup capsule switch is used to interrupt and restore capsule power for a short interval immediately following each maneuver and science gathering phase. The momentary, about 10 second, interruption is required to inhibit the array/battery load sharing mode utilized when array power capability is exceeded. The capsule switches are motor driven switches requiring low standby power and producing low contact drop. The special telemetry circuits are provided to monitor the performance of major power subsystem elements such as the battery or solar array.

The use of devices to protect the power subsystem against load faults is associated with those loads whose loss are not totally catastrophic to the mission. Load fault protection devices may consist of fuses, resettable circuit breakers, or overcurrent trips applied to latching relays identified for load control. Loads for consideration might be the capsule, heaters, or redundant tape recorders. The actual use of load fault protection must be determined from complete system optimization studies that consider such factors as reliability, weight, power penalty, and complexity. The protection devices could easily be incorporated as an integral part of the load switches.

3. PYROTECHNIC CONTROLLER

3.1. CONTROLLER OPERATION

The pyrotechnic controller converts the planetary vehicle ac power to dc power, stores the energy, and switches it to fire the electroexplosive devices (EED) as required and commanded during the mission. The controller consists of six capacitor banks for storing firing energy, each capacitor bank having eight (or nine, depending on the number of EED's) firing circuits. Each capacitor bank has a separate current circuit for telemetry monitoring of the firing pulse amplitude.

The controller is enabled, at planetary vehicle separation from the launch vehicle, by the closure of either of two redundant separation switches, applying ac power to all transformer-rectifier (T-R) circuits. The transformers provide isolation between vehicle power and the pyrotechnic subsystem. A block diagram of the pyrotechnic controller is shown in Figure 1.

A schematic diagram, illustrating the basic design approach for one EED switching circuit, is shown in Figure 2. The circuit operates as follows. The separation switch closes upon separation of the planetary vehicle from the booster and applies ac power to the transformer. The output of the transformer, rectified by diodes CR1 and CR2, is used to charge the firing capacitor bank, C1, through the charge limiting resistor R1. Diodes CR3 and CR4 rectify ac power for charging telemetry capacitor C2. A command signal (a switch closure) applies current from the command bus to the gate circuit of silicon controlled rectifier SCR2 through R16, turning the rectifier on. When SCR2 turns on, the command signal then goes through the gate circuit of SCR1 through R3 and SCR2 to the command return. This causes SCR1 to turn on, discharging the firing capacitor C1 through both SCR's and the EED (Apollo Standard Initiator) bridgewire.

Instrumentation circuits are provided to monitor the capacitor voltages and to determine the relative amplitude of the firing pulse. The firing pulse is monitored by T2, which uses the firing cable as a single turn primary. The pulse amplitude, if it is of sufficient amplitude, breaks down zener diode CR6 and turns on SCR3. When SCR3 turns on, capacitor C4, which is charged through resistor R10, discharges through the primary winding of T3.

The secondary winding of T3 picks up the signal and turns on transistor Q1, sending an output pulse to the telemetry (T/M) subsystem. Transformer T3 provides isolation between the pyrotechnic controller and the T/M subsystem, as required by range safety requirements.

Command power is supplied by diodes CR8 and CR9, charging capacitor C7. Each firing capacitor bank has a command bus which is applied to the gates of the SCR circuits by the command decoder or computer and sequencer. All SCR gate circuits for one bank are

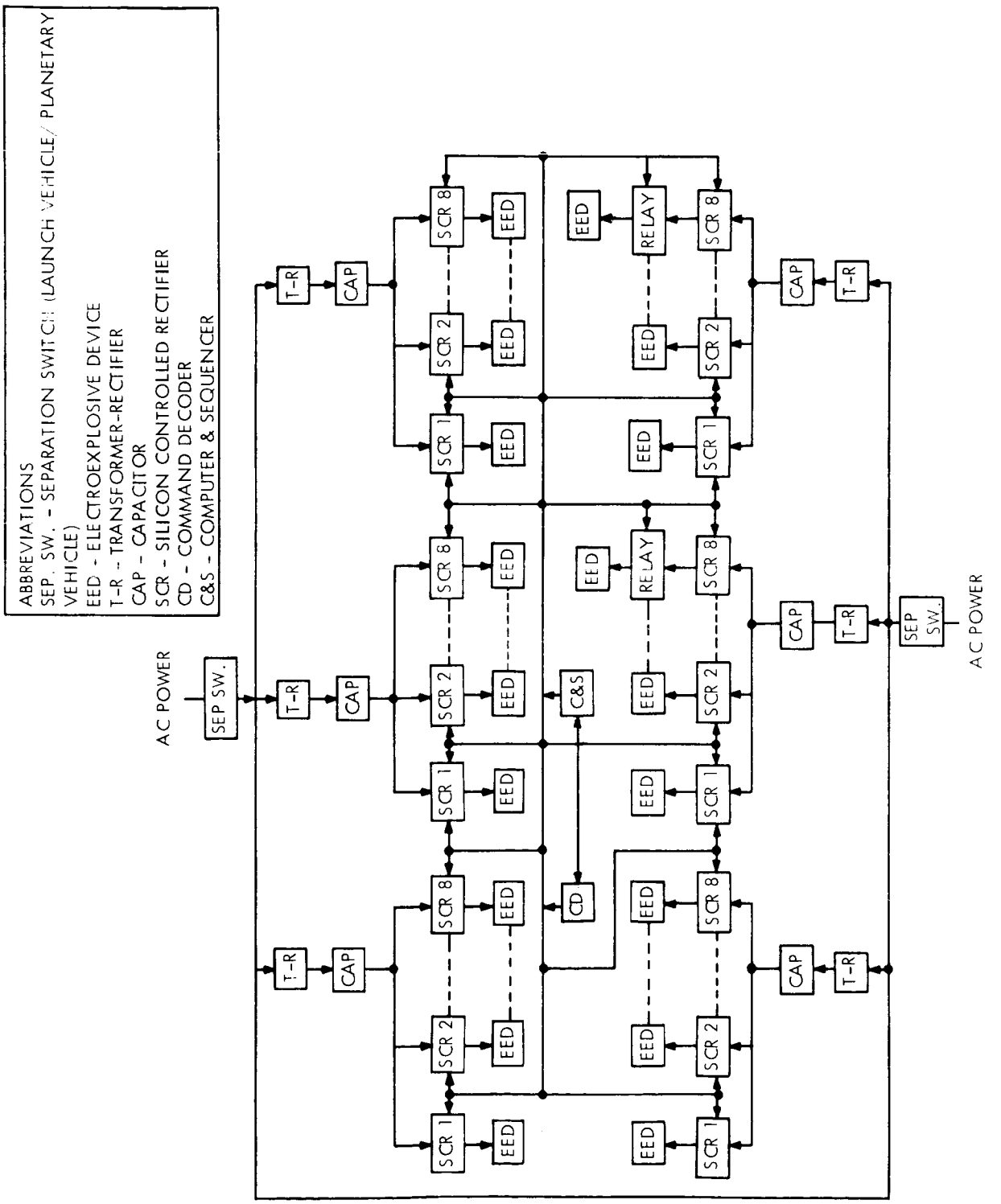

Figure 1. Block Daigram of Pyrotechnic Controller

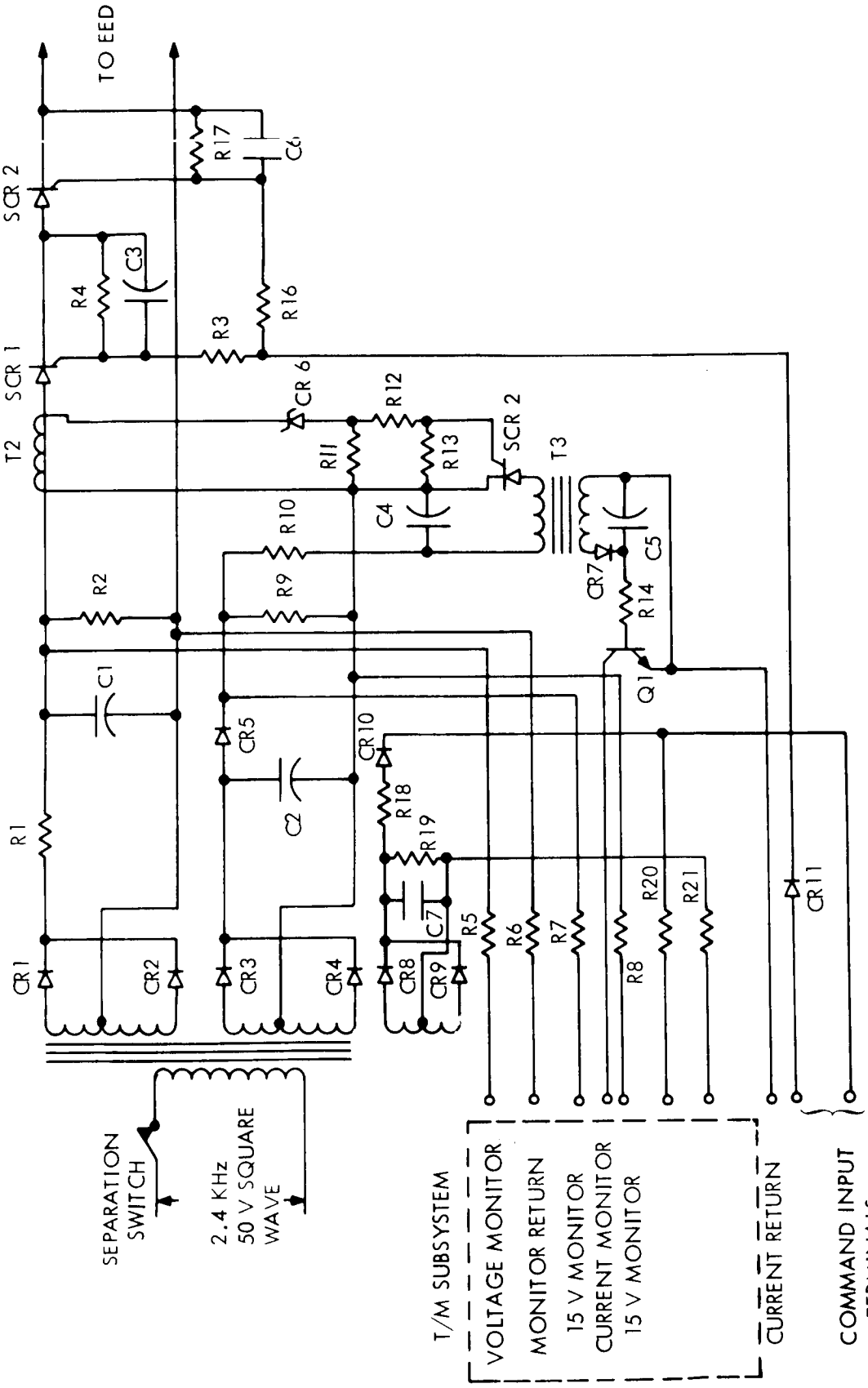

Figure 2. Pyrotechnic Switching Circuit For One Electroexplosive Device

connected to that command bus, and each command allows signals from the command bus to be sent to the proper gate circuits. Eight SCR circuits, identical to the one shown in Figure 2, are connected at all times for four of the six capacitor banks. Two capacitor banks have 7 SCR circuits connected at all times and each has one circuit disconnected by a relay for firing the final lock-up valves of the propulsion subsystem. The Apollo standard initiators (ASI's) used in the two propulsion valves are shorted through the normally closed contacts of the relay. A command to arm final lock-up switches the relay contacts connecting the ASI bridge circuit to the SCR. This circuit is illustrated in Figure 3.

Redundant initiation is provided for all pyromechanical devices, except for the pin-pullers which retract the inflight disconnect (IFD) and the explosive valves used in the propulsion subsystem. The IFD pin-pullers and the valves are not redundantly initiated but are used redundantly: two pin-pullers are used to retract the IFD with operation of either one capable of removing the IFD. The application of redundancy in the propulsion subsystem is explained in VOY-D-370.

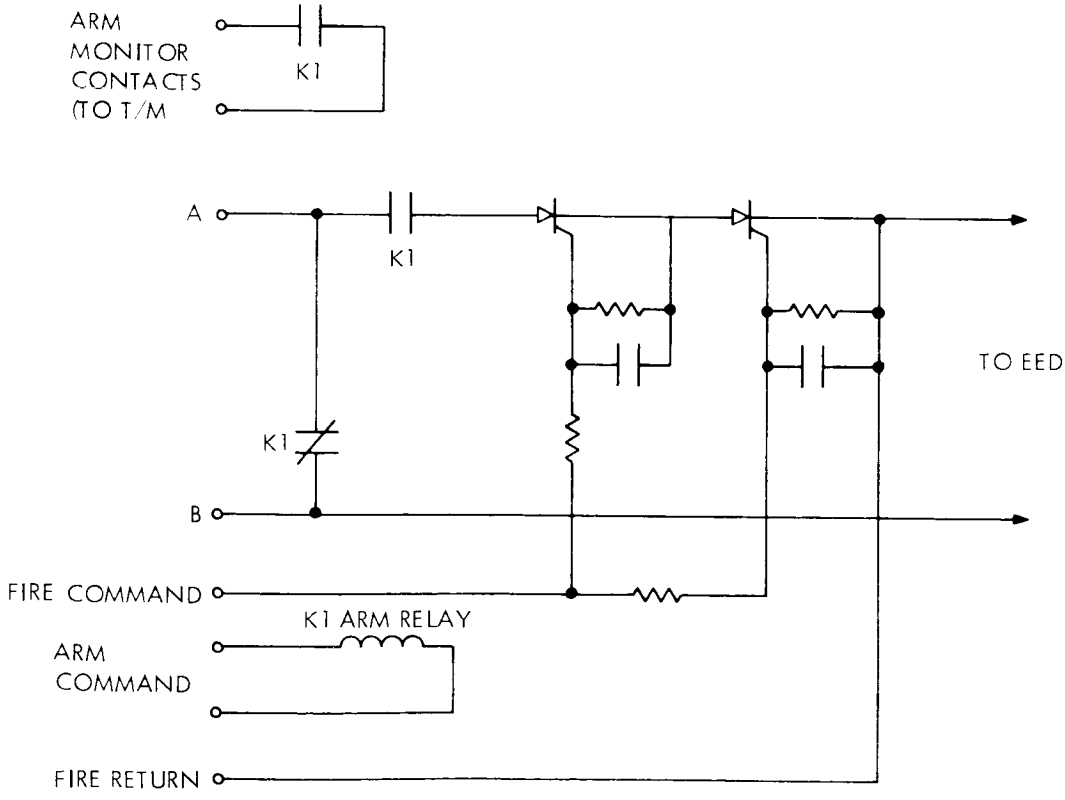

Figure 3. Final Lock-Up Firing Circuit

3.2. DESIGN CONSIDERATIONS - PYROTECHNIC CONTROLLER

The most important considerations in the design of the pyrotechnic controller are the holding current of the silicon controlled rectifiers and the total leakage current. One of the primary constraints on the firing circuits is that the firing capacitor must be disconnected from the ASI after initiation due to the low resistance between bridge pins after the ASI has been fired. The disconnection is accomplished by maintaining a capacitor charge current below the holding current of the SCR's. Therefore, as the firing capacitor discharges through the SCR's, the current drops below the holding current, is kept there by the charging resistor, and stops conduction through the SCR's. Two SCR's are used in series (see Figure 1) to prevent a single point failure from disabling the capacitor. That is, if a single SCR is used and it fails to stop conducting (due to any cause), current would flow through the fired ASI causing a decrease in voltage (and stored energy) on the firing capacitor. Therefore, the next firing from that capacitor would not switch sufficient energy to fire the ASI or any other ASI's connected to it. With two SCR's in series, both have to fail to disable the capacitor. The holding current of the SCR's limits the maximum charging current of the capacitor bank. The minimum charge current is determined by the total leakage current from the capacitor. Leakage currents will flow through the capacitor itself and through the SCR's to the ASI's connected to each capacitor.

Six capacitor banks are used in the Controller for the following reasons: (1) six ASI's can be fired at once, (2) the leakage current will be lower for a smaller number of devices connected to each capacitor, and (3) growth capability is provided. Forth-eight ASI's are required, of which 46 will be connected to capacitors during the mission. (The lock-up ASI's are disconnected by a safe-arm relay.) Thus four capacitors will have eight ASI's and two capacitors will have seven ASI's connected.

Examination of the characteristics of the SCR's shows that holding currents vary from 8 to 100 ma depending on the SCR current rating. For the larger current carrying SCR's, the holding currents are higher. Unfortunately, the leakage currents are also larger for these SCR's (3-5 ma). Since the typical characteristics of the SCR's overlap, that is, for low

leakage currents the holding currents are too low and for higher holding currents the leakage is too high, the characteristics of the SCR's must be specified and SCR's selected to meet them. These specifications are:

a. Maximum holding current - 50 ma

b. Minimum holding current - 20 ma

c. Maximum leakage current - 0.5 ma

d. Maximum peak conduction current - 50 amp

e. Minimum breakover voltage - 50 volts

These requirements are achievable; for example, the 2N1777 SCR has a typical leakage current of 1.0 ma when measured at 400 volts and 125°C. This is a pessimistic value; a typical value will be 0.1 ma or less at 50 volts. Therefore, specifying 0.5 ma maximum leakage is not unreasonable. The holding current of the 2N1777 is typically 8 ma but has a maximum of 50 ma. Therefore, limiting the holding current to 20 to 50 ma is also feasible. The 2N1777 has a peak current capability of 60 amperes, so it is possible that this SCR could be used. For these specified characteristics, the maximum leakage current from the firing capacitor through the SCR's will be 4.0 ma (8 x 0.5) for one capacitor. The charge current can then be limited to 15 ma, which is 5 ma below the holding current insuring SCR turn off.

Since the ASI can reliably be fired by a 91.4 microfarad capacitor charged to 29 volts, the capacitor in the pyrotechnic controller is chosen to be 660 microfarads charged to a minimum of 25 volts, allowing a sufficient margin. The leakage current for a polar, etched-tantalum-foil capacitor, 660 microfarads at 50 working volts dc, is 1.15 ma at 125°C (GE catalog No. 29F 3273). The total leakage current for a firing capacitor with eight ASI's is 5.15 ma and for a firing capacitor with seven ASI's is 4.65 ma. The capacitor voltage can be expressed as:

$$V_c = E_s - I_1 R_c$$

where

V_c = Capacitor Voltage

E_s = Source voltage (output of T-R)

I_1 = Total leakage current

R_c = Charging Resistor

and the maximum charging current is:

$$I_c = E_s/R_c$$

Substituting in the two equations, eliminating E_s; then rearranging and solving for R_c gives

$$R_c = \frac{V_c}{I_c - I_1}$$

since

V_c = 25 volts
I_c = 15 ma
I_1 = 5.15 ma.

Then R_c = 2.55 kilohms

and E_s = 38 volts.

This is the minimum source voltage for the above characteristics.

Since the power subsystem is distributing 50 volts ac, a 1:1 transformer can be used to produce a source voltage, E_s, for the controller, of 50 volts dc. Then the charging resistor will be 3.3 kilohms and the minimum capacitor voltage will be 33 volts. These characteristics are well above the minimum operating characteristics derived above.

Another problem which must be investigated is the decrease in capacitance due to low temperature. The decrease in capacitance cannot be defined until a realistic estimate of the temperature environment can be made. Derating of the capacitor can take into account this capacitance decrease to assure a high reliability firing energy.

3.3. INTERFACE REQUIREMENTS - PYROTECHNIC CONTROLLER

The pyrotechnic controller requires direct interfacing with the power, computer and sequencer, command decoder, and telemetry subsystems for its operation and control.

3.3.1. Power Subsystem Interfaces

The power required by the pyrotechnic controller will vary as the pyrotechnic events occur. During the periods when no events occur, the power subsystem must complement leakage with a maximum expected leakage power of 1.5 watts. When an event occurs, from one to six capacitors must be charged. The maximum charging is 15 milliamperes and therefore the maximum charging peak power required will be 4.5 watts, which will decay exponentially to zero in less than 20 seconds. The power peaks will occur at each pyrotechnic event, and the magnitude will depend on the number of capacitors which have been discharged.

3.3.2. Computer and Sequencer and Command Decoder Subsystem Interfaces

Commands to fire the various pyrotechnic devices will originate from the computer and sequencer (C&S). The command decoder will be used as a back-up system and will provide the capability of issuing all commands from the ground. The primary commands will be issued from the C&S, updated as required, and sent to the pyrotechnic controller at the proper time. The commands will be in the form of a transistor switch closure for 60 ±10 milliseconds. All commands, except the lockup arm command, will be used to allow signals from the command bus, in the pyrotechnic controller, to gate silicon controlled rectifiers. The lockup arm command will be used to switch two relays.

3.3.3. Telemetry Subsystem Interface

The pyrotechnic subsystem requires telemetry signals for the capacitor voltages, the firing pulses, and the position of the lockup arm relays. Six firing capacitors, six command capacitors, and six telemetry capacitor voltages will be monitored. Resistors are provided in the pyrotechnic controller to electrically isolate the controller from the T/M subsystem for these measurements. Each of the firing capacitor banks will use the main firing bus as

a single turn primary for the firing pulse monitor transformer. Each firing pulse, of the proper amplitude, will cause an electrical signal to be sent to the T/M subsystem. Firing pulses which do not have the correct amplitude will not trigger the monitor circuit. The lockup arm relay will provide contact closure for monitor purposes. When actuated, the monitor contacts will open.

4. ELECTRICAL HARNESSING

The electrical harnesses for the Voyager spacecraft consist of two main ring harness assemblies of many individual cables, six separate system interconnecting cables not part of the main harness, individual bay harnesses for each of the 15 electronics assemblies, and in-flight disconnecting cables to the launch vehicle and flight capsule. The harnessing has been designed to provide for the reliable transfer of electrical energy between related spacecraft subsystems and planetary vehicle interfaces throught the ground test, launch, and spacecraft flight operations.

In general, the harnesses are composed on one or more cables of insulated and twisted wires, either shielded or unshielded, bundled together and terminated at the ends by connectors. The harnessing for the Pyrotechnic Control is handled differently. All firing cables from the pyrotechnic controller to each Apollo standard initiator are twisted shielded pairs, balanced to and isolated from a continuous shield surrounding each pair. Firing circuits are routed separately from other wiring and do not go through any in-flight separation connectors. The ground return for the pyrotechnic subsystem is isolated from other subsystem grounds.

Based on design studies conducted during the system update activities, round wire cables and polyimide (Kapton) wire insulation have been selected for use in the electrical harnessing. Both choices can only be tentative at this time, due to the significant advances currently being made in industry in the design of wire cables and connectors. Further discussion of these design studies is presented in Paragraph 4. 5.

4.1. MAIN SYSTEM HARNESS

The main system harness consists of two rings (upper and lower) of individual cables, each capable of independent definition, fabrication, test, and installation. Figure 4 is an exploded view of the spacecraft depicting the two main harness rings. The harnesses are pre-assembled into a ring-type supporting structure and mount into the spacecraft above and below the electronic bays. The installed structure is utilized for the supplementary support of other spacecraft items, such as pneumatic lines and tank cradles.

Both the upper and lower harness rings provide cable interconnection between the various subsystems and electronic bays, and provide electrical test points. Figure 5 is a cut-away view of the electronic module, depicting typical upper and lower main harness ring connections at any one electronic bay. The design of the harness and support structure provides

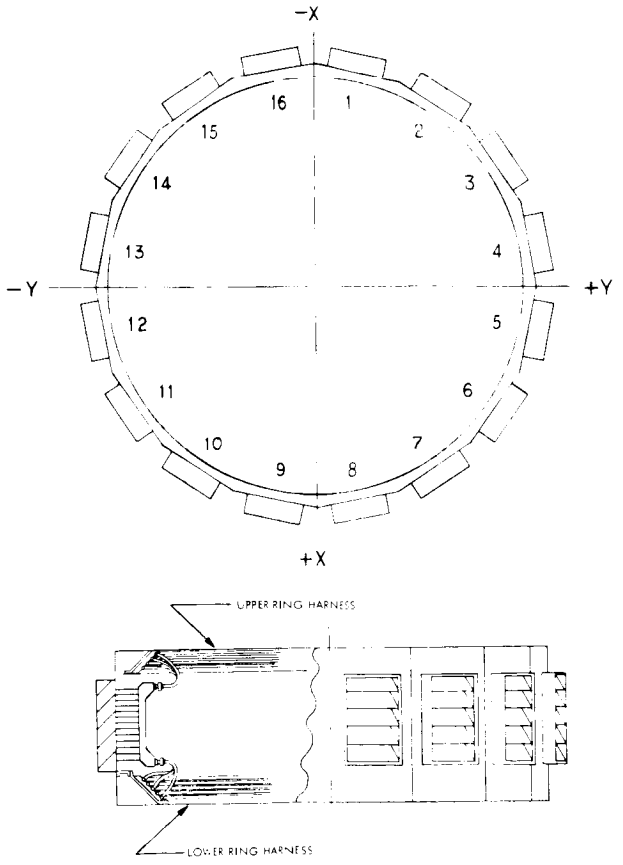

Figure 4. Spacecraft Exploded View

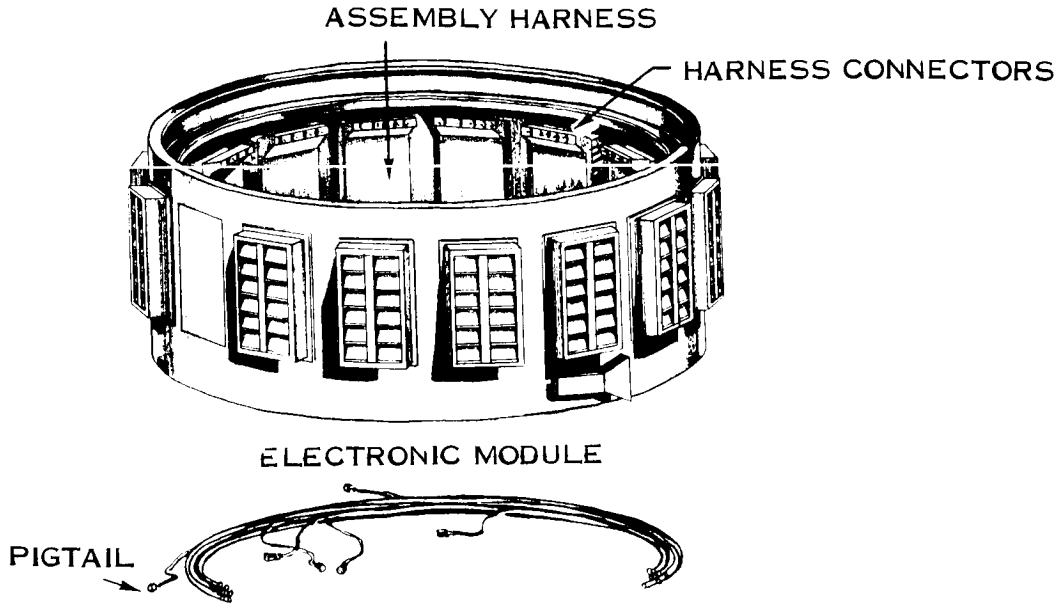

Figure 5. Electronic Module Cutaway

ready access to the test points and facilitates assembly and modification. Individual cables may be removed without removing the entire harness assembly. Breakouts of pigtails from the harness, as shown in Figure 5, mate to hard-mounted connectors at the top and bottom of each Level III electronic assembly.

4.2. OTHER SYSTEM CABLES

Individual cables connect the Canopus sensor, planet scan platform, and capsule to the system by means of connectors on the associated bays. The flexible cable to the scan platform accommodates the position changes of this unit through deployment, retraction, and the required operational scan angles.

4.3. BAY ASSEMBLY HARNESS

Each bay assembly harness, as shown in Figure 5, is an individual unit providing separate signal, command, telemetry, and power bundles from the subsystem assembly connectors

to the respective signal connectors and insulated copper bus bars. Interconnections between subassemblies generally follow the bundle groupings with short direct connections routed to cross the bundles at right angles. All interface connectors are hard mounted to the bay assembly chassis; float being provided in the connector to minimize alignment problems. System harness connectors are provided at both the top and bottom of each electronic assembly.

4.4. IN-FLIGHT DISCONNECTS

The cables to the launch vehicle and capsule interfaces are each terminated in connectors which form part of an in-flight disconnecting device at the separation joints. The launch vehicle cable forms part of the main ring harness, while the capsule cable is one of the individual cables at the top of the spacecraft.

4.5. ALTERNATIVE CONSIDERATIONS

During the system update activities, a design study was performed to evaluate some significant advances in wire cabling and insulation as they might be applicable to Voyager.

4.5.1. Wire Cable Study

The applicability of utilizing flexible flat cable for Voyager electrical interconnections was studied. It was found that flat cable harnesses can provide a significant weight savings; 50 percent and more over conventional round wire harnesses in some applications. However, experience to date concerning reliability indicates the need for further development in several areas. Although much developmental work has been performed at NASA's Astrionics Laboratory, particularly on techniques for handling and mating flat cable, indications are that the changeover to flat cable technology is not necessarily simple. Before flat cable can be recommended for Voyager, studies in depth should be made of environmental performance, stripping processes, repair and replacement methods, and mounting and attachment techniques.

4.5.2. Insulation Study

A comparison was made of polyimide-coated wire (Kapton, Spacewrap) and polyolefin-coated wire (Kynar). The study indicated that Kapton is superior to Kynar in the following areas:

a. Abrasion resistance.

b. Flexibility (especially at low temperatures).

c. Temperature range.

d. Outgassing.

e. Cut-through resistance.

Furthermore, the use of Kapton may also allow a significant weight saving. According to data published by Haveg-Supertemp, a 20 AWG Kynar wire with a weight of 4.57 pounds per 1000 feet is recommended for a 10 ampere capacity. However, Kapton wire of only 24 AWG, at 2.17 pounds per 1000 feet is necessary for the same rating. This reduction is possible as a result of the improved temperature rating, which permits use of a higher AWG number wire. Where identical AWG sizes are required in order to minimize voltage drop, the weight differential is not significant.

Kapton insulated wire is now being considered for many advanced spacecraft systems such as Apollo "LEM". Titan III, the Manned Orbiting Laboratory, and the gravity gradient satellite are all using Kapton. In consequence, it appears that polyimide (Kapton) cable harness material is most suitable for Voyager.